Modeling and Optimal Control for Aging-Aware Charging of Batteries

MODELING AND OPTIMAL CONTROL FOR AGING-AWARE CHARGING OF BATTERIES

Proefschrift

ter verkrijging van de graad van doctor aan de Technische Universiteit Eindhoven, op gezag van de rector magnificus prof.dr.ir. F.P.T. Baaijens, voor een commissie aangewezen door het College voor Promoties, in het openbaar te verdedigen op dinsdag 9 november 2021 om 16:00 uur

door

Zuan KHALIK

geboren te Salah Eddin, Irak.

Dit proefschrift is goedgekeurd door de promotoren en de samenstelling van de promotiecommissie is als volgt:

voorzitter:	prof.dr.ir. P.M.J. Van den Hof
promotoren:	prof.dr.ir. H.J. Bergveld
	dr.ir. M.C.F. Donkers
leden:	prof.dr. P.H.L. Notten
	prof.dr. F.M. Mulder (Technische Universiteit Delft)
	prof.dr.ir. M. Kinnaert (Université Libre de Bruxelles)
	prof.dr. S.J. Moura (University of Calfornia, Berkeley)
	prof.dr. D.M. Raimondo (Università di Pavia)

Het onderzoek dat in dit proefschrift wordt beschreven is uitgevoerd in overeenstemming met de TU/e Gedragscode Wetenschapsbeoefening.

This work has received financial support from the Horizon 2020 programme of the European Union under the grants 'Electric Vehicle Enhanced Range, Lifetime And Safety Through INGenious battery management' (EVERLASTING-713771) and 'Advancing fail-aware, fail-safe, and fail-operational electronic components, systems, and architectures for fully automated driving to make future mobility safer, affordable, and end-user acceptable' (AutoDrive-737469).

disc

This dissertation has been completed in fulfillment of the requirements of the Dutch Institute of Systems and Control (DISC) for graduate study.

Cover design by Erwin Timmerman and Zuan Khalik
Printing: ProefschriftMaken

A catalogue record is available from the Eindhoven University of Technology Library
ISBN: 978-90-386-5382-2

SUMMARY

Batteries have enabled the advent of electrified vehicles, which have the potential to reduce the output of harmful gases into the environment. A major challenge is to reduce the charging time of these batteries, while ensuring that the batteries do not age too quickly. Conventional charging algorithms use current and voltage constraints, while aging is determined by internal conditions that cannot be expressed in terms of current and voltage constrains. Thus, there is a need to develop more advanced charging algorithms that allow for a better trade-off between charging time and aging than the current methods can achieve.

A way to achieve this better trade-off between charging time and aging is to use an optimal-control-based approach. In doing so, the battery can be operated less conservatively, without making a sacrifice in battery aging, by computing an optimal charging current based on estimated internal states of the battery. These internal states can be obtained from electrochemistry-based battery models, such as the Doyle-Fuller-Newman (DFN) model. However, using electrochemistry-based battery models in battery management systems remains challenging due to their computational complexity and due to the difficulty of uniquely determining all model parameters. This thesis focuses on reducing the computational complexity of the DFN model, methods to parameterize the DFN model, and using the DFN model for the purpose of aging-aware charging.

In the first part of the thesis, we focus on battery modeling and parameterization. Here, we study for the first time the impact of several types of model simplifications on the trade-off between model accuracy and computation time for the DFN model. As a basis for comparison, we consider the so-called complete DFN (CDFN) model, which is a DFN model without any simplifications, and which includes the concentration dependency of parameters that have been studied in previous literature. Furthermore, we propose a highly efficient implementation of the CDFN model that leads to a considerable decrease in computation time, and that has been developed into a freely downloadable toolbox. We compare several simplified DFN models to the so-called single-particle model and the CDFN model. Here, we show that with the proposed implementation, and by selectively making the proposed simplifications, as well as selectively choosing the grid parameters, a model can be obtained that has a minor impact on model accuracy, achieving a simulation time of over 5000 times faster than real-time.

Furthermore, we propose a model parameterization approach of the DFN model, by first reparameterizing the DFN model through normalization and grouping, followed by a sensitivity analysis and a parameter estimation procedure. In the parameter estimation procedure, we show the influence of the number of estimated parameters, as well as the influence of the data length of the identification data, on the obtained model accuracy. Additionally, the model with parameters obtained using the proposed parameterization approach is compared to a model whose parameters have been obtained using cell teardown. Finally, the consistency and accuracy of the parameter estimation procedure is

analyzed by applying the estimation routine to a synthetic cell, represented by a DFN model with randomly chosen parameters. The results of this analysis show that while applying cell teardown to determine parameters can lead to more physically meaningful parameters, the parameter estimation approach that uses current/voltage data can lead to a significantly better output accuracy, which suggests a parameter estimation approach that combines both these methods.

In the second part of the thesis, we focus on aging-aware charging methods. In this part, we firstly utilize a DFN model including capacity-loss side reactions to present a model-based design method for multi-stage charging protocols. This design method allows for making a trade-off between charging time and battery aging in a more systematic way. We show that by obtaining the Pareto front that describes the optimal trade-off between charging time and battery aging for a single cycle, the results can be extended to the lifetime of the battery. Finally we show that the negative-electrode over-potential is not always a good indicator for aging, and that aging will occur even when the battery operates in over-potential regions that are considered not to lead to aging.

Furthermore, in the second part, we also present two optimal-control-based methods for aging-aware charging. The first approach uses a surrogate model. Here, a surrogate modeling approach is used to approximate aging-related DFN model states, where the surrogate model is a combination of a black-box finite-dimensional linear-time-invariant model and a static nonlinear model that is a function of the state-of-charge. We formulate the optimal-control problem as minimizing the side reactions for a given charging time and subject to several aging-related constraints that are commonly used in literature. We show that the aging-related DFN model states can be well approximated by the proposed surrogate model, with a significantly decreased computation time, allowing it to be used in an online closed-loop control setting. We also compare the Pareto front achieved with the proposed optimal-control-based method with the Pareto fronts achieved with various multi-stage charging protocols. Here, we show that the proposed optimal-control-based method achieves a significantly improved Pareto front over the multi-stage charging protocols.

In the second approach to optimal aging-ware charging, we use the (simplified) DFN model. We formulate the optimal-control problem as minimizing the side reactions for a given charging time, and solve this optimal-control problem using sequential quadratic programming (SQP). We compare the performance of the optimal-control-based method using various simplified DFN models, and compare it against the optimal-control-based method using the surrogate model and various multi-stage protocols. Here, we show that a significant reduction in computation time of the solution to the optimal-control problem can be achieved by using the proposed SQP algorithm, rather than using an off-the-shelf solver.

In the final part of the thesis, experimental results on optimal aging-aware charging are presented. Here, the aging resulting from the optimal-control-based method using the DFN model and a multi-stage charging protocol are experimentally compared.

CONTENTS

1

INTRODUCTION

1.1. MOTIVATION

In today's world, transportation is a key element of our society. However, as many modes of transportation rely on combustion engines, over the past decades, transportation has also had an enormous negative effect on society. The massive output of greenhouse gases that are the product of combustion engines have had a significant role in the global warming of the earth. In 2018, out of all transportation modes, road transportation accounted for 72% of greenhouse gas emissions [1]. In an attempt to reduce these harmful effects, road vehicles have been increasingly electrified. Hybrid electric vehicles (HEVs) can be seen as a first step in electrification. While HEVs still emit greenhouse gases, they offer the potential to reduce the fuel consumption of a vehicle by adding an electric motor with a high-voltage battery to a conventional powertrain. To fully eliminate the emission of greenhouse gases, battery electric vehicles (BEVs), have been considered a promising option, under the assumption that the electricity used to propel BEVs is produced from renewable energy sources. As BEVs have a completely electric powertrain consisting of a battery and an electric motor, they do not emit any greenhouse gases directly, which also means that BEVs do not contribute to local environmental issues, such as poor air quality. For these reasons, BEVs have seen a considerable growth over the past decade, and it is predicted that the global BEV stock will reach almost 150 million by 2030 [2], as shown in Fig. 1.1.

However, there are still key issues that need to be addressed before BEVs become widely accepted. One of the major issues identified is range anxiety [3, 4], which is the fear that the battery in the vehicle depletes before the next charging station is reached. Range anxiety is caused by several factors. One of the major factors is the limited range that BEVs provide compared to conventional vehicles. Furthermore, while conventional vehicles can be refueled in a matter of minutes, charging a BEV takes much longer, which has created a need for fast charging. Finally, since a battery replacement in a BEV can be expensive, consumers are concerned about battery life expectancy [4]. To tackle these

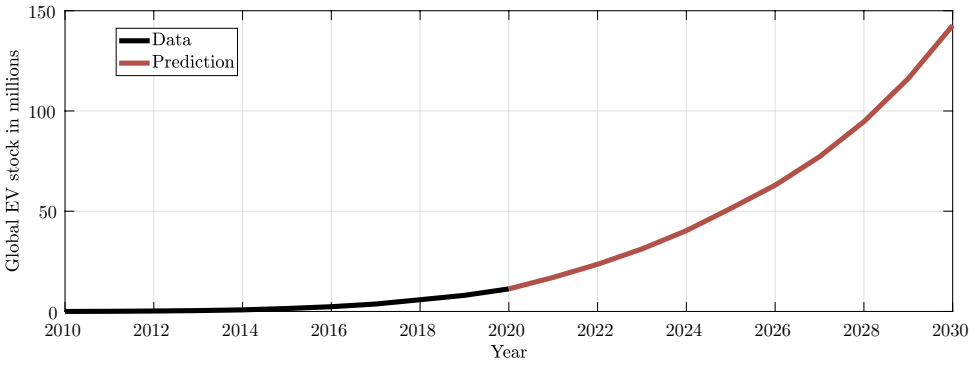

Figure 1.1: The growth of BEVs over the past decade, and the predicted growth. Adapted from [2].

issues, there are several approaches that can be taken

1. Improving battery technology to achieve more energy-dense batteries.
2. Extending the charging infrastructure.
3. Highly efficient powertrains.
4. Improving range prediction.
5. Developing aging-aware charging algorithms to allow for faster charging and limiting battery aging.

Improving battery technology seems to be the most logical choice to tackle range anxiety, by extending the range with more energy-dense batteries. Over the past decade, Li-ion batteries have grown rapidly in use, due to their high energy density and relatively long cycle life, compared to Nickel-based and lead-based batteries [5]. Meanwhile, Li-ion battery technology is continuously being improved as well [6, 7], leading to increasingly larger energy densities. Another way to extend the range is through highly efficient powertrains, where, e.g., energy management strategies [8] can be used in order to use the battery more efficiently. Coupled with that, the prediction of the range that the vehicle can drive can be improved so that the user can put more trust on the indicated range, which would alleviate the fear of not being able to reach the next charging station [9]. On the other hand, extending the charging infrastructure can ensure the user that there is always a reachable charging station nearby to reduce the anxiety of running out of energy.

Finally, in the approach of developing improved charging algorithms, the aim is to reduce charging times as well as limiting battery aging. However, reducing charging time and battery aging are generally two conflicting objectives. Still, a shorter charging time does not necessarily result in increased battery aging, if improved charging algorithms are used. The problem of finding such a charging algorithm can be described as an optimal-control problem that maximizes the trade-off between charging time and battery degradation. The main advantage of this approach is that an improved charging

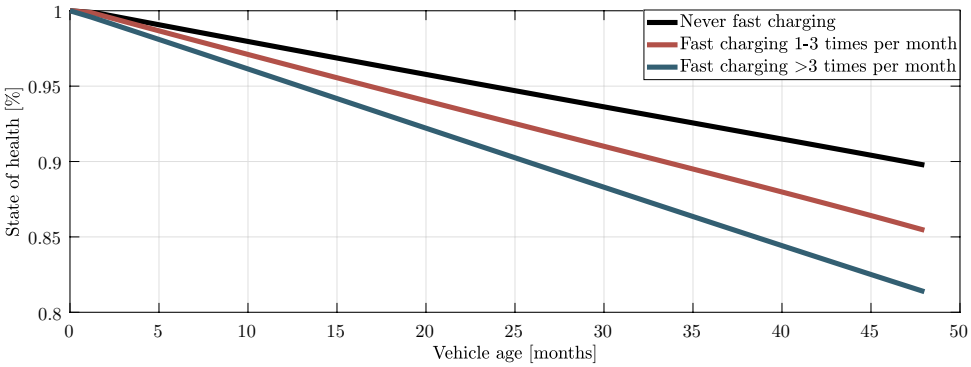

Figure 1.2: The impact of fast charging on battery degradation in BEVs in seasonal or hot climates. Adapted from [10].

algorithm is relatively easily implementable and does not require large hardware modifications, provided that the battery charger satisfies the required hardware specifications.

As mentioned before, besides range anxiety, another issue in BEVs is the concern by potential users that the battery does not last as long as expected, since the battery is an extensive component of a BEV [3, 4]. Meanwhile, current usage data of BEVs has shown that if the current degradation rates are maintained, the vast majority of batteries will outlast the usable life of the vehicle [10]. However, current BEV usage data has also shown that frequent fast charging of batteries has a significant effect on battery health, particularly in hot climates [10], as is shown in Fig. 1.2. This is particularly relevant for commercial BEVs, such as electric taxis or buses, where frequent fast charging, or aging-aware charging, is desired to operate the vehicles for as much time as possible. Therefore, aging-aware charging, mainly focused on Li-ion batteries, will be the topic that is treated in the remainder of this thesis, and the main objective of this thesis is given by:

Global Objective

Contribute to a more sustainable society by accelerating the adoption of electric vehicles through the advancement of aging-aware charging methods

1.2. AGING-AWARE CHARGING STRATEGIES

Generally, Li-ion batteries are charged using a so-called Constant-Current Constant-Voltage (CC-CV) protocol, see e.g., [11]. A CC-CV profile can be seen in Fig. 1.3a, where the battery is initially charged with a constant current $I_{\max}$, until a certain threshold voltage $V_{\max}$ is reached. Following this, the CV stage takes place, in which the voltage threshold is maintained until the current has decreased to a certain set value $I_{\min}$. The three parameters $V_{\max}$, $I_{\max}$ and $I_{\min}$ can be chosen freely, although usually $I_{\min}$ is preselected, since it defines when the battery is considered to be fully charged. Therefore, while increasing $I_{\min}$ leads to a shorter charging time, it will also result in a battery that has a relatively lower charge. Hence, the two tuning parameters are $V_{\max}$ and $I_{\max}$, and

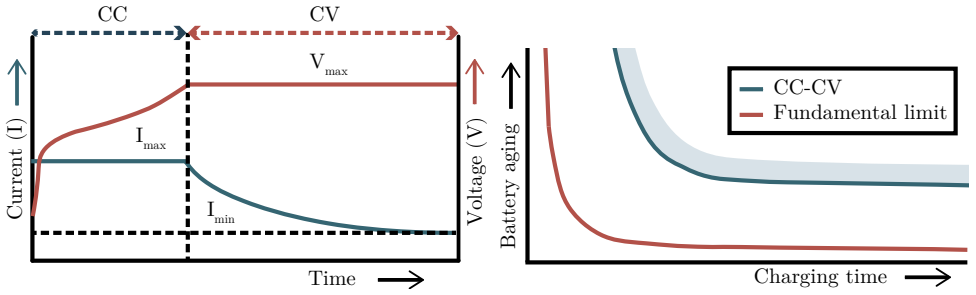

Figure 1.3: In (a), a schematic visualization of the CC-CV protocol is shown, and in (b), a sketch of the Pareto front for the CC-CV protocol and the fundamental limit that can be achieved is shown. The shaded blue region represents the objectively worse combinations of charging time and battery aging for CC-CV.

ideally, they should to be chosen to aim for a short charging time without battery degradation. However, while increasing $V_{\max}$ and $I_{\max}$ will lead to a shorter charging time, it will also quickly lead to a high battery degradation [12], which indicates that there is a trade-off between charging time and battery degradation. Hence, each combination of $V_{\max}$ and $I_{\max}$ will lead to a certain charging time and battery degradation, which are not uniquely determined, i.e., there may be multiple combinations of $V_{\max}$ and $I_{\max}$ to achieve a certain charging time and battery degradation.

However, there may also be combinations of $V_{\max}$ and $I_{\max}$ that have an objectively better performance (in the sense of charging time and battery degradation) than other combinations of $V_{\max}$ and $I_{\max}$, e.g. when one combination of $V_{\max}$ and $I_{\max}$ gives a certain charging time and battery degradation, while another combination gives a lower charging time with the same battery degradation. Note that the performance of these combinations also depends on ambient conditions. For example, for a different operating temperature, a different combination of $V_{\max}$ and $I_{\max}$ might be better. These combinations of $V_{\max}$ and $I_{\max}$ that give an objectively better charging performance, form the upper bound in charging performance that the CC-CV protocol can achieve, which is referred to as the "Pareto front". An illustration of this Pareto front for the CC-CV protocol can be seen in Fig. 1.3b. Note that there is not a single combination of charging time and battery degradation on the Pareto front that can be defined as the “best" charging performance. Objectives set on the charging performance determine which point of the curve in Fig. 1.3b is picked, e.g., an objective may be that a battery needs to be charged in a certain amount of time with minimal battery degradation. Then, the best charging performance that can be achieved is the battery degradation value at the required charging time on the trade-off curve.

Although the CC-CV protocol has low complexity and is easily implemented, intuitively, if more freedom is allowed in the charging profile, there may be better combinations of charging time and battery degradation than what CC-CV can achieve. This is the ultimate goal in aging-aware charging: to find charging strategies that allow for a better Pareto front, or the Pareto optimal front, which would be the fundamental limit of what can be achieved with any charging strategy and considered battery chemistry. This

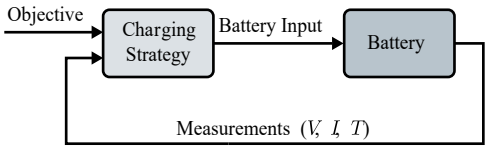

Figure 1.4: Topology of a battery charging system.

is again indicated in Fig. 1.3b. The ideal charging strategy would operate at the fundamental limit, although a strategy that lies in between the CC-CV protocol and the fundamental limit is also an improvement. Note that finding the Pareto front of any charging strategy is not trivial. It would require many experiments to identify this curve. Instead, charging strategies directly aim for a point on the Pareto front belonging to that strategy through objectives, by e.g., charging the battery with a certain charging time with the least possible ageing.

A high-level topology of a battery charging system can be seen in Fig. 1.4. The charger has a certain charging strategy that determines the battery charging input (charging voltage or current), based on a user-defined objective and measurements. Possible configurations for charging strategies can be seen in Fig. 1.5. From top to bottom, the configurations, on an implementation level, range from least complex to most complex. We will review these strategies below.

RULE-BASED CHARGING STRATEGIES

Rule-based chargers are a natural extension to the CC-CV charging protocol (which is a rule-based protocol as well) and determine the battery input based on a set of rules, which are set through an objective. A category of rule-based protocols are multi-stage CC-CV (MCCCV) protocols, which consider multiple CC or CV stages (rather than the standard CC-CV protocol) [13, 14]. Pulse-based protocols are another class of rule-based protocols, in which the battery is charged using charge pulses. The justification for this protocol is that short discharge pulses interspersed during the charging process can significantly decrease the concentration polarization, and increase the charging efficiency, thereby decreasing battery aging, which allows for a faster charging rate [15]. The justification for pulse-charging is debated in literature [15–17], since the exact reason for why pulse charging would result in any improvement is not known. In [18, 19], the battery degradation for a lithium-ion battery resulting from conventional CC-CV, multi-stage CC-CV charging protocols, and pulse-based charging protocols is compared. A final category of rule-based protocols are fuzzy-logic-based protocols e.g., [20, 21], in which fuzzy rules are defined based on intuitive understanding of the battery.

Just as in the CC-CV protocol, the aim in tuning the various tuning parameters or rules in rule-based protocols, such as the threshold voltages or pulse frequencies, is for the charging performance to fall on the Pareto curve. The aforementioned papers select the parameters based on intuition or by performing experiments for several sets of parameters, which provides no guarantee or even indication that the chosen set of parameters leads to a charging performance that lies on the Pareto curve. In principle, to find a point on the Pareto curve for the rule-based protocols, all possible sets of param-

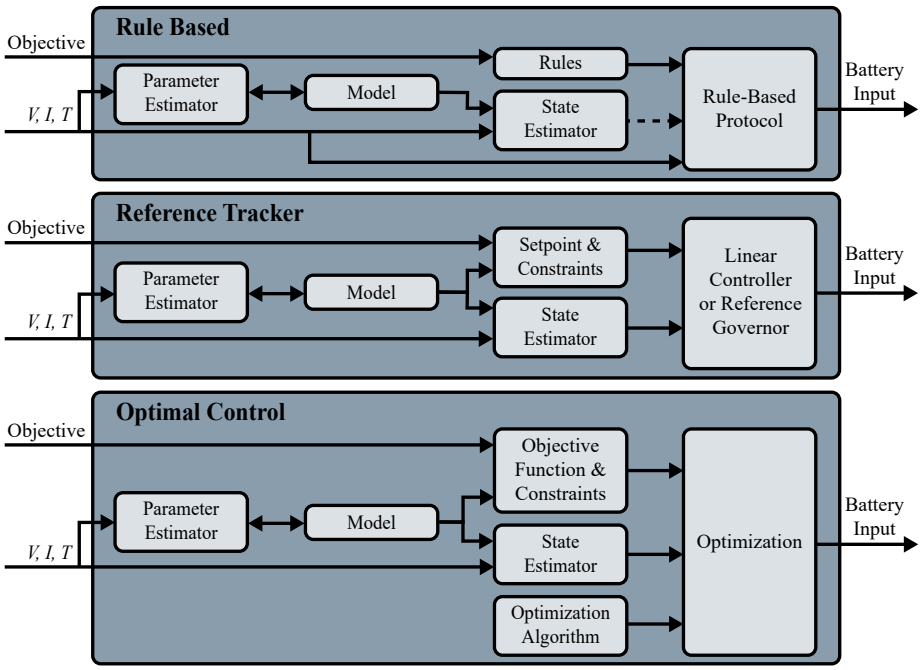

Figure 1.5: Possible configurations for aging-aware charging.

eters would have to be tested, which would require a large amount of experiments. In [22–24], the required number of experiments to find a point on the Pareto curve is substantially reduced using a so-called “Taguchi" method. However, such methods rely on aging indicators, such as charging efficiency or charged capacity, which are not directly related to ageing, and therefore the parameters that are found through these methods may not be optimal. Various other approaches use optimization techniques to select the parameter sets using experimental data for MCCCV, e.g. integer linear programming in [25], ant-colony-system algorithm in [26], particle-swarm optimization in [27], and machine learning in [28]. In [29–31] various search-based systems are designed to find optimal pulse frequencies. Note that in these papers rules are optimized using measurable indicators that affect battery degradation, such as battery efficiency [22, 25] or the impedance of the battery [30]. However, these battery degradation indicators do not consider the actual battery aging effects and may provide a conservative estimate of battery degradation.

Some of the aforementioned papers i.e., [22, 25, 28] use state-of-charge (SoC) information in the definition of the rules. Since SoC is an internal battery state that cannot be measured, a state estimator is needed to estimate the SoC, for which a model is required. However, even though an additional estimator is required for these charging strategies, the complexity is not much higher than rule-based strategies which do not require state estimators, since the strategy still revolves around a set of rules, and a large amount of literature and commercial systems already exist for SoC estimation.

While rule-based chargers are relatively simple in implementation, they have several disadvantages:

1. As mentioned before, generally a large number of experiments is required to find optimal rules. These experiments will have to be done for every different battery chemistry, unless more general (but conservative) rules are used that can apply to several battery chemistries.

2. Even when an optimal set of rules is found, rule-based protocols are not robust to changes in the battery behavior, that is, when the battery behavior ages differently than expected, because it is used under different ambient conditions, the set of rules found may not be optimal anymore.

REFERENCE TRACKER & OPTIMAL CONTROL

The reference tracker strategy and optimal-control strategy stem from a more control-theoretic approach. Reference trackers use a model to estimate internal battery states, such as lithium-ion concentration and battery over-potential, to constrain the battery from reaching states that result in battery degradation, while following a certain specified reference. Generally, the approach is to use a relatively simple controller such as a proportional-integral-derivative (PID) controller [32, 33] or a pulse-generating controller [34] to track a specified threshold on the measured or estimated states, such that this threshold is not exceedingly violated. Another way to achieve constraint satisfaction is through the use of more complex controllers, that allow for improved constraint satisfaction compared to the relatively simple controllers mentioned above, such as a reference governor [35, 36], generic model control [37], or linear quadratic tracking [38]. While reference trackers focus mostly on constraint satisfaction, optimal-control-based approaches use an optimization problem that is solved with the aim to find the optimal solution for the given objective and constraints. The problem can be solved off-line, i.e., the optimization problem is solved once and the obtained optimal current profile is implemented. The outcome of the off-line optimal-control problem can be used to charge the battery. However due to modeling errors, constraint admission is not guaranteed, which makes the off-line optimal-control approach mainly useful for analysis, and not for implementation. In order to make sure that constraints are not violated, the optimal-control problem can solved in closed-loop, i.e., the optimization problem can be updated routinely to compensate for modeling errors. Implementation-wise, closed-loop optimal control is similar to model-predictive control (MPC), with the difference being that the objective function in optimal control is chosen to be the actual objective of the problem, while in classical MPC, a quadratic objective function is chosen with weights to penalize the input and states. However, while solving an optimal-control problem gives the optimal solution, the solution is actually only as optimal as the model used in the optimization is accurate. Furthermore, for non-convex optimization problems, which may be the case for the considered optimization problem, a global solution is not guaranteed. Finally, an additional disadvantage of the optimal-control approach is that the requirement of solving an optimization problem can be computationally expensive. Nevertheless, optimal control is the only tool that can guarantee at least some level of optimality, and allows for making a systematic trade-off between aging and charging time.

1

In the following section, we will elaborate on the state of the art in optimal control for aging-aware charging.

1.3. STATE OF THE ART

The contributions in model-based optimal control for aging-aware charging in literature can be classified using three main aspects: models, optimization problem formulation and solution methods. In this section, we will elaborate on each of these aspects. Specifically, in Section 1.3.1, we will specify the types of models used to model the main reactions of the battery as well as the models used to describe battery aging. Here, we will also show the state of art in the parameter estimation of electrochemistry-based models, since having an accurate model is essential for the optimal-control approach. The modeling aspects will be described specifically for a Li-ion battery. In Section 1.3.2, we will describe how the optimal-control problem for aging-aware charging is formulated. Finally, in Section 1.3.3, we will show how the optimal-control problems are solved.

1.3.1. BATTERY MODELING

Li-ion batteries are complex and highly nonlinear systems, which can in turn lead to highly complex models, depending on the model purpose. Generally, most of the literature is focused on modeling the effects that result from the main (desirable) reduction-oxidation reactions in the battery. However, alongside the main reactions, additional (undesirable) side reactions and other degradation phenomena occur in the battery that lead to battery aging. Since the side reactions occur at a lower rate, their effects are less noticeable on a short time scale, which means that the effects only really start showing up after a large number of charge-discharge cycles. In this chapter, we will refer to the models that describe the effects that occur from the main reactions and side reactions as “main-reaction models" and “aging models", respectively. In main-reaction models, it is assumed that side reactions do not occur, which is a fair assumption on a short time scale. In literature, most of the control-oriented main-reaction and aging models fall into two categories. In the first category, models are derived from first principles, which allows the models to provide more insight into the internal (non-measurable) states of the battery. In the second category, an empirical modeling approach is taken in which a (possibly generic) model is fit to a set of data, which is mainly used to model the measured behavior of the battery. As there is literature available that already provides an overview on battery modeling e.g., [39, 40] for main-reaction models and [41] for aging models, we will aim to only provide a short review of battery modeling aspects.

MAIN-REACTION MODELS

For main-reaction models, empirical models exist in the form of equivalent-circuit models (ECM) [11], in which the battery behavior is modeled with circuit elements, such as shown in Fig. 1.6. In this figure, the ECM consists of a voltage source in combination with a resistor and 2 resistor-capacitor pairs. However, in general, there could be any number of resistor-capacitor pairs, as well as other (nonlinear) circuit elements. Thermal effects can be captured with empirical models such as introduced in [42]. ECMs can be computationally fast and accurate (in terms of capturing the output dynamics), which makes them attractive for control purposes. Unfortunately, they have the inher-

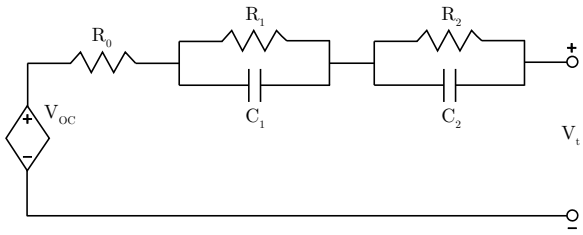

Figure 1.6: Example of an equivalent-circuit model.

ent disadvantage that internal physical states are not modeled, since ECMs are not based on the underlying physics of the battery. These internal states can be essential to limit battery aging, and they are also necessary states for physics-based battery aging models.

While more difficult to formulate, the internal physical states of a battery can be predicted using a physics-based model. The so-called Doyle-Fuller-Newman (DFN) model is a widely used physics-based model introduced in [43]. A detailed description of the model can be found in [44]. The DFN model is also often referred to as a pseudo-two-dimensional (P2D) model, since the model has in principle 1 dimension and an additional radial dimension. Fig. 1.7 illustrates the modeling approach for a Li-ion cell. In the x dimension, the cell is divided into three regions, namely the positive electrode, the negative electrode, and the separator. In the electrodes, at each (continuous) point on the x-axis, Li-ions exist essentially in two phases. In the solid phase, Li-ions are intercalated into the solid-phase material, which is represented by spheres with radius R_s, which can be different for the particles in the negative and positive electrode. In the electrolyte phase, Li-ions exist in a dissolved state in the electrolyte. In the separator, Li-ions exist only in the electrolyte phase. During charging, intercalated Li-ions exit the solid particles in the positive electrode and enter the solid particles in the negative electrode. During discharging, the opposite process happens.

The ability to describe this electrochemical behavior results in a high complexity of the DFN model. For this reason, there is a large amount of literature dedicated to simplifying the DFN model to decrease the computational burden. An often used simplified model is the so-called single-particle model (SPM) [45]. The SPM is defined by the main assumption that the diffusion dynamics inside the solid particles is the slowest process, and therefore dominates over the other dynamics [46], allowing for each of the electrodes to be represented by a single sphere. Furthermore, electrolyte dynamics are ignored, i.e., the Li-ion concentration and potential in the electrolyte is assumed to be constant. This reduces the original DFN model down to a single PDE for each of the electrodes. However, although these assumptions greatly simplify the DFN model, they are only valid under low-current conditions [47], while in the application of aging-aware fast charging, high currents may be desirable. To improve the accuracy of the SPM at high currents, the SPM has been extended with electrolyte dynamics [48–51]. Besides the SPM, many other simplified models have been formulated in literature, e.g. [52–58]. Finally, it has been recognized that many parameters depend on concentrations [59–63], while actually ignoring these dependencies could lead to a simplification of the governing model

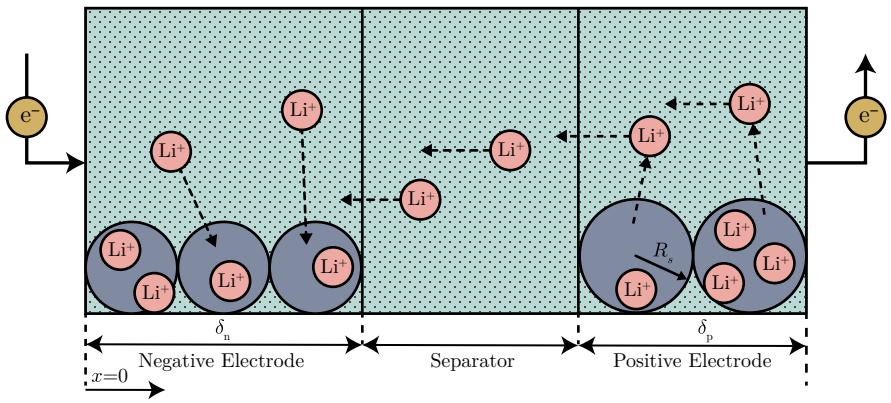

Figure 1.7: DFN modeling approach for a Li-ion cell (situation shown for charging).

equations.

The above-mentioned models simplify the DFN model through direct manipulation of the equations that may have a physical interpretation. A more recent trend to reduce model complexity is to apply model-order-reduction (MOR) techniques [64–67] or to make a polynomial approximation of the solid-phase concentration diffusion [52, 68]. In MOR, models are systematically simplified, in the sense that the least significant effects are filtered using some MOR technique. The main goal in MOR is to decrease computation times, rather than to preserve physical insight in the models, so that it can be used in control applications. However, the reduction is mostly in the number of equations, while the reduction in computation time is only marginal, when applied to the DFN model, as was shown in [66].

Besides addressing the complexity of the DFN model, another way to reduce computation time is to develop algorithms that compute the solution to the DFN model more efficiently, see e.g. [66, 69], and [70], where the latter proposes a computationally efficient model implementation in presence of the above-discussed simplified solid-phase dynamics. In these papers, the PDEs that describe the DFN model are spatially and temporally discretized, which results in a set of nonlinear algebraic equations (AEs). Numerical methods are then developed in an attempt to solve this set of AEs as efficiently as possible.

These advancements in reducing the computational complexity of the DFN model through either simplifications or implementation have contributed to obtain more computationally efficient electrochemistry-based models. However, a key issue in the above-mentioned work is that there is no consistent definition for the DFN model, where the exact set of equations that define the DFN model varies from paper to paper. This mainly stems from implicit simplifications that are made, for which generally no validation is given. For example, in most papers, the mean molar activity coefficient is (implicitly) ignored, e.g., in [54, 66, 70], while there are studies which claim that such transport properties may become important at high currents [59, 71]. On the other hand, due to experimental observations, several parameters are often modeled as being concentration-dependent, e.g., in [43, 66, 70]. However, as mentioned above, ignoring these dependen-

cies could lead to a simplification of the governing model equations, which has not yet been investigated. Finally, an issue in the above-mentioned work is that proposed simplified models are usually only validated for a single parameter set. While a simplified model could show good accordance with the DFN model for one parameter set, it may not be the case for another parameter set.

MODEL DISCRETIZATION

The choice of discretization is not a focus in aging-aware charging literature, which leads to most studies using the same discretization method, depending on the model choice. The choice of discretization may also depend on the choice of the model. If the model constitutes a set of ordinary differential equations, which is generally the case in empirical models, usually forward Euler discretization is used, e.g. [72, 73]. Physics-based models such as the DFN model consist of a set of PDEs, which are discretized using a spatial discretization method, after which a set of differential algabraic equations (DAEs) remains. In the case of the DFN model, in the x direction, the model is discretized using a finite-volume method [36], while in the radial direction in [36] Padé approximations or a finite-difference method in [74] are applied. The DAEs are temporally discretized using e.g. forward Euler discretization [36] or backward Euler discretization [74] to obtain a set of algebraic equations. In the process of discretization, there is a choice in the roughness of discretization, which can have a large impact on the computation time of the model. In [66] an investigation into the impact of the roughness of temporal discretization on the computional time and model accuracy has been done for the DFN model. However, a similar investigation for the impact of the roughness of spatial discretization for the DFN model is still missing in literature, to the author's knowledge. Studying this impact could lead to a considerable decrease in computation time of the DFN model.

BATTERY AGING MODELS

Although battery aging has been an extensive topic of study in literature, see e.g. [75], there has been less focus on developing control-oriented battery aging models. A widely used battery aging model is introduced in [76]. In this study, the authors have formulated an empirical model, which has been found by performing many charge-discharge cycles under different operating conditions and identifying a model that fits through the data. However, such an empirical modeling approach can be highly sensitive to operating conditions outside those that the model has been fit for. A more physics-based (semi-empirical) approach has been attempted in [77]. In this approach, the DFN model is extended by modeling the effects of side reactions. However, in this approach, only the buildup of the solid electrolyte interface (SEI) has been modeled. The SEI is formed upon the first charge of the battery, through a side reaction that consumes Li-ions [41]. Over the course of charge/discharge cycles, the SEI layer builds up further, slowly consuming Li-ions, which decreases the capacity of the cell. Another major degradation mechanism is the loss of active electrode material, through stress or fractures [41]. A model which describes this mechanism has been formulated in [78], while in [41], the authors have formulated a model which describes both Li-ion loss and active-material loss. However, these formulated models still do not describe all degradation phenomena, as there are other side reactions that can cause capacity loss, such as side reactions that consume

salts and solvents in the electrolyte [79]. Modeling the individual effects of all the possible degradation phenomena takes significant modeling effort, and leads to complex models. However, in the application of aging-aware charging, the effects of each individual degradation phenomena is not of interest. Instead, a model that describes the compound effect of all degradation phenomena, such that battery aging can be accurately predicted, meets the requirements for use in aging-aware charging.

PARAMETER ESTIMATION OF ELECTROCHEMISTRY-BASED MODELS

Due to the complexity of the DFN model, many parameters need to be determined, which is a challenge, especially as determination of some parameter values requires complex experimental techniques and a highly time-consuming effort for the measurement procedure. Therefore, simplified electrochemistry-based models, such as the single-particle model (SPM) [80], have been proposed, which have fewer parameters. Generally, the simplified electrochemistry-based models, such as the SPM, have fewer parameters and consequently, much of the focus in model parameterization has been on such simplified models in the time domain [81–87] and on linearized models in the frequency domain [88]. However, as mentioned above, the simplifications made in these models are usually at the cost of model accuracy, and therefore, parameterization of the DFN model, as has been done in, e.g., [89–98], is of interest.

Generally, the DFN model parameters can be determined in several ways. One way is to determine several parameters based on information provided by the cell manufacturers, who know the material properties that have been chosen during cell design. However, the manufacturer often does not have all the parameter values or might not want to disclose them. Another way is to measure the parameters by cell teardown and experimental testing [94, 95, 97]. Such methods generally involve costly equipment, and it is sometimes not allowed to tear down a cell by the cell manufacturer. Finally, parameters can be determined through parameter estimation using input-output data [89–93, 98]. In these methods, some, or all, of the parameters are estimated based on optimization of the model predictions to input/output measurements (i.e., external current/voltage measurements). Generally, two approaches are taken in the estimation of the parameters based on current/voltage measurements. One approach is to estimate some (or all) of the parameters simultaneously based on measured input/output data [89, 90, 92, 98]. Since the identifiability of the DFN model is poor [90], a sensitivity analysis can be done to determine the parameters to which the model output is most sensitive, in order to select a smaller set of parameters for estimation [89]. The other approach is to design experiments specifically in an attempt to isolate the effects of parameters in the output [84, 91, 93]. Here, the parameters are grouped based on their effect to the output, after which the groups of parameters are estimated separately using their respectively designed input current. However, often, there is no justification given for this approach [84, 91], or the approach is justified with the intuition that identifying too many parameters simultaneously may lead to unexpected uncertainty and errors [93]. However, this intuition has not yet been verified.

Due to the issues in the identifiability of the DFN model, when estimating the parameters based on only current/voltage measurements, the physical meaningfulness of the estimated parameters is not guaranteed. On the other hand, when estimating the parameters through cell teardown, the estimated parameters are based on measurements

of the internal characteristics of a battery. This gives more confidence in the physical meaningfulness of the estimated parameters, assuming that these parameters are homogeneous over the cell, which is not the case in practice. However, in doing so, the obtained model output voltage is not fit to voltage measurements, which results in a generally worse obtained model accuracy when estimating the parameters using cell teardown. Furthermore, the cell that is torn down is not the same as the cell that is actually used in the intended application, although this typically also applies to the other parameter estimation methods. While there have been contributions made in improving the identifiability of the DFN model through optimal experimental design, e.g., in [99], the identifiability of the DFN model still remains an issue. Therefore, estimating parameters that are both physically meaningful and lead to an accurate model remains an open problem in literature.

1.3.2. OPTIMAL-CONTROL PROBLEM FORMULATION

In the context of aging-aware charging, the optimal-control problem that is to be solved is to find an optimal charging profile such that a certain objective is satisfied. This optimal-control problem is expressed as an optimization problem, in which we want to minimize a certain objective function $J(x,u)$, which is a function of the input $u(t)$ (e.g. current), which can change with time t as well as the states $x(t)$ (e.g. potentials, Li-ion concentration), i.e.

$$\underset{x(t),u(t)}{\text{minimize}} \quad J(x(t),u(t)), \tag{1.1a}$$

subject to particular model equations expressed as

$$f(x(t),u(t)) = 0, \tag{1.1b}$$

and inequality constraints,

$$g(x(t),u(t)) \leq 0, \tag{1.1c}$$

which can serve to, e.g., limit Li-ion concentration at certain locations or set a minimal stored charge constraint. The input is generally chosen to be the applied current, while the states depend on the model choice. For example, if an ECM is chosen, the states may be capacitance voltages and SoC, and if a physics-based model is chosen, the states may be potentials and concentrations.

Since the goal in aging-aware charging is to make a Pareto-optimal trade-off between aging and charging time, the optimal-control problem can be formulated as either of the three following objectives, with the corresponding objective function and constraints.

1. Minimize a weighting between charging time and battery degradation.
2. Minimize charging time, subject to a certain battery degradation.
3. Minimize battery degradation, subject to a certain charging time.

As the most natural objective is to minimize charging time, so that the device can be used as quickly as possible, the optimal-control problem is most often formulated as minimizing charging time subject to aging-related constraints, see, e.g., [51, 100–105]. Note

that in most of these papers, the minimum charging time problem is approximated by an SoC-reference-tracking problem [100–103, 105]. However, also literature exists in which the optimal-control problem is formulated as minimizing a weighting between charging time and aging, see, e.g., [106–112], and minimizing aging subject to a specified charging time, e.g. [113]. Note that in many papers where an (classic) MPC approach is applied, a reference tracking problem is formulated, instead of solving one of the above-given objectives, see, e.g., [114–119]. However, by the definition of optimal aging-aware charging used in this thesis, such an approach does not achieve a Pareto-optimal trade-off between aging and charging time, since it does not achieve either of the three objectives formulated above. Further note that the problem of the maximization of charge transferred in a given time subject to aging-related constraints has also been formulated, e.g. in [74, 120–123]. However, this problem formulation, in principle, also does not achieve a Pareto-optimal trade-off between aging and charging time, since the amount of charge transferred cannot be used to make a direct trade-off between aging and charging time, as the amount of charge transferred also determines how much charge can be extracted from the battery afterwards. Therefore, a fair comparison between various charging protocols, that lead to a particular trade-off between aging an charging time, can only be made if the amount of charge transferred is equal.

One of the major challenges in aging-aware charging is in obtaining an accurate aging model. Therefore, many studies take the approach of using known indicators that cause battery aging. Some of these indicators can be modeled using empirical models such as an ECM or empirical thermal models, e.g., temperature applied in [100, 124]. Other indicators require physics-based models e.g., temperature (using a physics-based thermal model) [125], Li-ion concentration [51, 120], and negative-electrode overpotential [36, 101, 104, 105, 114, 119]. However, since incorporating electrochemistry-based models, and particularly the DFN model, into the optimization problem can lead to a computationally complex problem to solve, there have been approaches where aging-related DFN model states are approximated using a significantly less complex surrogate model [114–118] or a linearized electrochemistry-based model [101], which is then used for optimization. Nevertheless, the general approach taken in these papers is that by using such indicators as mentioned above, constraints can be set with the goal of avoiding excessive aging. Of course, aging can never be prevented and the transition between excessive and non-excessive aging is not necessarily a sharp transition. Therefore, another approach is to incorporate aging models into the optimization problem. One approach is to use an ECM in combination with an empirical aging model, e.g. [107, 109, 126]. Another approach is to use a physics-based model to constrain or minimize battery aging, where side-reaction models have been applied in [67, 108, 110, 111, 113, 115], and stress models have been applied in [74, 121]. Nevertheless, as such physics-based aging models are complex, aging indicators are still often used, even though, for the reasons mentioned above, such an approach might not allow for making an effective trade-off between charging time and aging.

In many studies, e.g. [51, 74, 105, 107–109, 113, 123, 127], the optimal-control problem (1.1) is solved in an off-line setting, in the sense that the optimization problem is solved once, after which the solution can be analyzed. Although such an analysis is valuable to provide insight into aging-aware charging, the solution itself is generally not use-

ful for implementation. Since modeling errors always occur, the solution found may steer the system into unwanted states. A way to compensate for the modeling errors is to solve the optimization problem periodically, and update the solution at each time instance. We will refer to such a scheme as a closed-loop optimal controller, although it can be categorized under MPC. However, while in (classic) MPC the objective function is chosen as a quadratic objective function with weighting terms on the input and states, in closed-loop optimal control the objective function is chosen as the actual objective that is to be satisfied. In literature, both approaches are utilized. The classic MPC approach is mostly used for reference tracking in e.g., [114–118], while the closed-loop optimal controller approach has not yet been done, to the author's knowledge. An approximation of the closed-loop optimal controller can be found in [106, 110–112], where the objective function is chosen as the actual desired objective. However due to the computational complexity of the DFN model considered in these papers, the actual model used in the closed-loop optimal controller is either linearized [106] or the choice for the control horizon of the MPC approach is limited [110–112], which leads to a sacrifice in the optimality of the obtained solution.

1.3.3. OPTIMAL CONTROL SOLUTION METHODS

Generally three different methods exist to solve an optimal-control problem. One of these methods is dynamic programming (DP) applied in [72, 123]. However, DP has the inherent disadvantage that the computational burden increases with the number of states. Although using an ECM, the number of states can be relatively low, physics-based models can have hundreds of states. Optimization methods based on the Pontryagin's Maximum Principle (PMP), see, e.g., [125, 128, 129] can handle the computational complexity of physics-based models. In PMP, the problem is reduced to solving a two-point boundary-value problem, which can be difficult to solve in the presence of state constraints. Static optimization methods are most often used in aging-aware charging (e.g., [36, 51, 74, 100, 105, 107–111, 113, 121, 122, 127]), since they can handle the complexity of physics-based models, as well as state constraints. However, in static optimization, a global solution is only guaranteed for a convex optimization problem. In many studies, commercial solvers such as IPOPT [74, 111, 113], GPOPS-II [51, 74, 107, 109, 121, 122], FMINCON [108, 110], or Genetic Algorithm Toolbox [100, 127] are used to directly obtain a solution to a given optimization problem. However, such off-the-shelf-solvers may limit the possibilities in taking advantage of the properties in the structure of the considered optimization problem.

1.4. RESEARCH QUESTIONS

In this section, we will state the main research question and main objective in this work. Starting from this main objective, we will reflect on the state-of-the-art in Section 1.3 to formulate research sub-questions that need to be addressed in order to fulfill the objective.

1.4.1. PROBLEM STATEMENT

The state of the art previously discussed shows that there are many different approaches to tackle the problem of aging-aware charging. These approaches range from relatively simple rule-based methods to optimal-control-based approaches which use complex physics-based models. However, in most of the literature, the proposed aging-aware charging methods are only validated against the conventional CC-CV protocol, even though other methods may have a similar performance to the proposed aging-aware charging method at a lower computational complexity. Furthermore, the state-of-the-art has shown that the use of complex electrochemistry-based (aging) models in an optimal-control-based approach with a low computational complexity is still difficult. Finally, due to the complexity of electrochemical aging models, many aging-aware charging approaches use aging indicators instead, with which making a trade-off between aging and charging time might be impossible. Consequently, we pose the following main research question:

Main Research Question

Do optimal-control-based charging algorithms that use electrochemical aging models lead to a better trade-off between aging and charging time compared to rule-based protocols, while having a manageable computational complexity?

From this research question, we can state the main objective of this thesis as follows. Design a battery charging algorithm such that it has the properties of being

1. *Optimal:* the charging performance must be as close as possible to the fundamental limit of the performance that can be achieved.

2. *Aging-aware:* the charging algorithm needs to be able to predict and restrict battery aging, instead of basing the decisions only on aging indicators.

3. *Adaptive:* the charging algorithm must work in a closed-loop setting, and be able to adapt to modeling errors and disturbances.

4. *Implementable:* the charging algorithm must have limited computational complexity, so that it can be implemented on a battery charger.

The suggested approach in this thesis is to use optimal control. In this approach, we must find or develop accurate models with limited computation times such that they can be applied in an on-line optimal controller. Furthermore, we must formulate an optimal-control problem and find or develop an optimization algorithm that solves it in a short enough time, such that it can be used in a closed-loop implementation. In the rest of this section, we will formulate the research sub-questions that arise from our main objective and the state-of-the-art.

1.4.2. BATTERY MODELING AND PARAMETERIZATION

As evidenced from the state-of-the-art, there is a general trade-off that can be made in battery modeling between computational complexity and accuracy through the choice

of model simplifications. However, in the current literature, the impact of the assumptions or simplifications made, sometimes unknowingly, e.g., in the case of concentration-dependent parameters, on the computational complexity and accuracy of the resulting model are not investigated. Therefore, the first research sub-question is given as follows:

Research Sub-Question 1

What is the impact of model simplifications on the trade-off between computational complexity and model accuracy of electrochemistry-based battery models?

This sub-question will be addressed in Chapter 2, where the impact of several types of model simplifications on the trade-off between model accuracy and computation time will be investigated for the DFN model. In this study, we will also consider the roughness of the spatial discretization scheme to make an additional trade-off between accuracy and computation time. As a basis for comparison, we will consider, to what we will refer as, the complete DFN (CDFN) model, which is a DFN model without any simplifications, and includes the concentration-dependency of parameters that have been studied in previous literature. This will show which model simplifications should be made in order to obtain an electrochemistry-based model in order to reach a desired trade-off in model accuracy and complexity.

While there are various approaches taken in literature to determine the parameters of electrochemistry-based models, a direct comparison between these methods is missing. In particular, in the approaches that use only current/voltage data to determine the model parameters, a good model accuracy, i.e., the terminal voltage fit, can be obtained, although an investigation into the physical meaningfulness of the parameters is missing. On the other hand, by obtaining the model parameters through cell teardown, a stronger guarantee can be given to the physical meaningfulness of the parameters, although the obtained model accuracy is generally worse than for the approaches based on only current/voltage data. Therefore, the second sub-question is given by:

Research Sub-Question 2

How can the parameters of electrochemistry-based battery models be determined to obtain an accurate model with physically meaningful parameters?

This sub-question will be addressed in Chapter 3, where a parameter determination approach using cell teardown and an approach using only current/voltage data are compared. In doing so, we will propose a model parameterization approach of the DFN model through normalization and grouping, followed by a sensitivity analysis and a parameter estimation procedure. The normalization and grouping procedure will reduce the number of parameters of the DFN model, while the sensitivity analysis is performed to select the most output-sensitive parameters for parameter estimation. For the approach based on cell teardown, we use experimentally determined parameters and current/voltage data, which are obtained from literature. By comparing both considered parameter determination approaches on this data, we will asses whether a better model accuracy can be obtained using the approach that uses only current/voltage data. Fur-

thermore, we will consider a synthetic cell, represented by a DFN model with randomly chosen (within specific and realistic intervals) parameters. By applying the proposed parameterization approach on the data generated using this synthetic cell, we can assess the physical meaningfulness of the parameters resulting from this approach.

1.4.3. AGING-AWARE CHARGING

A common approach in aging-aware charging is to use aging indicators, such as the negative-electrode over-potential, in order to restrict the battery from reaching states that result in excessive aging, such as lithium plating [47]. However, as we have reasoned above, aging can never be prevented and the transition between excessive and non-excessive aging is not necessarily a sharp transition. Still, as we have also seen above, this approach is commonly taken, even in recent literature (see, e.g., [35, 119]), and therefore, the third research question is given by:

Research Sub-Question 3

Can aging indicators, such as the negative-electrode over-potential, be used to effectively make a trade-off between charging time and battery aging?

This sub-question will be addressed in Chapter 4, where a DFN model including capacity-loss side reactions is utilized to compare several rule-based charging protocols by obtaining the Pareto front that describes the optimal trade-off between charging time and aging for the considered protocols. In this comparison, we will investigate the usefulness of the negative-electrode over-potential as an indicator for aging in making a trade-off between charging time and battery aging.

A large obstacle in optimal aging-aware charging is the use of the complex electrochemistry-based models, such as the DFN model in an optimal-control approach. A promising approach is then to use a surrogate model, which approximates aging-related DFN model states, such as those considered in [114–118]. However, in these papers, a black-box modeling approach is chosen, which may lead to a difficulty in estimating the inherent (nonlinear) dependency of some of the DFN model states on the state-of-charge of the battery. Consequently, the following sub-question is formulated:

Research sub-question 4

What modeling approach, with a lower computational complexity than the DFN model, is suitable to approximate aging-related DFN model states accurately, such that it can be used in optimal aging-aware charging?

We will investigate this sub-question mostly in Chapter 5, where we will present an optimal-control-based method for aging-aware charging using a surrogate model. In the proposed surrogate modeling approach, the aging-related DFN model states are approximated by a combination of a black-box finite-dimensional linear-time-invariant model and a static nonlinear model that is a function of state-of-charge. We will show how well the aging-related DFN model states can be approximated by the proposed surrogate model, while also comparing the computational time of the surrogate model to the

DFN model. In Chapter 6, we will compare the Pareto front obtained using this proposed approach to the best-possible Pareto front for a synthetic cell, to further validate this approach for aging-aware charging.

Although the surrogate modeling approach can achieve a good trade-off between charging time and aging, ideally, the goal is to use the DFN model directly in the optimal-control approach. However, in the current state-of-the-art, the DFN model has not been used in a closed-loop optimal-control strategy, due to the computational complexity of the DFN model. Hence, this leads to the following sub-question:

Research Sub-Question 5

Can the computational complexity of the optimal aging-aware charging problem using the DFN model be reduced such that it is suitable for a closed-loop implementation?

In Chapter 6, we will answer this sub-question, where we will present an optimal aging-aware charging approach using the DFN model. Here, we will use the resulting model implementation from Chapter 2 to reformulate the optimal-control problem with a reduced computational complexity compared to the originally formulated optimal-control problem. Furthermore, to solve the optimal-control problem, we will employ a proprietary algorithm, and compare this to an off-the-shelf non-linear optimization solver. To further reduce the computational complexity of the optimal-control problem, we will investigate the effect of spatial and temporal discretization of the resulting discrete-time optimal-control problem on the computational complexity and achieved trade-off between charging time and aging.

While several optimization-based charging methods have been experimentally validated, see, e.g., [110, 113], the validation is done through a comparison with the conventional CC-CV strategy only. However, it has been shown that multi-stage CC-CV charging protocols, which are substantially less complex than optimization-based methods, also achieve a significantly improved trade-off between charging time and aging compared to the commonly used CC-CV protocol, see, e.g., [24]. Therefore, in the experimental validation of optimal aging-aware charging methods, multi-stage CC-CV protocols should also be considered for comparison, which leads to the final research question:

Research Sub-Question 6

Do optimal-control-based charging algorithms that use electrochemistry-based models lead to a better trade-off between aging and charging time than rule-based algorithms in practice?

We will address this sub-question in Chapter 7, where we will experimentally validate an open-loop optimal aging-aware charging approach, and compare this approach to a multi-stage CC-CV protocol, as well as the conventional CC-CV protocol.

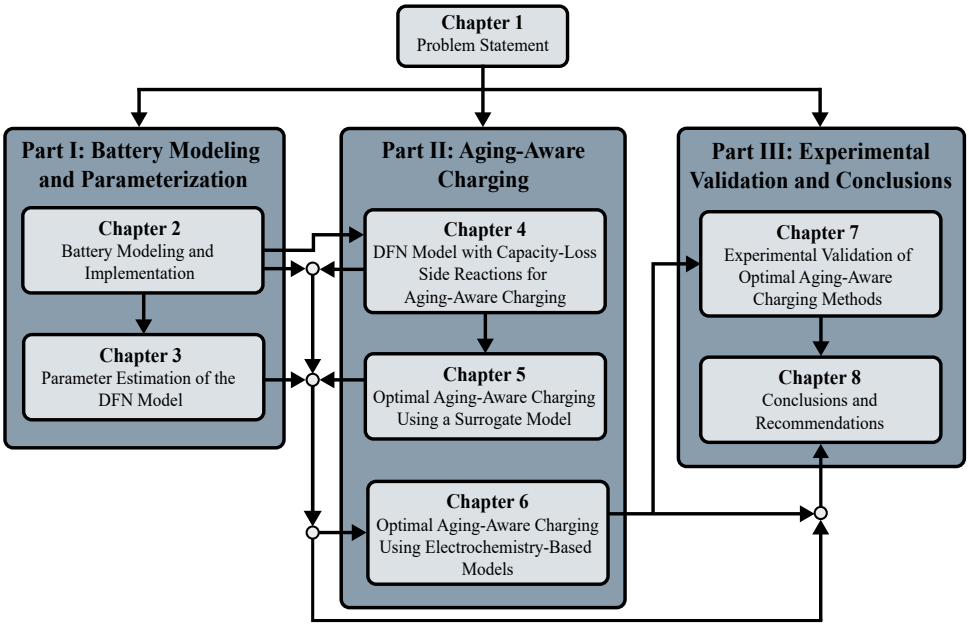

Figure 1.8: Thesis outline.

1.5. THESIS OUTLINE

The outline of this thesis is shown schematically in Fig. 1.8, where the thesis is divided into three main parts. All three parts are preceded by the problem statement that has been set in Section 1.4 of this chapter. Furthermore, we can see from Fig. 1.8 that the thesis can be read chronologically, due to the causal relationship between the three parts of this thesis. Specifically, in order to consider the aging-aware charging strategies in Part II, it is necessary to first investigate battery modeling and implementation in Part I. Then, an experimental validation of the aging-aware charging methods in Part III requires the study done in Part II. Finally, in Part III, conclusions and recommendations are made based on all the chapters that have preceded that point. However, at the same time, the chapters have been written such that they can also be read independently, which may lead to some repetitiveness in the introduction sections of the separate chapters, as well as the abstracts and conclusions. We will give an outline of the three main parts below.

PART I: BATTERY MODELING AND PARAMETERIZATION

In Chapter 2, we aim to find an electrochemistry-based modeling framework that is accurate and suitable for optimal aging-aware charging. This is done by studying the impact of several types of model simplifications on the trade-off between model accuracy and computation time for the DFN model. Furthermore, in Chapter 2, a model implementation is presented that significantly speeds up the DFN model simulation, regardless of the simplifications made. In Chapter 3, the problem of parameterizing the DFN model is addressed. Here, we aim for a model parameterization approach that leads to

physically intuitive parameters as well as an accurate model.

PART II: AGING-AWARE CHARGING

In Chapter 4, we formulate an electrochemistry-based aging model, that is based on the DFN model and a capacity-loss side-reaction model. Using this model, the Pareto front that describes the trade-off between charging time and aging for several rule-based protocols is obtained. Through this analysis, we will investigate the usefulness of the negative-electrode over-potential as an indicator for aging in making a trade-off between charging time and battery aging. Then, in Chapter 5, we will investigate the use of surrogate modeling for optimal aging-aware charging. The proposed surrogate model approximates the aging-related DFN model states from Chapter 4, while having a significantly lower computational complexity than the considered model that is approximated. This optimal-control-based approach using the surrogate model will then be compared to the rule-based protocols considered in Chapter 4. Finally, in Chapter 6, we will present an optimal aging-aware charging approach using the DFN model. Here, the resulting implementation from Chapter 2 is used to obtain an optimal-control problem that has a considerably reduced complexity compared to the originally formulated optimal-control problem. This proposed optimal-control-based approach using the DFN model is then compared to aging-aware charging approaches considered in Chapter 4 and Chapter 5.

PART III: EXPERIMENTAL VALIDATION AND CONCLUSIONS

An experimental validation of several aging-aware charging methods is done in Chapter 7. Specifically, several points on the Pareto front of the aging-aware charging method proposed in Chapter 6 are experimentally obtained. This Pareto front is compared to the experimental Pareto fronts of a multi-stage CC-CV charging protocol and the conventional CC-CV charging protocol. Finally, in Chapter 8, conclusions and recommendations are discussed.

1.6. LIST OF PUBLICATIONS

The contributions discussed in this thesis have been part of the following publications.

P.1 **Z. Khalik**, M. C. F. Donkers, J. Sturm and H. J. Bergveld, *Parameter Estimation of the Doyle-Fuller-Newman Model for Lithium-Ion Batteries by Parameter Normalization, Grouping, and Sensitivity Analysis*, Journal of Power Sources **449**, 229901 (2021).

P.2 **Z. Khalik**, M. C. F. Donkers and H. J. Bergveld, *Model Simplifications and Their Impact on Computational Complexity for an Electrochemistry-Based Battery Modeling Toolbox*, Journal of Power Sources **448**, 229427 (2021).

P.3 **Z. Khalik**, H. J. Bergveld and M. C. F. Donkers, *Ageing-Aware Charging of Lithium-ion Batteries Using a Surrogate Model*, IEEE American Control Conference (2021) pp. 4414-4420.

P.4 **Z. Khalik**, H. J. Bergveld and M. C. F. Donkers, *Ageing-Aware Charging of Lithium-ion Batteries Using an Electrochemistry-Based Model with Capacity-Loss Side Reactions*, IEEE American Control Conference (2020) pp. 2213-2218.

P.5 **Z. Khalik**, H. J. Bergveld and M. C. F. Donkers, *On Trade-offs Between Computational Complexity and Accuracy of Electrochemistry-based Battery Models*, IEEE Conference on Decision and Control (2019) pp. 7740-7745.

Part of this thesis has been included in the following unpublished article:

S.1 **Z. Khalik**, M. C. F. Donkers and H. J. Bergveld, *Optimal Ageing-Aware Charging of Lithium-Ion Batteries Using a Simplified Doyle-Fuller-Newman Model and Sequential Quadratic Programming* , in preparation (2021).

REFERENCES

[1] *EU transport in figures - Statistical pocketbook* (European Union, 2020).

[2] *Global EV Outlook 2021* (International Energy Agency, 2021).

[3] *Electric vehicles in Europe* (European Environment Agency, 2016).

[4] O. Egbue and S. Long, *Barriers to widespread adoption of electric vehicles: An analysis of consumer attitudes and perceptions,* Energy Policy **48**, 717 (2012).

[5] B. Scrosati and J. Garche, *Lithium batteries: Status, prospects and future,* Journal of Power Sources **195**, 2419 (2010).

[6] C. K. Chan, H. Peng, G. Liu, K. McIlwrath, X. F. Zhang, R. A. Huggins, and Y. Cui, *High-performance lithium battery anodes using silicon nanowires,* Nature Nanonotechnology **3**, 31 (2008).

[7] M. L. Terranova, S. Orlanducci, E. Tamburri, V. Guglielmotti, and M. Rossi, *Si/C hybrid nanostructures for Li-ion anodes: An overview,* Journal of Power Sources **246**, 167 (2014).

[8] S. F. Tie and C. W. Tan, *A review of energy sources and energy management system in electric vehicles,* Renewable and Sustainable Energy Reviews **20**, 82 (2013).

[9] G. De Nunzio and L. Thibault, *Energy-optimal driving range prediction for electric vehicles,* in *2017 IEEE Intelligent Vehicles Symposium (IV)* (2017) pp. 1608–1613.

[10] *What can 6,000 electric vehicles tell us about ev battery health?* `https://www.geotab.com/blog/ev-battery-health`.

[11] H. J. Bergveld, W. S. Kruijt, and P. H. L. Notten, *Battery Management Systems: Design by Modeling* (Kluwer Academic publishers, 2002).

[12] S. Zhang, K. Xu, and T. Jow, *Study of the charging process of a LiCoO2-based Li-ion battery,* Journal of Power Sources **160**, 1349 (2006).

[13] P. Notten, J. Op het Veld, and J. van Beek, *Boostcharging Li-ion batteries: A challenging new charging concept,* Journal of Power Sources **145**, 89 (2005).

[14] D. Anseán, M. González, J. Viera, V. García, C. Blanco, and M. Valledor, *Fast charging technique for high power lithium iron phosphate batteries: A cycle life analysis,* Journal of Power Sources **239**, 9 (2013).

[15] J. Li, E. Murphy, J. Winnick, and P. A. Kohl, *the effects of pulse charging on cycling characteristics of commercial lithium-ion batteries,* Journal of Power Sources **102**, 302 (2001).

[16] J. Zhang, J. Yu, C. Cha, and H. Yang, *the effects of pulse charging on inner pressure and cycling characteristics of sealed Ni/MH batteries,* Journal of Power Sources **136**, 180 (2004).

[17] F. Savoye, P. Venet, M. Millet, and J. Groot, *Impact of Periodic Current Pulses on Li-Ion Battery Performance,* IEEE Transactions on Industrial Electronics **59**, 3481 (2012).

[18] M. Abdel-Monem, K. Trad, N. Omar, O. Hegazy, P. Van den Bossche, and J. Van Mierlo, *Influence analysis of static and dynamic fast-charging current profiles on ageing performance of commercial lithium-ion batteries,* Energy **120**, 179 (2017).

[19] P. Keil and A. Jossen, *Charging protocols for lithium-ion batteries and their impact on cycle life—An experimental study with different 18650 high-power cells,* Journal of Energy Storage **6**, 125 (2016).

[20] H. Surmann, *Genetic optimization of a fuzzy system for charging batteries,* IEEE Transactions on Industrial Electronics **43**, 541 (1996).

[21] R. Aliev, R. Aliev, B. Guirimov, and K. Uyar, *Dynamic data mining technique for rules extraction in a process of battery charging,* Applied Soft Computing **8**, 1252 (2008).

[22] T. T. Vo, X. Chen, W. Shen, and A. Kapoor, *New charging strategy for lithium-ion batteries based on the integration of Taguchi method and state of charge estimation,* Journal of Power Sources **273**, 413 (2015).

[23] Y.-H. Liu and Y.-F. Luo, *Search for an Optimal Rapid-Charging Pattern for Li-Ion Batteries Using the Taguchi Approach,* IEEE Transactions on Industrial Electronics **57**, 3963 (2010).

[24] Y.-H. Liu, C.-H. Hsieh, and Y.-F. Luo, *Search for an Optimal Five-Step Charging Pattern for Li-Ion Batteries Using Consecutive Orthogonal Arrays,* IEEE Transactions on Energy Conversion **26**, 654 (2011).

[25] L.-R. Dung and J.-H. Yen, *ILP-based algorithm for Lithium-ion battery charging profile,* in *Industrial Electronics (ISIE), 2010 IEEE International Symposium on* (2010) pp. 2286–2291.

[26] Y.-H. Liu, J.-H. Teng, and Y.-C. Lin, *Search for an Optimal Rapid Charging Pattern for Lithium–Ion Batteries Using Ant Colony System Algorithm,* IEEE Transactions on Industrial Electronics **52**, 1328 (2005).

[27] S.-C. Wang and Y.-H. Liu, *A PSO-Based Fuzzy-Controlled Searching for the Optimal Charge Pattern of Li-Ion Batteries,* IEEE Transactions on Industrial Electronics **62**, 2983 (2015).

[28] P. M. Attia, A. Grover, N. Jin, K. A. Severson, T. M. Markov, Y.-H. Liao, M. H. Chen, B. Cheong, N. Perkins, Z. Yang, P. K. Herring, M. Aykol, S. J. Harris, R. D. Braatz, S. Ermon, and W. C. Chueh, *Closed-loop optimization of fast-charging protocols for batteries with machine learning,* Nature (2020).

[29] L.-R. Chen, *A Design of an Optimal Battery Pulse Charge System by Frequency-Varied Technique,* IEEE Transactions on Industrial Electronics **54**, 398 (2007).

[30] L.-R. Chen, S.-L. Wu, D.-T. Shieh, and T.-R. Chen, *Sinusoidal-Ripple-Current Charging Strategy and Optimal Charging Frequency Study for Li-Ion Batteries,* IEEE Transactions on Industrial Electronics **60**, 88 (2013).

[31] L.-R. Chen, *Design of Duty-Varied Voltage Pulse Charger for Improving Li-Ion Battery-Charging Response,* IEEE Transactions on Industrial Electronics **56**, 480 (2009).

[32] Z. Chu, X. Feng, L. Lu, J. Li, X. Han, and M. Ouyang, *Non-destructive fast charging algorithm of lithium-ion batteries based on the control-oriented electrochemical model,* Applied Energy **204**, 1240 (2017).

[33] Y. Li, M. Vilathgamuwa, E. Wikner, Z. Wei, X. Zhang, T. Thiringer, T. Wik, and C. Zou, *Electrochemical Model-Based Fast Charging: Physical Constraint-Triggered PI Control,* IEEE Transactions on Energy Conversion , 1 (2021).

[34] S.-Y. Choe, X. Li, and M. Xiao, *Fast Charging Method Based on Estimation of Ion Concentrations using a Reduced Order of Electrochemical Thermal Model for Lithium Ion Polymer Battery,* 2013 World Electric Vehicle Symposium and Exhibition (EVS27) , 1 (2013).

[35] R. Romagnoli, L. D. Couto, A. Goldar, M. Kinnaert, and E. Garone, *A feedback charge strategy for Li-ion battery cells based on Reference Governor,* Journal of Process Control (2019).

[36] H. Perez, N. Shahmohammadhamedani, and S. Moura, *Enhanced Performance of Li-Ion Batteries via Modified Reference Governors and Electrochemical Models,* IEEE/ASME Transactions on Mechatronics **20**, 1511 (2015).

[37] M. Pathak, S. Kolluri, and V. R. Subramanian, *Generic model control for lithium-ion batteries,* Journal of the Electrochemical Society **164**, A973 (2017).

[38] H. Fang, Y. Wang, and J. Chen, *Health-Aware and User-Involved Battery Charging Management for Electric Vehicles: Linear Quadratic Strategies,* IEEE Transactions on Control Systems Technology **25**, 911 (2017).

[39] A. Fotouhi, D. J. Auger, K. Propp, S. Longo, and M. Wild, *A review on electric vehicle battery modelling: From Lithium-ion toward Lithium–Sulphur,* Renewable and Sustainable Energy Reviews **56**, 1008 (2016).

[40] C. Zhang, K. Li, S. Mcloone, and Z. Yang, *Battery modelling methods for electric vehicles-A review,* in *IEE European Control Conference* (2014) pp. 2673–2678.

[41] A. A. Franco, M. L. Doublet, and W. G. Bessler, *Physical Multiscale Modeling and Numerical Simulation of Electrochemical Devices for Energy Conversion and Storage,* Green Energy and Technology (Springer London, 2016).

[42] X. Lin, H. E. Perez, S. Mohan, J. B. Siegel, A. G. Stefanopoulou, Y. Ding, and M. P. Castanier, *A lumped-parameter electro-thermal model for cylindrical batteries,* Journal of Power Sources **257**, 1 (2014).

[43] M. Doyle, T. F. Fuller, and J. Newman, *Modeling of galvanostatic charge and discharge of the lithium/polymer/insertion cell,* Journal of the Electrochemical society **140**, 1526 (1993).

[44] W. A. v. Schalkwijk and B. Scrosati, *Advances in lithium-ion batteries* (Kluwer Academic/Plenum publishers, 2005).

[45] S. Santhanagopalan, Q. Guo, P. Ramadass, and R. E. White, *Review of models for predicting the cycling performance of lithium ion batteries,* Journal of Power Sources **156**, 620 (2006).

[46] G. L. Plett, *Battery Management Systems, Volume I: Battery Modeling* (Artech House publishers, 2015).

[47] N. Chaturvedi, R. Klein, J. Christensen, J. Ahmed, and A. Kojic, *Algorithms for Advanced Battery-Management Systems,* IEEE Control Systems Magazine **30**, 49 (2010).

[48] P. Kemper and D. Kum, *Extended Single Particle Model of Li-Ion Batteries Towards High Current Applications,* in *IEEE Vehicle Power and Propulsion Conference* (2013) pp. 1–6.

[49] S. Khaleghi Rahimian, S. Rayman, and R. E. White, *Extension of physics-based single particle model for higher charge–discharge rates,* Journal of Power Sources **224**, 180 (2013).

[50] W. Luo, C. Lyu, L. Wang, and L. Zhang, *A new extension of physics-based single particle model for higher charge–discharge rates,* Journal of Power Sources **241**, 295 (2013).

[51] H. E. Perez, X. Hu, and S. J. Moura, *Optimal charging of batteries via a single particle model with electrolyte and thermal dynamics,* in *IEEE American Control Conference* (2016) pp. 4000–4005.

[52] T.-S. Dao, C. P. Vyasarayani, and J. McPhee, *Simplification and order reduction of lithium-ion battery model based on porous-electrode theory,* Journal of Power Sources **198**, 329 (2012).

[53] X. Han, M. Ouyang, L. Lu, and J. Li, *Simplification of physics-based electrochemical model for lithium ion battery on electric vehicle. Part II: Pseudo-two-dimensional model simplification and state of charge estimation,* Journal of Power Sources **278**, 814 (2015).

[54] P. Kemper, S. E. Li, and D. Kum, *Simplification of pseudo two dimensional battery model using dynamic profile of lithium concentration,* Journal of Power Sources **286**, 510 (2015).

[55] C. Zou, C. Manzie, and D. Nesic, *A Framework for Simplification of PDE-Based Lithium-Ion Battery Models,* IEEE Transactions on Control Systems Technology **24**, 1594 (2016).

[56] C. Lin and A. Tang, *Simplification and Efficient Simulation of Electrochemical Model for Li-ion Battery in EVs,* Energy Procedia **104**, 68 (2016).

[57] C. Manzie, C. Zou, and D. Nesic, *Simplification techniques for PDE-based Li-ion battery models,* in *IEEE Conference on Decision and Control* (2015) pp. 3913–3921.

[58] E. Prada, D. Di Domenico, Y. Creff, J. Bernard, V. Sauvant-Moynot, and F. Huet, *Simplified electrochemical and thermal model of LiFePO4-graphite Li-ion batteries for fast charge applications,* Journal of the Electrochemical Society **159**, A1508 (2012).

[59] L. O. Valøen and J. N. Reimers, *Transport properties of LiPF6-based Li-ion battery electrolytes,* Journal of the Electrochemical Society **152**, A882 (2005).

[60] P. Georén and G. Lindbergh, *Characterisation and modelling of the transport properties in lithium battery gel electrolytes: Part I. the binary electrolyte PC/LiClO4,* Electrochimica Acta **49**, 3497 (2004).

[61] C. Delacourt, M. Ati, and J. M. Tarascon, *Measurement of Lithium Diffusion Coefficient in Li y FeSO4F,* Journal of the Electrochemical Society **158**, A741 (2011).

[62] M. Safari and C. Delacourt, *Mathematical Modeling of Lithium Iron Phosphate Electrode: Galvanostatic Charge/Discharge and Path Dependence,* Journal of the Electrochemical Society **158**, A63 (2011).

[63] M. M. Doeff, L. Edman, S. E. Sloop, J. Kerr, and L. C. De Jonghe, *Transport properties of binary salt polymer electrolytes,* Journal of Power Sources **89**, 227 (2000).

[64] G. Fan, K. Pan, and M. Canova, *A comparison of model order reduction techniques for electrochemical characterization of Lithium-ion batteries,* in *IEEE Conference on Decision and Control* (2015) pp. 3922–3931.

[65] L. Cai and R. E. White, *Reduction of Model Order Based on Proper Orthogonal Decomposition for Lithium-Ion Battery Simulations,* Journal of the Electrochemical Society **156**, A154 (2009).

[66] L. Xia, E. Najafi, Z. Li, H. J. Bergveld, and M. C. F. Donkers, *A computationally efficient implementation of a full and reduced-order electrochemistry-based model for Li-ion batteries,* Applied Energy **208**, 1285 (2017).

[67] S. Bashash, S. J. Moura, J. C. Forman, and H. K. Fathy, *Plug-in hybrid electric vehicle charge pattern optimization for energy cost and battery longevity,* Journal of Power Sources **196**, 541 (2011).

[68] V. R. Subramanian, V. D. Diwakar, and D. Tapriyal, *Efficient Macro-Micro Scale Coupled Modeling of Batteries,* Journal of the Electrochemical Society **152**, A2002 (2005).

[69] S. Mazumder and J. Lu, *Faster-Than-Real-Time Simulation of Lithium Ion Batteries with Full Spatial and Temporal Resolution,* International Journal of Electrochemistry **2013**, 1 (2013).

[70] V. R. Subramanian, V. Boovaragavan, V. Ramadesigan, and M. Arabandi, *Mathematical Model Reformulation for Lithium-Ion Battery Simulations: Galvanostatic Boundary Conditions,* Journal of the Electrochemical Society **156**, A260 (2009).

[71] S. Stewart and J. Newman, *Measuring the Salt Activity Coefficient in Lithium-Battery Electrolytes,* Journal of the Electrochemical Society **155**, A458 (2008).

[72] Z. Chen, B. Xia, C. C. Mi, and R. Xiong, *Loss-Minimization-Based Charging Strategy for Lithium-Ion Battery,* IEEE Transactions on Industry Applications **51**, 4121 (2015).

[73] X. Hu, S. Li, H. Peng, and F. Sun, *Charging time and loss optimization for LiNMC and LiFePO4 batteries based on equivalent circuit models,* Journal of Power Sources **239**, 449 (2013).

[74] B. Suthar, P. W. C. Northrop, R. D. Braatz, and V. R. Subramanian, *Optimal Charging Profiles with Minimal Intercalation-Induced Stresses for Lithium-Ion Batteries Using Reformulated Pseudo 2-Dimensional Models,* Journal of the Electrochemical Society **161**, F3144 (2014).

[75] D. Li, D. L. Danilov, J. Xie, L. Raijmakers, L. Gao, Y. Yang, and P. H. Notten, *Degradation Mechanisms of C 6 /LiFePO 4 Batteries: Experimental Analyses of Calendar Aging,* Electrochimica Acta **190**, 1124 (2016).

[76] J. Wang, P. Liu, J. Hicks-Garner, E. Sherman, S. Soukiazian, M. Verbrugge, H. Tataria, J. Musser, and P. Finamore, *Cycle-life model for graphite-LiFePO4 cells,* Journal of Power Sources **196**, 3942 (2011).

[77] P. Ramadass, B. Haran, P. M. Gomadam, R. White, and B. N. Popov, *Development of First Principles Capacity Fade Model for Li-Ion Cells,* Journal of the Electrochemical Society **151**, A196 (2004).

[78] X. Zhang, W. Shyy, and A. Marie Sastry, *Numerical Simulation of Intercalation-Induced Stress in Li-Ion Battery Electrode Particles,* Journal of the Electrochemical Society **154**, A910 (2007).

[79] P. Arora, *Capacity Fade Mechanisms and Side Reactions in Lithium-Ion Batteries,* Journal of the Electrochemical Society **145**, 3647 (1998).

[80] J. Li, N. Lotfi, R. G. Landers, and J. Park, *A Single Particle Model for Lithium-Ion Batteries with Electrolyte and Stress-Enhanced Diffusion Physics,* Journal of the Electrochemical Society **164**, A874 (2017).

[81] S. Santhanagopalan, Q. Guo, and R. E. White, *Parameter Estimation and Model Discrimination for a Lithium-Ion Cell,* Journal of the Electrochemical Society **154**, A198 (2007).

[82] R. Masoudi, T. Uchida, and J. McPhee, *Parameter estimation of an electrochemistry-based lithium-ion battery model,* Journal of Power Sources **291**, 215 (2015).

[83] A. M. Bizeray, J. Kim, S. R. Duncan, and D. A. Howey, *Identifiability and Parameter Estimation of the Single Particle Lithium-Ion Battery Model,* IEEE Transactions on Control Systems Technology **27**, 1862 (2019).

[84] E. Namor, D. Torregrossa, R. Cherkaoui, and M. Paolone, *Parameter identification of a lithium-ion cell single-particle model through non-invasive testing,* Journal of Energy Storage **12**, 138 (2017).

[85] H. Pang, L. Mou, L. Guo, and F. Zhang, *Parameter identification and systematic validation of an enhanced single-particle model with aging degradation physics for Li-ion batteries,* Electrochimica Acta **307**, 474 (2019).

[86] A. P. Schmidt, M. Bitzer, r. W. Imre, and L. Guzzella, *Experiment-driven electrochemical modeling and systematic parameterization for a lithium-ion battery cell,* Journal of Power Sources **195**, 5071 (2010).

[87] A. Pozzi, G. Ciaramella, K. Gopalakrishnan, S. Volkwein, and D. M. Raimondo, *Optimal Design of Experiment for Parameter Estimation of a Single Particle Model for Lithiumion Batteries,* in *IEEE Conference on Decision and Control* (2018) pp. 6482–6487.

[88] X. Zhou and J. Huang, *Impedance-Based diagnosis of lithium ion batteries: Identification of physical parameters using multi-output relevance vector regression,* Journal of Energy Storage **31**, 101629 (2020).

[89] N. Jin, D. L. Danilov, P. M. Van den Hof, and M. Donkers, *Parameter estimation of an electrochemistry-based lithium-ion battery model using a two-step procedure and a parameter sensitivity analysis,* International Journal of Energy Research **42**, 2417 (2018).

[90] J. C. Forman, S. J. Moura, J. L. Stein, and H. K. Fathy, *Genetic identification and fisher identifiability analysis of the Doyle–Fuller–Newman model from experimental cycling of a LiFePO4 cell,* Journal of Power Sources **210**, 263 (2012).

[91] J. Marcicki, M. Canova, A. T. Conlisk, and G. Rizzoni, *Design and parametrization analysis of a reduced-order electrochemical model of graphite/LiFePO4 cells for SOC/SOH estimation,* Journal of Power Sources **237**, 310 (2013).

[92] L. Zhang, L. Wang, G. Hinds, C. Lyu, J. Zheng, and J. Li, *Multi-objective optimization of lithium-ion battery model using genetic algorithm approach,* Journal of Power Sources **270**, 367 (2014).

[93] Z. Chu, R. Jobman, A. Rodríguez, G. L. Plett, M. S. Trimboli, X. Feng, and M. Ouyang, *A control-oriented electrochemical model for lithium-ion battery. Part II: Parameter identification based on reference electrode,* Journal of Energy Storage **27**, 101101 (2020).

[94] M. Ecker, T. K. D. Tran, P. Dechent, S. Käbitz, A. Warnecke, and D. U. Sauer, *Parameterization of a Physico-Chemical Model of a Lithium-Ion Battery I. Determination of Parameters,* Journal of the Electrochemical Society **162**, A1836 (2015).

[95] J. Sturm, A. Rheinfeld, I. Zilberman, F. B. Spingler, S. Kosch, F. Frie, and A. Jossen, *Modeling and simulation of inhomogeneities in a 18650 nickel-rich, silicon-graphite lithium-ion cell during fast charging,* Journal of Power Sources **412**, 204 (2019).

[96] R. Jobman, M. S. Trimboli, and G. L. Plett, *Identification of lithium-ion physics-based model parameter values,* Journal of Energy Challenges and Mechanics **2**, 45 (2015).

[97] J. Schmalstieg, C. Rahe, M. Ecker, and D. U. Sauer, *Full Cell Parameterization of a High-Power Lithium-Ion Battery for a Physico-Chemical Model: Part I. Physical and Electrochemical Parameters,* Journal of the Electrochemical Society **165**, A3799 (2018).

[98] V. Ramadesigan, K. Chen, N. A. Burns, V. Boovaragavan, R. D. Braatz, and V. R. Subramanian, *Parameter Estimation and Capacity Fade Analysis of Lithium-Ion Batteries Using Reformulated Models,* Journal of the Electrochemical Society **158**, A1048 (2011).

[99] S. Park, D. Kato, Z. Gima, R. Klein, and S. Moura, *Optimal Input Design for Parameter Identification in an Electrochemical Li-ion Battery Model,* in *American Control Conference* (2018) pp. 2300–2305.

[100] J. Yan, G. Xu, H. Qian, and Y. Xu, *Battery fast charging strategy based on model predictive control,* in *IEEE 72nd Vehicular Technology Conference* (2010) pp. 1–8.

[101] C. Zou, X. Hu, Z. Wei, T. Wik, and B. Egardt, *Electrochemical Estimation and Control for Lithium-Ion Battery Health-Aware Fast Charging,* IEEE Transactions on Industrial Electronics **65**, 6635 (2018).

[102] M. A. Xavier and M. S. Trimboli, *Lithium-ion battery cell-level control using constrained model predictive control and equivalent circuit models,* Journal of Power Sources **285**, 374 (2015).

[103] A. Goldar, R. Romagnoli, L. D. Couto, A. Romero, M. Kinnaert, and E. Garone, *MPC strategies based on the equivalent hydraulic model for the fast charge of commercial Li-ion batteries,* Computers & Chemical Engineering **141**, 107010 (2020).

[104] R. Klein, N. A. Chaturvedi, J. Christensen, J. Ahmed, R. Findeisen, and A. Kojic, *Optimal charging strategies in lithium-ion battery,* in *IEEE American Control Conference* (2011) pp. 382–387.

[105] J. Liu, G. Li, and H. K. Fathy, *A Computationally Efficient Approach for Optimizing Lithium-Ion Battery Charging,* Journal of Dynamic Systems, Measurement, and Control **138**, 021009 (2015).

[106] C. Zou, C. Manzie, and D. Nešić, *Model Predictive Control for Lithium-Ion Battery Optimal Charging,* IEEE/ASME Transactions on Mechatronics **23**, 947 (2018).

[107] X. Hu, H. E. Perez, and S. J. Moura, *Battery charge control with an electro-thermal-aging coupling,* in *ASME Dynamic Systems and Control Conference* (2015) pp. V001T13A002–V001T13A002.

[108] F. Lam, A. Allam, W. T. Joe, Y. Choi, and S. Onori, *Offline Multiobjective Optimization for Fast Charging and Reduced Degradation in Lithium-Ion Battery Cells Using Electrochemical Dynamics,* IEEE Control Systems Letters **5**, 2066 (2021).

[109] H. E. Perez, X. Hu, S. Dey, and S. J. Moura, *Optimal Charging of Li-Ion Batteries With Coupled Electro-Thermal-Aging Dynamics,* IEEE Transactions on Vehicular Technology **66**, 7761 (2017).

[110] Y. Yin, Y. Bi, Y. Hu, and S.-Y. Choe, *Optimal Fast Charging Method for a Large-Format Lithium-Ion Battery Based on Nonlinear Model Predictive Control and Reduced Order Electrochemical Model,* Journal of the Electrochemical Society **167**, 160559 (2021).

[111] S. Lucia, M. Torchio, D. M. Raimondo, R. Klein, R. D. Braatz, and R. Findeisen, *Towards adaptive health-aware charging of Li-ion batteries: A real-time predictive control approach using first-principles models,* in *IEEE American Control Conference* (2017) pp. 4717–4722.

[112] A. Pozzi, M. Torchio, and D. M. Raimondo, *Film growth minimization in a Li-ion cell: a Pseudo Two Dimensional model-based optimal charging approach,* in *2018 European Control Conference (ECC)* (2018) pp. 1753–1758, 00014.

[113] M. Pathak, D. Sonawane, S. Santhanagopalan, R. D. Braatz, and V. R. Subramanian, *(Invited) Analyzing and Minimizing Capacity Fade through Optimal Model-based Control - Theory and Experimental Validation,* ECS Transactions **75**, 51 (2017).

[114] M. Torchio, L. Magni, R. D. Braatz, and D. M. Raimondo, *Design of Piecewise Affine and Linear Time-Varying Model Predictive Control Strategies for Advanced Battery Management Systems,* Journal of the Electrochemical Society **164**, A949 (2017).

[115] M. Torchio, L. Magni, R. D. Braatz, and D. M. Raimondo, *Optimal health-aware charging protocol for Lithium-ion batteries: A fast model predictive control approach,* IFAC-PapersOnLine **49**, 827 (2016).

[116] A. Pozzi, M. Torchio, R. D. Braatz, and D. M. Raimondo, *Optimal charging of an electric vehicle battery pack: A real-time sensitivity-based model predictive control approach,* Journal of Power Sources **461**, 228133 (2020).

[117] M. Torchio, L. Magni, R. D. Braatz, and D. M. Raimondo, *Optimal charging of a Li-ion cell: A hybrid model predictive control approach,* in *IEEE 55th Conference on Decision and Control* (2016) pp. 4053–4058.

[118] M. Torchio, N. A. Wolff, D. M. Raimondo, L. Magni, U. Krewer, R. B. Gopaluni, J. A. Paulson, and R. D. Braatz, *Real-time model predictive control for the optimal charging of a lithium-ion battery,* in *IEEE American Control Conference* (2015) pp. 4536–4541.

[119] S. Kolluri, S. V. Aduru, M. Pathak, R. D. Braatz, and V. R. Subramanian, *Real-time Nonlinear Model Predictive Control (NMPC) Strategies using Physics-Based Models for Advanced Lithium-ion Battery Management System (BMS),* Journal of the Electrochemical Society **167**, 063505 (2020).

[120] B. Suthar, V. Ramadesigan, P. W. Northrop, B. Gopaluni, S. Santhanagopalan, R. D. Braatz, and V. R. Subramanian, *Optimal control and state estimation of lithium-ion batteries using reformulated models,* in *IEEE American Control Conference* (2013) pp. 5350–5355.

[121] B. Suthar, V. Ramadesigan, S. De, R. D. Braatz, and V. R. Subramanian, *Optimal charging profiles for mechanically constrained lithium-ion batteries,* Physical Chemistry Chemical Physics **16**, 277 (2014).

[122] B. Suthar, D. Sonawane, R. D. Braatz, and V. R. Subramanian, *Optimal Low Temperature Charging of Lithium-ion Batteries,* IFAC-PapersOnLine **48**, 1216 (2015).

[123] R. Methekar, V. Ramadesigan, R. D. Braatz, and V. R. Subramanian, *Optimum Charging Profile for Lithium-Ion Batteries to Maximize Energy Storage and Utilization,* ECS Transactions **25**, 139 (2010).

[124] E. Inoa and J. Wang, *PHEV Charging Strategies for Maximized Energy Saving,* IEEE Transactions on Vehicular Technology **60**, 2978 (2011).

[125] S. Pramanik and S. Anwar, *Electrochemical model based charge optimization for lithium-ion batteries,* Journal of Power Sources **313**, 164 (2016).

[126] A. Abdollahi, X. Han, N. Raghunathan, B. Pattipati, B. Balasingam, K. Pattipati, Y. Bar-Shalom, and B. Card, *Optimal charging for general equivalent electrical battery model, and battery life management,* Journal of Energy Storage **9**, 47 (2017).

[127] A. R. Mandli, S. Ramachandran, A. Khandelwal, K. Y. Kim, and K. S. Hariharan, *Fast computational framework for optimal life management of lithium ion batteries,* International Journal of Energy Research **42**, 1973 (2018).

[128] Y. Parvini and A. Vahidi, *Maximizing charging efficiency of lithium-ion and lead-acid batteries using optimal control theory,* in *IEEE American Control Conference* (2015) pp. 317–322.

[129] S. Park, D. Lee, H. J. Ahn, C. Tomlin, and S. Moura, *Optimal Control of Battery Fast Charging Based-on Pontryagin's Minimum Principle,* in *IEEE Conference on Decision and Control* (2020) pp. 3506–3513.

PART I

BATTERY MODELING AND PARAMETERIZATION

2

BATTERY MODELING AND IMPLEMENTATION

Using electrochemistry-based battery models in aging-aware charging remains challenging due to their computational complexity. In this chapter, we study the impact of several types of model simplifications on the trade-off between model accuracy and computation time for the Doyle-Fuller-Newman (DFN) model. As a basis for comparison, we consider, to what we refer as, the complete DFN (CDFN) model, which is a DFN model without any simplifications, and which includes the concentration dependency of parameters that have been studied in previous literature. Furthermore, we propose a highly efficient implementation of the CDFN model that leads to a considerable decrease in computation time, and that has been developed into a freely downloadable toolbox. This toolbox allows the user to easily toggle between the studied simplifications to make the desired trade-off between model accuracy and computation time. We compare several simplified DFN models to the single-particle model and the CDFN model. Here, we show that with the proposed implementation, and by selectively making the proposed simplifications, as well as selectively choosing the grid parameters, a model can be obtained that has a minor impact on model accuracy, achieving a simulation time of over 5000 times faster than real-time.

This chapter is based on Publication **P.2**.

2.1. INTRODUCTION

As stated in Chapter 1, electrochemistry-based models are instrumental for aging-aware charging, as they allow for a description of the internal behavior of the battery. The Doyle-Fuller-Newman (DFN) model is a widely used electrochemistry-based model, which is described by a set of partial differential equations (PDEs) [1]. While the DFN model can describe internal states of the battery, its model complexity generally leads to large computation times. This model complexity, as well as the difficulty to uniquely determine all model parameters or to uniquely determine the internal states based on the measured voltages and currents, prohibits using the DFN model in battery-management-system functionalities.

There are several ways to reduce the computational burden of the DFN model. One way to reduce complexity is to apply model reduction to the DFN model. A common technique is to make a polynomial approximation of the solid-phase concentration diffusion [2, 3]. Model reduction is also applied on the DFN model through the use of techniques such as Galerkin projections [4] and proper orthogonal decomposition [5, 6]. An overview of this type of model reduction can be found in [7]. However, the reduction is mostly in the number of equations, while the reduction in computation time is only marginal, when applied to the DFN model, as was shown in [6]. Another way to reduce complexity is by simplifying the model equations, see, e.g., [3, 8–11]. A popular example is the so-called single-particle model (SPM) [12, 13], in which the equations for solid-phase concentration and potentials are simplified. Another approach is to linearize the governing equations of the DFN model, see, e.g., [14]. Finally, it has been recognized that many parameters depend on concentrations [15–19], while actually ignoring these dependencies leads to a simplification of the governing model equations [20].

Besides addressing the complexity of the DFN model, another way to reduce computation time is to develop algorithms that compute the solution to the DFN model equations more efficiently, see e.g. [6, 20, 21], and [22], where the latter proposes a computationally efficient model implementation in presence of above-discussed simplified solid-phase dynamics. In these papers, the PDEs that describe the DFN model are spatially and temporally discretized, which results in a set of nonlinear algebraic equations (AEs). Numerical methods are then developed in an attempt to solve this set of AEs as efficiently as possible.

In this chapter, we study the impact of several types of model simplifications on the trade-off between model accuracy and computation time for the DFN model. As a basis for comparison, we consider, to what we will refer as, the complete DFN (CDFN) model, which is a DFN model without any simplifications, and includes the concentration dependency of parameters that have been studied in previous literature [15–19]. The CDFN and the considered simplifications are given in Section 2.2. Furthermore, we propose a computationally efficient implementation of the CDFN model that leads to a significant reduction in computation time, which is presented in Section 2.3. After spatial and temporal discretization of the DFN model, we will show that through substitution of equations, the number of equations describing the DFN model can be considerably reduced to a small set of algebraic equations. This model implementation has been developed into a freely downloadable toolbox, which will also be presented in Section 2.3. This toolbox allows the user to easily toggle between the studied simplifications to make the

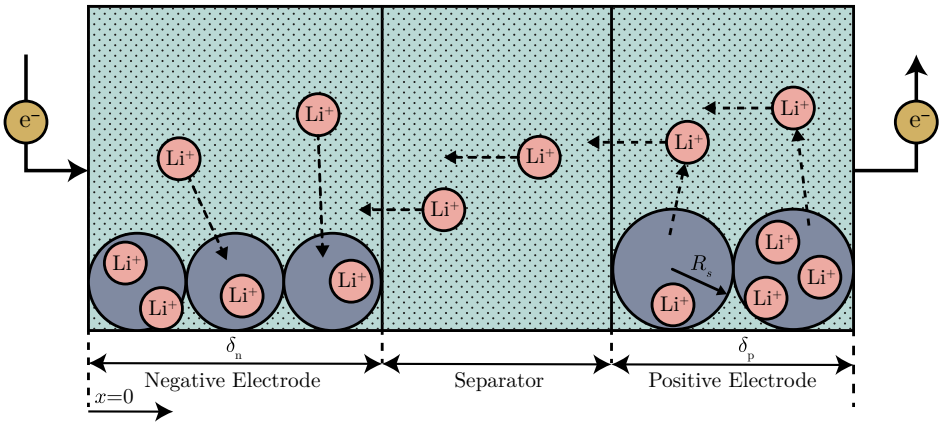

Figure 2.1: DFN modeling approach for a Li-ion cell (situation shown for charging).

desired trade-off between model accuracy and computation time.

We will study the impact of the proposed simplifications on model accuracy and computation time for two different sets of parameters, to show the validity of these simplifications and the trade-off between computation time and model accuracy that can be made. Furthermore, we will study the impact of varying spatial accuracy on the trade-off between model accuracy and computation time. We will validate the proposed model implementation against the implementation presented in [23], and also show that the proposed implementation is significantly faster than the model implementations presented in [23] and [6]. It is important to note here that the implementation in [23] relies on a variable-time-step solver, while the proposed implementation is based on a fixed-time-step discretization scheme. We will reflect on this choice in the results section. Finally, we will compare several simplified DFN models to the SPM and the CDFN model. The results of these studies are presented in Section 2.4, after which conclusions are drawn in Section 2.5.

2.2. BATTERY MODELING

In this section, we briefly formulate the DFN model, and introduce several simplifications, which we will show in Section 2.4 to have no significant impact on the accuracy of the model, both in the input-output behavior as well as the internal states. Further simplifications on the resulting model will be applied to arrive at the so-called SPM.

2.2.1. DOYLE-FULLER-NEWMAN MODEL

The DFN model is a widely used electrochemistry-based model introduced in [1]. Fig. 2.1 illustrates the modeling approach for a Li-ion cell. In the x dimension, the cell is divided into three regions, namely the negative electrode, the separator, and the positive electrode. In the electrodes, Li-ions exist essentially in two phases. In the solid phase, Li-ions are intercalated into the solid-phase material, which is represented by spheres with radius R_s. In the electrolyte phase, Li-ions exist in a dissolved state in the electrolyte.

In the separator, Li-ions exist only in the electrolyte phase. During charging, as shown in Fig. 2.1, intercalated Li-ions exit the solid particles in the positive electrode and enter the solid particles in the negative electrode. During discharging, the opposite process happens. We will shortly summarize the governing equations of the DFN model, which will be mostly based on the formulation given in [24]. The DFN model is governed by four coupled partial differential equations (PDEs):

1. The Li-ion concentration in the solid phase c_s for $x \in [0, \delta_n] \cup [L-\delta_p, L]$ is given by Fick's law as

$$\frac{\partial c_s}{\partial t} = \frac{D_s}{r^2}\frac{\partial}{\partial r}\Big(r^2 \frac{\partial c_s}{\partial r}\Big), \tag{2.1a}$$

with boundary conditions

$$\frac{\partial c_s}{\partial r}\Big|_{r=0} = 0, \quad -D_s \frac{\partial c_s}{\partial r}\Big|_{r=R_s} = j_n, \tag{2.1b}$$

with D_s the diffusion coefficient of lithium in the solid phase, and j_n is the net molar flux of Li-ions exiting the particle. Furthermore, δ_n and δ_p are the thickness of the negative electrode and positive electrode, respectively, and L is the thickness of the cell, see Fig. 2.1.

2. The Li-ion concentration in the electrolyte phase c_e for $x \in [0, L]$ is given by

$$\varepsilon_e \frac{\partial c_e}{\partial t} = \frac{\partial}{\partial x}\Big(D_e^{\text{eff}} \frac{\partial c_e}{\partial x}\Big) + a_s(1-t_+^0) j_n, \tag{2.2a}$$

with boundary conditions

$$D_e^{\text{eff}} \frac{\partial c_e}{\partial x}\Big|_{x=0} = D_e^{\text{eff}} \frac{\partial c_e}{\partial x}\Big|_{x=L} = 0, \tag{2.2b}$$

where $D_e^{\text{eff}} = D_e \varepsilon_e^p$ is the effective Li-ion diffusion coefficient in the electrolyte phase, in which ε_e is the electrolyte phase volume fraction, p is the Bruggeman porosity exponent, and D_e is the diffusion constant of Li-ions in the electrolyte. Furthermore, in (2.2), $a_s = 3\varepsilon_s / R_s$ is the specific interfacial surface area, in which ε_s is the active material volume fraction, and t_+^0 is the transference number of Li-ions.

3. The potential in the solid phase ϕ_s for $x \in [0, \delta_n] \cup [L-\delta_p, L]$ is given by Ohm's law, i.e.,

$$\frac{\partial}{\partial x}\Big(\sigma^{\text{eff}} \frac{\partial \phi_s}{\partial x}\Big) = a_s F j_n, \tag{2.3a}$$

with boundary conditions

$$\sigma^{\text{eff}} \frac{\partial \phi_s}{\partial x}\Big|_{x=0} = \frac{I_a}{A}, \quad \sigma^{\text{eff}} \frac{\partial \phi_s}{\partial x}\Big|_{x=\delta_n} = 0, \tag{2.3b}$$

$$\sigma^{\text{eff}} \frac{\partial \phi_s}{\partial x}\Big|_{x=L-\delta_p} = 0, \quad \sigma^{\text{eff}} \frac{\partial \phi_s}{\partial x}\Big|_{x=L} = \frac{I_a}{A}, \tag{2.3c}$$

where F is Faraday's constant, $\sigma^{\text{eff}} = \varepsilon_s \sigma$ is the effective electronic conductivity of a porous electrode, in which σ is the conductivity of the solid material, A is the area of the electrode plate, and I_a is the applied current through the battery, with $I_a > 0$ indicating charging.

4. The potential in the electrolyte phase ϕ_e for $x \in [0, L]$ is given by

$$\frac{\partial}{\partial x}\left(\kappa_{\text{eff}} \frac{\partial \phi_e}{\partial x} + \kappa_{\text{eff}} \nu \frac{2RT}{F} \frac{\partial \ln c_e}{\partial x}\right) = -a_s F j_n, \tag{2.4a}$$

with boundary conditions [1]

$$\kappa_{\text{eff}} \frac{\partial \phi_e}{\partial x}\Big|_{x=0} = \kappa_{\text{eff}} \frac{\partial \phi_e}{\partial x}\Big|_{x=L} = \kappa_{\text{eff}} \phi_e\big|_{x=L} = 0, \tag{2.4b}$$

in which $\kappa_{\text{eff}} = \kappa \varepsilon_e^p$ is the effective ionic conductivity, where κ is the ionic conductivity, R is the universal gas constant, and T is the absolute temperature. Furthermore, $\nu = (t_+^0 - 1)\left(1 + \frac{d \ln f_\pm}{d \ln c_e}\right)$, in which $f_\pm$ is the mean molar activity coefficient of the electrolyte.

The above PDEs (2.1)-(2.4) are coupled by a Butler-Volmer rate equation, which describes the electrochemical reaction rate at the solid/electrolyte interface. This rate equation is given by

$$j_n = \frac{i_0}{F}\left(\exp\left(\frac{\alpha_a F}{RT}\eta\right) - \exp\left(-\frac{\alpha_c F}{RT}\eta\right)\right), \tag{2.5a}$$

which is only defined for $x \in [0, \delta_n] \cup [L - \delta_p, L]$ and assumed zero for $x \in (\delta_n, L - \delta_p)$, since there are no particles in the separator. In (2.5a), α_a is the anodic transfer coefficient, α_c is the cathodic transfer coefficient, and the overpotential at the electrodes η is defined as

$$\eta = \phi_s - \phi_e - U, \tag{2.5b}$$

in which U denotes the equilibrium potential of the electrode, which can be given by a pre-defined function typically of the solid-phase concentration at the solid-electrolyte interface $c_{s,e}(x,t) = c_s(R_s, x, t)$. Furthermore, the exchange current density i_0 in (2.5a) is given by

$$i_0 = k_0 c_e^{\alpha_a} (c_s^{\max} - c_{s,e})^{\alpha_a} c_{s,e}^{\alpha_c}, \tag{2.5c}$$

where k_0 is the rate constant of the electrochemical reaction, and $c_s^{\max}$ is the maximum concentration in the solid phase. Finally, the terminal battery voltage is computed with

$$V(t) = \phi_s(L,t) - \phi_s(0,t) + \frac{R_{\text{cc}}}{A} I_a(t), \tag{2.6}$$

in which R_{cc} is an empirical contact resistance.

[1] Note that compared to **P2**, a correction has been made in (2.4b).

2.2.2. CONCENTRATION-DEPENDENT PARAMETERS

Aside from physical constants, such as the universal gas constant R and Faraday's constant F, the material properties that define the parameters of the DFN model (and SPM) need to be determined. However, numerous literature, e.g. [15–19], has shown that at least some of these material properties are not necessarily constant and can significantly change depending on the Li-ion concentration level of the material. Measuring these parameters can involve destructive procedures, such as opening of the battery cell, which makes determining the dependencies difficult.

Numerous results on the measurement and use of concentration-dependent parameters have been reported in the literature, e.g., [1, 5, 15–19, 23–32]. Since the electrolyte is relatively easy to isolate, electrolyte-related parameters, and more specifically, the transport properties, such as κ and D_e, are more often measured than the parameters of the electrodes, such D_s. The concentration dependency of the electrolyte transport properties have been measured and shown for various different electrolytes in e.g., [15, 16, 19]. The concentration-dependent parameters provided in these papers have been used in various literature, e.g. [1, 5, 23–27]. However, often $f_\pm$ is still assumed constant, and is therefore ignored in the DFN equations, even though in [15, 16, 33], $f_\pm$ is shown to significantly change over the concentration in the electrolyte. Out of all the parameters, the concentration dependency of the conductivity in the electrolyte κ seems to be the least difficult to determine, as it is most commonly taken as a concentration-dependent parameter in the DFN model, as done in e.g., [1, 24]. The other electrolyte transport properties, i.e., the mean molar activity coefficient $f_\pm$, transference number t_+^0, and diffusion coefficient D_e are generally more difficult to determine. The literature on the measurement of the concentration dependency of the electrode parameters is more scarce, with the exception of the diffusion coefficient D_s, of which its concentration-dependency has been shown in e.g. [17, 18, 28–30]. However, such results have not yet been widely applied in the context of the DFN model, with [34] being the only example, to the authors' knowledge.

In Fig. 2.2, some examples of concentration-dependent parameters are shown. Note that there seems to be a discrepancy between the examples obtained from [24] and [31], even though the authors in [24] (indirectly) cite the paper of [31] as their source of the concentration-dependent conductivity function. We further see that the parameters can change significantly, and in the case of D_s in orders of magnitudes, over a varying concentration. This would suggest that at large currents, which would induce large concentration gradients, the parameter values can significantly change, suggesting the need to implement them as a function of concentration. In Section 2.4, we will show that this may not necessarily be the case for any of the parameters shown in Fig. 2.2.

2.2.3. SIMPLIFICATIONS TO THE DOYLE-FULLER-NEWMAN MODEL

Adding parameter dependencies introduces additional complexity in the DFN model. Instead of increasing the complexity, we can also make several simplifications to the DFN model that aim at reducing complexity. In particular,

[S1]: The rate equation (2.5a) can be linearized with respect to the overpotential η around the origin, due to the fact that $\frac{F}{RT} \gg |\eta|$, which also implies that as $|\eta|$ becomes larger, the errors made due to this assumption also become larger. Note

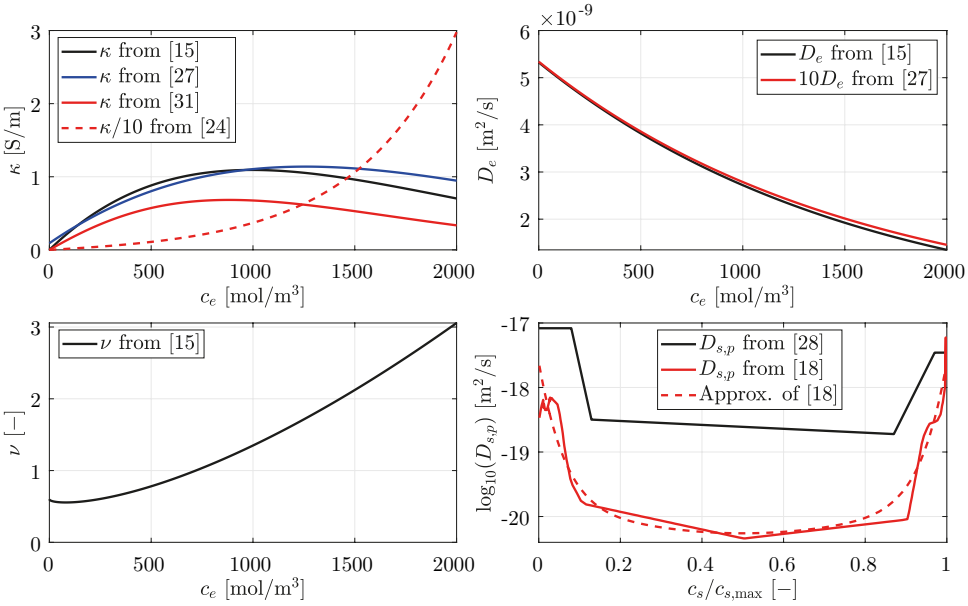

Figure 2.2: Various examples of concentration-dependent parameters resulting from various cell chemistries found in literature.

that $\alpha_a + \alpha_c = 1$ [36], which allows the resulting linearized Butler-Volmer equation of (2.5a)-(2.5b) to be written as

$$j_n = \frac{i_0}{RT}(\phi_s - \phi_e - U). \tag{2.7}$$

From Fig. 2.3, we can see that this is a reasonable approximation up to an overpotential of about $|\eta| < 0.01$.

[S2]: A zero-order Taylor approximation can be made for the concentration-dependent parameters, i.e., $\kappa(c_e) = \kappa(c_e^*)$, $D_e(c_e) = D_e(c_e^*)$, $\nu(c_e) = \nu(c_e^*)$, $D_s(s) = D_s(s^*)$, where s is the stoichiometry $c_{s,e}/c_s^{\max}$, c_e^* is the evaluation point chosen for c_e, and s^* is the evaluation point chosen for s, which can be chosen in either of the following ways.

- [S2-I]: The evaluation points are chosen dynamically, such that they vary over space and time. In this chapter, the evaluation point is chosen after time discretization, as the values of the concentration-dependent parameters at the previous time sample t_{k-1}, i.e., $\kappa(c_e^*) = \kappa(c_e(t_{k-1}))$, $D_e(c_e^*) = D_e(c_e(t_{k-1}))$, $\nu(c_e^*) = \nu(c_e(t_{k-1}))$, $D_s(s^*) = D_s(s(t_{k-1}))$.
- [S2-II]: The evaluation points are chosen as a constant value, such that the concentration-dependent parameters no longer vary over space and time, i.e., $\kappa(c_e^*) = \kappa(\tilde{c}_e)$, $D_e(c_e^*) = D_e(\tilde{c}_e)$, $\nu(c_e^*) = \nu(\tilde{c}_e)$, $D_s(s^*) = D_s(\tilde{s})$. Here, $\tilde{c}_e$ is the expected average concentration in the electrolyte, which

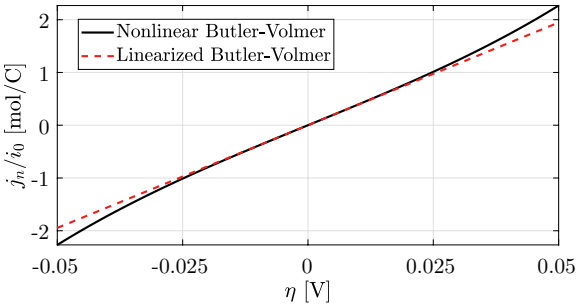

Figure 2.3: Comparison between the nonlinear Butler-Volmer equation given by (2.5a) and the linearized (with respect to the over-potential η) Butler-Volmer equation given by (2.7). The equations have been evaluated for $T = 298$ K.

can be chosen as $\tilde{c}_e = c_{e,a}$, where $c_{e,a}$ is the average concentration in the electrolyte in equilibrium, and $\tilde{s}$ is the expected average stoichiometry, which can be chosen as $\tilde{s} = (s_{100\%} + s_{0\%})/2$, in which $s_{100\%}$ is the stoichiometry at 100% state-of-charge and $s_{0\%}$ is the stoichiometry at 0% state-of-charge.

[S3]: Finally, a common simplification is to make a two-parameter polynomial approximation of the solid-phase diffusion [2, 35]. Here, the concentration profile within a particle is assumed to be a parabola over the radial dimension r. Then, by substituting this approximated concentration into (2.1a), volume-averaging the resulting expression, and evaluating the boundary conditions (2.1b), expressions for the bulk concentration $c_{s,\text{bulk}}$ and surface concentration $c_{s,e}$ can be obtained, i.e.,

$$\frac{\partial c_{s,\text{bulk}}}{\partial t} = \frac{-3}{R_s} j_n, \quad c_{s,e} = c_{s,\text{bulk}} - \frac{R_s}{5D_s} j_n. \tag{2.8}$$

The main advantage of this simplification is that the diffusion equation in (2.1), which is the only governing equation that depends on r, simplifies to merely two equations, describing the bulk and surface concentration of the particles in the solid phase as a function of x and t.

2.2.4. SINGLE-PARTICLE MODEL

The SPM is defined by the main assumption that the diffusion dynamics inside the solid particles is the slowest process, and therefore dominates over the other dynamics [36]. Under this assumption, we can formulate the following corresponding simplifications [12].

[S4]: The concentration in the solid phase c_s is constant over x.

[S5]: The exchange current density i_0 is approximated by $\tilde{i}_0 = i_0(c_{s,e}, \tilde{c}_e)$, where $\tilde{c}_e$ is the mean electrolyte concentration over each of the electrodes.

[S6]: The over-potential η is approximated by $\tilde{\eta} = \phi_s - \tilde{\phi}_e - U$, where $\tilde{\phi}_e$ is the mean electrolyte potential over each of the electrodes.

Note that as a consequence of [S4] and [S5], $\tilde{i}_0$ only changes over time. As a result of [S4], the flux of Li-ions at the solid-electrolyte interface j_n can be assumed to be equal for all particles in each of the electrodes, and hence j_n can be directly computed from (2.3), i.e.,

$$j_n(x,t) = \begin{cases} -\frac{I_a(t)}{Aa_s\delta_n F} & \text{for } x \in [0, \delta_n], \\ \frac{I_a(t)}{Aa_s\delta_p F} & \text{for } x \in [L-\delta_p, L]. \end{cases} \tag{2.9}$$

The solid-phase potential ϕ_s can then be computed from (2.5), with $\phi_e = \tilde{\phi}_e$. Note that, as a result of (2.9), we have that (2.1), (2.2), and (2.4) are no longer coupled, which means that these equations can be solved explicitly for a given I_a.

We will refer to this model, given by (2.1), (2.2),(2.4), (2.5), (2.6), (2.9), as the SPM. Note that in literature the SPM that includes electrolyte dynamics, as presented above is usually referred to as the SPMe (Single-Particle Model with electrolyte dynamics), while SPM is usually referred to the model that is obtained under the additional assumption that electrolyte dynamics, corresponding to (2.2) and (2.4), are ignored. We further note that in our formulation of the SPM, the parameters can be concentration-dependent, and therefore Simplifications [S1]-[S3] can also be applied to the SPM.

2.3. MODEL IMPLEMENTATION

The objective of this chapter is to compare the computational complexity and the accuracy of several electrochemistry-based models, and to implement the DFN model such that a trade-off can be made between computational complexity and accuracy. The DFN model formulated in Section 2.2.1, under the assumption that the parameters considered in Section 2.2.2 are concentration-dependent, can be seen as the (most) complete DFN model (CDFN). From this CDFN, any of the simplifications formulated in Section 2.2.3 can be applied to arrive at a simplified form of the CDFN. The implementation of the CDFN and its corresponding simplifications involves several steps. Firstly, fairly standard spatial and temporal discretization is applied to arrive at a set of AEs. Secondly, the set of AEs is reduced to a smaller set of AEs through substitution, after which the resulting set of AEs can be solved using Newton's method. The discretization procedure described here is similar to the procedure presented in [6]. Therefore, in this section, we will shortly summarize this procedure to formulate the set of AEs that arises from the discretization. For further details on the discretization approach, the reader is referred to [6]. Note that a key difference between the discretization described in [6] and this chapter, is that in the finite-volume method (FVM) discretization, to determine the edge parameter values of the control volumes, the harmonic mean of two neighboring control volumes is used, as described in [23]. Finally, we will present a freely downloadable toolbox to simulate the DFN model based on the proposed implementation, which can be used without any knowledge on the proposed model implementation.

2.3.1. DISCRETIZATION

As a first step, spatial discretization is applied on the PDEs (2.1) - (2.4). The equation describing the diffusion of the solid-phase concentration (2.1) is discretized along the radial direction using a finite-difference method (FDM), to arrive at a set of differential algebraic equations (DAEs). The other equations (2.2)-(2.4) are discretized using an FVM, after which the resulting set of nonlinear DAEs can be written as

$$\frac{d}{dt}\mathbf{c}_s = A_{c_s}\mathbf{c}_s + B_{c_s}\mathbf{j}_n, \tag{2.10a}$$

$$\frac{d}{dt}\mathbf{c}_e = A_{c_e}\mathbf{c}_e + B_{c_e}\mathbf{j}_n, \tag{2.10b}$$

$$0 = A_{\phi_s}\boldsymbol{\phi}_s + B_{\phi_s}\mathbf{j}_n + C_{\phi_s}I_a, \tag{2.10c}$$

$$0 = A_{\phi_e}\boldsymbol{\phi}_e + B_{\phi_e}\mathbf{j}_n + D_{\phi_e}\ln(\mathbf{c}_e), \tag{2.10d}$$

where the bold faced characters refer to their respective vector variables, which are defined as[2]

$$\begin{aligned}
\mathbf{c}_s(t) &= [\,\mathbf{c}_{s,n}(x_1,t)\ \dots\ \mathbf{c}_{s,n}(x_{n_n},t)\ \mathbf{c}_{s,p}(x_{n_n+n_s+1},t)\ \dots\ \mathbf{c}_{s,p}(x_{n_n+n_s+n_p},t)\,]^\top,\\
\mathbf{c}_{s,n}(x,t) &= [\,c_s(x,r_{n,1},t)\ \dots\ c_s(x,r_{n,n_{r,n}},t)\,]^\top, \quad \mathbf{c}_{s,p}(x,t) = [\,c_s(x,r_{p,1},t)\ \dots\ c_s(x,r_{p,n_{r,p}},t)\,]^\top,\\
\mathbf{c}_e(t) &= [\,c_e(x_1,t)\ \dots\ c_e(x_{n_n+n_s+n_p},t)\,]^\top,\\
\boldsymbol{\phi}_s(t) &= [\,\phi_s(x_1,t)\ \dots\ \phi_s(x_{n_n},t)\ \phi_s(x_{n_n+n_s+1},t)\ \dots\ \phi_s(x_{n_n+n_s+n_p},t)\,]^\top,
\end{aligned} \tag{2.11}$$

where x_l for $l \in \{1,\dots,n_n+n_s+n_p\}$, r_{n,m_n} for $m_n \in \{1,\dots,n_{r,n}\}$, and r_{p,m_p} for $m_p \in \{1,\dots,n_{r,p}\}$ are the grid points of the discretization, and $\boldsymbol{\phi}_e$, $\mathbf{j}_n$ are defined similarly to $\mathbf{c}_e$ and $\boldsymbol{\phi}_s$, respectively. In (2.11), n_n, n_s, n_p are the number of elements of the FVM discretization, in the negative electrode, separator, and positive electrode, respectively. Furthermore, $n_{r,n}, n_{r,p}$ are the number of elements of the FDM discretization, in the negative electrode, and the positive electrode, respectively. How to construct matrices $A_i, B_i, i \in \{c_s, c_e, \phi_s, \phi_e\}$, C_{ϕ_s}, and D_{ϕ_e} is explained in detail in [6]. The four sets of DAEs (2.10) are coupled by the Butler-Volmer rate equation, written as

$$\mathbf{j}_n = \operatorname{diag}\left(\frac{\mathbf{i}_0(\bar{\mathbf{c}}_e,\bar{\mathbf{c}}_s)}{F}\right)\left(\exp\left(\frac{\alpha_a F}{RT}(\boldsymbol{\phi}_s - \bar{\boldsymbol{\phi}}_e - \mathbf{U}(\bar{\mathbf{c}}_s))\right) - \exp\left(-\frac{\alpha_c F}{RT}(\boldsymbol{\phi}_s - \bar{\boldsymbol{\phi}}_e - \mathbf{U}(\bar{\mathbf{c}}_s))\right)\right), \tag{2.12}$$

in which the $\operatorname{diag}(v)$ denotes a diagonal matrix with the elements of vector v on the main diagonal. Furthermore, in (2.12), the barred boldfaced variables $\bar{\mathbf{c}}_s$, $\bar{\mathbf{c}}_e$, and $\bar{\boldsymbol{\phi}}_e$ refer to selected version of their non-barred boldfaced counterparts, where $\bar{\mathbf{c}}_s$ denotes the vector of solid-phase surface concentrations, and $\bar{\mathbf{c}}_e$ and $\bar{\boldsymbol{\phi}}_e$ denote the parts of $\mathbf{c}_e$ and $\boldsymbol{\phi}_e$ given in the electrodes, respectively. Mathematically, $\bar{\mathbf{c}}_s, \bar{\mathbf{c}}_e, \bar{\boldsymbol{\phi}}_e$ and $\mathbf{c}_s, \mathbf{c}_e, \boldsymbol{\phi}_e$ are related, respectively, as follows

$$\bar{\mathbf{c}}_s = \bar{A}_{c_s}\mathbf{c}_s, \quad \bar{\mathbf{c}}_e = \bar{A}_{c_e}\mathbf{c}_e, \quad \bar{\boldsymbol{\phi}}_e = \bar{A}_{\phi_e}\boldsymbol{\phi}_e, \tag{2.13}$$

[2] Note that compared to **P.2**, a correction has been made in (2.11).

where

$$\bar{A}_{c_s} = \text{diag}\Big(I_{n_n} \otimes [\mathbf{0}_{1\times n_{r,n}-1}, 1], I_{n_p} \otimes [\mathbf{0}_{1\times n_{r,p}-1}, 1]\Big),$$
$$\bar{A}_{c_e} = \bar{A}_{\phi_e} = \begin{bmatrix} I_{n_n} & 0 & 0 \\ 0 & 0 & I_{n_p} \end{bmatrix},$$

in which $\otimes$ is the Kronecker product. The DAEs (2.10a) and (2.10b) can further be discretized in time with sampling time δ_t using a backward Euler scheme, to arrive at the following set of AEs

$$0 = \hat{A}_{c_s}\mathbf{c}_s(t_k) + \hat{B}_{c_s}\mathbf{j}_n(t_k) + \mathbf{c}_s(t_{k-1}), \tag{2.14a}$$
$$0 = \hat{A}_{c_e}\mathbf{c}_e(t_k) + \hat{B}_{c_e}\mathbf{j}_n(t_k) + \mathbf{c}_e(t_{k-1}), \tag{2.14b}$$
$$0 = A_{\phi_s}\boldsymbol{\phi}_s(t_k) + B_{\phi_s}\mathbf{j}_n(t_k) + C_{\phi_s}I_a(t_k), \tag{2.14c}$$
$$0 = A_{\phi_e}\boldsymbol{\phi}_e(t_k) + B_{\phi_e}\mathbf{j}_n(t_k) + D_{\phi_e}\ln(\mathbf{c}_e(t_k)), \tag{2.14d}$$

where $t_k = k\delta_t$ for $k \in \{1,...,N\}$, in which N is the number of simulation steps. Furthermore, $\hat{A}_{c_s} = \delta_t A_{c_s} - \mathbf{I}_{n_n n_{r,n} + n_p n_{r,p}}$, $\hat{B}_{c_s} = \delta_t B_{c_s}$, $\hat{A}_{c_e} = \delta_t A_{c_e} - \mathbf{I}_{n_n+n_s+n_p}$, and $\hat{B}_{c_e} = \delta_t B_{c_e}$.

2.3.2. SOLUTION METHOD

The set of nonlinear AEs (2.14) obtained after discretization can be solved using any root-finding algorithm, such as Newton's method. However, due to the relatively large number of state variables, the use of such algorithms can be computationally slow. Namely, a large part of the computational effort is in the computation of the inverse of the Jacobian of the AEs (2.14). Therefore, in [6] a method was proposed in which Newton's method was applied sequentially to each set of equations of (2.14), thereby reducing the computation of the inverse of a single large Jacobian to the computation of the inverses of four smaller Jacobians. However, in doing so, some information of the large Jacobian is lost, which means that a quadratic convergence rate can no longer be achieved. Still, the computation time of the large Jacobian can be sufficiently large, such that the method proposed in [6] is still faster than solving (2.14) directly using Newton's method.

Rather than sequentially solving (2.14), we propose a solution method, which retains the full information of the Jacobian of (2.14), but reduces the number of AEs. This can be done by substitution of equations, such that one state variable remains. In doing so, the full information of the Jacobian of (2.14) is contained in a smaller Jacobian related to the equations of the remaining variable. The goal is to express $\mathbf{j}_n$, $\mathbf{c}_s$, $\mathbf{c}_e$, and $\boldsymbol{\phi}_e$ as a function of $\boldsymbol{\phi}_s$, such that (2.12) is a non-linear equation that only depends on $\boldsymbol{\phi}_s$. Hence, the set of AEs (2.14) will be reduced to one set of AEs in $\boldsymbol{\phi}_s$ that can be solved using Newton's method, from which $\mathbf{c}_s$,$\mathbf{c}_e$,$\boldsymbol{\phi}_e$ can be obtained.

The derivation of the reduced set of AEs is as follows. First, by solving (2.14c) for $\mathbf{j}_n$, $\mathbf{j}_n$ can be expressed as a function of $\boldsymbol{\phi}_s$, i.e.,

$$\mathbf{j}_n(t_k) = -B_{\phi_s}^{-1}\left(A_{\phi_s}\boldsymbol{\phi}_s(t_k) + C_{\phi_s}I_a(t_k)\right). \tag{2.15}$$

This expression allows the state variables $\bar{\mathbf{c}}_s, \bar{\mathbf{c}}_e$ to be expressed as a function of $\boldsymbol{\phi}_s$ by first substituting $\mathbf{j}_n$ in (2.15) into their respective associated equations given in (2.14), i.e.,

$$\hat{A}_{c_i}\mathbf{c}_i(t_k) - \hat{B}_{c_i}B_{\phi_s}^{-1}\left(A_{\phi_s}\boldsymbol{\phi}_s(t_k) + C_{\phi_s}I_a(t_k)\right) + \mathbf{c}_i(t_{k-1}) = 0,$$

for $i \in \{s, e\}$, then solving this for their respective state variables and pre-multiplying by A_{c_s}, A_{c_e}, resulting in

$$\bar{\mathbf{c}}_i(t_k) = \Gamma_{c_i} I_a(t_k) + \Phi_{c_i} \boldsymbol{\phi}_s(t_k) + \Theta_{c_i}, \tag{2.16a}$$

where

$$\begin{aligned}
\Gamma_{c_i} &= \bar{A}_{c_i} \hat{A}_{c_i}^{-1} \hat{B}_{c_i} B_{\phi_s}^{-1} C_{\phi_s}, \\
\Phi_{c_i} &= \bar{A}_{c_i} \hat{A}_{c_i}^{-1} \hat{B}_{c_i} B_{\phi_s}^{-1} A_{\phi_s}, \\
\Theta_{c_i} &= -\bar{A}_{c_i} \hat{A}_{c_i}^{-1} \mathbf{c}_i(t_{k-1}),
\end{aligned}$$

for $i \in \{s, e\}$. Note the presence of the full state vectors $\mathbf{c}_s$ and $\mathbf{c}_e$, which can be obtained by (2.16a), except without the pre-multiplication by $\bar{A}_{c_s}$ and $\bar{A}_{c_e}$, respectively. Similarly, $\bar{\boldsymbol{\phi}}_e$ can be expressed as a function of $\boldsymbol{\phi}_s$ and $\mathbf{c}_e$ by substituting (2.15) into (2.14d), i.e.,

$$A_{\phi_e} \boldsymbol{\phi}_e(t_k) - B_{\phi_e} B_{\phi_s}^{-1} \left(A_{\phi_s} \boldsymbol{\phi}_s(t_k) + C_{\phi_s} I_a(t_k) \right) + D_{\phi_e} \ln(\mathbf{c}_e(t_k)) = 0, \tag{2.16b}$$

then solving (2.14d) for $\boldsymbol{\phi}_e$ and pre-multiplying by $\bar{A}_{\phi_e}$, giving

$$\bar{\boldsymbol{\phi}}_e(t_k) = \Gamma_{\phi_e} I_a(t_k) + \Phi_{\phi_e} \boldsymbol{\phi}_s(t_k) + \Theta_{\phi_e} \ln(\mathbf{c}_e(t_k)), \tag{2.16c}$$

in which

$$\begin{aligned}
\Gamma_{\phi_e} &= \bar{A}_{\phi_e} A_{\phi_e}^{-1} B_{\phi_e} B_{\phi_s}^{-1} C_{\phi_s}, \\
\Phi_{\phi_e} &= \bar{A}_{\phi_e} A_{\phi_e}^{-1} B_{\phi_e} B_{\phi_s}^{-1} A_{\phi_s}, \\
\Theta_{\phi_e} &= -\bar{A}_{\phi_e} A_{\phi_e}^{-1} D_{\phi_e}.
\end{aligned}$$

The above steps allow the number of AEs given in (2.14) to be reduced, by substituting (2.15), (2.16a), and (2.16c) into (2.12), leading to an expression of the form $\mathscr{F}(\boldsymbol{\phi}_s(t_k)) = 0$, which can be solved using Newton's method, i.e.,

$$\boldsymbol{\phi}_s^{m+1}(t_k) = \boldsymbol{\phi}_s^m(t_k) - \mathscr{J}(\boldsymbol{\phi}_s^m(t_k))^{-1} \mathscr{F}(\boldsymbol{\phi}_s^m(t_k)), \tag{2.17}$$

where $m \in \{1, \ldots, M\}$, in which M is the maximum number of iterations, represents the current iteration in Newton's method, and $\mathscr{J}$ is the Jacobian of $\mathscr{F}$. Note that the Jacobian of $\mathscr{F}$ has $(n_n + n_p)$ rows and columns, which is considerably smaller than the Jacobian of (2.14), which would have $(3 + n_{r,n})n_n + (3 + n_{r,p})n_p + 2n_s$ rows and columns.

Since $A_{c_s}, A_{c_e}, A_{\phi_e}, D_{\phi_e}$ are actually concentration-dependent, these matrices, and the matrices derived from these matrices, need to be updated at every iteration m. As we will show in the next section, the computation of these matrices will be the largest bottleneck in the algorithm. Therefore, especially Simplifications [S2-I] and [S2-II] lead to a large decrease in computation time. When applying [S2-II], the matrices $A_{c_s}, A_{c_e}, A_{\phi_e}, D_{\phi_e}$ become constant, which means that these matrices only need to be computed once. When applying [S2-I], the matrices need to be updated every time step, if the evaluation points c_e^* and θ^* are chosen as $c_e(t_{k-1})$ and $\theta(t_{k-1})$, respectively. However, even after applying Simplification [S2-I] or [S2-II], $\Theta_i, i \in \{c_s, c_e\}$ still change at every time step, and therefore these matrices have to be updated at every time step in all cases. This summarizes the implementation of the DFN model.

2.3.3. TOOLBOX FOR FAST BATTERY SIMULATION (TOOFAB)

The DFN model with the implementation described in the previous subsection has been coded in MATLAB and developed into a toolbox. While there are already several battery simulation toolboxes (freely) available that solve the DFN model equations, e.g. [23, 27, 37], our developed toolbox provides several advantages compared to the currently available toolboxes. Firstly, with the proposed solution method described in this section, the computation times are generally significantly smaller than the currently available toolboxes, as we will show in Section 2.4. Secondly, because the model equations given by (2.10) and (2.12) have been solved directly, without the use of any other software or MATLAB toolboxes, the developed battery simulation toolbox does not require installing any other toolboxes. This is an advantage over the battery simulation toolbox presented in [23], which, to the authors' knowledge, is the only other published toolbox that solves the DFN model equations implemented in MATLAB, where SUNDIALS [38] and CasADi [39] are used to solve the model equations. Finally, for the same reason as given in the previous point, i.e., that the model equations are solved directly without any other toolboxes, the MATLAB code is fairly easily translatable into C-code, which can either be made into an executable for even faster simulation, or can be used to implement the model on an embedded system, which are generally programmed in C. Note that while we have not considered a thermal model in this chapter, a lumped thermal model, as described in [40], has been implemented in the battery simulation toolbox. The TOOlbox for FAst Battery simulation (TOOFAB) is freely available for download at: `https://github.com/Zuan-Khalik/TOOFAB`.

TOOFAB can be interfaced with the `DFN` function defined as

Table 2.1: Arguments of the `DFN` function.

Argument	Type	Comment
`out`	`struct`	Contains all the output variables, such as the output voltage, the concentrations and the potentials.
`input_current`	scalar/ array/ function handle	Contains information about the current profile. This field can be provided either as a scalar representing the desired applied current from time 0 to `final_time`, an array which contains the current levels at each specified sample time, or as a function which takes the output voltage, current, concentration and potentials, and the parameters as input and mainly provides the current as output. The latter form is especially useful when the battery is desired to be controlled in closed-loop. Example functions for `input_current` are provided with the toolbox.
`final_time`	scalar	Specifies the final simulation time.
`init_cond`	scalar/ `struct`	Specifies the initial condition, which can be either an initial state-of-charge, as a value between 0 and 1, an initial voltage, or a MATLAB `struct` where the initial condition for a non-steady-state c_s, c_e, and T can be specified. Further details on how `init_cond` can be specified can be found in the documentation of the toolbox.
`param`	`struct`	Can be used to change user-configurable parameters, such as all the model parameters, and simulation parameters, e.g., the temporal and spatial grid discretization variables. Note that this field is optional, and a default set of parameters is already contained in the `DFN` function. Parameter files containing the parameters of [23] and [24] are also included with the toolbox.

```
out = DFN(input_current, final_time, init_cond, param),
```

where the definition of the input and output arguments can be found in Table 2.1. The scripts required to reproduce the results shown in the simulation study section below are included with the toolbox. Using the configurable parameters, the toolbox allows the user to easily apply any of Simplifications [S1]-[S3], as well as varying the coarseness of the spatial and temporal discretization. This allows in making a desired trade-off between model accuracy and computation time. Several example scripts are provided with the toolbox to show how the various functions and features can be used. A more detailed user guide is also supplemented with the toolbox. In the next section, amongst other results, we will show the impact of Simplifications [S1]-[S3] to demonstrate how this trade-off can be made effectively.

2.4. SIMULATION STUDY

In this section, we will study the performance and accuracy of the CDFN model described in Section 2.2.1, and its simplified versions. Specifically, we will first study the impact of Simplifications [S1]-[S3] made in Section 2.2.3 on the accuracy and computational speed compared to the CDFN model. Then, the impact of discretization of the DFN model on model accuracy and computation time is studied. This is followed by a comparison of the numerical methods presented in [23] and [6] with the numerical method described in Section 2.3. This comparison will also serve as a validation of the model implementation with the implementation of [23], which in turn has been validated against a DFN model implemented in COMSOL [37]. Finally, based on the observations of the impact of simplifications and discretization on accuracy and computation speed, we will define several simplified DFN (SDFN) models and SPMs, and compare these with the CDFN model in terms of model accuracy and computational performance.

The simulation results have been obtained using MATLAB R2020b on a desktop PC with a 6-core 3.6-GHz processor and a memory size of 16 GB. Furthermore, unless otherwise stated, the computation times shown will be only the time it takes to compute

Table 2.2: Functions for the concentration-dependent parameters used in the high-power (HP) and high-energy (HE) parameter sets.

HP	
$\kappa^{(a)}$	$15.8\times10^{-4}c_e\exp(-0.85(c_e/1000)^{1.4})$
$D_e^{(b)}$	$0.134\times10^{-8.43-54/(T-229-5(c_e/1000))-0.22(c_e/1000)}$
$\nu^{(b)}$	$-(0.6-0.24(\frac{c_e}{1000})^{0.5}+0.98(1-0.0052(T-294))(\frac{c_e}{1000})^{1.5})$
$D_{s,p}^{(d)}$	$55782\times10^{-20.26+534.9(s-0.5)^8+2.263(s-0.5)^2}$
HE	
$\kappa^{(c)}$	$0.0413+0.5\frac{c_e}{1000}-0.47(\frac{c_e}{1000})^2+0.15(\frac{c_e}{1000})^3-0.016(\frac{c_e}{1000})^4$
$D_e^{(b)}$	$0.000233\times10^{-8.43-54/(T-229-5(c_e/1000))-0.22(c_e/1000)}$
$\nu^{(b)}$	$-(0.6-0.24(\frac{c_e}{1000})^{0.5}+0.98(1-0.0052(T-294))(\frac{c_e}{1000})^{1.5})$
$D_{s,p}^{(d)}$	$1315383\times10^{-20.26+534.9(s-0.5)^8+2.263(s-0.5)^2}$

$^{(a)}$Obtained from [31], $^{(b)}$Adapted from [15], $^{(c)}$Obtained from [23], $^{(d)}$Approximated and adapted from [18], see Fig. 2.2.

the solutions of (2.17), which includes the computation of $\mathscr{F}$ and $\mathscr{J}$ in (2.17). The simulation studies will be done using two different sets of parameters, obtained from [24] and [23]. Interestingly, the parameter set from [24] has been parametrized with a high-power (HP) cell (unspecified battery chemistry), while the parameter set from [23] has been parameterized with a high-energy (HE) cell (LiC_6 negative electrode and $LiCoO_2$ positive electrode chemistry). Since the original parameter sets from [24] and [23] do not consider all concentration-dependent parameters, i.e. κ, D_e, ν, $D_{s,p}$, we have extended the respective parameter sets with the missing concentration-dependent parameters. The functions used for the concentration-dependent parameters are summarized in Table 2.2. The time-step size has been chosen as $\delta_t = 1s$ in all the simulation studies, and, the tolerance to terminate the Newton's method has been chosen, unless otherwise stated, as, 2×10^{-3} and 10^{-2}, for the HP cell and HE cell, respectively, as these values were found to strike a good trade-off between accuracy and computation time. Furthermore, all the reported computation times in this section have been obtained from an average of 10 repetitions. Some striking differences between the two parameter sets will be observed below.

2.4.1. IMPACT OF MODEL SIMPLIFICATIONS

In order to investigate the impact of Simplifications [S1]-[S3] described in Section 2.2.3 on model accuracy and computational speed, the CDFN model has been compared to a DFN model with varying simplifications for two parameter sets. The current profile used to produce the simulation results can be seen in Fig. 2.4 and the grid parameters have been chosen as $n_n = n_s = n_p = n_{r,n} = n_{r,p} = 10$. To express the difference in accuracy of the various simplifications, we will use a normalized root-mean-square error (NRMSE), defined as

$$\text{NRMSE}(p,q) = \frac{\sqrt{\frac{1}{N}\sum_{k=1}^{N}(p_k - q_k)^2}}{\max_k\left\{\frac{1}{2}(p_k+q_k)\right\} - \min_k\left\{\frac{1}{2}(p_k+q_k)\right\}}, \tag{2.18}$$

for some vectors p and q. For the comparison of the output voltage between different models, p and q are of length N, while for the comparison of internal states, p and q are stacked vectors of the vectors as defined in (2.11) over the sample times.

Table 2.3: The effect of Simplification [S1]-[S3] introduced in Section 2.2 on accuracy for the high-power (HP) [24] and high-energy (HE) [23] parameter sets.

NRMSE [10^{-3}]	V		ϕ_e		c_e		$\bar{c}_s$		j_n	
	HP	HE	HP	HE	HP	HE	HP	HE	HP	HE
Full model	-	-	-	-	-	-	-	-	-	-
[S1]	0.0019	4.0	0.019	2.9	0.0094	1.1	0.0022	0.73	0.17	3.11
[S2-I]-all	0.059	0.041	0.036	0.044	0.017	0.069	0.026	0.014	0.24	0.042
[S2-II]-κ	0.0056	3.8	0.30	6.1	0.020	3.1	0.017	3.3	0.075	1.2
[S2-II]-D_e	0.0068	1.0	0.33	1.5	0.58	12	0.020	0.94	0.064	0.36
[S2-II]-ν	0.0093	1.1	0.46	1.7	0.027	0.72	0.027	1.1	0.19	0.40
[S2-II]-$D_{s,p}$	16	7.6	0.27	4.6	0.14	2.3	6.9	1.9	0.74	3.8
[S2-II]-all	17	9.0	1.2	10	0.62	10	6.9	5.3	0.74	4.2
[S3]	*	1.7	*	1.3	*	0.36	*	1.1	*	0.94

*Simulation not converged.

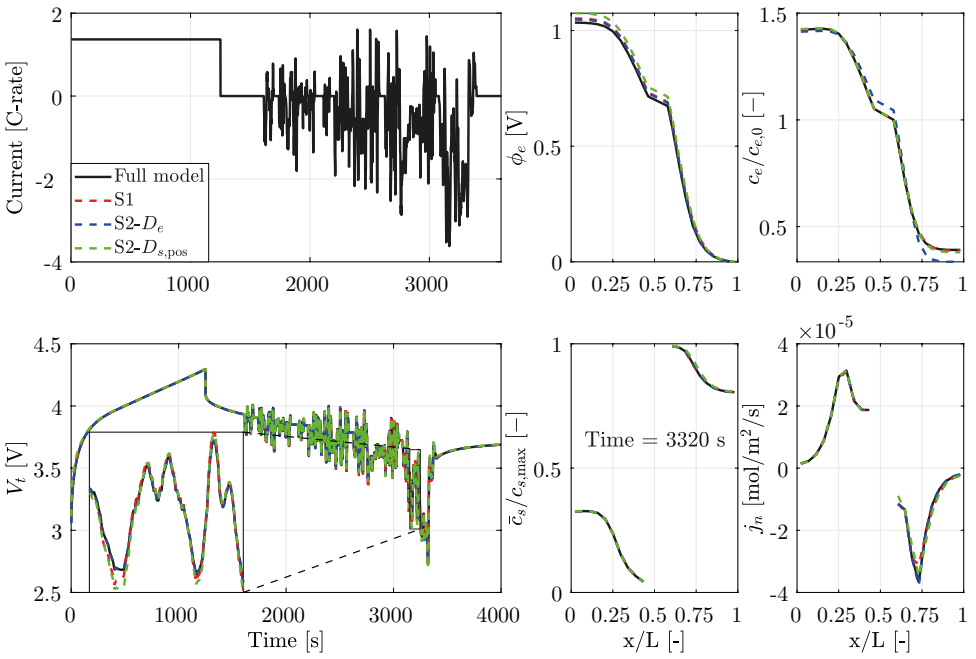

Figure 2.4: Visualization of the errors made using Simplifications S1 and S2-II with the high-energy parameter set [23].

In Table 2.3 the NRMSE of various quantities of the full and simplified models are shown for the HP and HE parameter sets. We can first observe that the errors made due to applying Simplification [S2-I] are negligibly small for both parameter sets. We can further observe that, generally, the errors made due to simplifications are smaller with the HP parameter set than the HE parameter set. This can be explained by the fact that the current density levels in the HP cell are much smaller than in the HE cell, which in turn leads to smaller over-potentials, and therefore smaller concentration gradients, particularly in the electrolyte. Simplification [S1], therefore leads to very small errors in the HP case, while in the HE case the errors are significantly larger. This can also be seen in Fig. 2.4, where we can see that at some points the output voltage deviates somewhat from the CDFN model. It should be noted, however, that throughout most of the simulation, the over-potentials do stay relatively small, which means that overall, Simplification [S1] can still considered reasonable, even for the HE cell. Even when (small) voltage differences do occur, e.g. at 3320s, the differences in the internal states are still small.

The conductivity κ, diffusivity D_e and activity coefficient ν do not deviate significantly from their nominal values in the HP cell, making the simplification that they are constant (Simplification [S2-II]) quite reasonable. This small deviation can be explained by the fact that the electrolyte concentration gradients are very small under the considered applied current profile. However, as the diffusion coefficient D_s in the electrodes is two orders of magnitude smaller in the HP cell than in the HE cell, even with the smaller

Table 2.4: The effect of Simplification [S1]-[S3] introduced in Section 2.2 on simulation time for the high-power (HP) [24] and high-energy (HE) [23] parameter sets.

	Sim. time [s]	
	HP	HE
Full model	5.60	9.88
[S1]	5.52	6.41
[S2-I]-all	3.19	3.78
[S2-II]-κ	5.04	8.55
[S2-II]-D_e	4.84	8.35
[S2-II]-ν	5.62	9.71
[S2-II]-$D_{s,p}$	2.41	4.54
[S2-II]-all	0.59	1.29
[S3]	*	4.98

*Simulation not converged.

over-potentials, there is still a large concentration gradient within the radius of the particles. This in turn makes the simplification for a constant D_s less reasonable in the HP case. Finally, we see that Simplification [S3] is reasonable for the HE cell, while with the HP cell, the errors made were so large, that the simulation would not converge. This can again be explained by the fact that diffusion gradients in the radius of the electrodes in the HP cell is much larger than the HE cell. This means that the diffusion dynamics in the HP cell becomes more important, while in the HE cell, the two-parameter approximation is sufficient. These results show that making parameters concentration-dependent does not always lead to a significant change in the model, since even the relatively (to the other simplifications) large errors observed can still considered to be small as far as usual modeling errors go.

When looking at the simulation times in Table 2.4, we can observe that in both the HE cell and HP cell, simplifications on parameter $D_{s,p}$ lead to the largest reduction in simulation time. The reason for this is that $D_{s,p}$ affects the matrix A_{c_s}, which is generally the largest matrix, and takes substantially more computational effort to compute than the other matrices. Note, however, that considering the simplifications individually does not paint the full picture. When applying [S2-II] on all the considered concentration-dependent parameters, an implementation can be obtained that is much more computationally efficient than the full model. This is because with the proposed implementation presented in Section 2.3, computation of the matrices A_{c_s}, A_{ϕ_e}, D_{ϕ_e}, A_{c_e} becomes the bottleneck in the computation of the solution. If these matrices can be pre-computed, as is the case with Simplification [S2-II], then the computation of the solution can be made much faster. However, we also observe that there is some sacrifice in accuracy.

2.4.2. IMPACT OF DISCRETIZATION

In the discretization approach described in Section 2.3, there is freedom in selecting the number of volume elements n_n, n_s, n_p of the FVM discretization and the number of elements $n_{r,n}, n_{r,p}$ of the FDM discretization. Choosing these parameters large enough leads to a better approximation of the diffusion dynamics in the battery. However, a finer discretization also leads to an increased computation time. To analyze this trade-

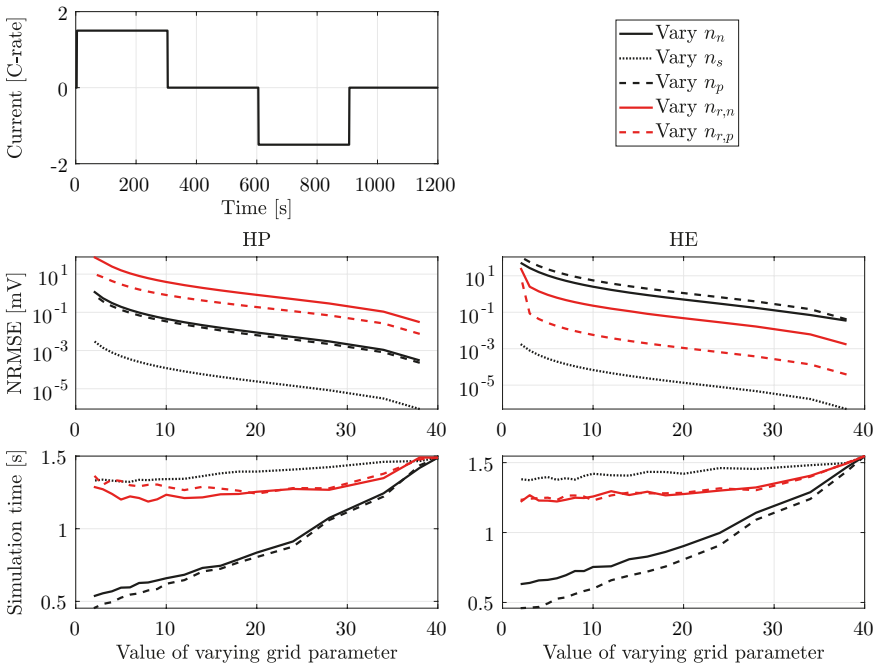

Figure 2.5: NRMSE of the output voltage and computation time for varying grid parameters for the high-power (HP) [24] and the high-energy (HE) [23] parameter set.

off, a study has been done where the DFN model has been simulated with various sets of grid parameters $n_n, n_s, n_p, n_{r,n}, n_{r,p}$. Specifically, we will take a DFN model with Simplifications [S1] and [S2-II] applied. As a first case, a certain set of base grid parameters $n_n, n_s, n_p, n_{r,n}, n_{r,p} = 40$ has been chosen as a baseline. Then, each grid parameter has been varied (one at the time) between 1 and 40, for which the NRMSE of the output voltage (with respect to the simulation with the base grid parameters) and simulation time have been computed.

In Fig. 2.5, the results of this first case study are shown. We see that, generally, in both parameter sets, as the value of the grid parameter increases, the NRMSE decreases, while computation time increases. However, some grid parameters seem to have a larger impact on the RMS error and computation time than others. With the HP parameter set, the grid parameters that relate to the solid-phase diffusion $n_{r,n}$ and $n_{r,p}$ have the largest impact on the NRMSE, while the impact of n_n, n_s, n_p is at least an order of magnitude smaller than that of $n_{r,n}$ and $n_{r,p}$. This indicates that diffusion dynamics in the solid phase largely dominates diffusion dynamics in the electrolyte phase, as, apparently, diffusion along the length of the cell does not need a high discretization. Thus, for the HP parameter set, to retain model accuracy and limit computation time, $n_{r,n}$ and $n_{r,p}$ need to be relatively large, while n_n, n_s, n_p can be small. For the HE parameter set, the grid parameters related to the electrodes have the most impact on the NRMSE. Here, to retain model accuracy and computation time, n_n and n_p need to be chosen relatively large.

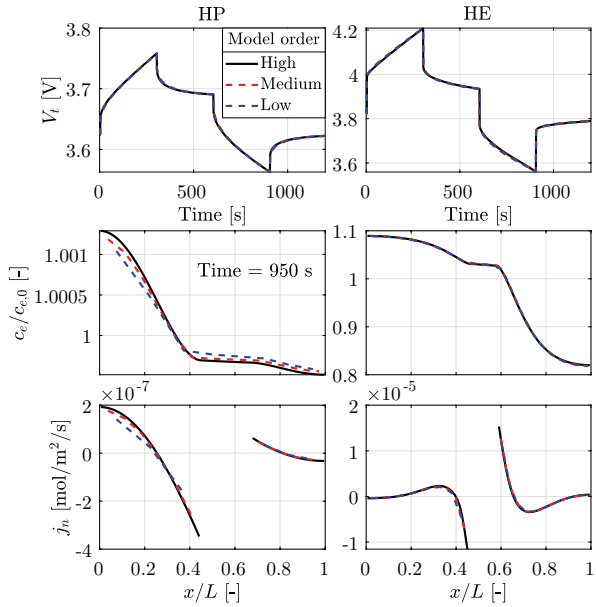

Figure 2.6: Output voltage and various internal variables for varying degrees of model order corresponding to Table. 2.5 for the high-power (HP) [24] and the high-energy (HE) [23] parameter set.

Furthermore, we can see that the effect of the grid parameters on the computation time is similar for both parameter sets, which is to be expected.

In Fig. 2.6, the output voltage and normalized electrolyte concentration are shown, where the considered DFN model has been simulated with varying degrees of model order for the two parameter sets. The selected model orders are based on the analysis above, to show the trade-off that can be made between model accuracy and computation time. The specific grid parameters of each model order, together with their respective computation time and NRMSE, are shown in Table 2.5. The reported NRMSEs have been computed in relation to the model with the base set of grid parameters. The low-, medium-, and high-order models have been chosen such that the NRMSE is at most 6×10^{-3}, 3×10^{-3}, and 10^{-3}, respectively, and that there is a somewhat reasonable,

Table 2.5: Selected grid parameters of the varying degrees of model orders shown in Fig. 2.6.

	Model order	Grid param.*	NRMSE [10^{-3}]	Comp. time [s]
HP [24]	low	[3,2,3,9,9]	5.3	0.12
	medium	[5,5,5,16,14]	2.1	0.14
	high	[10,5,10,20,20]	0.97	0.20
HE [23]	low	[9,2,12,3,3]	5.7	0.19
	medium	[12,8,15,3,3]	3.0	0.23
	high	[22,10,23,3,7]	1.0	0.44

*The order of the grid parameters is $[n_n, n_s, n_p, n_{r,n}, n_{r,p}]$.

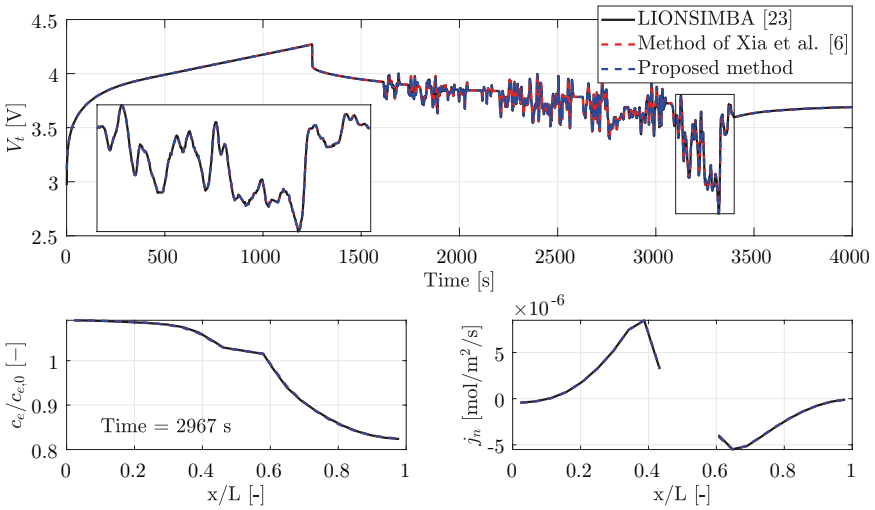

Figure 2.7: Comparison of output voltage and several internal variables between various model implementations.

good, and very good agreement of the internal states with the baseline model, respectively. We observe that output voltage can be modeled well with a relatively coarse discretization over the cell length, especially in the HP case. However, in order to model the internal states well, both in the HP and HE case, n_n, n_s, n_p are important, as they relate to diffusion across the cell.

2.4.3. COMPARISON OF NUMERICAL METHODS

In order to validate the model implementation presented in Section 2.3, the proposed numerical method of this chapter will be compared to the numerical methods proposed in [23] and [6]. The numerical method of [23] in turn has been validated against a DFN model validated in COMSOL [37]. To ensure that the model equations are the same in all cases, the parameter set used in this chapter has been adapted exactly to that used in [23] under isothermal conditions. This amounts to choosing $\nu = 0$, and applying [S2-II] on the parameters D_e and $D_{s,p}$. Thus, κ is the only remaining concentration-dependent parameter. The results for the numerical method of [23] have been obtained using the LIONSIMBA toolbox presented in the aforementioned paper, while the numerical method of [6] has been implemented according to the description of the method, with the same discretization as presented in this chapter, in order to obtain the respective results. Since the chosen tolerances to terminate the algorithms can have a significant effect on computation times, to ensure a fair comparison, the tolerances for the methods have been chosen such that for each method, the NRMSEs of the considered state variables in Table 2.3 between the model with a tolerance of 10^{-6} and the model with a largest possible chosen tolerance do not exceed 10^{-4}. From this requirement, the tolerances in LIONSIMBA [23] have been set to 2×10^{-5}, the tolerance in the method of [6] has been set to 0.009, and the tolerance of the proposed method has been set to 0.03.

A simulation of the DFN model using the various numerical methods with the current profile that can be seen in Fig. 2.4 is shown in Fig. 2.7. We observe that both in the output voltage and internal variables, the results are visually identical. The computation times and NRMSEs for the results shown in Fig. 2.7 can be seen in Table 2.6. The total computation time represents the total time taken to simulate the model, while the computation time of the solutions only accounts for the actual computations required to compute the solution itself, without overhead in computing additional variables or pre-computation of matrices. From Table 2.6, we can first observe that in accordance to our earlier observation of Fig. 2.7, the NRMSE values are sufficiently small to consider the numerical methods to be equivalent. The computation times, however, vary significantly between the different numerical methods, in particular when the total computation time is considered, where the computation time of the method proposed in this chapter is almost 400 times smaller than the computation time of the method of [23]. However, comparing this to the computation time of the solutions, we observe that, apparently, there is a large amount of overhead in the LIONSIMBA toolbox. Even so, the method proposed in this chapter is over 50 times faster than the method of [23] and over 45 times faster than the method of [6]. It should be noted that the method of [23] uses a variable-time-step solver, which becomes especially slow when dynamic current profiles are applied, while in the method of this chapter the time-step size is constant (set to 1s). However, we report that with constant currents, i.e., the first 1600s of the applied current profile shown in Fig. 2.4, it takes 1.4s and 0.63s to compute the solution with the method of [23] and the method proposed in this chapter, respectively. Thus, even with constant current profiles, the method proposed in this chapter is still faster than the method of [23]. We should further note that as a consequence of having a fixed-time-step solver, discretization errors can be larger than when using a variable-time-step solver, particularly when simulating over a very large time frame. However, as can also be observed from the results in Table 2.6, in the considered simulations, the discretization errors were not significantly large.

2.4.4. COMPARISON OF MODELS

With the numerical method proposed in this chapter validated, and with the observations made in Section 2.4.1 and Section 2.4.2, a selection of SDFN models and SPMs can be made and compared to the CDFN model to show how a general trade-off can be made between accuracy and computational speed with the numerical method proposed in this chapter. Based on the analysis of the trade-off that can be made between model accuracy and computation time using Simplifications [S1]-[S3] and the choice of grid parameters, for each parameter set, high-fidelity (HIFI) and low-fidelity (LOFI)

Table 2.6: Computation times and NRMSEs of various numerical methods for the results shown in Fig. 2.7.

	Computation time [s]		NRMSE [10^{-3}]	
	Total	Solutions	V_t	Internal states*
LIONSIMBA [23]	1106	137.0	-	-
Method of Xia et al. [6]	129.3	129.2	1.6	0.46
Proposed method	2.78	2.71	1.6	0.46

*Taken as the mean value of the NRMSE values of ϕ_e, c_e, $\bar{c}_s$, and η.

models have been defined. The choices for the simplifications and grid parameters for these models are shown in Table. 2.7. Here we note that since Simplification [S2-I] had a negligible effect on the model accuracy, the CDFN model is considered with this simplification applied. We further note that [S3] is not additionally applied for the LOFI models in the HE case, since it does not lead to any decrease in computation time if used in combination with [S2]-$D_{s,p}$. Similar to the SDFN models, HIFI and LOFI versions are considered for the SPM, with the same choice of simplifications and grid parameters. The so-called common DFN model is additionally included, to show how the considered models compare to the DFN models typically found in literature, where usually either κ and/or D_e are considered as concentration-dependent parameter, e.g. [23, 24, 37]. The selected grid parameters for the common DFN model are based on those used in the LIONSIMBA toolbox [23]. A first comparison of some of the models is made in Fig. 2.8, where the discharge curves for the CDFN model, SDFN-HIFI model and SPM-HIFI are shown under several C-rates for both of the parameter sets. With the HP cell, until 10C, the SPM models have a good agreement with the CDFN model, while at 20C the agreement becomes worse. The SDFN-HIFI model, on the other hand, has a good agreement at all C-rates, except for some observed difference in the normalized electrolyte concentration. This difference is mainly due to Simplification [S2-II]-D_e, since, in the HP case, at very high C-rates the electrolyte concentration gradient becomes sufficiently large for the effect of the concentration dependency to show. For the HE cell, we can observe that now the SPM fails to represent the output voltage at all C-rates, while the effect on the normalized concentration is somewhat less pronounced. In terms of output voltage and ionic flux j_n, the SDFN-HIFI model has still a very good agreement with the CDFN model, while for similar reasons as in the HP case, some discrepancy can be observed in the electrolyte concentration.

In Fig. 2.9, the selected models have been simulated with the current profile shown in Fig. 2.4 for both parameter sets. Here we see again that the SPM agrees well with the CDFN model, especially so the SPM-HIFI model, since the solid-phase diffusion coefficient is still varying with solid-phase concentration. The Simplification [S2-II]-$D_{s,p}$, therefore, seems to have the largest effect on the perceived differences between the LOFI models and the CDFN model. However, it should be noted that the errors are still small in this case. When observing the results of the HE cell, we see that the errors made with

Table 2.7: Choice of simplifications and grid parameters of the presented models.

		Simplifications*	Grid param.**
CDFN	HP	[S2-I]-all	[10,5,10,20,20]
	HE	[S2-I]-all	[22,10,23,3,7]
Common DFN	HP	[S2-II]-ν,$D_{s,p}$	[10,10,10,10,10]
	HE	[S2-II]-ν,$D_{s,p}$	[10,10,10,10,10]
HIFI models	HP	[S1],[S2-II]-κ,D_e,ν	[5,5,5,16,14]
	HE	[S3],[S2-II]-κ,D_e,ν	[12,8,15,3,3]
LOFI models	HP	[S1],[S2-II]-all	[3,2,3,9,9]
	HE	[S1],[S2-II]-all	[9,2,12,3,3]

*Unless stated otherwise, the concentration-dependent parameters have been simplified according to [S2-I].

**The order of the grid parameters is $[n_n, n_s, n_p, n_{r,n}, n_{r,p}]$.

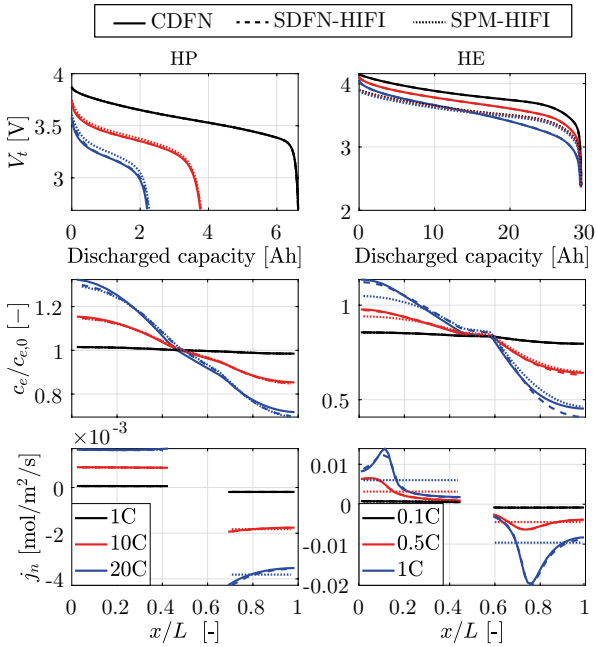

Figure 2.8: Comparison of discharge curves of various models under several C-rates for the high-power (HP) [24] and high-energy (HE) [23] parameter sets. The internal variables are shown at the point corresponding to 80% of the discharged capacity.

the SPM are, again, considerably large, and show entirely different dynamics than the CDFN model. The SDFN models, on the other hand, both show a good agreement with the CDFN model.

The computation times and NRMSE values for the results shown in Fig. 2.9 can be seen in Table 2.8. As expected, the computation times of the SPM are the lowest, since the SPM has the lowest complexity, although with the HE parameter set, the NRMSE is unacceptable. The SDFN models, on the other hand, have low errors in all cases for both parameter sets, while the computation times are not much higher than the SPM. We can also see how a trade-off can be made between accuracy and computation time, where, e.g., in the HE case, the computation time of the SDFN-HIFI model is approximately

Table 2.8: Computation times and NRMSEs of the selected models for the results shown in Fig. 2.9.

	Computation time [s]		NRMSE V_t [10^{-3}]	
	HP [24]	HE [23]	HP [24]	HE [23]
CDFN	6.0	8.6	-	-
Common DFN	1.6	2.3	17	9.3
SDFN-HIFI	1.4	1.8	0.99	5.6
SDFN-LOFI	0.40	0.72	17	10
SPM-HIFI	0.30	0.30	0.65	89
SPM-LOFI	0.13	0.14	17	88

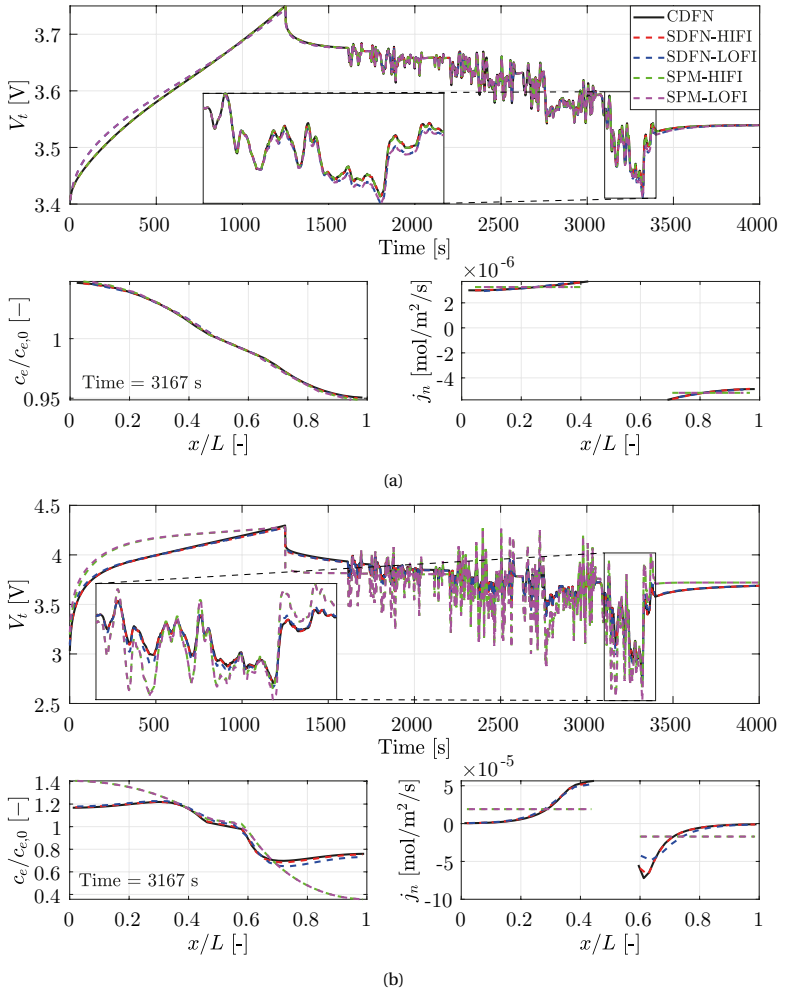

Figure 2.9: Comparison of output voltage and internal states of various models for (a) the high-power [24] and (b) high-energy [23] parameter sets.

twice that of the SDFN-LOFI model, whereas the NRMSE is approximately twice as low. However, the NRMSE values of the SDFN-LOFI model can actually still be considered to be highly accurate, since the common DFN model has similar error for both parameter sets. This suggests that most of the errors made originate from Simplification [S2-II]-$D_{s,p}$, which, to the authors' knowledge, is a parameter that has been considered to be concentration-dependent only in [34]. Therefore, the usual considered concentration-dependent parameters, i.e., κ and D_e can be assumed constant with practically no loss in model accuracy of the output. These results show that with the proposed implementation, and by selectively making the proposed simplifications, as well as selectively choosing the grid parameters, a model can be obtained that has a small impact on model ac-

curacy, while the computation time can be drastically decreased, to achieve a simulation time of over 5000 times faster than real-time.

2.5. CONCLUSIONS

In this chapter, we have studied the impact of several types of model simplifications on the trade-off between model accuracy and computation time for the DFN model. Furthermore, we have proposed a computationally efficient implementation of the CDFN model that has led to a significant reduction in computation time. The proposed model implementation has been developed into a freely downloadable toolbox, which has also been presented in this chapter. In the validation of the model simplifications, we have shown that linearizing the Butler-Volmer equation (2.5) (Simplification [S1]) and simplifying concentration-dependent parameters to constant parameters (Simplification [S2-II]) has a small effect on the model dynamics in most cases, while leading to a large decrease in computation time. Furthermore, we have studied the impact of the coarseness of the spatial discretization, where we have shown that the discretization grid parameters can be chosen differently depending on the modeled cell characteristics to make a good trade-off between model accuracy and computation time. To validate the proposed numerical method, a comparison has been made with the numerical methods of [23] and [6], where we have also shown that the numerical method proposed in this chapter is substantially faster than the aforementioned numerical methods. Finally, we have compared several simplified DFN models to the SPM and the CDFN model. Here we have shown that with the proposed implementation, and by selectively making the proposed simplifications, as well as selectively choosing the grid parameters, a model can be obtained that has a small impact on model accuracy in terms of battery voltage and internal states, while the computation time can be drastically decreased, to achieve a simulation time of over 5000 times faster than real-time.

REFERENCES

[1] M. Doyle, T. F. Fuller, and J. Newman, *Modeling of galvanostatic charge and discharge of the lithium/polymer/insertion cell,* Journal of the Electrochemical society **140**, 1526 (1993).

[2] V. R. Subramanian, V. D. Diwakar, and D. Tapriyal, *Efficient Macro-Micro Scale Coupled Modeling of Batteries,* Journal of the Electrochemical Society **152**, A2002 (2005).

[3] T.-S. Dao, C. P. Vyasarayani, and J. McPhee, *Simplification and order reduction of lithium-ion battery model based on porous-electrode theory,* Journal of Power Sources **198**, 329 (2012).

[4] M. A. Kehs, M. D. Beeney, and H. K. Fathy, *Computational efficiency of solving the DFN battery model using descriptor form with Legendre polynomials and Galerkin projections,* in *American Control Conference* (2014) pp. 260–267.

[5] L. Cai and R. E. White, *Reduction of Model Order Based on Proper Orthogonal Decomposition for Lithium-Ion Battery Simulations,* Journal of the Electrochemical Society **156**, A154 (2009).

[6] L. Xia, E. Najafi, Z. Li, H. J. Bergveld, and M. C. F. Donkers, *A computationally efficient implementation of a full and reduced-order electrochemistry-based model for Li-ion batteries,* Applied Energy **208**, 1285 (2017).

[7] G. Fan, K. Pan, and M. Canova, *A comparison of model order reduction techniques for electrochemical characterization of Lithium-ion batteries,* in *IEEE Conference on Decision and Control* (2015) pp. 3922–3931.

[8] C. Zou, C. Manzie, and D. Nesic, *A Framework for Simplification of PDE-Based Lithium-Ion Battery Models,* IEEE Transactions on Control Systems Technology **24**, 1594 (2016).

[9] X. Han, M. Ouyang, L. Lu, and J. Li, *Simplification of physics-based electrochemical model for lithium ion battery on electric vehicle. Part I: Diffusion simplification and single particle model,* Journal of Power Sources **278**, 802 (2015).

[10] X. Han, M. Ouyang, L. Lu, and J. Li, *Simplification of physics-based electrochemical model for lithium ion battery on electric vehicle. Part II: Pseudo-two-dimensional model simplification and state of charge estimation,* Journal of Power Sources **278**, 814 (2015).

[11] P. Kemper, S. E. Li, and D. Kum, *Simplification of pseudo two dimensional battery model using dynamic profile of lithium concentration,* Journal of Power Sources **286**, 510 (2015).

[12] S. J. Moura, F. B. Argomedo, R. Klein, A. Mirtabatabaei, and M. Krstic, *Battery state estimation for a single particle model with electrolyte dynamics,* IEEE Transactions on Control Systems Technology **25**, 453 (2017).

[13] S. Khaleghi Rahimian, S. Rayman, and R. E. White, *Extension of physics-based single particle model for higher charge–discharge rates,* Journal of Power Sources **224**, 180 (2013).

[14] X. Li, G. Fan, G. Rizzoni, M. Canova, C. Zhu, and G. Wei, *A simplified multi-particle model for lithium ion batteries via a predictor-corrector strategy and quasi-linearization,* Energy **116**, 154 (2016).

[15] L. O. Valøen and J. N. Reimers, *Transport properties of LiPF6-based Li-ion battery electrolytes,* Journal of the Electrochemical Society **152**, A882 (2005).

[16] P. Georén and G. Lindbergh, *Characterisation and modelling of the transport properties in lithium battery gel electrolytes: Part I. the binary electrolyte PC/LiClO4,* Electrochimica Acta **49**, 3497 (2004).

[17] C. Delacourt, M. Ati, and J. M. Tarascon, *Measurement of Lithium Diffusion Coefficient in Li y FeSO4F,* Journal of the Electrochemical Society **158**, A741 (2011).

[18] M. Safari and C. Delacourt, *Mathematical Modeling of Lithium Iron Phosphate Electrode: Galvanostatic Charge/Discharge and Path Dependence,* Journal of the Electrochemical Society **158**, A63 (2011).

[19] M. M. Doeff, L. Edman, S. E. Sloop, J. Kerr, and L. C. De Jonghe, *Transport properties of binary salt polymer electrolytes,* Journal of Power Sources **89**, 227 (2000).

[20] Z. Khalik, H. J. Bergveld, and M. C. F. Donkers, *On Trade-offs Between Computational Complexity and Accuracy of Electrochemistry-based Battery Models,* in *IEEE 58th Conference on Decision and Control* (2019) pp. 7740–7745.

[21] S. Mazumder and J. Lu, *Faster-Than-Real-Time Simulation of Lithium Ion Batteries with Full Spatial and Temporal Resolution,* International Journal of Electrochemistry **2013**, 1 (2013).

[22] V. R. Subramanian, V. Boovaragavan, V. Ramadesigan, and M. Arabandi, *Mathematical Model Reformulation for Lithium-Ion Battery Simulations: Galvanostatic Boundary Conditions,* Journal of the Electrochemical Society **156**, A260 (2009).

[23] M. Torchio, L. Magni, R. B. Gopaluni, R. D. Braatz, and D. M. Raimondo, *LIONSIMBA: A matlab framework based on a finite volume model suitable for Li-ion battery design, simulation, and control,* Journal of the Electrochemical Society **163**, A1192 (2016).

[24] K. A. Smith, C. D. Rahn, and C.-Y. Wang, *Control oriented 1D electrochemical model of lithium ion battery,* Energy Conversion and Management **48**, 2565 (2007).

[25] P. W. Northrop, V. Ramadesigan, S. De, and V. R. Subramanian, *Coordinate transformation, orthogonal collocation, model reformulation and simulation of electrochemical-thermal behavior of lithium-ion battery stacks,* Journal of the Electrochemical Society **158**, A1461 (2011).

[26] R. Klein, N. A. Chaturvedi, J. Christensen, J. Ahmed, R. Findeisen, and A. Kojic, *Electrochemical Model Based Observer Design for a Lithium-Ion Battery,* IEEE Transactions on Control Systems Technology **21**, 289 (2013).

[27] J. Newman, *Fortran programs for the simulation of electrochemical systems,* `http://www.cchem.berkeley.edu/jsngrp/fortran.html` (accessed November 10, 2020).

[28] M. Farkhondeh and C. Delacourt, *Mathematical Modeling of Commercial LiFePO4 Electrodes Based on Variable Solid-State Diffusivity,* Journal of the Electrochemical Society **159**, A177 (2011).

[29] X.-C. Tang, L.-X. Li, Q.-L. Lai, X.-W. Song, and L.-H. Jiang, *Investigation on diffusion behavior of Li+ in LiFePO4 by capacity intermittent titration technique (CITT),* Electrochimica Acta **54**, 2329 (2009).

[30] P. P. Prosini, M. Lisi, D. Zane, and M. Pasquali, *Determination of the chemical diffusion coefficient of lithium in LiFePO4,* Solid State Ionics **148**, 45 (2002).

[31] M. Doyle and Y. Fuentes, *Computer Simulations of a Lithium-Ion Polymer Battery and Implications for Higher Capacity Next-Generation Battery Designs,* Journal of the Electrochemical Society **150**, A706 (2003).

[32] M. Ecker, T. K. D. Tran, P. Dechent, S. Käbitz, A. Warnecke, and D. U. Sauer, *Parameterization of a Physico-Chemical Model of a Lithium-Ion Battery I. Determination of Parameters,* Journal of the Electrochemical Society **162**, A1836 (2015).

[33] Y. Ma, M. Doyle, T. F. Fuller, M. M. Doeff, L. C. D. Jonghe, and J. Newman, *the Measurement of a Complete Set of Transport Properties for a Concentrated Solid Polymer Electrolyte Solution,* Journal of the Electrochemical Society **142**, 1859 (1995).

[34] M. Ecker, S. Käbitz, I. Laresgoiti, and D. U. Sauer, *Parameterization of a Physico-Chemical Model of a Lithium-Ion Battery II. Model Validation,* Journal of the Electrochemical Society **162**, A1849 (2015).

[35] C. Y. Wang, W. B. Gu, and B. Y. Liaw, *Micro-Macroscopic Coupled Modeling of Batteries and Fuel Cells I. Model Development,* Journal of the Electrochemical Society **145**, 3407 (1998).

[36] G. L. Plett, *Battery Management Systems, Volume I: Battery Modeling* (Artech House publishers, 2015).

[37] L. Cai and R. E. White, *Mathematical modeling of a lithium ion battery with thermal effects in COMSOL Inc. Multiphysics (MP) software,* Journal of Power Sources **196**, 5985 (2011).

[38] A. C. Hindmarsh, P. N. Brown, K. E. Grant, S. L. Lee, R. Serban, D. E. Shumaker, and C. S. Woodward, *SUNDIALS: Suite of nonlinear and differential/algebraic equation solvers,* ACM Transactions on Mathematical Software **31**, 363 (2005).

[39] J. A. E. Andersson, J. Gillis, G. Horn, J. B. Rawlings, and M. Diehl, *CasADi: a software framework for nonlinear optimization and optimal control,* Mathematical Programming Computation **11**, 1 (2019).

[40] L. Rao and J. Newman, *Heat-Generation Rate and General Energy Balance for Insertion Battery Systems,* Journal of the Electrochemical Society **144**, 2697 (1997).

3

PARAMETER ESTIMATION OF THE DOYLE-FULLER-NEWMAN MODEL

Besides the computational complexity of electrochemistry-based models, another challenge in using electrochemistry-based battery models for aging-aware charging is uniquely determining all model parameters. This chapter proposes a model parameterization approach of the Doyle-Fuller-Newman (DFN) model, by first reparameterizing the DFN model through normalization and grouping, followed by a sensitivity analysis and a parameter estimation procedure. In the parameter estimation procedure, we show the influence of the number of estimated parameters, as well as the influence of the data length of the identification data, on the obtained model accuracy (in terms of the output). Additionally, the model with parameters obtained using the proposed parameterization approach is compared to a model whose parameters have been obtained using cell teardown. Finally, the consistency and accuracy of the parameter estimation procedure is analyzed by applying the estimation routine to a synthetic cell, represented by a DFN model with randomly chosen (within specific and realistic intervals) parameters. The results of this analysis show that the parameter estimation approach using current/voltage data can lead to a significantly better output accuracy, while it might not lead to physically meaningful parameters. This motivates the need for an approach that combines both and where cell tear-down can assist the parameter estimation using current/voltage data in achieving physically meaningful parameters.

This chapter is based on Publication **P.1**.

3.1. INTRODUCTION

One of the goals of this thesis is to investigate the use of electrochemistry-based models for aging-aware charging. In the previous chapter, we have addressed the computational complexity of the Doyle-Fuller-Newman (DFN) model, which is a popular electrochemistry-based battery model [1]. However, as stated in Chapter 1, another challenge in the use of electrochemistry-based models is uniquely identifying all the model parameters. In the remaining part of this introduction, we will summarize the methods that are used to determine the parameters of the DFN model, which will lead to the problem formulation of this chapter. For a more complete overview of parameter estimation for electrochemistry-based models, we refer the reader to Chapter 1.

Generally, the DFN model parameters can be determined in several ways. One way is to determine several parameters based on information provided by the cell manufacturers, who know the material properties that have been chosen during cell design. However, the manufacturer often does not have all the parameter values or might not want to disclose them. Another way is to measure the parameters by cell teardown and experimental testing [2–4]. Such methods generally involve costly equipment, and it is sometimes not allowed to tear down a cell by the cell manufacturer. Finally, parameters can be determined through parameter estimation using input-output data [5–10]. In these methods, some, or all, of the parameters are estimated based on optimization of the model predictions to input/output measurements (i.e., external current/voltage measurements). Generally, two approaches are taken in the estimation of the parameters based on input/output measurements. One approach is to estimate some (or all) of the parameters simultaneously based on measured input/output data [5, 6, 8, 10]. Since the identifiability of the DFN model is poor [6], a sensitivity analysis can be done to determine the parameters to which the model output is most sensitive, in order to select a smaller set of parameters for estimation [5]. The other approach is to design experiments specifically in an attempt to isolate the effects of parameters in the output [7, 9, 11]. Here, the parameters are grouped based on their effect to the output, after which the groups of parameters are estimated separately using their respectively designed input current. However, often, there is no justification given for this approach [7, 11], or the approach is justified with the intuition that identifying too many parameters simultaneously may lead to unexpected uncertainty and errors [9]. However, this intuition has not yet been verified.

In this chapter, we propose a model parameterization approach of the DFN model, by first reparameterizing the DFN model through normalization and grouping, followed by a sensitivity analysis of [12] that will show that some parameters have only a limited influence on the input-output behavior, and a parameter estimation procedure. The sensitivity analyis is similar to the approach taken in [5], in which the procedure of [12] is applied to a DFN model, but in which the parameters have not been grouped and normalized. The normalization and grouping procedure is similar to the approach taken in [13, 14], in which no sensitivity analysis has been done. For the model parameterization, two cases are considered: one where the individual electrode potentials have been characterized, for which we have one set of experimental data available for parameterization, and one where only the electro-motive force (EMF)/open-circuit potential (OCP) measurements of the complete cell are provided, but for which we have 3 experimental

data sets available. In the parameter estimation routine, we will study the influence of the number of estimation parameters on the obtained model accuracy for both cases, as well as the influence of data length of identification data on accuracy. Finally, we will study the consistency and accuracy of the parameter estimation routine by analyzing the parameter estimation routine for a so-called synthetic cell, which is represented by a DFN model with a randomly chosen (within specific and realistic intervals) set of parameters. This will show how consistently and accurately the parameters of the DFN model can be estimated, and how far the resulting internal states deviate from the true internal states. Through introducing additional model equations on the synthetic cell, this study will also show the impact of modeling errors on the meaningfulness of the estimated model parameters and internal states.

The remainder of this chapter is organized as follows. In Section 3.2, the DFN model is formulated and the reparameterization procedure is described. In Section 3.3, the model parameterization approach to identify the parameters of the reparameterized model is explained. In Section 3.4, the results for the model parametrization approach are presented, i.e., the sensitivity analysis and the parameter estimation results are explained and discussed. Finally, conclusions are drawn in Section 3.5.

3.2. BATTERY MODELING

The objective of this chapter is to parameterize the Doyle-Fuller-Newman (DFN) model using measured voltage and current data. This section first presents the DFN model, including its parameters and, subsequently, proposes to reparameterize the model to reduce the number of unknown parameters using an approach similar to that proposed in [13].

3.2.1. DOYLE-FULLER-NEWMAN MODEL EQUATIONS

The DFN model is a widely used electrochemistry-based model introduced in [1]. Fig. 4.1 illustrates the functionality of the model schematically for a Li-ion cell. The DFN model is often referred to as a pseudo-two-dimensional model, since the model describes concentrations and potentials in two dimensions, namely in a radial direction r along the radius of the particle, and in the x dimension, along the thickness of the electrode stack. In the x dimension, the cell is divided into three regions, namely the negative electrode, the separator, and the positive electrode. The reader is referred to [15] for a detailed description of the DFN model, and the underlying assumptions made.

The original model equations, i.e., before reparameterization, are based on the formulation given in Chapter 2, and references therein. These equations have been summarized in Table 3.1, given by (3.1)-(3.6). For compactness of notation, where possible, the time and space dependency of the variables have been left out of the equations. The symbols used in the original DFN model equations together with their respective descriptions are given in Table 3.2. Note that U in (3.5d) denotes the equilibrium potential of the electrode, which can be given by a pre-defined function typically of the solid-phase concentration at the solid-electrolyte interface ($c_{s,e}(x,t) = c_s(R_s,x,t)$). Further note that there are a few small differences with the formulation of the DFN model in Chapter 2. Firstly, in Chapter 2, we did not consider a film resistance R_f which now

Table 3.1: Model equations of the original DFN model[1].

Solid-phase Li-ion concentration	$\frac{\partial c_s}{\partial t} = \frac{D_s}{r^2}\frac{\partial}{\partial r}(r^2\frac{\partial c_s}{\partial r})$	(3.1a)
Boundary Condition	$\frac{\partial c_s}{\partial r}\|_{r=0}=0,\ -D_s\frac{\partial c_s}{\partial r}\|_{r=R_s}=j_n$	(3.1b)
Electrolyte-phase Li-ion concentration	$\varepsilon_e\frac{\partial c_e}{\partial t} = \frac{\partial}{\partial x}(D_e\varepsilon_e^p\frac{\partial c_e}{\partial x}) + \frac{3\varepsilon_s(1-t_+^0)}{R_s}j_n$	(3.2a)
Boundary condition	$\frac{\partial c_e}{\partial x}\|_{x=0} = \frac{\partial c_e}{\partial x}\|_{x=L} = 0$	(3.2b)
Solid-phase potential	$\frac{\partial}{\partial x}(\sigma\varepsilon_s\frac{\partial \phi_s}{\partial x}) = \frac{3\varepsilon_s F}{R_s}j_n$	(3.3a)
Boundary condition	$\sigma\varepsilon_s\frac{\partial \phi_s}{\partial x}\|_{x=0} = \sigma\varepsilon_s\frac{\partial \phi_s}{\partial x}\|_{x=L} = \frac{I_a}{A}$	(3.3b)
	$\frac{\partial \phi_s}{\partial x}\|_{x=\delta_n} = \frac{\partial \phi_s}{\partial x}\|_{x=L-\delta_p} = 0$	(3.3c)
Electrolyte-phase potential	$\frac{\partial}{\partial x}\left(\kappa\varepsilon_e^p\frac{\partial \phi_e}{\partial x} + \kappa\varepsilon_e^p(t_+^0\text{-}1)\frac{2RT}{F}\frac{\partial \ln c_e}{\partial x}\right) = -\frac{3\varepsilon_s F}{R_s}j_n$	(3.4a)
Boundary condition	$\frac{\partial \phi_e}{\partial x}\|_{x=0} = \frac{\partial \phi_e}{\partial x}\|_{x=L} = \phi_e\|_{x=L} = 0$	(3.4b)
Butler-Volmer kinetics	$j_n = \frac{i_0}{F}\left(\exp\left(\frac{\alpha_a F}{RT}\eta\right) - \exp\left(-\frac{\alpha_c F}{RT}\eta\right)\right)$	(3.5a)
Exchange current density	$i_0 = k_0 c_e^{\alpha_a}(c_s^{\max} - c_{s,e})^{\alpha_a} c_{s,e}^{\alpha_c}$	(3.5b)
Particle surface concentration	$c_{s,e}(x,t) = c_s(R_s,x,t)$	(3.5c)
Electrode over-potential	$\eta = \phi_s - \phi_e - U - FR_f j_n$	(3.5d)
Terminal voltage	$V(t) = \phi_s(L,t) - \phi_s(0,t) + \frac{R_{cc}}{A}I_a(t)$	(3.6)
Maximum reversible capacity constraint	$Q = AF\delta_i\epsilon_{s,i}c_{s,i}^{\max}(s_{i,100\%} - s_{i,0\%}),\ i\in\{n,p\}$	(3.7)

appears in (3.5d). Secondly, in this chapter, we assume that the mean molar activity coefficient $f_\pm$ is a constant (which is a common assumption, see e.g., [1, 16–21]), and therefore it does not appear in (3.4a). The solid-phase variables (i.e., $c_s(r,x,t)$, $\phi_s(x,t)$, $i_0(x,t)$, $U(x,t)$, and $\eta(x,t)$) are defined only in the electrodes, i.e., for $x\in[0,\delta_n]\cup[L-\delta_p,L]$, while the electrolyte-phase variables (i.e., $c_e(x,t)$ and $\phi_e(x,t)$), are defined over the whole length of the cell, i.e., for $x\in[0,L]$.

Over the three regions, the model parameters are defined as, e.g.,

$$\varepsilon_e(x) = \begin{cases} \varepsilon_{e,n} & \text{for } x\in[0,\delta_n], \\ \varepsilon_{e,\text{sep}} & \text{for } x\in[\delta_n, L-\delta_p], \\ \varepsilon_{e,p} & \text{for } x\in[L-\delta_p, L], \end{cases} \tag{3.8}$$

where the subscripts n, sep, and p refer to the negative electrode, separator, and positive

[1]Note that compared to **P.1**, corrections has been made in (3.4b) and (3.6).

electrode, respectively, and the other parameters are defined similarly. Because the parameters that only define a property of the electrodes, e.g., D_s or σ, do not have a value defined in the separator region, i.e., for $x \in [\delta_n, L-\delta_p]$, the total number of parameters of the DFN model as formulated in Table 3.1 amounts to 35. Note that depending on how the DFN model is formulated, and what kind of assumptions are made, this number can vary. For example, in Chapter 2 and most papers, e.g. [13, 22], either the particle surface film resistance R_f or the current-collector resistance R_{cc} are considered as a parameter

Table 3.2: List of symbols used in the original DFN model equations

Symbol	Description	Unit
Latin		
A	Active electrode area	[m^2]
c_e	Electrolyte-phase Li-ion concentration	[mol/m^3]
$c_{e,a}$	Average electrolyte concentration*	[mol/m^3]
c_s	Solid-phase Li-ion concentration	[mol/m^3]
$c_{s,e}$	Particle surface concentration	[mol/m^3]
$c_{s,n}^{\max}, c_{s,p}^{\max}$	Maximum solid-phase concentration*	[mol/m^3]
D_e	Li-ion diffusion coefficient in electrolyte*	[m^2]
$D_{s,n}, D_{s,p}$	Solid-phase Li-ion diffusion coefficient*	[m/s]
F	Faraday's constant	[C/mol]
i_0	Exchange current density	[A/m^2]
I_a	Applied current	[A]
j_n	Pore wall flux of Li-ions	[$\text{mol/m}^2\text{/s}$]
$k_{0,n}, k_{0,p}$	Kinetic constant*	**
L	Cell thickness*	[m]
p_n, p_{sep}, p_p	Bruggeman porosity exponent*	[−]
Q	Maximum reversible cell capacity	[C]
r	Radial position across a spherical particle	[m]
R	Universal gas constant	[J/mol/K]
R_{cc}	Current collector contact resistance*	[Ωm^2]
$R_{f,n}, R_{f,p}$	Particle surface film resistance resistance*	[Ωm^2]
$R_{s,n}, R_{s,p}$	Radius of active material particles*	[m]
$s_{n,0\%}, s_{p,0\%}$	Stoichiometry at 0% state of charge*	[−]
$s_{n,100\%}, s_{p,100\%}$	Stoichiometry at 100% state of charge*	[−]
t	Time	[s]
t_+^0	Transference number*	[−]
U	Electrode equilibrium potential	[V]
V	Terminal voltage	[V]
x	Position across cell	[m]
Greek		
α_a	Anodic charge-transfer coefficient*	[−]
α_c	Cathodic charge-transfer coefficient*	[−]
δ_n, δ_p	Electrode thickness*	[m]
$\varepsilon_{e,n}, \varepsilon_{e,\text{sep}}, \varepsilon_{e,p}$	Electrolyte volume fraction*	[−]
$\varepsilon_{s,n}, \varepsilon_{s,p}$	Active-particles volume fraction*	[−]
η	Electrode over-potential	[V]
κ	Ionic conductivity*	[S/m]
σ_n, σ_p	Electrical conductivity*	[S/m]
ϕ_e	Electrolyte-phase potential	[V]
ϕ_s	Solid-phase potential	[V]

* Considered parameters of the DFN model.
** [C/s · (m/mol)^(1 + 3α_c)]

Table 3.3: Model equations of the reparameterized DFN model[2].

Solid-phase Li-ion concentration	$\frac{\partial \hat{c}_s}{\partial t} = (\frac{\hat{D}_s}{\hat{r}^2}) \frac{\partial}{\partial \hat{r}} (\hat{r}^2 \frac{\partial \hat{c}_s}{\partial \hat{r}})$	(3.9a)
Boundary Condition	$\frac{\partial \hat{c}_s}{\partial \hat{r}} \mid_{\hat{r}=0} = 0,\ -\hat{D}_s \frac{\partial \hat{c}_s}{\partial \hat{r}} \mid_{\hat{r}=1} = \hat{j}_n$	(3.9b)
Electrolyte-phase Li-ion concentration	$\hat{\varepsilon}_e \frac{\partial \hat{c}_e}{\partial t} = \frac{\partial}{\partial \hat{x}} (\hat{D}_e \hat{p} \frac{\partial \hat{c}_e}{\partial \hat{x}}) + \hat{j}_n$	(3.10a)
Boundary condition	$\frac{\partial \hat{c}_e}{\partial \hat{x}} \mid_{\hat{x}=0} = \frac{\partial \hat{c}_e}{\partial \hat{x}} \mid_{\hat{x}=3} = 0$	(3.10b)
Solid-phase potential	$\frac{\partial}{\partial \hat{x}} (\hat{\sigma} \frac{\partial \phi_s}{\partial \hat{x}}) = \hat{j}_n$	(3.11a)
Boundary condition	$\hat{\sigma} \frac{\partial \phi_s}{\partial \hat{x}} \mid_{\hat{x}=0} = \hat{\sigma} \frac{\partial \phi_s}{\partial \hat{x}} \mid_{\hat{x}=3} = I_a$	(3.11b)
	$\frac{\partial \phi_s}{\partial \hat{x}} \mid_{\hat{x}=1} = \frac{\partial \phi_s}{\partial \hat{x}} \mid_{\hat{x}=2} = 0$	(3.11c)
Electrolyte-phase potential	$\frac{\partial}{\partial \hat{x}} \left(\hat{\kappa} \hat{p} \frac{\partial \phi_e}{\partial \hat{x}} + \hat{\kappa} \hat{p} (t_+^0 - 1) \frac{2RT}{F} \frac{\partial \ln \hat{c}_e}{\partial \hat{x}} \right) = -\hat{j}_n$	(3.12a)
Boundary condition	$\frac{\partial \phi_e}{\partial \hat{x}} \mid_{\hat{x}=0} = \frac{\partial \phi_e}{\partial \hat{x}} \mid_{\hat{x}=3} = \phi_e \mid_{\hat{x}=3} = 0$	(3.12b)
Butler-Volmer kinetics	$\hat{j}_n = \hat{i}_0 \left(\exp\left(\frac{\alpha_a F}{RT} \eta \right) - \exp\left(-\frac{(1-\alpha_a)F}{RT} \eta \right) \right)$	(3.13a)
Exchange current density	$\hat{i}_0 = \hat{k}_0 \hat{c}_e^{\alpha_a} (\hat{c}_s^{\max} - \hat{c}_{s,e})^{\alpha_a} \hat{c}_s^{1-\alpha_a}$	(3.13b)
Particle surface concentration	$\hat{c}_{s,e}(x,t) = \hat{c}_s(1,x,t)$	(3.13c)
Electrode over-potential	$\eta = \phi_s - \phi_e - U - \hat{R}_f \hat{j}_n$	(3.13d)
Terminal voltage	$V(t) = \phi_s(3,t) - \phi_s(0,t) + \hat{R}_{\text{cc}} I_a(t)$	(3.14)
Maximum reversible capacity constraint	$3Q = \hat{c}_{s,i}^{\max} (s_{i,100\%} - s_{i,0\%}),\ i \in \{n,p\}$	(3.15)

to model any additional voltage drop that is generally observed at the output. However, as both these parameters can be linked to a physical phenomenon, in this chapter, we consider both of these effects, i.e., film resistance and current-collector resistance, as having separate parameters, in order to study their sensitivity to the output.

3.2.2. PARAMETER NORMALIZATION AND GROUPING

From the equations of the DFN model in Table 3.1, it can be observed that the variation of certain parameters leads to the same physical effect. For example, by decreasing the diffusion coefficient D_s and increasing the particle size R_s accordingly, the diffusion dynamics in the solid phase remain unchanged. Thus, intuitively speaking, this means that one of these parameters is redundant, and the desired effect can instead be described with a single parameter. Mathematically, this can be achieved by normalization of (3.1), where the radial coordinate r is normalized through division by R_s. This results in a new

[2]Note that compared to **P.1**, corrections has been made in (3.12b) and (3.14).

radial coordinate $\hat{r} = r/R_s \in [0,1]$, after which the parameter R_s can be absorbed in a new parameter $\hat{D}_s = D_s/R_s^2$. Similarly, in the other equations (3.2)-(3.4), the coordinate x can be redefined to

$$\hat{x} = \begin{cases} \frac{x}{\delta_n} & \text{for } 0 \le x \le \delta_n, \\ 1 + \frac{x-\delta_n}{L-\delta_p-\delta_n} & \text{for } \delta_n \le x \le L-\delta_p, \\ 2 + \frac{x-L+\delta_p}{\delta_p} & \text{for } L-\delta_p \le x \le L, \end{cases} \tag{3.16}$$

and the parameters can be grouped. This results in a new set of normalized equations (3.9)-(3.14), shown in Table 3.3, with a new set of parameters resulting from the grouping of the original set of parameters, shown in Table 3.4. In the process, some of the variables have also been redefined, i.e.,

$$\hat{j}_n = \frac{3\epsilon_s FA\delta_i}{R_s} j_n, \qquad \hat{c}_e = \frac{c_e}{c_{e,a}}, \qquad \frac{\hat{c}_s}{3} = \epsilon_s FA\delta_i c_s, \tag{3.17}$$

where $i = n$ for $x \in [0, \delta_n]$, $i = p$ for $x \in [L-\delta_p, L]$.

Note that, although the approach taken here is similar to the one in [13], there are a few differences. The differences mainly originate from the formulation of the original DFN model. In [13], the current collector resistance R_{cc} is not accounted for, and the diffusion and conductivity coefficients are formulated as their effective counterparts, e.g.,

Table 3.4: Parameters of the reparameterized DFN model

Parameter	Grouping	Range	Unit
Q	Q	N/A	[C]
$s_{n,0\%}$	$s_{n,0\%}$	$[0.002, 0.04]$	[−]
$s_{p,0\%}$	$s_{p,0\%}$	$[0.86, 0.97]$	[−]
$s_{n,100\%}$	$s_{n,100\%}$	$[0.75, 0.89]$	[−]
$s_{p,100\%}$	$s_{p,100\%}$	$[0.22, 0.44]$	[−]
$\hat{D}_{s,n}$	$D_{s,n}/R_{s,n}^2$	$[0.00013, 0.0016]$	$[\text{s}^{-1}]$
$\hat{D}_{s,p}$	$D_{s,p}/R_{s,p}^2$	$[0.0004, 0.63]$	$[\text{s}^{-1}]$
$\hat{D}_e$	$D_e FAc_{e,a}/(1-t_+^0)$	$[4.1\cdot10^{-7}, 7.9\cdot10^{-6}]Q^*$	$[\text{Cs}^{-1}]$
$\hat{p}_n$	$\epsilon_{e,n}^{p_n}/\delta_n$	$[50, 5700]$	[−]
$\hat{p}_p$	$\epsilon_{e,p}^{p_p}/\delta_p$	$[58, 4100]$	[−]
$\hat{p}_{\text{sep}}$	$\epsilon_{e,\text{sep}}^{p_{\text{sep}}}/(L\text{-}\delta_n\text{-}\delta_p)$	$[3700, 31000]$	[−]
t_+^0	t_+^0	$[0.26, 0.38]$	[−]
$\hat{\sigma}_n$	$\sigma_n \epsilon_{s,n} A/\delta_n$	$[1.2, 170]Q^*$	$[\Omega^{-1}]$
$\hat{\sigma}_p$	$\sigma_p \epsilon_{s,p} A/\delta_p$	$[0.011, 8.3]Q^*$	$[\Omega^{-1}]$
$\hat{\kappa}$	κA	$[7\cdot10^{-6}, 2\cdot10^{-5}]Q^*$	$[\Omega^{-1}]$
$\hat{R}_{f,n}$	$R_{f,n}R_{s,n}/(3A\delta_n\epsilon_{s,n})$	$[20, 330]/Q^*$	$[\Omega]$
$\hat{R}_{f,p}$	$R_{f,p}R_{s,p}/(3A\delta_p\epsilon_{s,p})$	$[0, 0]/Q^*$	$[\Omega]$
$\hat{R}_{\text{cc}}$	R_{cc}/A	$[32, 170]/Q^*$	$[\Omega]$
α_a	α_a	$[0.48, 0.52]$	[−]
$\hat{k}_{0,n}$	$k_{0,n}c_{e,a}^{\alpha_a}/(R_{s,n}F)$	$[5.7\cdot10^{-5}, 0.00078]$	**
$\hat{k}_{0,p}$	$k_{0,p}c_{e,a}^{\alpha_a}/(R_{s,p}F)$	$[7.9\cdot10^{-5}, 0.001]$	**
$\hat{\epsilon}_{e,n}$	$\epsilon_{e,n}FA\delta_n c_{e,a}/(1-t_+^0)$	$[0.017, 0.76]Q^*$	[C]
$\hat{\epsilon}_{e,p}$	$\epsilon_{e,p}FA\delta_p c_{e,a}/(1-t_+^0)$	$[0.01, 0.14]Q^*$	[C]
$\hat{\epsilon}_{e,sep}$	$\epsilon_{e,\text{sep}}FA(L\text{-}\delta_n\text{-}\delta_p)c_{e,a}/(1-t_+^0)$	$[0.0049, 0.083]Q^*$	[C]

*Note that some parameter ranges are scaled with the cell capacity Q.
** $[\text{s}^{-1}\cdot(\text{m/mol})\hat{}(3(1-2\alpha_a))]$

$D_e^{\text{eff}} = D_e \varepsilon_e^p$, from which D_e^{eff} is chosen as the original model parameter. By treating the non-effective diffusion and conductivity coefficients as the model parameters, and basing the reparameterization procedure on this parameter set, an effectively lower amount of parameters is obtained here than in [13]. Furthermore, by considering the maximum reversible capacity constraint (3.7), an additional parameter is reduced, as $c_{s,n}^{\max}$ and $c_{s,p}^{\max}$ can be determined from the reversible capacity Q using this constraint. The total number of parameters of the reparameterized model is 24. While the total number of parameters of the reparameterized model presented in [13] is also 24, it has to be considered that we have an additional parameter (R_{cc}), and in [13] a further assumption is made that $\alpha_a = \alpha_c = 0.5$, which leads to reduction of an additional parameter. Thus, the reparameterized model proposed here has effectively two parameters less.

3.3. MODEL PARAMETERIZATION APPROACH

This section describes a systematic parameterization approach to identify the parameters of the reparameterized model. First, an equilibrium potential model, which is used to identify the stoichiometric values and maximum concentrations, is described. Then the steps to identify the remaining parameters are explained, which include defining new ranges, the sensitivity analysis, and the parameter estimation procedure.

3.3.1. EQUILIBRIUM POTENTIAL MODEL

Besides the determination of the 24 parameters listed in Table 3.4, the equilibrium potential curves U_n and U_p need to be characterized. The equilibrium potential curves give the so-called EMF (or the OCP) of the battery as

$$U_{\text{EMF}}(s_c) = U_p(s_p) - U_n(s_n), \tag{3.18a}$$

where s_c refers to the state of charge (SoC) of the cell, and s_p and s_n, refer to the stoichiometry at the negative and positive electrode, respectively, defined as

$$s_i = \frac{\hat{c}_s}{\hat{c}_{s,i}^{\max}}, \tag{3.18b}$$

where $i = n$ for $\hat{x} \in [0,1]$, $i = p$ for $\hat{x} \in [2,3]$. The electrodes of the battery generally have a larger capacity than the reversible capacity of the cell, and therefore s_n and s_p generally do not cycle between 0 and 1. Instead, when the battery is empty, i.e., at 0% SoC ($s_c = 0$), s_n and s_p have a certain pre-defined value (related to the balancing of the cell) of $s_{n,0\%}$ and $s_{p,0\%}$, respectively. Similarly, at 100% SoC ($s_c = 1$), s_n and s_p have a certain pre-defined value of $s_{n,100\%}$ and $s_{p,100\%}$, respectively. These parameters, together with U_n, U_p, and the maximum reversible cell capacity Q comprise the equilibrium potential model. Note that while the same EMF-SoC relation can be reached with any choice between 0 and 1 for the parameter values of $s_{n,0\%}$, $s_{n,100\%}$, $s_{p,0\%}$, $s_{n,100\%}$, these parameters also affect the dynamics of the cell through the $(\hat{c}_{s,\max} - \hat{c}_{s,e})^{\alpha_a}$ term in (3.13b). Therefore, these parameters should be considered in the parameter estimation routine, rather than assuming their values from literature to complete the equilibrium potential model, as done in, e.g., [5, 23].

Generally, to determine the equilibrium electrode potential curves of the cell, the EMF of the cell needs to be determined as a function of SoC from input/output data.

There are several techniques available to determine the EMF, where an overview can be found in [24]. From these measurements, the maximum reversible battery capacity Q can also be determined. However, in principle, the equilibrium potential curves of the electrodes cannot be determined individually from input/output data, and different techniques are required depending on whether a cell teardown can be performed or not. We therefore consider the following two cases:

1. The electrode equilibrium potential curves cannot be determined through cell teardown. In this case, the electrode equilibrium potential curves can be determined using (3.18a), by assuming the negative equilibrium potential U_n from literature, from which U_p can be determined, as done in e.g. [5, 23, 25]. Since the negative electrode is generally the same or similar (usually a graphite-based composite) across different types of battery chemistries, and the negative-electrode equilibrium potential U_n is relatively small compared to U_p, we propose to take U_n from literature. In this approach, it is necessary to choose the values of $s_{n,0\%}$, $s_{n,100\%}$, $s_{p,0\%}$, $s_{n,100\%}$, before U_p can be determined.

2. The electrode equilibrium potentials can be measured through cell teardown. In this case, the equilibrium potential curves are measured in relation to the stoichiometry of the electrode over a sufficiently wide range of the stoichiometry. Then, the stoichiometric values $s_{n,0\%}$, $s_{n,100\%}$, $s_{p,0\%}$, $s_{n,100\%}$ are chosen such that the difference between the measured $U_p - U_n$ and the measured U_{EMF} is minimized in some way [2–4]. For further details on how the stoichiometric values are chosen in this case, we refer to the aforementioned papers.

Note that in the first case, information on the chemistry of the electrode materials is not required. If the chemistry of the electrode materials is known, but the electrode equilibrium potentials cannot be measured through cell teardown, then it is possible to determine an equilibrium potential model by taking the approach described for the second case, by taking the equilibrium potential curves from a database or literature, as done (or described) in, e.g., [7, 8, 11, 13, 26]. However, since the EMF can vary even between individual cells that were made in the same factory, the obtained EMF using this method may not sufficiently describe the measured EMF of the considered cell, especially if the purpose is to estimate some or all of the remaining DFN model parameters from input/output data. Deviations of the modeled EMF from the measured EMF can significantly impact the identifiability of the model parameters, as also shown in [27]. Therefore, even if the chemistry of the electrode materials is known, it may still be preferable to use the approach described in the first case, since in that approach it is ensured that the modeled EMF coincides exactly with the measured EMF (by definition). Furthermore, we note that even if the electrode equilibrium potentials can be measured through cell teardown, it may still be preferable to use the approach described in the first case, since the electrode equilibrium potentials, and therefore the EMF, can also vary from cell to cell of the exact same type. However, in this case the information resulting from cell teardown is still useful, as the stoichiometric values found and the measured electrode equilibrium potentials can be used for the approach described in the first case.

We should further note that the obtained U_p using the approach described in the first case often leads to a physically non-intuitive function for U_p. Fig. 3.1 demonstrates this,

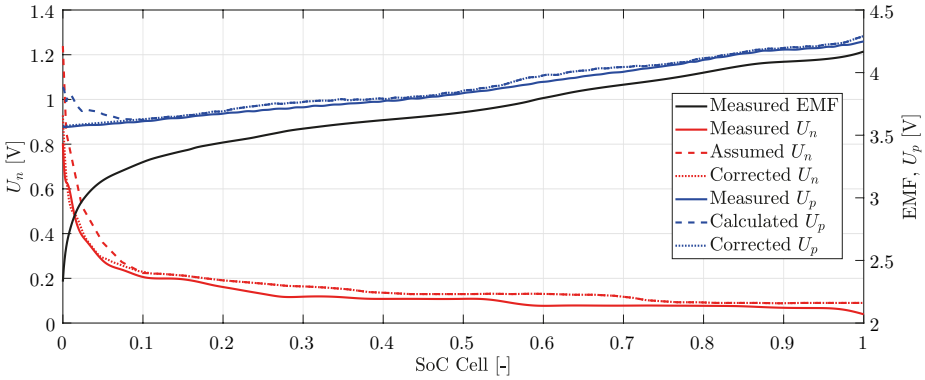

Figure 3.1: Illustration of the correction of the calculated equilibrium potentials. Here, the measured equilibrium potentials are taken from [3], and the assumed negative electrode equilibrium potential curve is taken from [2].

where the measured electrode equilibrium potentials from [3] are compared to the calculated electrode equilibrium potentials. Here, the assumed U_n has been obtained from [2], from which U_p is calculated from the measured EMF shown in Fig. 3.1 using the method described in the first case above. We can observe that around 10% SoC towards 0% SoC, the calculated U_p rises significantly, which is contrary to what would be physically intuitive, as is demonstrated by the measured U_p. To correct for this, we replace the values of U_p from 0% to 10% SoC with a linear function, where the resulting corrected U_p is shown in Fig 3.1 with the dotted lines. Here, the slope is chosen as the mean of the slope of the modeled U_p curve between 10% and 40% SoC. Note that to ensure that the modeled EMF still matches the measured EMF, U_n must also be corrected, which can be computed from the measured EMF and the corrected U_p as $U_n = U_p - U_{\text{EMF}}$. This corrected U_n is also shown in Fig. 3.1, where we can see that the corrected U_n also more closely matches the measured U_n, compared to the initially assumed U_n.

3.3.2. RANGES OF THE GROUPED PARAMETERS

After the parameters of the equilibrium potential model have been determined, the rest of the parameters can be determined through a parameter estimation routine, similar to what has been done in [5] for a model without normalized and grouped parameters. This involves performing a sensitivity analysis, and estimating (some of the) parameters from input/output data. The sensitivity analysis requires a range of values that the estimation parameters can have in order to assess the sensitivity of each parameter. Furthermore, the ranges can be used as bounds in the parameter estimation routine.

The ranges of the reparameterized model parameters are shown in Table 3.4. These parameter ranges have been obtained by gathering a set of values for each of the parameters from various papers, i.e., [2–4, 28–32], where largely actual measurements have been done to obtain the parameter values (rather than using parameter estimation techniques to determine the parameters). The batteries for which the parameter ranges apply are of various chemical compositions, where the negative electrode chemistry generally con-

sists of graphite or silicon-doped graphite, and the chemical composition of the positive electrode is a nickel-manganese-cobalt material in [3, 4, 30], $LiMn_2O_4$ in [28, 32], $LiCoO_2$ in [29, 31], and $LiMnCoO_2$ in [2]. Since the parameters given in these papers are for the non-reformulated DFN model, the parameters need to be converted to the parameters of the reformulated model, which can be done using Table 3.4. Note that in the computation of the reformulated DFN model parameter values, many of these parameters have a grouping that contains any of the parameters A, L, $\epsilon_{s,n}$, and $\epsilon_{s,p}$, which are related to the capacity of the cell. In order to account for this, the parameters that have any of the capacity-related parameters in their grouping are scaled by the capacity of the cell, as can be seen in Table 3.4. Further note that the range of $\hat{R}_{f,p}$ is $[0,0]$, since we could not find any non-zero values for $\hat{R}_{f,p}$ in the prior-mentioned literature that we have used to determine the parameter ranges.

Within the given ranges, every parameter can be expressed on a linear or a logarithmic scale, i.e,

$$\theta_i = \beta_i \underline{\theta}_i + (1-\beta_i)\overline{\theta}_i, \tag{3.19a}$$

$$\log\theta_i = \beta_i \log\underline{\theta}_i + (1-\beta_i)\log\overline{\theta}_i, \tag{3.19b}$$

where $\beta_i \in \boldsymbol{\beta} \in [0,1]$, in which $\boldsymbol{\beta}$ denotes the vector of normalized parameters, $\theta_i \in \boldsymbol{\theta}$ denotes every parameter, in which $\boldsymbol{\theta}$ denotes the vector of all parameters, and $\underline{\theta}_i, \overline{\theta}_i$ denotes the minimum and maximum value of the parameter, respectively. For parameters whose range is in the same order of magnitude, i.e., $\overline{\theta}_i/\underline{\theta}_i \leq 10$, (3.19a) is used and for parameters whose range is of a different order of magnitude, i.e., $\overline{\theta}_i/\underline{\theta}_i > 10$, (3.19b) is used.

3.3.3. SENSITIVITY ANALYSIS OF THE GROUPED PARAMETERS

With the parameter ranges determined, a sensitivity analysis can be performed in order to determine the sensitivity of the output to the variation of the parameters. The results of the analysis can be used to select the appropriate (most sensitive) estimation parameters, in order to avoid solving an ill-conditioned optimization problem in the parameter estimation routine. The sensitivity analysis is done as described in [5], which in turn is based on the work of [12], where a parameter sensitivity ranking is obtained by orthogonalization of the sensitivity matrix of a model. Therefore, we will shortly summarize the sensitivity analysis approach, and refer to [12] and [5] for a more detailed description.

If we define the model output $\hat{V}$ as a nonlinear function g of the parameters $\boldsymbol{\theta}(\boldsymbol{\beta})$, input I_a, and initial conditions x_0, i.e., $\hat{V} = g(\boldsymbol{\theta}(\boldsymbol{\beta}), I_a, x_0)$, the sensitivity of the model output $\hat{V}$ to the parameters $\boldsymbol{\theta}$ can be defined as

$$S(\boldsymbol{\theta}(\boldsymbol{\beta}), I_a, x_0) = \frac{\partial \hat{V}}{\partial \boldsymbol{\beta}}, \tag{3.20}$$

where the gradient $\frac{\partial \hat{V}}{\partial \boldsymbol{\beta}} \in \mathbb{R}^{n\times m}$, in which n is the number of time samples and m is the number of parameters, is numerically approximated using a finite-difference method.

A permutation matrix $P \in \mathbb{R}^{m\times m}$ to determine the ranking of the sensitivity can be obtained using the pivoted QR decomposition of S such that

$$SP = QR, \tag{3.21}$$

where $Q \in \mathbb{R}^{n\times n}$ is an orthogonal matrix, and $R \in \mathbb{R}^{n\times m}$ is an upper-triangular matrix. If $\Pi_{\text{init}} = [1, 2, ..., m]$ denotes the initial ordering of the parameters, the set of rank-ordered parameters Π_{ranked} can be obtained through $\Pi_{\text{ranked}} = \Pi_{\text{init}} P$. Information on the magnitude of sensitivity M_s of the parameters is contained in the matrix R, and the magnitudes are given by the absolute value of the values on the diagonal of R, i.e., $M_s = |\text{diag}(R)|$. Note that the sensitivity matrix as defined in (3.20), and therefore the parameter ranking Π_{ranked}, depend on the chosen input profile as well as the initial conditions. For the purpose of selecting the appropriate estimation parameters, the input profile and initial conditions can be chosen the same as in the parameter estimation routine.

3.3.4. ESTIMATING THE GROUPED PARAMETERS

After performing the sensitivity analysis and determining the ranking order, the selected estimation parameters $\boldsymbol{\beta}_s$ can be optimized to the model output by minimizing the sum of the squared error between the experimental voltage V_{exp} and the predicted voltage $\hat{V}$, i.e.,

$$\hat{\boldsymbol{\beta}}_s := \arg\min_{\boldsymbol{\beta}} \sum_{i=1}^{n} (V_{\text{exp}}(t_i) - \hat{V}(\boldsymbol{\theta}(\boldsymbol{\beta}), t_i))^2, \tag{3.22}$$

where $\hat{\boldsymbol{\beta}}_s$ is the vector of optimized parameters, and t_i denotes the time at which measurement $i \in \{1, ..., n\}$ is taken. This optimization problem can be solved using any nonlinear least-squares algorithm. The parameters that are not very sensitive will not be optimized and are selected as the nominal value in their ranges, i.e., by setting $\beta_i = 0.5$ in (3.19).

3.4. RESULTS AND VALIDATION

In this section, we will use the model parameterization approach presented in the previous section for two different cells. For one cell, only the EMF (or OCP) data of the complete cell is provided (Cell 1, see [33]), but 3 sets of experimentally obtained current and voltage measurements are available, and for the other cell, the equilibrium potential functions of the individual electrodes have been provided (Cell 2, see [3, 34]), but for which we only have one set of current and voltage measurements available. The battery chemistry of Cell 2 consists of a silicon-doped graphite negative electrode and a nickel-manganese-cobalt positive electrode [3, 34], whereas the battery chemistry of Cell 1 is unspecified. We will first show the parameter sensitivity ranking for the two cells, and then investigate the influence of the number of estimation parameters and the data length of identification data on obtained model accuracy. Furthermore, for Cell 2, a DFN model has already been parameterized in [3], where some of the parameters have been determined experimentally, and others have been assumed as values obtained from literature. We will compare the model accuracy obtained using the parameters from [3], which were determined through cell teardown, and the model accuracy obtained using

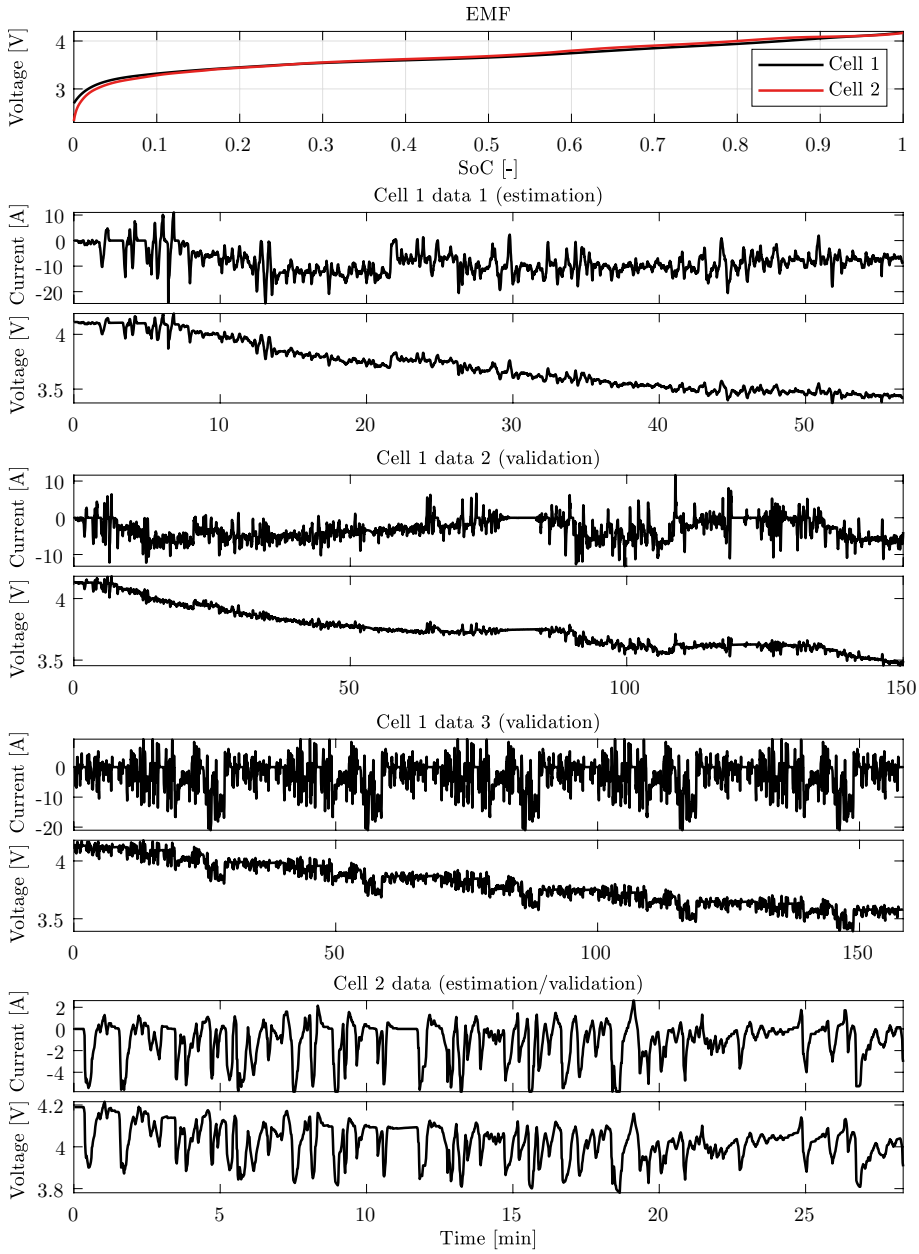

Figure 3.2: Experimental data from Cell 1 and Cell 2 used for model parameterization.

the model parameterization approach described in Section 3.3, and show that a significant improvement can be made by using the presented model parameterization approach. Finally, we will analyze the consistency and accuracy of the parameter estima-

tion routine using a synthetic cell, represented by a DFN model of which its parameters have been randomly selected (within specific and realistic intervals). The estimated parameters, and the resulting internal states will be compared to the true known parameters and states of the synthetic model when the model used for estimation is equal to the true system, and when there are modeling errors present. This will show how consistently and accurately the parameters of the DFN model can be estimated, and how far the resulting internal states deviate from the true internal states. Note that in this investigation of the physical meaningfulness of the parameters and internal states, measurements cannot be used, since measured parameters and states are not available from current-voltage measurements.

The experimental data sets used for the sensitivity analysis and parameter estimation are shown in Fig. 3.2. For Cell 1, three different data sets were available, where one is used for the estimation of the parameters, and the other two are used for validation of the obtained parameters. However, for Cell 2, only one data set was available, which is used for both estimation as well as validation, where only a part of the data is used for estimation and the entire data is used for validation. Furthermore, for Cell 2, the equilibrium potentials have been measured in [3], which are shown in Fig. 3.1, while for Cell 1, the equilibrium potentials have been obtained from the EMF measurements, with the method described in the first case in Section 3.3.1.

3.4.1. SENSITIVITY ANALYSIS

In order to show how to make a selection of parameters to be estimated in the parameter estimation routine, the sensitivity analysis described in Section 3.3.3 has been applied. The current input profiles for the sensitivity matrix S in (3.20) have been chosen as the estimation profiles shown in Fig. 3.2. Note that, therefore, the model used for the sensitivity analysis of both cells is the same, with the only differences being the current input profiles and the EMFs, leading to different results of the sensitivity analysis. The parameter sensitivity ranking Π_{ranked} and the normalized magnitude of sensitivity (to the most sensitive parameter) $M_s/\max(M_s)$ of each parameter obtained for the two cells can be seen in Fig. 3.3. Note that since we assume that the reversible capacity Q is measurable and because the range of $\hat{R}_{f,p}$ in Table 3.4 was determined to be $[0,0]$, the remaining number of parameters to be estimated is 22. We can observe that, while the normalized magnitudes and the order of the ranking are slightly different, the parameters occur roughly in the same order for both cells. Based on these rankings, for any desired number of estimation parameters, a selection of parameters can be made. These results have also been used in the studies shown below.

3.4.2. INFLUENCE OF THE NUMBER OF ESTIMATED PARAMETERS ON THE ACCURACY

With a choice of the number of estimation parameters, the parameter estimation routine described in Section 3.3.4 has been done using the estimation current profiles shown in Fig. 3.2 for both cells. The nonlinear least-squares problem formulated in (3.22) has been solved using the `lsqnonlin` function in MATLAB with the trust-region-reflective algorithm, in which the parameter bounds have been selected as those listed in Table 3.4, and the initial parameter guesses have been obtained by setting $\boldsymbol{\beta}_s = 0.5$ for the estima-

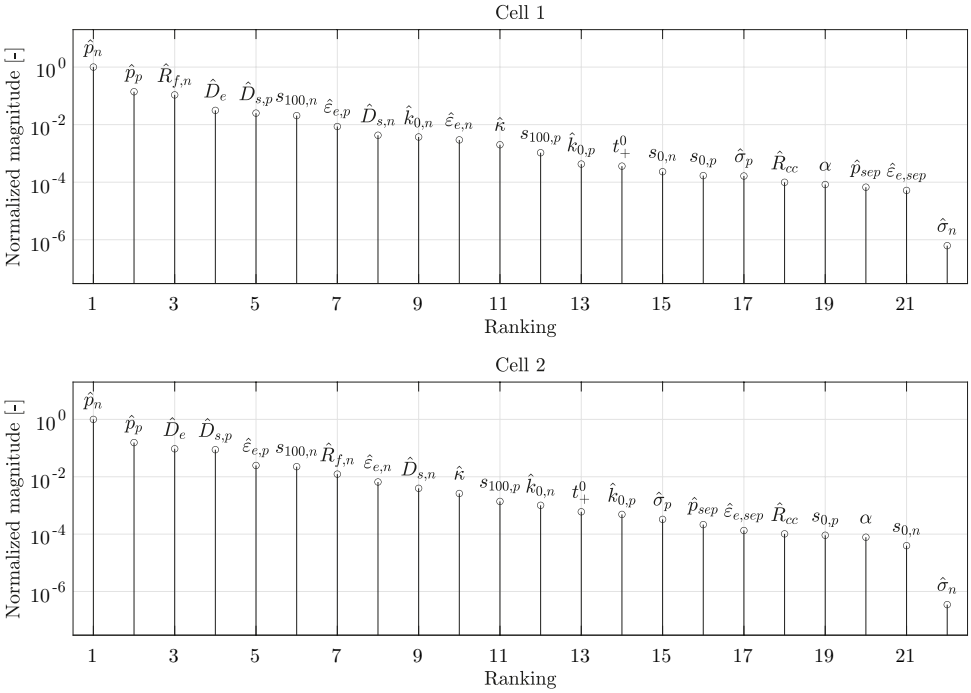

Figure 3.3: Normalized magnitude of sensitivity for Cell 1 and Cell 2, where the parameters are ranked by decreasing magnitude of sensitivity.

tion parameters. For Cell 1, the model with the estimated parameters can be validated using a different data set than the one used for estimation. Note that based on the results shown in Fig. 3.4b, which will be further explained below, only 90% of Data 1 has been used for estimation, while the entire length of Data 1 as well as the remaining data have been used for validation. For Cell 2, as only one dataset was available, the first 70% of the data has been used for estimation, and the entire data has been used for validation.

Fig. 3.4a shows the variation in root-mean-square error (RMSE) between the various data of Fig. 3.2 and the model with a varying number of estimated parameters. Here, the selected estimation parameters have been chosen in the order that corresponds to the ranking shown in Fig. 3.3. For both cells, we can see that after about 12 parameters the RMSE for all data sets does not significantly change. This seems to indicate that 12 estimation parameters is a fair selection in order to reach a small RMSE. For both cells, the RMSE seems to fluctuate somewhat at some points, e.g., for Cell 2, the validation RMSE with 14 estimation parameters is lower than with 15 estimation parameters, even though the estimation RMSE does not show this fluctuation. This can be explained by the fact that the parameter estimation problem is non-convex, and therefore there are multiple local minima, as we will also show further below.

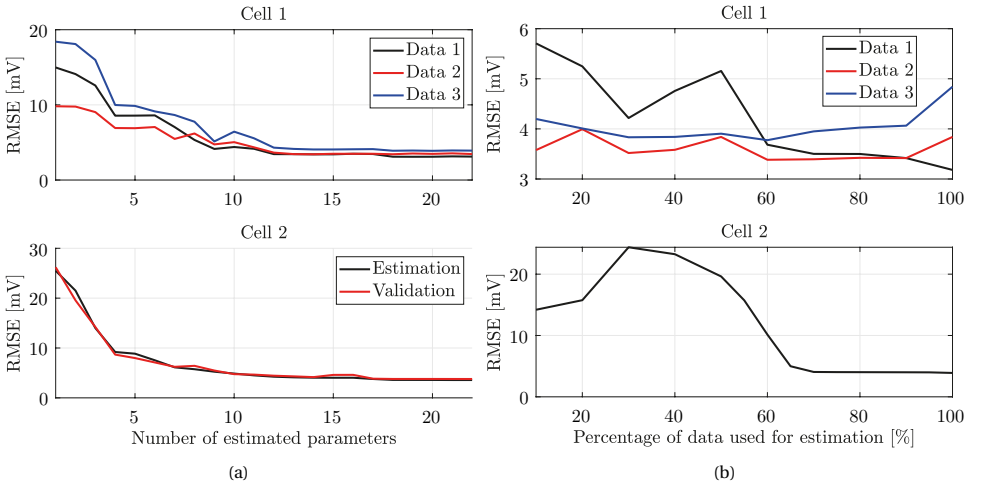

Figure 3.4: RMSE between the measured data and simulated data for (a) a varying number of estimated parameters used in the estimation procedure and (b) a varying data length used in the estimation procedure, where for Cell 1, the percentage data used from Data 1 has been varied.

3.4.3. INFLUENCE OF THE LENGTH OF ESTIMATION DATA

The lack of a second set of data for Cell 2 means that the estimated model can only be validated using the original data used for estimation. Of course, validating a model with the exact same data as the model has been estimated with, does not give much confidence that this model will also accurately predict the output using a different current profile. Therefore, one way is to only use a subset of the available data for estimation, and then using the entire data for validation, as we have done in the previous subsection, where 70% of the data was used for estimation. However, the choice for the length of the estimation data is not obvious, as having less estimation data can lead to a worse estimate, while having less validation data can lead to false conclusions. In order make this apparent trade-off between a better model fit with more estimation data and a higher confidence in validation with more validation data, in Fig. 3.4b, the RMSE of the validation for both cells is shown for a varying percentage of data used for estimation. Note that for Cell 1, the percentage is varied for the estimation data, and validated for all available data. We can observe that for both cells, the RMSE varies considerably based on the percentage of data used. It seems that for both cells, choosing at least around 70% of the estimation data is required to obtain a good model fit, which leaves 30% of the data to be validated over if there is only one data set available. Also notable is that for Cell 1, the RMSE is relatively small for all data sets even when only using 10% of the data. This is in contrast to Cell 2, where the obtained errors until using 65% of the data are much larger. This could be caused by more unmodeled behavior showing up in the experimental voltage of Cell 2 than of Cell 1.

In the lower plot of Fig. 3.5, we can see a comparison of the errors obtained using 30% of the data, 65% of the data, and with the parameters from [3]. We can see that when using 30% of the data for estimation (corresponding to the first 510 s), the errors

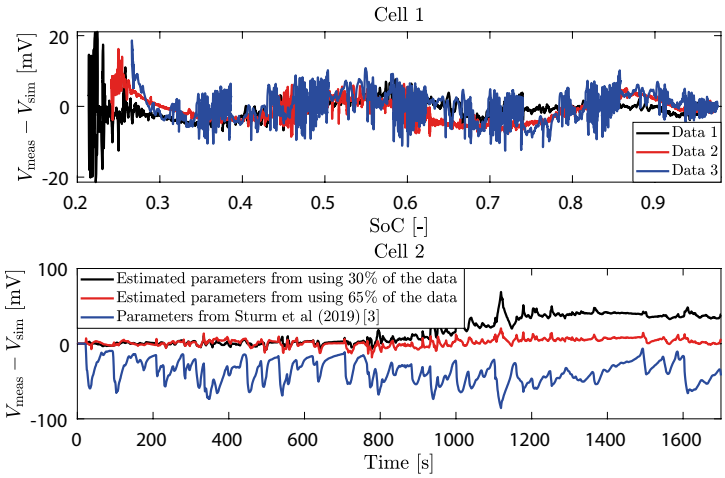

Figure 3.5: Error between the measured voltage V_{meas} and the simulated voltage V_{sim} for both cells and their available data. For Cell 2, the error from using a DFN model with the parameters from [3] is also shown. The parameters used for simulation for Cell 1 have been obtained from using 60% of Data 1 for simulation with 14 estimated parameters and the parameters used for simulation for Cell 2 have been obtained from using 30% and 65% of the data for simulation with 14 estimated parameters.

are relatively small until 800 s, after which the error increases considerably again. When using 65% of the data (corresponding to the 1105 s), the error remains small, for the entire data. This could indicate that between 800 s and 1105 s there are some significantly large unmodeled effects leading to large errors when less than 65% of the data is used. Furthermore, we can see that the simulation using the parameters from [3] shows a clear deviation from the experimental voltage, even larger than when using 30% of the data for estimation. Thus, we can see that by estimating some of the parameters, rather than relying on experiments and values from literature, a significantly more accurate model output can be obtained. However, we may still question whether the internal states represented by the model obtained from estimating the parameters are still physically meaningful. This will be discussed in the remaining subsections below.

Furthermore in Fig. 3.4b, for Cell 1, we can see that with 100% of data used for estimation, there seems to be a sharp rise in the RMSE of Data 2 and Data 3, whereas the RMSE of Data 1 decreases considerably compared to using 90% of the estimation data. This indicates that there is a considerable case of increased overfitting of the parameters when using 100% of the estimation data. If we observe the upper plot in Fig. 3.5, we can see that for Data 1 there are significantly larger errors at the beginning, between 0.2 and 0.25 SoC, which explains the large increase in RMSE seen from 90% length of estimation data used in Fig. 3.4b. These observations show that it is crucial to study where the unmodeled effects in the measured output occur the most, in order to avoid overfitting of the parameters to this unmodeled behavior as much as possible.

3.4.4. CONSISTENCY AND ACCURACY OF THE ESTIMATED PARAMETERS

The goal of parameter estimation is to find model parameters through fitting the modeled output and the measured output. If the identifiability of the parameters is sufficiently large, the estimated parameters should correspond to physically meaningful parameters. However, identifiability has been a key issue for the DFN model [6], which means that not all parameters can be found reliably. Furthermore, the nonlinear nature of the DFN model also means that there are multiple local minima, further complicating the issue. Finally, due to modeling errors, it can occur that even when the (internal) dynamics of the actual system is actually closer to a particular DFN model, a larger error in the validation of the terminal voltage is seen. Consequently, a smaller output validation error from a particular DFN model does not necessarily imply a better representation of the internal states of the system. In order to get an idea of how much these issues affect the parameter estimation procedure, we can perform a Monte Carlo simulation, where the parameter estimation procedure is done from several random initial conditions, and study the obtained parameters. Specifically, for Cell 1, we have done the parameter estimation routine, with 22 estimation parameters and 90% of Data 1 used for estimation, for 50 different random initial conditions of the parameter estimation routine.

The results of this study are shown in the upper plot of Fig. 3.6, where a boxplot representation is used to show the obtained data for each of the parameters. We can see here that it is also clear that most parameters can be estimated consistently. However, it also seems that many of the estimated parameters are at the extremal values, e.g., parameter 6 ($s_{100,n}$) and 8 ($\hat{D}_{s,n}$). This could be caused either by the unmodeled behavior in the experimental voltage, to which the parameters are being fit, or it could be that the ranges chosen for the parameters are too small. Therefore, we have done the same study, but this time with an increased range for the parameters, where the lower bound is found by setting $\beta_i = -0.3$ in (3.19) and the upper bound is found by setting $\beta_i = 1.3$ in (3.19). We can now see that, as could be expected, the variability of the estimated parameters increases. The variability is especially more for the lower ranked parameters, which is expected, as these were also found to be the least sensitive parameters according to the sensitivity analysis done above. For example, parameter 6 ($s_{100,n}$), which was consistently estimated as $\beta = 1$, now varies between around 0 and 1.3 (where we should point out that with $\beta = 1.3$, the parameter value is still physically meaningful, i.e., $s_{100,n} < 1$), although the median is still around $\beta = 1$. It could be somewhat unexpected that the parameter after extending the range also has estimated values that are below $\beta = 1$, since with the original ranges it did not go below $\beta = 1$. However, because the parameters have some dependency on each other, by extending the ranges, the number of combinations of parameters that achieves a local minimum increases. This can explain why, for parameter 6 with the extended ranges, we get combinations within the original range that would not show up with the original ranges in the upper plot of Fig. 3.6.

Of course, it could also be that the physically meaningful or "true" parameters of the cell are in fact in the original ranges, but that the parameters have been fit so much to the unmodeled behavior that they tend to go to the extremes of the ranges. In order to investigate the impact of unmodeled behavior on the estimation of the parameters, we have generated a synthetic cell, of which its parameters have been chosen randomly (within the specified ranges). In this case, the estimation model is now exactly the same

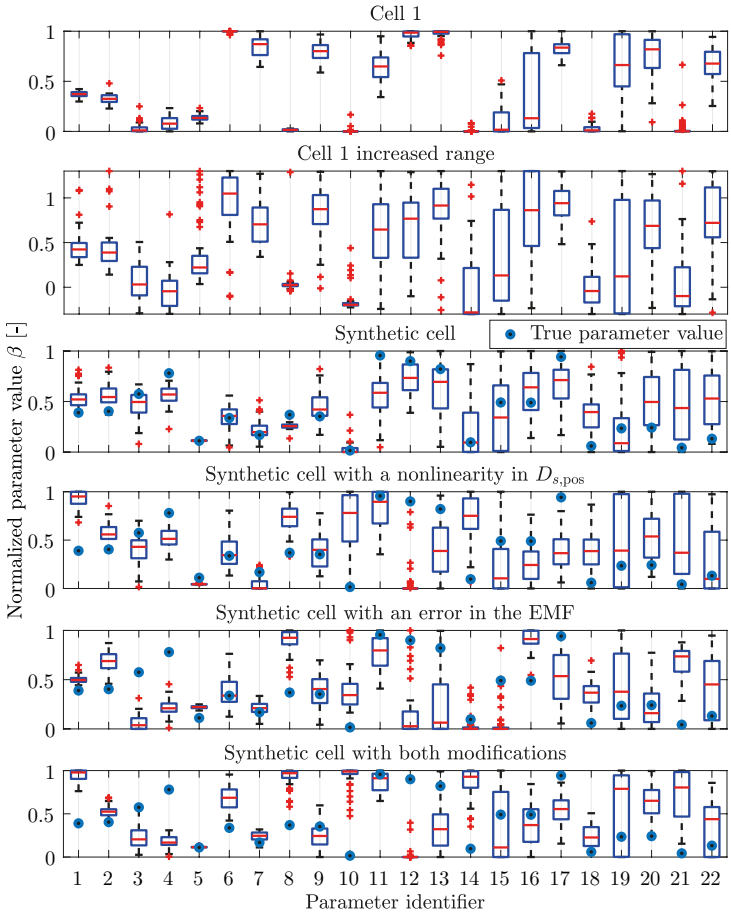

Figure 3.6: Boxplots showing the variability and accuracy of the parameter estimation routine for Cell 1 and the synthetic cell. The parameter identifiers relate to the ranking shown in Fig. 3.3.

as the system that is to be estimated, which is considered to be the ideal scenario for parameter estimation. With this modeled cell, we can do the same study as outlined above (with the same input data used for simulation), where we start from 50 different random initial conditions.

The results of this simulation study are shown in the third plot of Fig. 3.6. We can now see that the variability of the parameters is considerably more than for Cell 1 in Fig. 3.6 (upper plot). This can be explained by the fact that for the synthetic cell, the values of the parameters fall within their respective parameter ranges (as this is how the parameters have been selected), while with Cell 1, this is not guaranteed, where the "true" parameter values can be out of their respectively chosen parameter ranges. Generally, as we have seen from the discussion of Fig. 3.6, when one parameter shows a higher variability, it will also lead to a higher variability in the other parameters, since there is an inter-dependency between the parameters. Therefore, when the value of a parameter is

consistently at the edge of the range, i.e., its estimated values are always close to $\beta = 0$ or $\beta = 1$, as is the case for some parameters in the case of Cell 1, the other parameters will show a smaller variation. We can also observe that especially for the first 10 parameters, the estimated parameters are close to the true parameters, with a relatively small variability. Notably, parameter 5 ($\hat{D}_{s,\text{pos}}$) seems to be the most identifiable parameter, since it has a very small variability and the estimated values are very close to the true value. This implies that the model output is very sensitive to $\hat{D}_{s,\text{pos}}$, while at the same time there is a low inter-dependency of $\hat{D}_{s,\text{pos}}$ with the other parameters.

To see the effect of unmodeled behavior on the estimated parameters, we first add a nonlinearity in $\hat{D}_{s,\text{pos}}$ in the synthetic cell, since this parameter has a large effect on the output. Specifically, we change $\hat{D}_{s,\text{pos}}$ into a concentration-dependent parameter equal to

$$\hat{D}_{s,\text{pos}}(s_p) = 5.705 \times 10^{-4+8(s_p-0.5)^2}.$$

Note that the scaling 5.705 is chosen such that $\hat{D}_{s,\text{pos}}((s_{100,p} + s_{0,p})/2)$ is equal to the originally chosen parameter value for $\hat{D}_{s,\text{pos}}$, since we would like to discount the effect of a bias in the parameter as much as possible. We then also introduce an error in the EMF, which translates into an error in U_p, as

$$U_{\text{EMF}}(s_c) = \bar{U}_{\text{EMF}} + 0.003\sin(4\pi s_c),$$

where $\bar{U}_{\text{EMF}}$ is the original EMF. The various values in the modifications are chosen such that the RMSE between the original model output and the modified model output after parameter estimation is approximately 1.2 mV using the current profile of Data 1, which is in the same range as the errors shown in the upper plot of Fig. 3.5. The results for these modified models are shown in the bottom three plots in Fig. 3.6. We observe that when only adding a nonlinearity in $\hat{D}_{s,\text{pos}}$, apart from parameters 1 and 8, the first 9 parameters are still estimated almost as well as the synthetic cell without any modifications. However, when adding an error in U_p, the estimates deviate significantly more from the true values than when adding a nonlinearity in $\hat{D}_{s,\text{pos}}$, even though the added errors are similar in magnitude.

This is further supported by Table 3.5, where we can see the median of the RMSE between the estimated parameters and the true parameters. As a reference, the median RMS error (MRMSE) between random sets of parameters and the true parameters is also shown. Here, we observe that the MRMSE of the parameters for the synthetic cell is clearly smaller than the MRMSE of a random set of parameters. This indicates that in the ideal circumstance, when there are no modeling errors, there is a correlation between the closeness of the estimated parameters to the true parameters and the closeness of the resulting output to the true output. However, when adding modeling errors, we can see that this correlation no longer holds. In fact, the MRMSE of the parameters with both of the modifications is almost equal to the MRMSE using a random set of parameters. Interestingly, when computing the MRMSE using only the first 9 parameters, we can see that with a nonlinearity in $\hat{D}_{s,\text{pos}}$, the MRMSE is still significantly lower than the MRSE of random sets of parameters. This means that under this circumstance, with a nonlinearity in $\hat{D}_{s,\text{pos}}$, the first 9 parameters can still be somewhat reliably estimated.

With an error in EMF, the MRMSE of the parameters is still close to the MRMSE of random sets of parameters. This suggests that EMF modeling errors affect the identifiability of the parameters significantly more than neglecting the concentration-dependency of parameters. Therefore, when designing experiments for the parameter estimation routine, it is critical that EMF modeling errors are minimized. This might seem obvious as the battery voltage mostly depends on the EMF, see [35], but it demonstrates once more that when designing experiments, it is critical that the EMF is accurately determined.

3.4.5. CONSISTENCY AND ACCURACY OF THE INTERNAL STATES

The results presented above show the consistency and accuracy of the estimated parameters. However, in some applications, such as fast charging of batteries, see e.g., [36–38], and Chapter 4 of this thesis, only certain internal states are of interest, which are not necessarily significantly affected by all the parameters of the DFN model. Generally, the internal states of interest are the stoichiometry in the electrodes s_n and s_p, which either are constrained directly, e.g., [38], or are constrained through particle stress models, which depend on the stoichiometry of the electrodes, e.g., [36]. Side-reaction models are also used for the purpose of fast charging, in e.g., [37] and Chapter 4 of this thesis, which mainly depend on the potential drop between the solid and electrolyte phase $\phi_s - \phi_e$ in the negative electrode. Finally, constraints on electrolyte concentration c_e are also used in [38] for the purpose of fast charging.

In Fig. 3.7, the lower and upper bound of these aforementioned internal states from simulations using the estimated parameters resulting from the study above in Section 3.4.4 is shown. For the synthetic cell without modifications, we can see that the true states are within the bounds for all internal states. This is no longer the case for the synthetic cell with modifications, where we see that the estimated s_p and c_e in the positive electrode deviate substantially from their respective true states. This also shows that identifiability of the parameters is in principle not a large issue when the desire is to obtain parameters that lead to a good representation of the considered states. Rather, the bigger issue in this case are modeling errors which lead to a biased estimate of the parameters, leading to estimated states that can be far from the true states. This would be an issue when these estimated models are used in fast charging, especially when there are constraints imposed on the electrolyte concentration. In the example of this synthetic cell, the constraint would be activated conservatively, since the estimated positive electrode c_e varies much more in magnitude than the true c_e. This would lead to a conservative use of the battery. On the other hand, it could equally occur that the estimated states show a smaller variation in magnitude, which could lead to the scenario where for

Table 3.5: Median of the output RMS error (RMSE) and the median deviation from the true parameters of the obtained estimated parameters from the various synthetic models. The notation $\beta_{\text{est},N}$ indicates that first N parameters have been used for the calculation of the RMSE.

Median of	Synthetic cell	Nonlinearity in $\hat{D}_{s,\text{pos}}$	Error in EMF	Random parameters
RMSE $V_{\text{est}} - V_{\text{true}}$	0.13	1.19	1.17	36.2
RMSE $\beta_{\text{est},22} - \beta_{\text{true}}$	0.30	0.43	0.44	0.43
RMSE $\beta_{\text{est},9} - \beta_{\text{true}}$	0.14	0.22	0.34	0.38

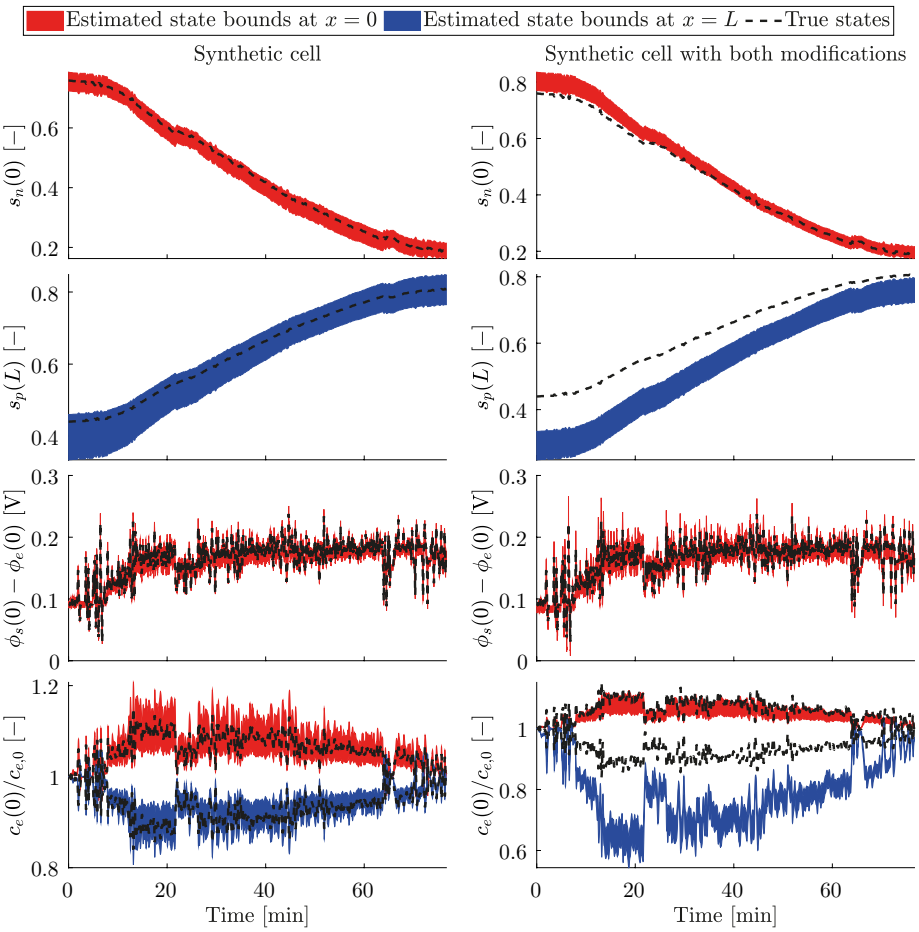

Figure 3.7: Upper and lower bounds of the resulting estimated states obtained using the estimated parameter sets.

the true cell the constraints are violated.

The results shown in this section signify the importance of both the work done in determining the parameters through cell teardown and the work done in determining the parameters based on input/output measurements. As we have shown, using only input/output measurements can lead to a model that does not sufficiently represent the internal states of the cell. On the other hand, we have shown in Fig. 3.5 that by measuring the parameters, the obtained model does not sufficiently represent the output of the cell. Therefore, in determining a model that both sufficiently represents the internal states and the output, it is crucial that both these approaches in determining model parameters are combined in some way. For example, as we have seen in Fig. 3.6, determining tighter parameter ranges leads to more consistent parameter estimates, while at the same time limits the deviation that the estimated parameters can have from the

true parameters. Note that experimentally determining parameters, as done in e.g., [2] and [3], is thus especially useful in defining tighter parameter ranges, which again shows the usefulness of this approach in combination with parameter estimation based on input/output measurements.

3.5. CONCLUSIONS

In this chapter, we have proposed a model parametrization approach of the DFN model, by first reparameterizing the DFN model through normalization and grouping, followed by a sensitivity analysis and a parameter estimation procedure. We have presented results for the parameterization of two cells using experimental data of current and voltage measurements, one where only the EMF (or OCP) measurements of the complete cell have been provided, and one where the individual electrode potentials had been been characterized. Here, we have studied the influence of the number of estimated parameters and the length of identification data on the obtained model accuracy. We have found that for both cells, estimating 12 out of all 22 model parameters is sufficient to obtain an accurate model (with respect to the output voltage), and we have found that the length of the identification data should be carefully selected to avoid overfitting of the parameters to modeling errors as much as possible. Finally, we have shown the consistency and accuracy of the parameter estimation routine by analyzing the parameter estimation routine for a synthetic cell. Through this analysis, we have demonstrated that modeling errors, and in particular EMF modeling errors, can lead to a large bias and variability in the estimated parameters. We have further shown that this bias and variability can be reduced by determining tighter parameter ranges, which can be done through cell teardown. The results of this analysis motivate the need for an approach that combines parameter estimation using current/voltage data and parameter estimation through cell teardown. While the former approach can lead to a significantly better model accuracy, it might lead to parameters that are not as physically meaningful as those resulting from the latter approach.

REFERENCES

[1] M. Doyle, T. F. Fuller, and J. Newman, *Modeling of galvanostatic charge and discharge of the lithium/polymer/insertion cell,* Journal of the Electrochemical society **140**, 1526 (1993).

[2] M. Ecker, T. K. D. Tran, P. Dechent, S. Käbitz, A. Warnecke, and D. U. Sauer, *Parameterization of a Physico-Chemical Model of a Lithium-Ion Battery I. Determination of Parameters,* Journal of the Electrochemical Society **162**, A1836 (2015).

[3] J. Sturm, A. Rheinfeld, I. Zilberman, F. B. Spingler, S. Kosch, F. Frie, and A. Jossen, *Modeling and simulation of inhomogeneities in a 18650 nickel-rich, silicon-graphite lithium-ion cell during fast charging,* Journal of Power Sources **412**, 204 (2019).

[4] J. Schmalstieg, C. Rahe, M. Ecker, and D. U. Sauer, *Full Cell Parameterization of a High-Power Lithium-Ion Battery for a Physico-Chemical Model: Part I. Physical*

and Electrochemical Parameters, Journal of the Electrochemical Society **165**, A3799 (2018).

[5] N. Jin, D. L. Danilov, P. M. Van den Hof, and M. Donkers, *Parameter estimation of an electrochemistry-based lithium-ion battery model using a two-step procedure and a parameter sensitivity analysis,* International Journal of Energy Research **42**, 2417 (2018).

[6] J. C. Forman, S. J. Moura, J. L. Stein, and H. K. Fathy, *Genetic identification and fisher identifiability analysis of the Doyle–Fuller–Newman model from experimental cycling of a LiFePO4 cell,* Journal of Power Sources **210**, 263 (2012).

[7] J. Marcicki, M. Canova, A. T. Conlisk, and G. Rizzoni, *Design and parametrization analysis of a reduced-order electrochemical model of graphite/LiFePO4 cells for SOC/SOH estimation,* Journal of Power Sources **237**, 310 (2013).

[8] L. Zhang, L. Wang, G. Hinds, C. Lyu, J. Zheng, and J. Li, *Multi-objective optimization of lithium-ion battery model using genetic algorithm approach,* Journal of Power Sources **270**, 367 (2014).

[9] Z. Chu, R. Jobman, A. Rodríguez, G. L. Plett, M. S. Trimboli, X. Feng, and M. Ouyang, *A control-oriented electrochemical model for lithium-ion battery. Part II: Parameter identification based on reference electrode,* Journal of Energy Storage **27**, 101101 (2020).

[10] V. Ramadesigan, K. Chen, N. A. Burns, V. Boovaragavan, R. D. Braatz, and V. R. Subramanian, *Parameter Estimation and Capacity Fade Analysis of Lithium-Ion Batteries Using Reformulated Models,* Journal of the Electrochemical Society **158**, A1048 (2011).

[11] E. Namor, D. Torregrossa, R. Cherkaoui, and M. Paolone, *Parameter identification of a lithium-ion cell single-particle model through non-invasive testing,* Journal of Energy Storage **12**, 138 (2017).

[12] B. F. Lund and B. A. Foss, *Parameter ranking by orthogonalization—Applied to nonlinear mechanistic models,* Automatica **44**, 278 (2008).

[13] R. Jobman, M. S. Trimboli, and G. L. Plett, *Identification of lithium-ion physics-based model parameter values,* Journal of Energy Challenges and Mechanics **2**, 45 (2015).

[14] Z. Chu, G. L. Plett, M. S. Trimboli, and M. Ouyang, *A control-oriented electrochemical model for lithium-ion battery, Part I: Lumped-parameter reduced-order model with constant phase element,* Journal of Energy Storage **25**, 100828 (2019).

[15] G. L. Plett, *Battery Management Systems, Volume I: Battery Modeling* (Artech House publishers, 2015).

[16] M. Torchio, L. Magni, R. B. Gopaluni, R. D. Braatz, and D. M. Raimondo, *LIONSIMBA: A matlab framework based on a finite volume model suitable for Li-ion battery design, simulation, and control,* Journal of the Electrochemical Society **163**, A1192 (2016).

[17] L. Cai and R. E. White, *Reduction of Model Order Based on Proper Orthogonal Decomposition for Lithium-Ion Battery Simulations,* Journal of the Electrochemical Society **156**, A154 (2009).

[18] P. W. Northrop, V. Ramadesigan, S. De, and V. R. Subramanian, *Coordinate transformation, orthogonal collocation, model reformulation and simulation of electrochemical-thermal behavior of lithium-ion battery stacks,* Journal of the Electrochemical Society **158**, A1461 (2011).

[19] R. Klein, N. A. Chaturvedi, J. Christensen, J. Ahmed, R. Findeisen, and A. Kojic, *Electrochemical Model Based Observer Design for a Lithium-Ion Battery,* IEEE Transactions on Control Systems Technology **21**, 289 (2013).

[20] J. Newman, *Fortran programs for the simulation of electrochemical systems,* `http://www.cchem.berkeley.edu/jsngrp/fortran.html` (accessed November 10, 2020).

[21] K. A. Smith, C. D. Rahn, and C.-Y. Wang, *Control oriented 1D electrochemical model of lithium ion battery,* Energy Conversion and Management **48**, 2565 (2007).

[22] L. Xia, E. Najafi, Z. Li, H. J. Bergveld, and M. C. F. Donkers, *A computationally efficient implementation of a full and reduced-order electrochemistry-based model for Li-ion batteries,* Applied Energy **208**, 1285 (2017).

[23] K. Smith and C.-Y. Wang, *Solid-state diffusion limitations on pulse operation of a lithium ion cell for hybrid electric vehicles,* Journal of Power Sources **161**, 628 (2006).

[24] H. J. Bergveld, W. S. Kruijt, and P. H. L. Notten, *Battery Management Systems: Design by Modeling* (Kluwer Academic publishers, 2002).

[25] A. P. Schmidt, M. Bitzer, r. W. Imre, and L. Guzzella, *Experiment-driven electrochemical modeling and systematic parameterization for a lithium-ion battery cell,* Journal of Power Sources **195**, 5071 (2010).

[26] H. Pang, L. Mou, L. Guo, and F. Zhang, *Parameter identification and systematic validation of an enhanced single-particle model with aging degradation physics for Li-ion batteries,* Electrochimica Acta **307**, 474 (2019).

[27] A. M. Bizeray, J. Kim, S. R. Duncan, and D. A. Howey, *Identifiability and Parameter Estimation of the Single Particle Lithium-Ion Battery Model,* IEEE Transactions on Control Systems Technology **27**, 1862 (2019).

[28] P. Arora, M. Doyle, A. S. Gozdz, R. E. White, and J. Newman, *Comparison between computer simulations and experimental data for high-rate discharges of plastic lithium-ion batteries,* Journal of Power Sources **88**, 219 (2000).

[29] P. Ramadass, B. Haran, P. M. Gomadam, R. White, and B. N. Popov, *Development of First Principles Capacity Fade Model for Li-Ion Cells,* Journal of the Electrochemical Society **151**, A196 (2004).

[30] S. V. Erhard, P. J. Osswald, P. Keil, E. Höffer, M. Haug, A. Noel, J. Wilhelm, B. Rieger, K. Schmidt, S. Kosch, F. M. Kindermann, F. Spingler, H. Kloust, T. Thoennessen, A. Rheinfeld, and A. Jossen, *Simulation and Measurement of the Current Density Distribution in Lithium-Ion Batteries by a Multi-Tab Cell Approach,* Journal of The Electrochemical Society **164**, A6324 (2017).

[31] M. Doyle and Y. Fuentes, *Computer Simulations of a Lithium-Ion Polymer Battery and Implications for Higher Capacity Next-Generation Battery Designs,* Journal of the Electrochemical Society **150**, A706 (2003).

[32] J. N. Reimers, M. Shoesmith, Y. S. Lin, and L. O. Valoen, *Simulating High Current Discharges of Power Optimized Li-Ion Cells,* Journal of the Electrochemical Society **160**, A1870 (2013).

[33] H. P. G. J. Beelen, H. J. Bergveld, and M. C. F. Donkers, *On Experiment Design for Parameter Estimation of Equivalent-Circuit Battery Models,* in *IEEE Conference on Control Technology and Applications* (2018) pp. 1526–1531.

[34] J. Sturm, S. Ludwig, J. Zwirner, C. Ramirez-Garcia, B. Heinrich, M. F. Horsche, and A. Jossen, *Suitability of physicochemical models for embedded systems regarding a nickel-rich, silicon-graphite lithium-ion battery,* Journal of Power Sources **436**, 226834 (2019).

[35] J. Sturm, A. Frank, A. Rheinfeld, S. V. Erhard, and A. Jossen, *Impact of Electrode and Cell Design on Fast Charging Capabilities of Cylindrical Lithium-Ion Batteries,* Journal of the Electrochemical Society **167**, 130505 (2020).

[36] B. Suthar, P. W. C. Northrop, R. D. Braatz, and V. R. Subramanian, *Optimal Charging Profiles with Minimal Intercalation-Induced Stresses for Lithium-Ion Batteries Using Reformulated Pseudo 2-Dimensional Models,* Journal of the Electrochemical Society **161**, F3144 (2014).

[37] R. Klein, N. A. Chaturvedi, J. Christensen, J. Ahmed, R. Findeisen, and A. Kojic, *Optimal charging strategies in lithium-ion battery,* in *IEEE American Control Conference* (2011) pp. 382–387.

[38] H. E. Perez, X. Hu, and S. J. Moura, *Optimal charging of batteries via a single particle model with electrolyte and thermal dynamics,* in *IEEE American Control Conference* (2016) pp. 4000–4005.

Part II

Aging-Aware Charging

4

Doyle-Fuller-Newman Model with Capacity-Loss Side Reactions for Aging-Aware Charging

In this chapter, we utilize a Doyle-Fuller-Newman (DFN) model including capacity-loss side reactions to present a model-based design method for multi-stage charging protocols. This design method allows for making a trade-off between charging time and battery aging in a more systematic way. The results are leveraged by a highly efficient implementation of the DFN model, that has a short computation time. We show that by obtaining the Pareto front that describes the optimal trade-off between charging time and battery aging for a single cycle, the results can be extended to the lifetime of the battery. Finally, we show that the negative-electrode over-potential is not always a good indicator for aging, and that aging will occur even when the battery operates in over-potential regions that are considered not to lead to aging.

This chapter is based on Publication **P.4**.

4.1. INTRODUCTION

As mentioned in the introduction of this thesis, lithium-ion batteries are commonly charged using a so-called constant-current-constant-voltage (CC-CV) protocol, see e.g., [1], where the battery is initially charged at a set constant current, followed by a phase where the battery is kept at a constant voltage, until the current drops below a certain value. This current limit and voltage limit are determined by a trade-off between a short charging time and long cycle life. Indeed, besides the main chemical reactions, i.e., the ones that store energy in the battery, several side reactions occur that eventually lead to capacity fade and power fade [2]. Shortening the charging times without affecting the longevity of the battery is of interest, particularly for electric vehicles, where the relatively long charging times (when compared to refueling time of a conventional vehicle) are considered to be problematic.

Optimizing the charging protocol to achieve short charging times and limited aging has received ample attention in both the electrochemical as well as the control-systems literature. A traditional approach has been to improve on the CC-CV protocol by introducing additional CC or CV stages, e.g., the CV-CC-CV protocol [3], or the CC-CC-CV protocol [4]. However, the selection of current and voltage limits is not trivial. To find the limits that provide a good trade-off between battery aging and charging time, many experiments need to be performed, see e.g., [5–7].

A more recent trend lies in the use of model-based control to systematically make the trade-off between battery aging and charging time. The models used in these papers can vary from empirical models, such as the so-called equivalent-hydraulic model [8] or equivalent-circuit model (ECM) [9] to electrochemistry-based models that describe the main electrochemical reactions (i.e., the reactions that leads to storing energy) such as the Doyle-Fuller-Newman (DFN) model [10], e.g. in [11–13] or the single-particle model (SPM) [14], e.g. in [15, 16]. However, since these models do not describe the aging of the battery, these papers rely on estimated states obtained through battery models, and define regions based on these states that should be avoided in order not to promote excessive aging. These regions are incorporated as constraints in the optimization problem, and show the potential of model-based control for aging-aware charging.

Of course, aging can never be prevented and the transition between excessive and non-excessive aging is not necessarily a sharp transition. Therefore, alongside this approach, there has been attention into incorporating aging models into the optimization problem. These aging models can be empirical as done in, e.g. [17], which are used in conjunction with ECMs, or they can be electrochemical, such as the side-reaction model introduced in [18, 19], which are incorporated into the DFN model. Some results using such side-reaction models exist in literature, e.g. [20], which uses external toolboxes such as CasADi [21] for simulation. However, the use of such toolboxes does not necessarily provide for a computationally efficient model, which restricts the prediction horizon in the model-predictive control (MPC) approach taken in [20].

In this chapter, we present a model-based design method for multi-stage charging protocols, where this leads to a trade-off between charging times and aging. The results are leveraged by the highly efficient implementation of the DFN model presented in Chapter 2. This highly efficient model has low computation times, which allows this model to be used in model-based optimization methods. To investigate the use of this

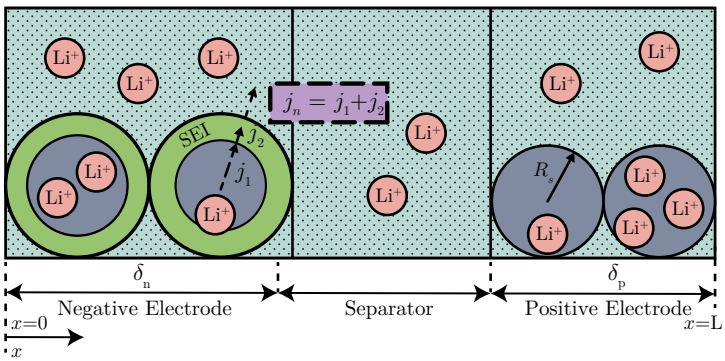

Figure 4.1: DFN modeling approach for a Li-ion cell.

model for aging-aware charging, in this chapter, we will focus on multi-stage charging protocols. Extensions to full model-based charging can be done based on the model implementation presented in this chapter, and will be presented in the next chapters of this thesis. Finally, we will show that the negative-electrode over-potential is not always a good indicator for aging, and that an effective trade-off between charging time and aging cannot be made by merely setting constraints on this over-potential.

The remainder of this chapter is as follows. In Section 4.2, the DFN model, and the aging model are introduced. Furthermore, in Section 4.2, the implementation of this aforementioned model is shortly described. In Section 4.3, the aging-aware charging protocol design will be discussed. Finally, conclusions are drawn in Section 4.4.

4.2. BATTERY MODELING

In this section, we briefly formulate the DFN model, including the modeling of capacity-loss side reactions. The model represents the side reactions, in which Li-ions are consumed to form a so-called solid-electrolyte interface (SEI) layer at the negative electrode [18]. Furthermore, we will formulate the equations that describe the aging model, which is used to compute the capacity of an aged cell. Finally, we will briefly describe a computationally efficient implementation of the DFN model considering this side reaction, which is based on the approach taken in Chapter 2 of this thesis.

4.2.1. DOYLE-FULLER-NEWMAN MODEL WITH CAPACITY-LOSS SIDE REACTIONS

In this chapter, the DFN model will again be considered, and will be extended with a side-reaction model, where this modeling approach is illustrated in Fig. 4.1. In the considered side-reaction model [18], the particles in the negative electrode have an SEI layer, which is formed at the first charge of the battery. During the operation of the cell over its lifetime, side reactions consume Li-ions which leads to a continuous growth of the SEI. This consumption of Li-ions leads to capacity fade of the cell, while the build-up of the SEI layer leads to power fade of the cell. In Table 4.1, we have shortly summarized the governing equations of the DFN model considering side reactions. The formulation of

Table 4.1: Equations of the DFN model with capacity-loss side reactions

Solid-phase Li-ion concentration	$\frac{\partial c_s}{\partial t} = \frac{D_s}{r^2}\frac{\partial}{\partial r}(r^2\frac{\partial c_s}{\partial r})$	(4.1a)
Boundary Condition	$\frac{\partial c_s}{\partial r}\|_{r=0}=0,\ -D_s\frac{\partial c_s}{\partial r}\|_{r=R_s}=j_1$	(4.1b)
Electrolyte-phase Li-ion concentration	$\varepsilon_e\frac{\partial c_e}{\partial t} = \frac{\partial}{\partial x}(D_e\varepsilon_e^p\frac{\partial c_e}{\partial x}) + \frac{3\varepsilon_s(1-t_+^0)}{R_s}j_n$	(4.2a)
Boundary condition	$\frac{\partial c_e}{\partial x}\|_{x=0} = \frac{\partial c_e}{\partial x}\|_{x=L} = 0$	(4.2b)
Solid-phase potential	$\frac{\partial}{\partial x}(\sigma\varepsilon_s\frac{\partial \phi_s}{\partial x}) = \frac{3\varepsilon_s F}{R_s}j_n$	(4.3a)
Boundary condition	$\sigma\varepsilon_s\frac{\partial \phi_s}{\partial x}\|_{x=0} = \sigma\varepsilon_s\frac{\partial \phi_s}{\partial x}\|_{x=L} = \frac{I_a}{A}$	(4.3b)
	$\frac{\partial \phi_s}{\partial x}\|_{x=\delta_n} = \frac{\partial \phi_s}{\partial x}\|_{x=L-\delta_p} = 0$	(4.3c)
Electrolyte-phase potential	$\frac{\partial}{\partial x}\left(\kappa\varepsilon_e^p\frac{\partial \phi_e}{\partial x} + \kappa\varepsilon_e^p(t_+^0\text{-}1)\frac{2RT}{F}\frac{\partial \ln c_e}{\partial x}\right) = -\frac{3\varepsilon_s F}{R_s}j_n$	(4.4a)
Boundary condition	$\frac{\partial \phi_e}{\partial x}\|_{x=0} = \phi_e\|_{x=L} = 0$	(4.4b)
Net reaction flux	$j_n = j_1 + j_2$	(4.5)
Main reaction flux	$j_1 = \frac{i_{0,1}}{F}\left(\exp\left(\frac{\alpha_a F}{RT}\eta_1\right) - \exp\left(-\frac{\alpha_c F}{RT}\eta_1\right)\right)$	(4.6a)
Exchange current density	$i_{0,1} = k_0 c_e^{\alpha_a}(c_s^{\max} - c_{s,e})^{\alpha_a} c_{s,e}^{\alpha_c}$	(4.6b)
Particle surface concentration	$c_{s,e}(x,t) = c_s(R_s,x,t)$	(4.6c)
Electrode over-potential	$\eta_1 = \phi_s - \phi_e - U - FR_f j_n$	(4.6d)
Side reaction flux	$j_2 = -\frac{i_{0,2}}{F}\exp\left(-\frac{2\alpha_{c,2}F}{RT}\eta_2\right)$	(4.7a)
Electrode over-potential	$\eta_2 = \phi_s - \phi_e - U_2 - FR_f j_n$	(4.7b)
Terminal voltage	$V(t) = \phi_s(L,t) - \phi_s(0,t) + \frac{R_{cc}}{A}I_a(t)$	(4.8)

the DFN model is mostly based on the formulation given in Chapter 2, and the references therein, while the side-reactions model is based on [18]. For compactness of notation, where possible, the time and space dependency of the variables have been left out of the equations. While the symbols used in Table 4.1 are mostly the same as those introduced in the previous chapters, for the sake of convenience, all the symbols used in Table 4.1 have been summarized in Table 4.2. Note that U in (4.6d) denotes the equilibrium potential of the electrode, which is a a pre-defined function that typically depends on the solid-phase concentration at the solid-electrolyte interface ($c_{s,e}(x,t) = c_s(R_s,x,t)$). Further note that $I_a > 0$ indicates charging.

From Table 4.1, we can see a few key differences as a result of the addition of the side-reaction model to the DFN model. Firstly, in (4.1b), in contrast to (3.1b) we can see

Table 4.2: List of symbols used in the DFN model with capacity-loss side reactions

Symbol	Description	Unit
Latin		
A	Active electrode area	[m^2]
c_e	Electrolyte-phase Li-ion concentration	[mol/m^3]
$c_{e,a}$	Average electrolyte concentration	[mol/m^3]
c_s	Solid-phase Li-ion concentration	[mol/m^3]
$c_{s,e}$	Particle surface concentration	[mol/m^3]
$c_s^{\max}$	Maximum solid-phase concentration	[mol/m^3]
D_e	Li-ion diffusion coefficient in electrolyte	[m^2]
D_s	Solid-phase Li-ion diffusion coefficient	[m/s]
F	Faraday's constant	[C/mol]
$i_{0,1}$	Exchange current density of the main reaction	[A/m^2]
$i_{0,2}$	Exchange current density of the side reaction	[A/m^2]
I_a	Applied current	[A]
j_1	Main reaction flux	[$mol/m^2/s$]
j_2	Side reaction flux	[$mol/m^2/s$]
j_n	Net reaction flux	[$mol/m^2/s$]
k_0	Kinetic constant	*
L	Cell thickness	[m]
p	Bruggeman porosity exponent	[−]
r	Radial position across a spherical particle	[m]
R	Universal gas constant	[J/mol/K]
R_{cc}	Current-collector contact resistance	[Ωm^2]
R_f	Particle surface film resistance	[Ωm^2]
R_s	Radius of active material particles	[m]
t	Time	[s]
t_+^0	Transference number	[−]
U	Electrode equilibrium potential	[V]
U_2	Equilibrium potential of the side reaction	[V]
V	Terminal voltage	[V]
x	Position across cell	[m]
Greek		
α_a	Anodic charge-transfer coefficient	[−]
α_c	Cathodic charge-transfer coefficient	[−]
$\alpha_{c,2}$	Cathodic charge-transfer coefficient of the side reaction	[−]
δ_n	Negative electrode thickness	[m]
δ_p	Positive electrode thickness	[m]
ε_e	Electrolyte volume fraction	[−]
ε_s	Active-particles volume fraction	[−]
η	Electrode over-potential	[V]
κ	Ionic conductivity	[S/m]
σ	Electrical conductivity	[S/m]
ϕ_e	Electrolyte-phase potential	[V]
ϕ_s	Solid-phase potential	[V]

* [C/s · (m/mol)^(1 + 3α_c)]

that the boundary condition of the solid-phase Li-ion concentration equation is only changed by the main reaction flux j_1, since we no longer assume that there are no side reactions, as we had done implicitly in Chapter 2 and Chapter 3. Secondly, in contrast to Table 4.1, we can observe the addition of the equation describing the side-reaction flux by a Tafel equation in (4.8), in which the exchange current density of the side reaction $i_{0,2}$ is assumed to be a constant. Note that we consider only SEI build-up in the negative

electrode, and therefore in the separator and in the positive electrode $j_2 = 0$.

4.2.2. AGING MODEL

In the considered aging model, power fade is described by an increase of the negative-electrode film resistance, due to the build-up of the SEI layer, as follows

$$\frac{\partial R_f}{\partial t} = -\frac{\tilde{V}_f}{\sigma_f} j_2, \tag{4.9}$$

with initial condition $R_f(x,0) = R_{f,0}$, and where $\tilde{V}_f$ is the molar volume and σ_f is the conductivity of the SEI. The amount of charge lost due to loss of Li-ions as a result of side reactions can be computed as [18]

$$\frac{dQ_l}{dt} = -a_s AF \int_0^{\delta_n} j_2 dx. \tag{4.10}$$

The Li-ion loss does not directly result into loss of battery capacity [19]. To see this, it should be noted that the total amount of charge stored in a fresh cell is given by

$$Q_{\text{tot}} = s_{n,\max}\gamma_n + s_{p,\min}\gamma_p = s_{n,\min}\gamma_n + s_{p,\max}\gamma_p, \tag{4.11a}$$

where $\gamma_i = \varepsilon_{s,i}\delta_i c_{\text{s,i}}^{\max} AF$, for $i \in \{n,p\}$, where n and p denote the values of the parameters at the negative and postive electrode, respectively. Furthermore, s_n and s_p denote the stoichiometric values at the negative and positive electrode, respectively, while the subscripts min and max indicate the minimum and maximum values of s_n and s_p, respectively, for a fresh cell. The stoichiometric values at 0% and 100% state of charge (SoC) for an aged battery must satisfy

$$\begin{aligned} s_{n,0\%}\gamma_n + s_{p,0\%}\gamma_p &= Q_{\text{tot}} - Q_l, \\ s_{n,100\%}\gamma_n + s_{p,100\%}\gamma_p &= Q_{\text{tot}} - Q_l. \end{aligned} \tag{4.11b}$$

Note that for a fresh cell, $s_{n,0\%}$, $s_{n,100\%}$, $s_{p,0\%}$, $s_{p,100\%}$ correspond to $s_{n,\min}, s_{n,\max}, s_{p,\max}, s_{p,\min}$, respectively. Furthermore, since 0% SoC and 100% SoC are defined at specified voltages, the equilibrium potentials must satisfy

$$\begin{aligned} U_p(s_{p,0\%}) - U_n(s_{n,0\%}) &= V_{\min}, \\ U_p(s_{p,100\%}) - U_n(s_{n,100\%}) &= V_{\max}, \end{aligned} \tag{4.11c}$$

where $V_{\max} = U_p(s_{p,\min}) - U_n(s_{n,\max})$, and $V_{\min} = U_p(s_{p,\max}) - U_n(s_{n,\min})$. By solving (4.11) , solutions for $s_{n,0\%}$, $s_{n,100\%}$, $s_{p,0\%}$, and $s_{p,100\%}$ are obtained. These solutions can be used to compute the degraded capacity of the cell Q_{bat}, i.e.,

$$Q_{\text{bat}} = (s_{n,100\%} - s_{n,0\%})\gamma_n = (s_{p,0\%} - s_{p,100\%})\gamma_p. \tag{4.12}$$

How the aging reaction affects the battery capacity is illustrated in Fig. 4.2a. In this figure, it can be seen that for an aged cell, the charge in the positive and negative electrodes decreases as Li-ions are lost, which leads to a decrease in battery capacity. The capacity drop of the battery, however, is not necessarily equal to the amount of Li-ions consumed by the side reaction, as the side reaction also leads to a shift in the equilibrium potential of the electrodes, as also illustrated in Fig. 4.2b.

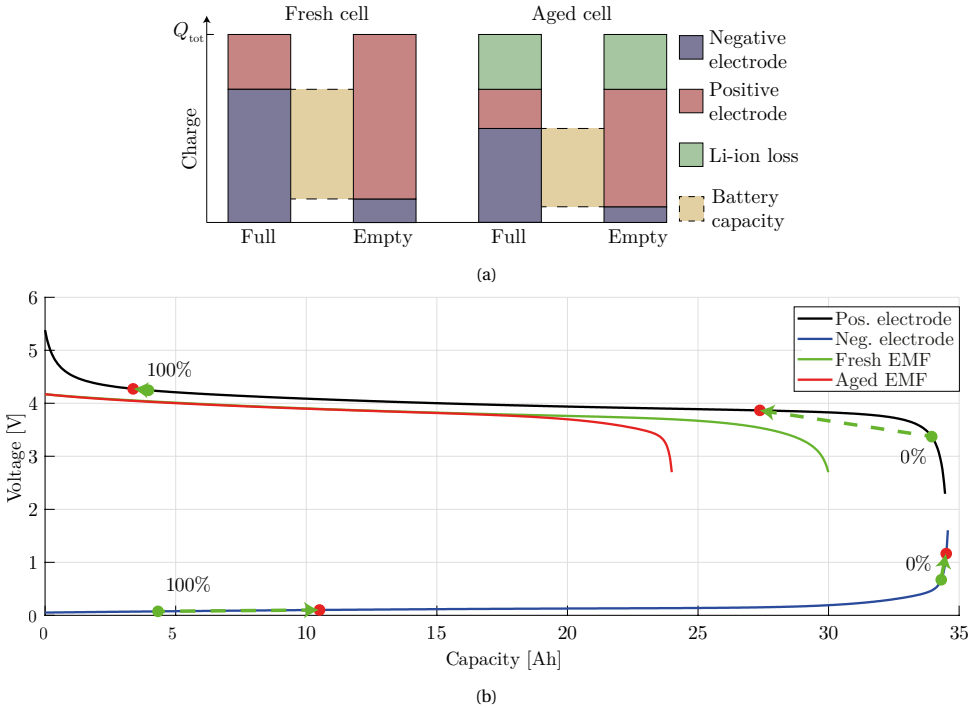

Figure 4.2: In (a), a schematic representation of the aging model is shown. In (b), a schematic representation of the shifting of the equilibrium potential of the electrodes due to Li-ion loss is shown. The green dots represent the fresh cell stoichiometric values and the red dots represent the resulting stoichiometric values of an aged cell. The green arrows show how the stoichiometric values shift.

4.2.3. MODEL IMPLEMENTATION

The implementation of the DFN model described by (4.1a)-(4.8) is largely the same approach as taken in Chapter 2. After spatial and temporal discretization of the model, the resulting set of algebraic equations (AEs) can be reduced to a much smaller set of AEs through substitution of equations, which can then be solved using Newton's method. However, since the above model considers side reactions, we will shortly summarize the implementation of the DFN model. For further details on the discretization of the model, we refer the reader to [22], and for further details on the implementation approach we refer the reader to Chapter 2 of this thesis.

First, after spatial and temporal discretization, the DFN model equations can be written in the form

$$0 = \hat{A}_{c_s}\mathbf{c}_s(t_k) + \hat{B}_{c_s}\mathbf{j}_1(t_k) + \mathbf{c}_s(t_{k-1}), \tag{4.13a}$$

$$0 = \hat{A}_{c_e}\mathbf{c}_e(t_k) + \hat{B}_{c_e}\mathbf{j}_n(t_k) + \mathbf{c}_e(t_{k-1}), \tag{4.13b}$$

$$0 = A_{\phi_s}\boldsymbol{\phi}_s(t_k) + B_{\phi_s}\mathbf{j}_n(t_k) + C_{\phi_s}I_a(t_k), \tag{4.13c}$$

$$0 = A_{\phi_e}\boldsymbol{\phi}_e(t_k) + B_{\phi_e}\mathbf{j}_n(t_k) + D_{\phi_e}\log(\mathbf{c}_e(t_k)), \tag{4.13d}$$

where $t_k \in \delta_t k, k \in \mathbb{N}$ is the sample time, in which δ_t is the sampling time. Furthermore,

$\hat{A}_{c_s} = (\delta_t A_{c_s} - \mathbf{I}_{n_r n_{np}})$, $\hat{B}_{c_s} = \delta_t B_{c_s}$, $\hat{A}_{c_e} = (\delta_t A_{c_e} - \mathbf{I}_{n_x})$, and $\hat{B}_{c_e} = \delta_t B_{c_e}$. In (4.13), $\mathbf{j}_n(t_k) = \mathbf{j}_1(t_k) + \mathbf{j}_2(t_k)$, where $\mathbf{j}_1(t_k)$ and $\mathbf{j}_2(t_k)$ are given by

$$\mathbf{j}_1 = \text{diag}\left(\frac{\mathbf{i}_{0,1}}{F}\right)\left(\exp\left(\frac{\alpha_a F}{RT}\boldsymbol{\eta}_1\right) - \exp\left(-\frac{\alpha_c F}{RT}\boldsymbol{\eta}_1\right)\right), \tag{4.14}$$

in which $\text{diag}(v)$ denotes a diagonal matrix with the elements of vector v on the main diagonal, and $\mathbf{i}_{0,1}$ is given by

$$\mathbf{i}_{0,1} = \mathbf{k}_0 \mathbf{c}_e^{\alpha_a}\left(\mathbf{c}_s^{\max} - \bar{\mathbf{c}}_s\right)^{\alpha_a} \bar{\mathbf{c}}_s^{\alpha_c}. \tag{4.15}$$

Furthermore, in (4.14), $\boldsymbol{\eta}_1 = \boldsymbol{\phi}_s - \bar{\boldsymbol{\phi}}_e - \mathbf{U}(\bar{\mathbf{c}}_s) - F\mathbf{R}_f \mathbf{j}_n$, and

$$\mathbf{j}_2 = -\text{diag}\left(\frac{i_{0,2}}{F}\right)\left(\exp\left(-\frac{2\alpha_{c,2} F}{RT}\boldsymbol{\eta}_2\right)\right), \tag{4.16}$$

where $\boldsymbol{\eta}_2 = \boldsymbol{\phi}_s - \bar{\boldsymbol{\phi}}_e - U_2 - F\mathbf{R}_f \mathbf{j}_n$. Note that R_f given by (4.9) varies through space and time. However, since the dynamics of R_f are very slow, for computational efficiency, it can be pseudo-linearized such that

$$\mathbf{R}_f(x, t_k) = \mathbf{R}_f(x, t_{k-1}) - \delta_t \frac{\tilde{V}_f}{\sigma_f} j_2(t_{k-1}), \tag{4.17}$$

To solve this set of AEs, similar to as done in Chapter 2, we can solve (4.13c) for $\mathbf{j}_n$, to get

$$\mathbf{j}_n(t_k) = -B_{\phi_s}^{-1}\left(A_{\phi_s}\boldsymbol{\phi}_s(t_k) + C_{\phi_s} I_a(t_k)\right). \tag{4.18}$$

Then, by substituting (4.14) and (4.16) into (4.13a), (4.13b), (4.13d), and solving each of the equations (4.13a), (4.13b), (4.13d) for $\mathbf{c}_s$, $\mathbf{c}_e$, $\boldsymbol{\phi}_e$, respectively, the resulting equations can be substituted into (4.18), to arrive at a set of AEs of the form $\mathscr{F}(\boldsymbol{\phi}_s) = 0$. This resulting set of AEs can then be solved using Newton's method.

4.3. AGING-AWARE CHARGING PROTOCOL DESIGN

In this section, we will study the impact of several charging strategies on battery aging. First, we will study aging over a single cycle, to determine the Pareto optimal set of parameters of several charging strategies that lead to the ideal trade-off that can be made between charging time and battery aging. Then, we will study aging over a long period, by simulating the Pareto optimal set of parameters over the lifetime of the battery. Finally, we investigate the use of over-potential information to limit battery aging. The parameters of the main-reaction model (including the electrode equilibrium-potential expressions) are taken from [21], which are based on a battery with a LiC_6 negative electrode and $LiCoO_2$ positive electrode chemistry. Note that this set of parameters represents a high-energy cell, for which it is generally known that the minimum charging time that can be achieved is generally higher than for a high-power cell. The parameters of the side-reaction model have been selected such that a somewhat realistic amount of aging is observed, i.e., 80% of the capacity is left after around 600 charge-discharge cycles. These side-reaction model parameters have been listed in Table 4.3.

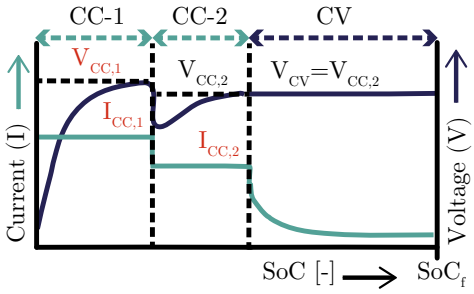

Figure 4.3: The 2-CC-CV(3) protocol shown as an example of a multi-stage charging protocol used for simulation. The red-colored variables indicate the design-adjustable parameters.

4.3.1. CHARGING PROTOCOLS

The simulation studies have been done using a CC-CV (Constant-Current-Constant-Voltage) charging protocol and several multi-stage charging protocols. Note that for the remainder of this chapter the following notation will be used to indicate the multi-stage charging protocols: N-CC-CV(D), where N denotes the number of CC stages, and D denotes the amount of design-adjustable variables. As an example of a multi-stage charging protocol, the 2-CC-CV(3) charging protocol is shown in Fig. 4.3. In this protocol, the battery is first charged with a constant current $I_{\text{CC},1}$ until a voltage $V_{\text{CC},1}$ is reached. Then, the battery is charged with a constant current $I_{\text{CC},2}$ until the next voltage limit $V_{\text{CC},2}$ is reached. Finally, a CV stage follows where the battery is kept at a constant voltage V_{CV} until a final state of charge SoC_f is reached. For this protocol there are three design-adjustable parameters, namely $I_{\text{CC},1}$, $I_{\text{CC},2}$, and $V_{\text{CC},1}$. The value for $V_{\text{CC},2} = V_{\text{CV}}$ is chosen as $V_{\max}$ in (4.11c) for a fresh cell, and SoC_f is fixed to $\text{SoC}_f = 95\%$. Note that, for the remainder of the chapter, we constrain $V_{\text{CV}} = V_{\text{CC},n}$, where n indicates the last CC stage. Further note that we use SoC to terminate the charging algorithm to ensure a fair comparison between different charging profiles, while in practice generally the CV stage is terminated when the current drops below a certain value $I_{\min}$. The CC-CV charging protocol is defined in a similar way, except that there is only one CC stage, and therefore the only design-adjustable parameter is $I_{\text{CC},1}$. Other charging strategies that are considered in this chapter are the CC-CV(2), 2-CC-CV(2), and 3-CC-CV(3). For CC-CV(2), the design-adjustable parameters are the CC current $I_{\text{CC},1}$ and the CV voltage V_{CV}. For 2-CC-CV(2), the design adjustable parameters are CC currents $I_{\text{CC},1}$ and $I_{\text{CC},2}$. Finally, for 3-CC-CV(3), the design-adjustable parameters are CC currents $I_{\text{CC},1}$, $I_{\text{CC},2}$, and $I_{\text{CC},3}$.

Table 4.3: Parameters for the side-reaction model. Parameters U_2 and σ_f have been extracted from [19].

Symbol	Unit	Value
$i_{0,2}$	[Am^{-2}]	1.178×10^{-7}
U_2	[V]	0.21
$\tilde{V}_f$	[$\text{m}^3\text{mol}^{-1}$]	1×10^{-5}
σ_f	[$\Omega^{-1}\text{m}^{-1}$]	2.3×10^{-6}
$R_{f,0}$	[Ωm^2]	5.5×10^{-3}

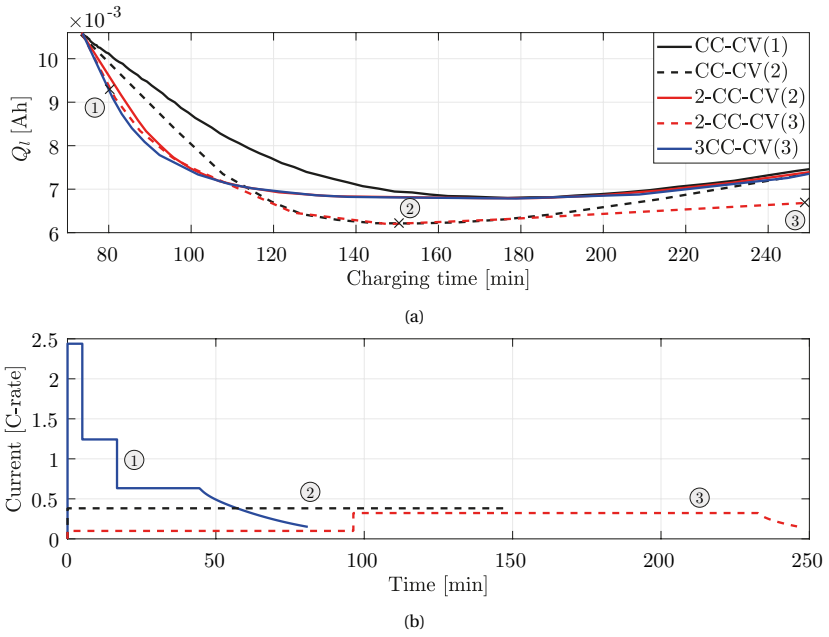

Figure 4.4: In (a), a comparison of degradation vs charging time of several charging protocols is shown. In (b), selected current profiles at several points on (a) are shown.

Note that in the case of 2-CC-CV(2) and 3-CC-CV(3), the voltage limits, e.g. $V_{\mathrm{CC},1}$, are fixed as $V_{\max}$.

4.3.2. PARETO OPTIMAL FRONT FOR A SINGLE CYCLE

In Fig. 4.4a, the degradation of the cell, in terms of Li-ions lost, i.e., Q_l, is plotted against charging time, for the CC-CV and multi-stage charging protocols. In order to obtain these results, the design-adjustable parameters for the charging protocols have been varied over a range of values. Specifically, the CC-stage currents have been varied in the range of 0.1 C to 2.5 C, and the voltage limits have been varied in the range of 3.7 V to 4.4 V, and in the case of CC-CV(2), V_{CV} has been varied in the range of 4.125 V to 4.4 V. The curves in Fig. 4.4 are then obtained by taking the minimal degradation for a given charging time, for each charging protocol. Note that for the CC-CV protocol, since there is only 1 design-adjustable parameter, all the simulated points have by definition the minimal degradation for a given charging time. Note that, as an example, the trade-off curve for the 3-CC-CV(3) was constructed using 8000 charge-cycle simulations, while the other trade-off curves have been constructed using fewer simulations. As each charge cycle takes about 1 second to compute (on average) using the model implemented presented in this chapter, even the trade-off curve for the 3-CC-CV(3) protocol can be computed within 2.5 hours, which shows the potential of the presented implementation for (off-line) model-based optimization.

In Fig. 4.4a, we can first observe that the degradation of the multi-stage protocols

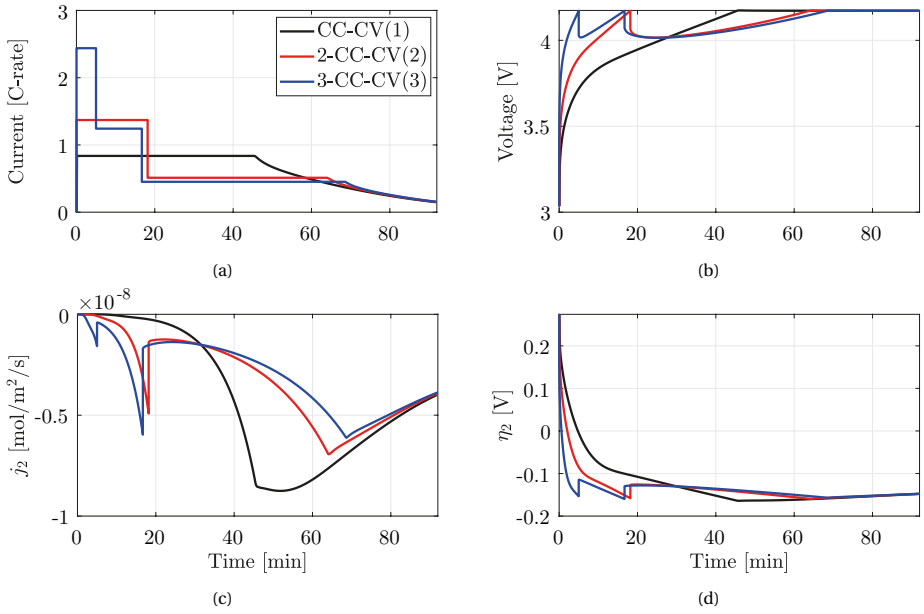

Figure 4.5: Comparison of the CC-CV(1), 2-CC-CV(2), and 3-CC-CV(3) charging protocols at a specified charging time of 92 minutes, where in (a) the current, (b) the voltage, (c) the side-reaction flux j_2, and (d) the side-reaction over-potential η_2 is shown.

is always equal to or less than the degradation using the CC-CV protocol. This is to be expected, since multi-stage protocols are a generalization of the CC-CV protocol. Furthermore, we see that up to around 170 min charging time, the curves follow an intuitive trend, where the battery degradation becomes smaller as charging time increases. However, after around 170 min charging time, the opposite trend happens, where battery degradation increases with increasing charging time. This can be explained by the fact that the degradation is computed through an integral over time. Therefore, as charging time increases, the integral is taken over a longer time, leading to higher degradation.

Another interesting observation is that a larger amount of CC-stages seems to give better performance at lower charging times, until around 115 minutes, while the charging protocols that provide more flexibility in the adjustment of the voltage limits, i.e., CC-CV(2) and 2-CC-CV(3), give better performance at higher charging times. This can be explained by investigating the current profiles shown in Fig. 4.4b. Here, we see that at the lower charging times (point 1), the flexibility in CC-stage currents allows to maximize the effect that the side-reaction over-potential η_2 is smaller at lower voltages. This effect can be seen in Fig. 4.5, where the CC-CV(1), 2-CC-CV(2), and 3-CC-CV(3) charging protocols are compared at a charging time of 92 minutes. When we observe the side-reaction over-potential $\eta_2 = \phi_s - \phi_e - U_2 - FR_f j_n$, we can see that, generally η_2 is smaller at lower voltages than at higher voltages, for the same current. This is especially visible with the 3-CC-CV-(3) protocol, where we can see that at around 5 minutes and 18 minutes, the peaks in η_2 are approximately equal, even though the current at 5 minutes is

around twice as large as at 18 minutes. This then also results in a comparatively lower side-reaction flux j_2 at lower voltages than at higher voltages, and in turn comparatively less Li-ion loss. Thus, by charging the battery more at lower voltages, less charge needs to be put in at higher voltages, which explains why additional flexibility of the multi-stage protocols leads to a lower Li-ion loss for the same charging time.

The better performance of the algorithms with more flexibility in selecting the voltage levels at higher charging times in Fig. 4.4a, can be explained by observing the current shown in Fig. 4.4b at point 2. Here, we see that the battery is simply charged with a constant current rate until the desired SoC of 95% is reached. The CC-CV(2) and 2-CC-CV-(3) protocols allow this, since the voltage limit can be chosen sufficiently high such that it is never reached until the battery is full. Note that the CV stage in general takes a significant amount of time when charging, which explains why charging in CC stages as long as possible is effective.

Finally, if we observe point 3 (the dashed-red line) in Fig. 4.4b, we can see that at high charging times, the best strategy to minimize degradation is to start with a low charging current, followed by a larger charging current. This seems counter-intuitive to what was observed in point 1 (the solid blue line). This can be explained by the fact that, because η_2 is smaller at lower battery voltages than at higher battery voltages, as explained above, it also means that the battery generally ages more at higher battery voltages. Therefore, when the battery is to be charged over a large duration of time, it is not beneficial to charge the battery quickly, only for it to remain at rest at full charge, and consequently a high voltage, for the remaining duration of time. Instead, the battery should ideally remain at rest until the point where the remaining amount of time corresponds to the point on the Pareto curve where the battery can be charged with the least amount of aging. For example, for the CC-CV(2) and 2-CC-CV(3) protocol, this point corresponds to a charging time of about 150 minutes, as we can observe in Fig. 4.4a. This corresponds to what can be observed at point 3 in Fig. 4.4b, where the battery is charged with the lowest possible current, until about 150 minutes charging time remains, after which the battery is essentially charged using the CC-CV(2) protocol.

4.3.3. LIFETIME DEGRADATION

In Fig. 4.6a, the battery cycle life is plotted against the average charging time during the course of the lifetime of the cell. This result has been obtained by taking the Pareto optimal combinations found in Fig. 4.4, and simulating for each of these combinations over the lifetime of cell, i.e., when the capacity of the battery reaches 80% of the initial capacity. However, rather than performing a single continuous simulation, the simulations have been done for each cycle separately. Here, the stoichiometric values at 0% and 100% are computed and updated at each cycle using (4.11). This is mainly done for the reason that the difference in scale between j_1 and j_2 causes numerical inaccuracies which add up over the lifetime of the cell. Note that the results in Fig. 4.4 have been obtained using only charge cycles, while the results shown in Fig. 4.6 have been obtained from discharge-charge cycles in order to represent actual use of the battery. The discharge cycle occurs at a rate of -0.1 C, until a lower voltage limit $V_{\min}$, computed from (4.11c), is reached, after which the battery is charged.

As could be expected, the multi-stage charging protocols perform better than the CC-

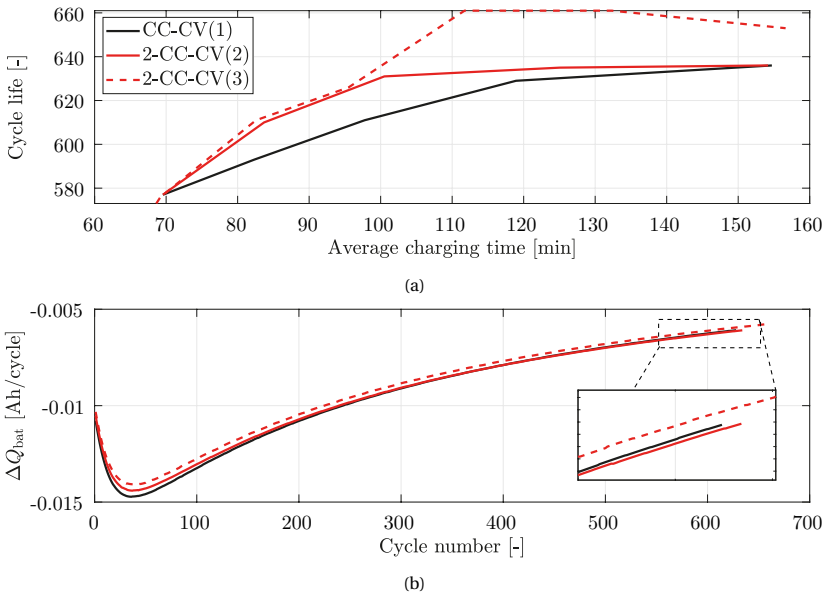

Figure 4.6: In (a), cycle life vs average charging time for several charging protocols is shown. In (b), the differential capacity loss ΔQ_{bat} is shown. The crosses in (a) indicate at which charging time the curves in (b) are evaluated for.

CV(1) protocol. Furthermore, the trends observed in Fig. 4.4a are still visible, in which the performance of the 2-CC-CV(2) and 2-CC-CV(3) are almost equal up to around 100 minutes charging time, and the performance of the 2-CC-CV(3) protocol is much better than the 2-CC-CV(2) after around 100 minutes charging time. Therefore, we can conclude that the trends observed over a single cycle can be roughly extrapolated over the lifetime of the cell.

However, while the trends at the end-of-life of the cell are conserved, this is not necessarily true over the whole lifetime of the cell. In Fig. 4.6b, the differential capacity loss ΔQ_{bat} of the considered charging protocols at a charging time of around 130 minutes is shown over the lifetime of the cell. We can observe that the difference in differential capacity loss between the charging protocols varies over the lifetime of the cell. Until around 50 cycles, this difference gets larger, while after 50 cycles the difference becomes smaller. In the case of the difference between the CC-CV(1) and 2-CC-CV(2) protocol, after 250 cycles, this difference becomes visually indiscernible. This could suggest that when the battery ages, there is less to gain when choosing different charging strategies. However, if we observe the zoomed-in plot in Fig. 4.6b, we can also see that at some point, the 2-CC-CV(2) protocol actually has a higher ΔQ_{bat} compared to the CC-CV(1) protocol, while it had a lower ΔQ_{bat} than the CC-CV(1) in the beginning stages of its lifetime. This suggests then that even if a charging strategy is better than another for a fresh battery, it does not necessarily mean that it is better than the other strategy over the lifetime of the cell. Thus, we can conclude that in order to retain optimal performance over the lifetime of the cell, it is crucial to have a smart (model-based) charging strategy,

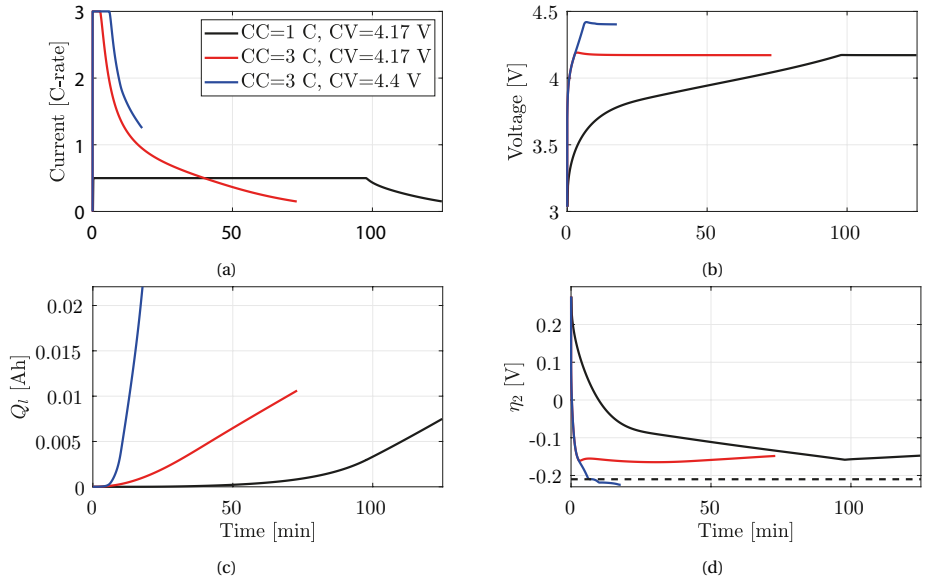

Figure 4.7: Results showing the side-reaction over-potential η_2 for combinations of CC and CV levels with the CC-CV charging protocol, where (a), (b), (c), and (d) show the current, voltage, Li-ion loss Q_l, and η_2, respectively. The black dotted line indicates the points where $\eta_2 \leq -U_2$.

which can adapt to the changing conditions of the cell over its lifetime.

4.3.4. SIDE-REACTION OVER-POTENTIAL AS AGING INDICATOR

The side-reaction over-potential η_2 over time plotted for combinations of CC and CV levels for the CC-CV(2) protocol can be seen in Fig. 4.7d. We can see that as C-rates in the CC stage get larger, the over-potential becomes more negative, and as the CV voltage gets larger, the over-potential also becomes more negative. The constraint $\phi_s - \phi_e > 0$ is often used to prevent lithium plating in the battery [8, 11–13]. This constraint is equivalent to $\eta_2 > -U_2$, which is the black dotted line shown in Fig. 4.7d. However, from Fig. 4.7c, we can see that even at the highest C-rate, where a relatively short charging time of around 75 minutes is reached, this constraint is still not violated. The blue curve shows a scenario where this constraint is violated, which is at a combination of high currents and high voltages. From Fig. 4.7c, we can also see that when $\eta_2 \leq -U_2$, the Li-ion loss increases significantly. Note that the blue curve is not actually fully charged, as the solid-phase concentration became saturated before the battery could become fully charged. Of course, even in the other two cases of the black and red curves, even though the over-potential constraint is not violated, there is still a difference in how much the battery ages with each of the current profiles, as we can see from Fig. 4.7c. Still, it can serve as a hard constraint to prevent extreme scenarios that lead to lithium plating. However, as shown by the above analysis, side-reaction over-potential cannot be used to make a trade-off between charging time and battery degradation effectively.

4.4. CONCLUSIONS

In this chapter, we have utilized a Doyle-Fuller-Newman (DFN) model including capacity-loss side reactions to present a model-based design method for multi-stage charging protocols, which has led to a trade-off between charging times and battery aging. The results have been leveraged by a highly efficient implementation of the DFN model, which has a short computation time, presented in Chapter 2 of this thesis. We have shown that by obtaining the Pareto front that describes the optimal trade-off between charging time and battery aging for a single cycle, the results can be extended to the lifetime of the battery. Finally, we have shown that the negative-electrode over-potential is not always a good indicator for aging, and that aging will occur even when the battery operates in over-potential regions that are considered not to lead to aging.

REFERENCES

[1] H. J. Bergveld, W. S. Kruijt, and P. H. L. Notten, *Battery Management Systems: Design by Modeling* (Kluwer Academic publishers, 2002).

[2] P. Arora, *Capacity Fade Mechanisms and Side Reactions in Lithium-Ion Batteries,* Journal of the Electrochemical Society **145**, 3647 (1998).

[3] P. Notten, J. Op het Veld, and J. van Beek, *Boostcharging Li-ion batteries: A challenging new charging concept,* Journal of Power Sources **145**, 89 (2005).

[4] D. Anseán, M. González, J. Viera, V. García, C. Blanco, and M. Valledor, *Fast charging technique for high power lithium iron phosphate batteries: A cycle life analysis,* Journal of Power Sources **239**, 9 (2013).

[5] Y.-H. Liu, C.-H. Hsieh, and Y.-F. Luo, *Search for an Optimal Five-Step Charging Pattern for Li-Ion Batteries Using Consecutive Orthogonal Arrays,* IEEE Transactions on Energy Conversion **26**, 654 (2011).

[6] T. T. Vo, X. Chen, W. Shen, and A. Kapoor, *New charging strategy for lithium-ion batteries based on the integration of Taguchi method and state of charge estimation,* Journal of Power Sources **273**, 413 (2015).

[7] P. M. Attia, A. Grover, N. Jin, K. A. Severson, T. M. Markov, Y.-H. Liao, M. H. Chen, B. Cheong, N. Perkins, Z. Yang, P. K. Herring, M. Aykol, S. J. Harris, R. D. Braatz, S. Ermon, and W. C. Chueh, *Closed-loop optimization of fast-charging protocols for batteries with machine learning,* Nature (2020).

[8] R. Romagnoli, L. D. Couto, A. Goldar, M. Kinnaert, and E. Garone, *A feedback charge strategy for Li-ion battery cells based on Reference Governor,* Journal of Process Control (2019).

[9] Y. Gao, C. Zhang, Q. Liu, Y. Jiang, W. Ma, and Y. Mu, *An optimal charging strategy of lithium-ion batteries based on polarization and temperature rise,* in *Transportation Electrification Asia-Pacific* (2014) pp. 1–6.

[10] M. Doyle, T. F. Fuller, and J. Newman, *Modeling of galvanostatic charge and discharge of the lithium/polymer/insertion cell,* Journal of the Electrochemical society **140**, 1526 (1993).

[11] R. Klein, N. A. Chaturvedi, J. Christensen, J. Ahmed, R. Findeisen, and A. Kojic, *Optimal charging strategies in lithium-ion battery,* in *IEEE American Control Conference* (2011) pp. 382–387.

[12] H. Perez, N. Shahmohammadhamedani, and S. Moura, *Enhanced Performance of Li-Ion Batteries via Modified Reference Governors and Electrochemical Models,* IEEE/ASME Transactions on Mechatronics **20**, 1511 (2015).

[13] Z. Chu, X. Feng, L. Lu, J. Li, X. Han, and M. Ouyang, *Non-destructive fast charging algorithm of lithium-ion batteries based on the control-oriented electrochemical model,* Applied Energy **204**, 1240 (2017).

[14] S. Santhanagopalan, Q. Guo, P. Ramadass, and R. E. White, *Review of models for predicting the cycling performance of lithium ion batteries,* Journal of Power Sources **156**, 620 (2006).

[15] C. Zou, X. Hu, Z. Wei, T. Wik, and B. Egardt, *Electrochemical Estimation and Control for Lithium-Ion Battery Health-Aware Fast Charging,* IEEE Transactions on Industrial Electronics **65**, 6635 (2018).

[16] H. E. Perez, X. Hu, and S. J. Moura, *Optimal charging of batteries via a single particle model with electrolyte and thermal dynamics,* in *IEEE American Control Conference* (2016) pp. 4000–4005.

[17] H. E. Perez, X. Hu, S. Dey, and S. J. Moura, *Optimal Charging of Li-Ion Batteries With Coupled Electro-Thermal-Aging Dynamics,* IEEE Transactions on Vehicular Technology **66**, 7761 (2017).

[18] P. Ramadass, B. Haran, P. M. Gomadam, R. White, and B. N. Popov, *Development of First Principles Capacity Fade Model for Li-Ion Cells,* Journal of the Electrochemical Society **151**, A196 (2004).

[19] R. Fu, S.-Y. Choe, V. Agubra, and J. Fergus, *Development of a physics-based degradation model for lithium ion polymer batteries considering side reactions,* Journal of Power Sources **278**, 506 (2015).

[20] S. Lucia, M. Torchio, D. M. Raimondo, R. Klein, R. D. Braatz, and R. Findeisen, *Towards adaptive health-aware charging of Li-ion batteries: A real-time predictive control approach using first-principles models,* in *IEEE American Control Conference* (2017) pp. 4717–4722.

[21] M. Torchio, L. Magni, R. B. Gopaluni, R. D. Braatz, and D. M. Raimondo, *LIONSIMBA: A matlab framework based on a finite volume model suitable for Li-ion battery design, simulation, and control,* Journal of the Electrochemical Society **163**, A1192 (2016).

[22] L. Xia, E. Najafi, Z. Li, H. J. Bergveld, and M. C. F. Donkers, *A computationally efficient implementation of a full and reduced-order electrochemistry-based model for Li-ion batteries,* Applied Energy **208**, 1285 (2017).

5

Optimal Aging-Aware Charging Using a Surrogate Model

In this chapter, we present an optimal-control-based method for aging-aware charging. A surrogate modeling approach is used to approximate aging-related Doyle-Fuller-Newman (DFN) model states, where the surrogate model is a combination of a black-box finite-dimensional linear-time-invariant model and a static nonlinear model that is a function of state of charge. We formulate the optimal-control problem as minimizing the side reactions for a given charging time and subject to several aging-related constraints that are commonly used in literature. We will show that the aging-related DFN model states can be well approximated by the proposed surrogate model. Furthermore, we will show that with the surrogate modeling approach, even in an open-loop execution of the optimal-control-based method, the considered constraints are only marginally violated when applied to the DFN model. Finally, we will compare the Pareto front achieved with the proposed optimal-control-based method with the Pareto fronts achieved with various multi-stage charging protocols, obtained from Chapter 4. Here, we will show that the proposed optimal-control-based method achieves a significantly improved Pareto front over the multi-stage charging protocols.

This chapter is based on Publication **P.3**.

5.1. INTRODUCTION

One of the objectives of this thesis is to develop optimal aging-aware charging algorithms. In the previous chapter, we have considered multi-stage constant-current (CC) constant-voltage (CV) charging protocols. While we have shown that these protocols allow for a better trade-off between charging time and aging compared to the conventionally used CC-CV protocol, they do not provide for any guarantee of optimality. As reasoned in Chapter 1 of this thesis, optimal-control-based methods should at least provide for some level of optimality. However, in order to restrict or minimize aging effectively, an electrochemistry-based aging model is required, such as the Doyle-Fuller-Newman (DFN) model with capacity-loss side reactions, introduced in Chapter 4. The proposed highly computationally efficient implementation of the DFN model presented in Chapter 2 has substantially reduced the computation times of the DFN model, although empirical models, such as equivalent-circuit models (ECMs) [1] still have a lower complexity. However, while empirical models are computationally fast, they do not describe the actual electrochemical processes in the battery, which are necessary to effectively restrict or minimize aging.

An alternative approach to using electrochemistry-based models, while still having a description of the internal states, is the use of surrogate models [2–4], or by using a linearized electrochemistry-based model [5]. However, a linearized model is typically only accurate around the linearization point. In the surrogate modeling approach, several states of a desired (complex) model are approximated by a model of a lower complexity. However, in the aformentioned papers that consider surrogate models, a black-box modeling approach is chosen for the surrogate model, which may lead to a difficulty in estimating the inherent (nonlinear) dependency of some of the DFN model states on the state of charge of the battery.

In this chapter, we present an off-line optimal-control-based method for aging-aware charging, where an a-priori-computed optimal current profile is applied (in open loop) to the battery. A surrogate modeling approach is used to approximate aging-related DFN model states, such as the side-reaction over-potential, similar to the approach taken in [2]. Compared to [2], we use a grey-box model to approximate the aging-related DFN model states, whereas in [2] black-box models such as the AutoRegressive Exogenous (ARX) model or the piece-wise affine ARX model are used. The surrogate model proposed in this chapter consists of a combination of a black-box finite-dimensional linear-time-invariant model and a static nonlinear model that is a function of state of charge. Using the surrogate model, we can formulate the optimal-control problem as minimizing the side reactions for a given charging time and subject to several aging-related constraints that are commonly used in literature. We will validate the proposed surrogate model with the DFN model, and we will furthermore compare the Pareto front achieved with the proposed optimal-control-based method with the Pareto fronts achieved with the multi-stage charging protocols as studied in Chapter 4 of this thesis.

The remainder of this chapter is structured as follows. In Section 5.2, we present the surrogate modeling method. In Section 5.3, the optimal-control problem is formulated. In Section 5.4, we will show the results, where the semi-empirical model is validated against the DFN model, the Pareto optimal fronts of the various aging-aware charging methods are compared, and the performance, in terms of constraint satisfaction, of the

proposed optimal-control-based method is validated. Finally, conclusions are drawn in Section 5.5.

5.2. BATTERY MODELING

In this section, the surrogate modeling method to model various considered states of the DFN model is described. First, we formulate the proposed surrogate modeling method, which is followed by the selection of the to-be-modeled DFN model states, after which the surrogate modeling method is applied to the selected DFN model states obtaining a surrogate model that describes these states.

5.2.1. THE SURROGATE MODELING APPROACH

The model that we base the surrogate model on is the DFN model considering side reactions, formulated in Chapter 4. Therefore we refer the reader to Chapter 4 for the equations of this model. The DFN model describes the internal electrochemical reactions, from which some of the states relate to the aging of the cell. Since only these states are of interest, it is seemingly inefficient to compute all the other states, just to get a description of the variables that are of interest. Thus, there has been some work in obtaining an adequate description of the variables of interest with a minimal computational effort, e.g. by using black-box modeling techniques as done in [2]. However, in black-box modeling methods, estimating the inherent (nonlinear) dependency of some of the DFN model states on the state of charge of the battery is difficult. For example, the terminal voltage V_t is often described with an equivalent-circuit model, e.g. [6], where V_t is expressed as a sum of the output of a finite-dimensional (FD) linear-time-invariant (LTI) model and a static non-linearity, i.e., the electro-motive force (EMF), that is a function of the state of charge (SoC). With many of the other DFN model states showing a similar static dependency on the SoC, this empirical model can be extended to also model these DFN model states. This extended empirical model, which can also be referred to as a surrogate model of the DFN model, is depicted in Fig. 5.1 as an input/output model, where the input is the applied current, and the output is the predicted voltage and the predicted virtual outputs, representing the relevant parts of the DFN model states. The relevant parts of the DFN model states are represented as virtual outputs, since in an actual battery cell, these states cannot be measured.

In a discrete-time representation, y_k being the vector of the voltage and virtual outputs of the surrogate model at time $k\delta_t$, in which k is the discrete time instant, and δ_t is the sampling time, is given by

$$y_k = \bar{y}_k + h(s_k), \tag{5.1a}$$

where $\bar{y}_k$ is the output of an FD-LTI model, and $h(s_k)$ is a static model with the SoC s_k as the input, in which s_k is given by the coulomb counting equation as

$$s_{k+1} = s_k + \frac{\delta_t}{Q} I_{a,k}, \tag{5.1b}$$

where $I_{a,k}$ is the applied current and Q is the reversible capacity of the battery. The choice for $h(s)$ can be reasoned through the mechanisms of the DFN model.

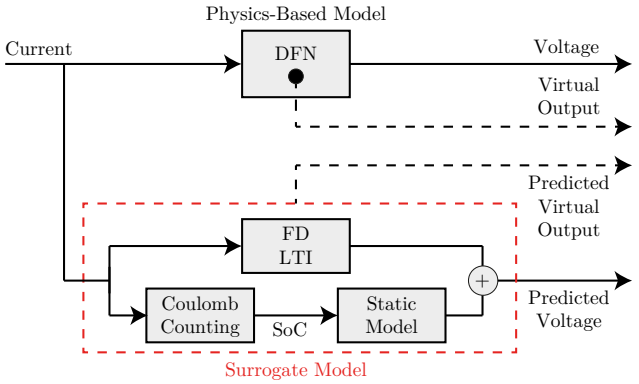

Figure 5.1: Schematic illustration of the surrogate modeling method, where the (virtual) outputs of the Doyle-Fuller Newman (DFN) model are approximated with a surrogate model, of which its output is a combination of a finite-dimensional (FD) linear-time-invariant (LTI) model and a static model.

5

The choice for the FD-LTI model can, in principle, be any of the (possibly linear) input/output models that are commonly used for system identification [7]. However, since the various outputs of the model are dynamically interconnected, it is sensible to choose a model that allows for the possibility to include this interconnection between the outputs, such as the AutoRegressive Exogenous (ARX) model [7]. The ARX model with n_y number of outputs and the single input $I_{a,k}$ can be formulated as a one-step-ahead predictor where the prediction $\hat{y}_k$ can be written as

$$\hat{y}_k = B_{\text{ARX}}(q,\theta) I_{a,k} - A_{\text{ARX}}(q,\theta)\bar{y}_k, \tag{5.1c}$$

where q is the forward shift operator, such that $I_{a,k-1} = q^{-1} I_k$, and θ are the parameters of the ARX model. Furthermore, in (5.1c), A_{ARX} is an $n_y \times n_y$ matrix of polynomials of q^{-1}, where the polynomials contain a delay of at least one sample, i.e., they start with zero, and B_{ARX} is an $n_y \times 1$ matrix of polynomials of q^{-1}, where the polynomials are monic, i.e., the leading coefficients are one. As defined in the MATLAB System Identification Toolbox [7], the choice for the order of the polynomials of A_{ARX} can be expressed by a matrix $N_A \in \mathbb{R}^{n_y \times n_y}$, where every element of N_A indicates the order of the polynomial of the corresponding element of A_{ARX}. Similarly, the orders of the polynomials of each element of B_{ARX} can be expressed by a matrix $N_B \in \mathbb{R}^{n_y \times 1}$. With a certain choice for N_A and N_B, and data obtained from the simulation of the DFN model, the parameters θ of the ARX model can be determined by minimizing a least-squares criterion of the form

$$\sum_{k \in \mathcal{K}} ||\bar{y}_k - \hat{y}_k(\theta)||, \tag{5.2}$$

for $k \in \mathcal{K} = \{0, 1, ..., K-1\}$, where $K = t_f / \delta_t$ is the time horizon with t_f the final time step, and $\bar{y}_k$ can be computed from the measurements y_k using (5.1a), assuming that $h(s_k)$ is known.

The system (5.1) can then be written as a state-space model as

$$x_{k+1} = A\xi_k + BI_{a,k}, \tag{5.3a}$$
$$y_k = C\xi_k + DI_{a,k} + h(s_k), \tag{5.3b}$$

where $x = \begin{bmatrix} s & \bar{x} \end{bmatrix}^\top$, $A = \mathrm{diag}(1, \bar{A})$, $B = \begin{bmatrix} \delta_t / C_b & \bar{B} \end{bmatrix}^\top$, $C = \begin{bmatrix} 0 & \bar{C} \end{bmatrix}$, $D = \bar{D}$, in which $\bar{x}$, $\bar{A}$, $\bar{B}$, $\bar{C}$, and $\bar{D}$ are obtained from any state-space representation of (5.1c).

5.2.2. SELECTION OF DFN MODEL STATES FOR THE SURROGATE MODEL

In general, any combination of the DFN model states can be chosen as virtual output for the surrogate model. However, for the purpose of aging-aware charging, not all the variables of the DFN model are equally interesting, as there are only several variables of the DFN model that are typically associated with the aging of the battery. When the objective is to constrain or minimize side reactions, as e.g. in [8], the variable of interest is η_2. Besides the side-reaction overpotential, the stoichiometries in the electrodes s_n and s_p are also of interest, which either are constrained directly, e.g. in [9], or are constrained through particle stress models, which depend on the stoichiometries of the electrodes, e.g. in [10]. Furthermore, constraints on electrolyte concentration c_e are also used in [9] for the purpose of aging-aware charging. Finally, constraining the terminal voltage V_t should also be considered, since there may be unmodeled reactions at extreme voltages that can lead to potentially dangerous scenarios.

As we can observe from (4.1)-(4.4) in Table 4.1, each of the states is infinite-dimensional, due to the nature of the partial differential equations. While after spatial and temporal discretization, as done in e.g., Chapter 2, a finite number of states is obtained, generally the number of states is still significantly large. Modeling these states with the proposed surrogate modeling method would lead to a system with a large number of states, defying the purpose of generating a simpler model than the DFN model. However, not all the states are necessary in order to constrain or minimize the aging of the cell. As we can see from Fig. 5.2, while charging, every state generally experiences its extreme at either ends of the electrodes or at either ends of the cell. Therefore, to constrain these variables, it is sufficient to only describe the states at the extreme ends that are of interest.

Typically, s_n and s_p are upper and lower bounded, respectively, during charging, in order to avoid excessive stress (in the negative electrode) and lithium depletion (in the positive electrode), in the particles [9, 10]. While charging, assuming a positive applied current $I_a > 0$, Li-ions strictly move from the positive electrode to the negative electrode. Therefore, in the negative electrode the total number of Li-ions increases, while in the positive electrode, the total number of Li-ions decreases. As the Li-ions diffuse throughout the cell in this process, in the negative and positive electrode, Li-ions accumulate and are removed, respectively, more near the separator than at the other ends of the electrodes. Thus, over the gradient of s_n, s_n is largest at $x = \delta_n$ and over the gradient of s_p, s_p is smallest at $x = L - \delta_p$, as we can also see in Fig. 5.2. This means that to prevent lithium depletion and excessive stress on the particles while charging, it is sufficient to bound s_n from above at $x = \delta_n$ and to bound s_p from below at $x = L - \delta_p$. Similarly, c_e is typically upper and lower bounded, in order to avoid lithium saturation and depletion,

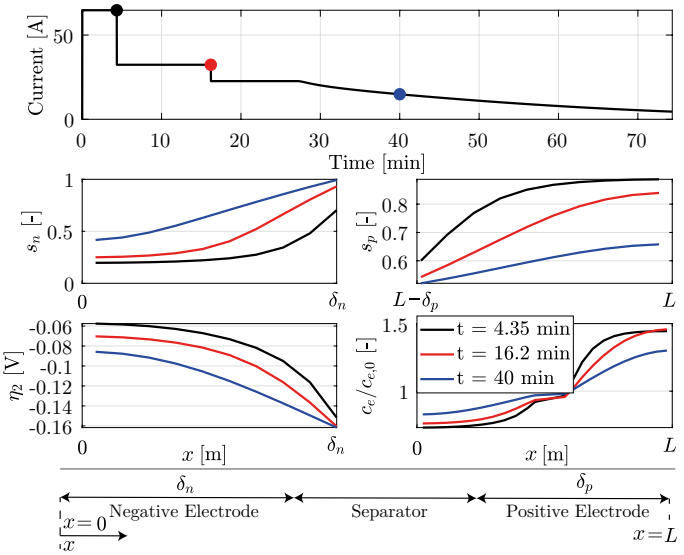

Figure 5.2: The DFN model variables of interest for the purpose of aging-aware charging. The colored dots indicate the times where the variables are shown.

respectively, in the electrolyte [9]. Therefore, it would be sufficient to have a description of c_e at $x = 0$ and $x = L$, as the extremes occur at these points, as we can see from Fig. 5.2.

The side-reaction overpotential η_2 is typically either minimized through Q_l in (4.10), e.g., in Chapter 4, in order to minimize side reactions, and/or has a constraint to have a certain lower bound, in order to prevent lithium plating, e.g. [8]. For the purpose of preventing lithium plating, we can see from Fig. 5.2 that over the gradient of η_2, the lowest potential occurs at $x = \delta_n$. Therefore, it is sufficient to bound η_2 from below at $x = \delta_n$. When the objective is to minimize Li-ion loss due to side reactions, i.e., to minimize Q_l in (4.10), the integral $\int_0^{\delta_n} j_2 \mathrm{d}x$ suggests that a description of j_2, and therefore η_2, over the entire negative electrode is necessary. To simplify the problem, the integral $\int_0^{\delta_n} j_2(t)\mathrm{d}x$ can be simplified to $j_2(\delta_n, t)\delta_n$. From Fig. 5.3, we can see that while there is a significant difference between $\int_0^{\delta_n} j_2(t)\mathrm{d}x$ and $j_2(\delta_n, t)\delta_n$, they still generally show the same crucial behavior, i.e., applying a certain current at a lower state of charge leads a lower magnitude of j_2 than at a higher state of charge.

To summarize, the selection of the DFN model states for the surrogate modeling method is V_t, $\bar{\eta}_2(t) = \eta_2(t, \delta_n)$, $\bar{s}_n(t) = s_n(t, \delta_n)$, $\bar{s}_p(t) = s_p(t, L-\delta_p)$, $\bar{c}_{e,0}(t) = c_e(t, 0)/c_{e,a}$, and $\bar{c}_{e,L}(t) = c_e(t, L)/c_{e,a}$, where $c_{e,a}$ is the average electrolyte concentration.

5.2.3. APPLICATION OF THE SURROGATE MODELING APPROACH TO THE SELECTED DFN MODEL STATES

We apply the surrogate modeling approach to obtain a model that describes the selection of the DFN model states of interest for aging-aware charging made in Section 5.2.2. The surrogate model output y_k and static functions $h(s_k)$ in (5.3b) are then, respectively,

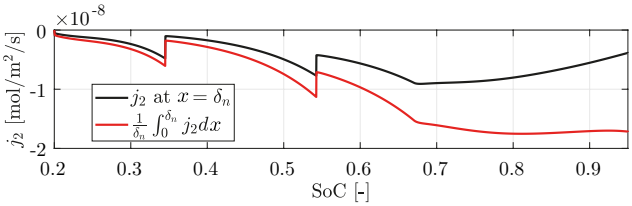

Figure 5.3: Comparison of $\frac{1}{\delta_n}\int_0^{\delta_n} j_2(t)\mathrm{d}x$ and j_2 at $x = \delta_n$, in order to indicate the impact of the simplification of $\int_0^{\delta_n} j_2(t)\mathrm{d}x$ to $j_2(\delta_n, t)\delta_n$ in (4.10), with the simulation done with the current profile shown in Fig. 5.2.

given by

$$\begin{aligned} y_k &= [\, V_{t,k} \;\; \bar{\eta}_{2,k} \;\; \bar{s}_{n,k} \;\; \bar{s}_{p,k} \;\; \bar{c}_{e,0,k} \;\; \bar{c}_{e,L,k} \,]^\top, \\ h(s_k) &= [\, U_p(s_k) - U_n(s_k) \;\; U_n(s_k) - U_2 \;\; \bar{s}_{n,e}(s_k) \;\; \bar{s}_{p,e}(s_k) \;\; 1 \;\; 1 \,]^\top, \end{aligned} \tag{5.4}$$

where U_p and U_n are the positive- and negative-electrode equilibrium potential, respectively, which are pre-defined functions of s, and U_2 is the equilibrium potential of the side reactions, given as a fixed value. Furthermore, $\bar{s}_{i,e}$, $i \in \{n, p\}$, in which n indicates the negative electrode and p the positive electrode, is the equilibrium stoichiometry in electrode i, which can be computed as $\bar{s}_{i,e} = (s_{100,i} - s_{0,i})s + s_{0,i}$, in which $s_{100,i}$ and $s_{0,i}$ are the stoichiometries in electrode i at 100% state of charge and 0% state of charge, respectively.

5.3. OPTIMAL AGING-AWARE CHARGING

The goal of this chapter is to develop an aging-aware charging method that can systematically make a trade-off between charging time and aging. We propose to do this using optimal control, based on the surrogate model presented in Section 5.2. As mentioned in Chapter 1, to achieve a Pareto-optimal combination of battery aging and charging time, the optimal-control problem can be generally formulated in three different ways. First, most commonly, the charging time is minimized subject to certain aging-related constraints, see, e.g., [8, 9]. The minimum charging time problem can be approximated by an SoC-reference-tracking problem, e.g., [11], where the reference SoC is the desired final SoC. Secondly, another way to reach a Pareto-optimal trade-off between battery aging and charging time is to minimize a weighting between charging time and battery aging, as done in, e.g., [6, 11, 12]. Thirdly, aging can be minimized for a given charging time. In this chapter, we choose the latter approach, as this problem formulation avoids the difficulties that come with a minimum-time optimization problem, while still achieving a Pareto-optimal combination of battery aging and charging time. To solve this optimal-control problem efficiently, we employ a sequential-quadratic-programming algorithm (SQP). In this section, the optimal-control problem for aging-aware charging is formulated and the SQP algorithm for the application of the proposed optimal-control-based method is given.

5.3.1. PROBLEM FORMULATION

We consider the problem formulation where the Li-ion loss due to side reactions Q_l in (4.10), with the integral $\int_0^{\delta_n} j_2(t)\mathrm{d}x$ simplified to $j_2(\delta_n, t)\delta_n$, is minimized with a given charging time t_f, i.e.,

$$\min_{\xi_k, I_{a,k}} Q_l(\xi_k, I_{a,k}) = \min_{\xi_k, I_{a,k}} \sum_{k\in\mathcal{K}} \alpha_1 \exp(\alpha_2 \eta_{2,k}(\xi_k, I_{a,k})), \tag{5.5a}$$

where $\alpha_1 = i_{0,2} a_s A_{\text{surf}} \delta_t$, $\alpha_2 = \frac{-2\alpha_{c,2}F}{RT}$, $\eta_{2,k}(\xi_k, I_{a,k}) = C_2\xi_k + D_2 I_{a,k} + h_2(s_k)$, where, C_2, D_2, and $h_2(s_k)$ indicate the second row of C, D, and $h(s_k)$ in (5.3b), respectively. The objective (5.5a) is subject to the state dynamics (5.3a) for $k \in \mathcal{K} = \{0, 1, ..., K-1\}$, where $K = t_f/\delta_t$ is the optimization horizon with x_0 given, and $\delta_t > 0$ is the step size, which is chosen such that $\delta_t K \in \mathbb{N}$. Note that the optimization horizon K can have a different value from the K used to fit the model in (5.2). The objective (5.5a) is further subject to the bounds on the input I_k

$$I_{a,\min} \le I_{a,k} \le I_{a,\max}, \tag{5.5b}$$

for $k \in \mathcal{K}$ and the output y_k in (5.3b), i.e.,

$$y_{\min} \le y_k(\xi_k, I_{a,k}) \le y_{\max}, \tag{5.5c}$$

where $y_k(\xi_k, I_{a,k}) = Cx_k + DI_{a,k} + h(s_k)$ for $k \in \mathcal{K}$, and the (undefined) output y_K is assumed to be given by $y_K = Cx_K + DI_{a,K-1} + h(s_K)$ in order to constrain the terminal outputs. Finally, (5.5a) is also subject to a minimum stored charge constraint, i.e.,

$$s_K = s_0 + \frac{\delta_t}{C_b} \sum_{k\in\mathcal{K}} I_{a,k} \ge s_f, \tag{5.5d}$$

for a given initial SoC s_0 and a final (desired) SoC s_f.

5.3.2. SOLUTION METHOD

We can observe that the optimization problem (5.5) is nonlinear, due to the exponential and the nonlinear term $h_2(s_k)$ in $\eta_2(x_k, I_{a,k})$ in the objective function (5.5a) and the nonlinear output constraints (5.5c). Since $h(s_k)$ in the output (5.5c) can, in principle, be given by any (nonlinear) function, the problem (5.5) is also possibly nonconvex. Therefore, the solution of (5.5) requires a nonlinear optimization solver. In this paper, we have solved (5.5) using SQP [13], which aims at solving a nonlinear optimization problem by sequentially solving linearly constrained quadratic programs (LCQP), which are formed, e.g., by approximating the objective function with a quadratic equation and linearizing the constraints. In this paper, each SQP subproblem is derived by making a quadratic approximation of (5.5a), and linearizing the nonlinear constraints (5.5c). For a more detailed description of the SQP algorithm, we refer the reader to Chapter 6.

5.4. RESULTS

In this section, we will show the results of the aging-aware charging simulation study. We will first show the validation of the surrogate model on the DFN model. Then, we

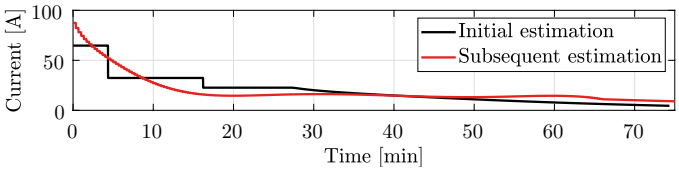

Figure 5.4: Current profiles used for the parameterization of the ARX model for the surrogate model.

consider the problem of aging-aware charging with active constraints on the virtual outputs. Finally, we will compare the Pareto front of the proposed optimal-control-based aging-aware charging method with several multi-stage charging protocols considered in Chapter 4. The parameters of the DFN model used in this chapter can be found in Chapter 4.

5.4.1. VALIDATION OF THE SURROGATE MODEL

The surrogate model is given by (5.3) with y_k and $h(s_k)$ given in (5.4). The parameterization of the ARX model has been done using the System Identification Toolbox [7] in MATLAB, where the matrices N_A and N_B have been chosen such that a good compromise between model accuracy and model complexity is achieved, and are given by

$$N_A = \begin{bmatrix} 0 & 1 & 1 & 1 & 1 & 1 \\ 0 & 1 & 1 & 1 & 0 & 1 \\ 0 & 1 & 1 & 0 & 1 & 0 \\ 0 & 1 & 0 & 2 & 1 & 0 \\ 0 & 1 & 1 & 0 & 1 & 1 \\ 0 & 1 & 0 & 1 & 1 & 1 \end{bmatrix}, \quad N_B = \begin{bmatrix} 2 \\ 2 \\ 2 \\ 2 \\ 1 \\ 1 \end{bmatrix}. \tag{5.6}$$

With a chosen current profile, the DFN model can be simulated to obtain data from which the ARX model (5.1c) can be parameterized with the least-squares criterion (5.2). This parameterization will be done in two stages. First, a multi-stage charging current profile, as shown in Fig. 5.4, is used to get an initial surrogate model. This resulting model is used to compute an optimal solution for a charging time of 75 minutes using the optimal-control-based method described in Section 5.3, where the step size δ_t of the optimization problem is chosen as $\delta_t = 20$ s. The obtained solution shown in Fig. 5.4 is then used to get a subsequent surrogate model. This is the model that is used for obtaining the remaining results presented in this chapter, as its parameters are determined with a current profile that is representative of the expected solutions to the optimization problem (5.5). The model has been validated using the optimal solution with a charging time of 100 minutes, which is shown in Fig. 5.5. To indicate the computational advantage of the surrogate model, the DFN model simulation using the implementation of Chapter 2 took 1.75 s, while the surrogate model simulation merely took 0.024 s on a consumer-grade PC. We should note here that the DFN model implementation is highly efficient. In Fig. 5.5, we observe that there is some mismatch between the DFN model and the surrogate model, although generally the obtained fit can be considered to be good enough for optimal control, especially considering the computational advantage of the surrogate model over the DFN model.

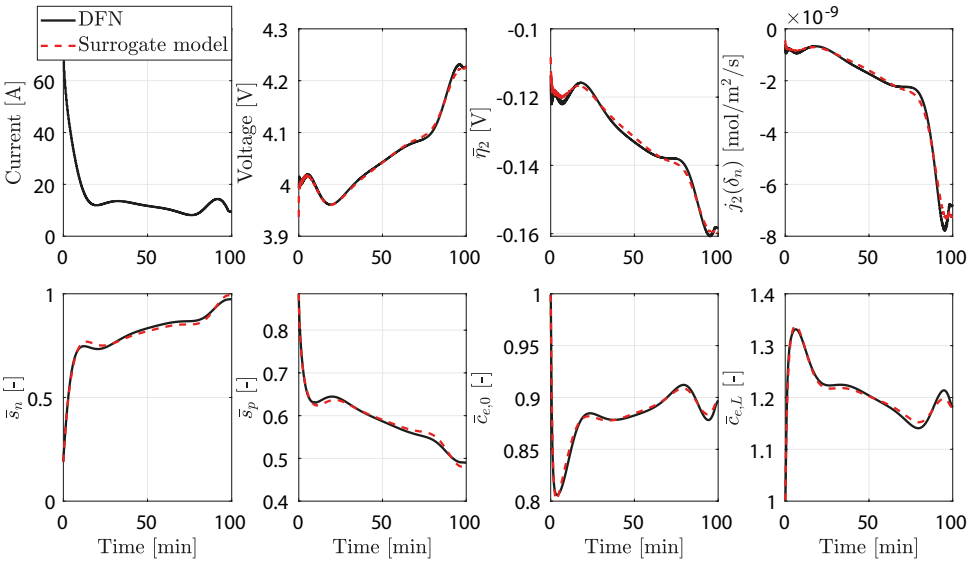

Figure 5.5: Validation of the surrogate model with the DFN model, where the current, voltage, side-reaction over-potential η_2, side-reaction flux j_2 at $x = \delta_n$, stoichiometry in the negative electrode $\bar{s}_n$ at $x = \delta_n$, stoichiometry in the positive electrode $\bar{s}_p$ at $x = L - \delta_p$, normalized electrolyte concentration at $x = 0$ $\bar{c}_{e,0}$, and normalized electrolyte concentration at $x = L$ $\bar{c}_{e,L}$ are shown.

5.4.2. OPTIMAL SOLUTION WITH VIRTUAL OUTPUT CONSTRAINTS

In this chapter, we consider an open-loop optimal-control-based aging-aware charging method, where an a-priori-computed current profile is applied (in open loop) to the battery. In order to test the validity of this method under active virtual output constraints (5.5c), we will create an artificial scenario where most of these constraints are active. In doing so, we consider the problem of solving (5.5) in a given time t_f of 100 minutes, with $\bar{s}_{n,\max} = 0.93$, $\bar{s}_{p,\min} = 0.52$, $\bar{c}_{e,0,\min} = 0.85$, $\bar{c}_{e,L,\max} = 1.27$. The step size of the optimization problem has been chosen as $\delta_t = 50$ s, which we have found to strike a good balance between accuracy and computation time of the optimization problem. Note that the values chosen in these constraints are entirely artificial and are not representative of what the values should be in order to realistically restrict aging. Ideally, these constraints should be chosen in the least restrictive way possible and are only meant to restrict the battery into reaching states that lead to unmodeled aging phenomena. In this case, most likely, the considered constraints restrict the battery conservatively in order to show to what extend the considered constraints are violated due to modeling errors. In Fig. 5.6, we can see the solution to the considered problem, where both the simulation using the DFN model and the surrogate model are shown. We observe that, as could be expected from the model validation, the constraints are violated slightly by the DFN model. However, since aging is not an on-off behavior, a slight violation of the constraints is not necessarily an issue for the purpose of aging-aware charging.

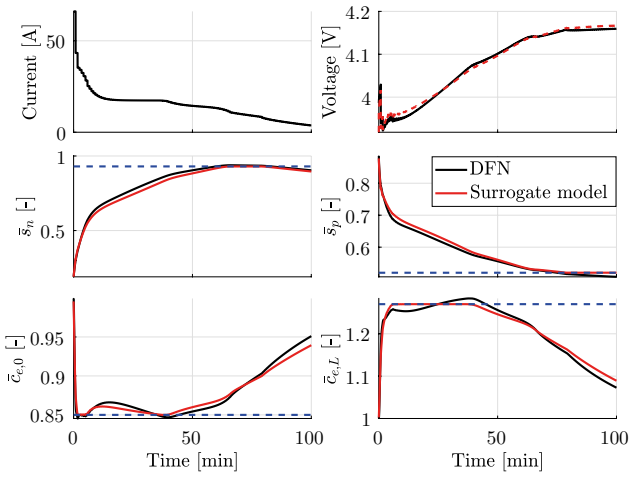

Figure 5.6: The solution to the virtual-output-constrained problem simulated with the DFN model and the surrogate model, where the current, voltage, stoichiometry in the negative electrode $\bar{s}_n$ at $x = \delta_n$, stoichiometry in the positive electrode $\bar{s}_p$ at $x = L - \delta_p$, normalized electrolyte concentration at $x = 0$ $\bar{c}_{e,0}$, and normalized electrolyte concentration at $x = L$ $\bar{c}_{e,L}$ are shown. The blue dashed lines indicate the constraints.

5.4.3. PARETO OPTIMAL FRONT COMPARISON

In Fig. 5.7, the degradation of the cell, in terms of Li-ions lost due to side reactions, i.e., Q_l, is plotted against charging time, for the proposed optimal-control-based method, CC-CV, CC-CV(2), and 2-CC-CV(2). The multi-stage charging protocol CC-CV(2) indicates a protocol where the CC-stage current and the CV-stage voltage limit can be varied, whereas 2-CC-CV(2) indicates a protocol with 2 CC stages followed by a CV stage, where the two CC-stage currents can be varied, with a fixed voltage limit throughout. For further details on how the multi-stage charging protocols are defined, we refer the reader to Chapter 4. In the proposed optimal-control-based method, we consider two cases, where one is the optimal problem (5.5) with only the minimum-charge constraint (5.5d) and one with an additional maximum-current constraint chosen as $I_{\max} = 1C$. Note that in both of these cases, we still use the constraint $\bar{s}_n < 1$, since a violation of this constraint leads to numerical issues in the simulation of the DFN model. Further note that we refer the reader to Chapter 4 for a detailed description of how one charging protocol achieves a better Pareto front than another.

We observe in Fig. 5.7(a) that the Pareto front obtained using the optimal-control-based method is a significant improvement over the multi-stage protocols. For example, when the battery is charged in 80 minutes, the optimal-control-based method ages the battery about 25% less than when using the multi-stage protocol. Alternatively, the battery can be charged in 70 minutes using the optimal-control-based method, while with the multi-stage protocols it would take about 87 minutes with the same amount of aging. Notably, the optimal-control-based method shows the most improvement over the multi-stage protocols at low charging times, while the improvement decreases as the charging time is increased. This is explained by the fact that when the charging time is large, a large initial current is not as beneficial, since this current must be compensated

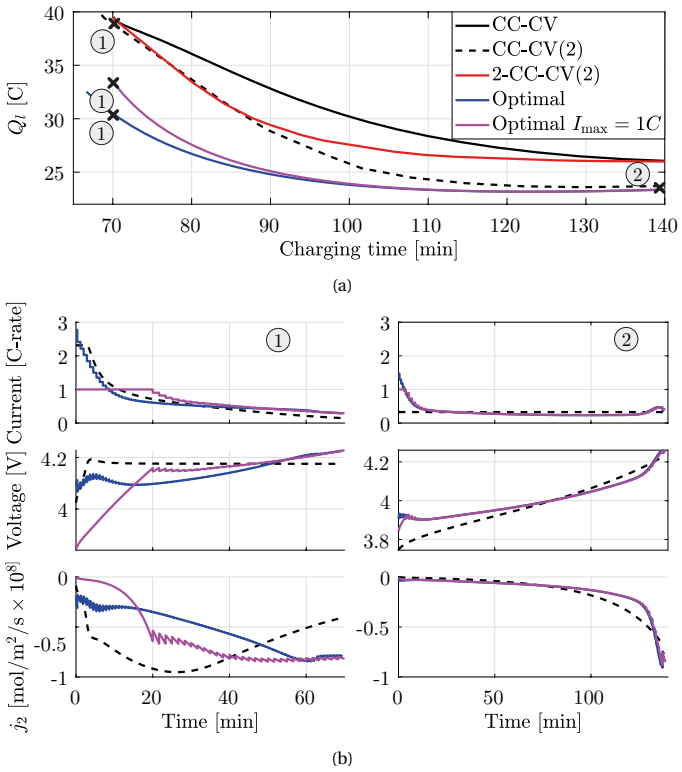

Figure 5.7: Trade-off between charging time and Li-ion loss (Q_l) for the various considered aging-aware charging methods in (a), and the current, voltage, and side-reaction flux j_2 for the indicated charging times of about 70 minutes (1) and 140 minutes (2) in (b).

elsewhere at higher SoCs, where the side reactions are generally more sensitive to the magnitude of the current. This leads to a flattening of the current profile, as we can also see in Fig. 5.7(b). This could also suggest that the method proposed in this chapter and the CC-CV(2) protocol are already close to the best possible Pareto front at high charging times.

In Fig. 5.7, we can also see the effect of imposing a maximum applied current of 1 C. As could be expected, the Pareto front using this constraint is worsened compared to the case without the constraint. Even so, we can see that the achieved trade-off between charging time and aging is still a significant improvement over the multi-stage charging protocols, even when these use higher currents than 1 C. This shows that large charging currents are not necessary to achieve a good trade-off between charging time and aging. Note that in this work, we have only presented the trade-off between charging time and aging for a single cycle. Over the lifetime of the battery, the battery degrades, leading to a change in the dynamics of the battery over its lifetime. Therefore, in a practical application of the proposed aging-aware charging method, the changing dynamics should be taken into account in the surrogate modeling framework, which will be facilitated by a

computationally fast model, such as the proposed surrogate model of this chapter.

5.5. CONCLUSIONS

In this chapter, we have presented an optimal-control-based method for aging-aware charging. A surrogate modeling approach has been used to approximate aging-related DFN model states, where the surrogate model is a combination of a black-box finite-dimensional linear-time-invariant model and a static nonlinear model that is a function of state of charge. This surrogate modeling approach has been applied to a DFN model that considers the capacity loss due to side reactions.

We have shown that the aging-related DFN model states can be well approximated by a surrogate model. Furthermore, we have shown that with this surrogate model, even in an open-loop execution of the optimal-control-based method, the considered constraints are only narrowly violated. Finally, we have compared the Pareto front achieved with the proposed optimal-control-based method with the Pareto fronts achieved with various multi-stage charging protocols considered in Chapter 4 of this thesis. Here, we have shown that the proposed optimal-control-based method achieves a significantly improved Pareto front over the multi-stage charging protocols.

REFERENCES

[1] H. J. Bergveld, W. S. Kruijt, and P. H. L. Notten, *Battery Management Systems: Design by Modeling* (Kluwer Academic publishers, 2002).

[2] M. Torchio, L. Magni, R. D. Braatz, and D. M. Raimondo, *Design of Piecewise Affine and Linear Time-Varying Model Predictive Control Strategies for Advanced Battery Management Systems,* Journal of the Electrochemical Society **164**, A949 (2017).

[3] A. Pozzi, M. Torchio, R. D. Braatz, and D. M. Raimondo, *Optimal charging of an electric vehicle battery pack: A real-time sensitivity-based model predictive control approach,* Journal of Power Sources **461**, 228133 (2020).

[4] M. Torchio, L. Magni, R. D. Braatz, and D. M. Raimondo, *Optimal charging of a Li-ion cell: A hybrid model predictive control approach,* in *IEEE 55th Conference on Decision and Control* (2016) pp. 4053–4058.

[5] C. Zou, X. Hu, Z. Wei, T. Wik, and B. Egardt, *Electrochemical Estimation and Control for Lithium-Ion Battery Health-Aware Fast Charging,* IEEE Transactions on Industrial Electronics **65**, 6635 (2018).

[6] H. E. Perez, X. Hu, S. Dey, and S. J. Moura, *Optimal Charging of Li-Ion Batteries With Coupled Electro-Thermal-Aging Dynamics,* IEEE Transactions on Vehicular Technology **66**, 7761 (2017).

[7] L. Ljung, *System Identification Toolbox: User's Guide* (the MathWorks Inc, 1988).

[8] R. Klein, N. A. Chaturvedi, J. Christensen, J. Ahmed, R. Findeisen, and A. Kojic, *Optimal charging strategies in lithium-ion battery,* in *IEEE American Control Conference* (2011) pp. 382–387.

[9] H. E. Perez, X. Hu, and S. J. Moura, *Optimal charging of batteries via a single particle model with electrolyte and thermal dynamics,* in *IEEE American Control Conference* (2016) pp. 4000–4005.

[10] B. Suthar, P. W. C. Northrop, R. D. Braatz, and V. R. Subramanian, *Optimal Charging Profiles with Minimal Intercalation-Induced Stresses for Lithium-Ion Batteries Using Reformulated Pseudo 2-Dimensional Models,* Journal of the Electrochemical Society **161**, F3144 (2014).

[11] S. Lucia, M. Torchio, D. M. Raimondo, R. Klein, R. D. Braatz, and R. Findeisen, *Towards adaptive health-aware charging of Li-ion batteries: A real-time predictive control approach using first-principles models,* in *IEEE American Control Conference* (2017) pp. 4717–4722.

[12] A. Pozzi, M. Torchio, and D. M. Raimondo, *Film growth minimization in a Li-ion cell: a Pseudo Two Dimensional model-based optimal charging approach,* in *2018 European Control Conference (ECC)* (2018) pp. 1753–1758, 00014.

[13] P. T. Boggs and J. W. Tolle, *Sequential Quadratic Programming **, Acta Numerica **4**, 1 (1995).

6

Optimal Aging-Aware Charging Using Electrochemistry-Based Models

In this chapter, we present an optimal aging-aware charging approach using the Doyle-Fuller-Newman (DFN) model. In this approach, an optimal-control problem is formulated that has a low computational complexity. Furthermore, to solve the optimal-control problem, we employ a sequential-quadratic-programming (SQP) algorithm, which can solve nonlinear optimization problems in a computationally efficient manner. To further reduce the computional complexity of the optimal-control problem, we investigate the effect of spatial and temporal discretization of the resulting discrete-time optimal-control problem on the computational complexity and achieved trade-off between charging time and aging. In the validation of the proposed optimal aging-aware charging approach, we show that with the employed SQP algorithm, the formulated optimal-control problem can be solved roughly an order of magnitude faster than with an off-the-shelf solver. Furthermore, we show that with a well-considered choice of spatial and temporal discretization of the optimal-control problem, and with the employed SQP algorithm, the optimal-control problem can be solved in about 0.1 s. This makes the proposed optimal aging-aware charging approach suitable for a closed-loop implementation.

6.1. INTRODUCTION

As introduced in Chapter 1, batteries are commonly charged using so-called constant-current-constant-voltage (CC-CV) protocol [1]. In order to improve the trade-off between charging time and aging that can be made compared to the CC-CV protocol, multi-stage CC-CV protocols, e.g., [2, 3], and Chapter 4 of this thesis, have been investigated, as well as model-based aging-aware methods, e.g., [4–8], where both methods aim to make a Pareto-optimal trade-off between battery aging and charging time. For an overview of aging-aware charging methods, we refer the reader to Chapter 1.

To make an effective and systematic trade-off between battery aging and charging time, optimal aging-aware charging methods are particularly of interest, where the aging-aware charging problem is formulated as an optimal-control problem using a particular battery model. Since electrochemistry-based models can provide a description of the internal states of the batteries, such models are often used in optimal aging-aware charging, see, e.g., [4, 5, 8–11]. Among the electrochemistry-based models used in optimal aging-aware charging, the Doyle-Fuller-Newman (DFN) model is typically used as a benchmark to evaluate other (simplified) models against, as the DFN model provides a most complete description of the internal states, at the cost of a high computational complexity. Therefore, simplified electrochemistry-based models, such as the single-particle model (SPM) [12] or reduced-order models are often used in optimal aging-aware charging, e.g. in [5, 9], and Chapter 5 of this thesis. However, while such simplified models are computationally less complex than the DFN model, they typically also lead to a sacrifice in accuracy.

The use of the DFN model in optimal aging-aware charging has often been considered infeasible, due to the high computational complexity of the DFN model, where the computation time of obtaining an optimal solution using the DFN model has been reported to be several hours in [4], which makes the DFN model seemingly impractical for a closed-loop implementation. Meanwhile, the use of the DFN model has been proposed in closed-loop optimal aging-aware charging methods, e.g. the model-predictive control (MPC) approach taken in [10, 11]. However, due to the computational complexity of the DFN model, the choice for the control horizon of the MPC approach is limited in the aforementioned papers, which leads to a sacrifice in the optimality of the obtained solution. Alongside these developments, focus has been put on reducing the computational complexity of the DFN model, as also studied in Chapter 2. Such methods for reducing the computional complexity of the DFN model may also reduce the computional complexity of the resulting optimization problem using a DFN model. Furthermore, in optimal aging-aware charging approaches, typically off-the-shelf-solvers, such as IPOPT [13] in [11] or MATLAB's fmincon in [10] are used. Such off-the-shelf-solvers may limit the possibilities in taking advantage of the properties in the structure of the considered optimization problem.

In this chapter, we present an optimal aging-aware charging approach using the DFN model. Here, we apply the method of the substitution of equations presented in Chapter 2 to arrive at a reformulated optimal-control problem with a reduced computational complexity to the originally formulated optimal-control problem. Furthermore, to solve the optimal-control problem, we employ a sequential-quadratic-programming (SQP) algorithm [14], which, as we have shown in [15], can solve nonlinear optimization

problems in a computationally efficient manner. The aging-aware charging problem is formulated similarly to the formulation in Chapter 5, where the side reactions leading to solid-electrolyte interface (SEI) growth are minimized for a given charging time. To further reduce the computional complexity of the optimal-control problem, we will investigate the effect of spatial and temporal discretization of the resulting discrete-time optimal-control problem on the computational complexity and achieved trade-off between charging time and aging. To validate the proposed optimal aging-aware charging approach, we will compare our proposed approach with a simplified DFN (SDFN) model, as introduced in 2, to several rule-based protocols, such as those considered in Chapter 4, as well as optimal aging-aware approaches using the SPM and the surrogate modeling approach that we proposed in Chapter 5. To reflect the effect of modeling errors on the achieved trade-off between charging time and aging, we define a so-called synthetic cell, which is a DFN model with concentration-dependent parameters and an electro-motive force (EMF) that is different from the DFN model used for the proposed approach, similar to the study done in Chapter 3 of this thesis.

The remainder of this chapter is structured as follows. In Section 6.2, the optimal aging-ware charging approach is given, where the optimal aging-aware charging problem is first formulated, after which the SQP approach to solve this problem is given. In Section 6.3, the results for the comparison between the various aging-aware charging methods is presented, which will serve as a validation of the proposed aging-aware charging method. Finally, conclusions are drawn in Section 6.4.

6.2. OPTIMAL AGING-AWARE CHARGING

The goal of this chapter is to develop an aging-aware charging method that can systematically make a trade-off between charging time and aging. We propose to do this using optimal control with the DFN model formulated in Chapter 4. For the reasons stated in Chapter 5, we formulate the optimal-control problem as minimizing Li-ion loss due to side reactions subject to a given charging time. To solve this optimal-control problem efficiently, we employ an SQP algorithm [14]. In this section, the optimal-control problem for aging-aware charging is formulated. Here, we will first formulate the optimal aging-aware charging problem in continuous time, after which we will give the discretized problem formulation. Finally, we will formulate the SQP approach for the considered optimal aging-aware problem.

6.2.1. PROBLEM FORMULATION

The problem of minimizing Li-ion loss due to side reactions Q_l in (4.10) can be formulated as

$$\min_{c_s,c_e,\phi_s,\phi_e,j_1,j_2,I_a} Q_l(j_2) = \min_{c_s,c_e,\phi_s,\phi_e,j_1,j_2,I_a} -a_s AF \int_{t_0}^{t_f} \int_0^{\delta_n} j_2(x,t)\mathrm{d}x\mathrm{d}t, \tag{6.1a}$$

where t_0 and t_f are the initial and final time, respectively. The objective function in (6.1a) is minimized subject to the DFN model dynamics given by (4.2)-(4.8), and lower and upper bounds on the input current, i.e.,

$$I_{a,\min} < I_a(t) \leq I_{a,\max}. \tag{6.1b}$$

Furthermore, (6.1a) may also be subject to particular inequality constraints, i.e.,

$$\mathscr{G}(c_s(x,r,t), c_e(x,t), \phi_s(x,t), \phi_e(x,t), j_1(x,t), j_2(x,t), I_a(t)) \leq 0, \tag{6.1c}$$

which can be e.g., a constraint on the negative electrode overpotential to avoid lithium plating [16] or to impose a maximum solid-phase concentration constraint to prevent over-charging, and, finally, a minimum stored-charge constraint, i.e.,

$$s_f = s_0 + \frac{1}{Q}\int_{t_0}^{t_f} I_a(t)\mathrm{d}t, \tag{6.1d}$$

for $t \in [t_0, t_f]$, and a given initial SoC $s_0 = s(0)$, $c_s(x,t_0)$, $c_e(x,t_0)$, and a final (desired) SoC $s_f = s(t_f)$. Note that for compactness of notation, in (6.1), where possible, the time and space dependency of the variables given have been left out of the equations.

To arrive at a finite-dimensional optimization problem, we discretize (6.1) at time $t_k = k\delta_t$, with $k \in \mathscr{K} = \{1, ..., K\}$ using a backward Euler discretization, where $K = (t_f - t_0)/\delta_t$ is the time horizon, in which the step size δ_t is chosen such that $\delta_t(t_f - t_0) \in \mathbb{N}$. Furthermore, (6.1) is discretized in space at position along the width of the cell x_l for $l \in \{1, \ldots, n_n + n_s + n_p\}$ using the finite-volume method, and positions along the radial direction of the particles r_{n,m_n} for $m_n \in \{1, \ldots, n_{r,n}\}$ and r_{p,m_p} for $m_p \in \{1, \ldots, n_{r,p}\}$ in the negative electrode and positive electrode, respectively, using the finite-difference method, as described in Chapter 2. This gives a discrete-time nonlinear optimal-control problem with objective function

$$\min_{\mathbf{c}_{s,k}, \mathbf{c}_{e,k}, \boldsymbol{\phi}_{s,k}, \boldsymbol{\phi}_{e,k}, \mathbf{j}_{1,k}, \mathbf{j}_{2,k}, I_{a,k}} = \frac{\delta_t \delta_n a_s A F}{n_n} \sum_{k \in \mathscr{K}} \sum_{l=1}^{n_n} j_2(x_l, t_k), \tag{6.2a}$$

subject to the model dynamics

$$\mathscr{F}(\mathbf{c}_{s,k}, \mathbf{c}_{e,k}, \boldsymbol{\phi}_{s,k}, \boldsymbol{\phi}_{e,k}, \mathbf{j}_{1,k}, \mathbf{j}_{2,k}, I_{a,k}) = 0, \tag{6.2b}$$

where $\mathscr{F}(\cdot)$ in (6.2b) is given by (4.13)-(4.16), the bounds on the input current,

$$I_{a,\min} < I_{a,k} \leq I_{a,\max}, \tag{6.2c}$$

the inequality constraints,

$$\mathscr{G}(\mathbf{c}_{s,k}, \mathbf{c}_{e,k}, \boldsymbol{\phi}_{s,k}, \boldsymbol{\phi}_{e,k}, \mathbf{j}_{1,k}, \mathbf{j}_{2,k}, I_{a,k}) \leq 0, \tag{6.2d}$$

and the minimum stored-charge constraint,

$$s_K = s_0 + \frac{\delta_t}{Q} \sum_{k \in \mathscr{K}} I_{a,k} \geq s_f, \tag{6.2e}$$

with a given s_0, $\mathbf{c}_{s,0}$, $\mathbf{c}_{e,0}$, s_f. Furthermore, in (6.2), the bold-faced variables are similarly defined as in (2.11), and $\boldsymbol{\phi}_{s,k}$, for example, denotes $\boldsymbol{\phi}_s(k)$. For the remainder of this chapter, the bold-faced variables without a time index indication, e.g. $\boldsymbol{\phi}_s$, will denote

$$\boldsymbol{\phi}_s = [\,\boldsymbol{\phi}_{s,0}\ \boldsymbol{\phi}_{s,1}\ \ldots\ \boldsymbol{\phi}_{s,K-1}\,]^\top. \tag{6.3}$$

The optimization problem as formulated in (6.2) is, computationally speaking, highly complex as the number of decision variables of the optimization problem, given by $\big((5+n_{r,n})n_n+(5+n_{r,p})n_p+2n_s+1\big)K$, quickly increases with the fineness of the chosen discretization. To reduce the computational complexity of (6.2), we can perform a substitution of equations, similar to the method presented in Chapter 2. Since the steps taken in this substitution of equations are largely the same as those in Chapter 2, we refer the reader to the appendix of this chapter for the complete derivation. The resulting reformulated optimization problem, which is given by

$$\min_{\boldsymbol{\phi}_s, I} = Q_l(\boldsymbol{\phi}_s, \mathbf{I}_a), \tag{6.4a}$$

subject to

$$\mathscr{F}_{\text{rf}}(\boldsymbol{\phi}_s, \mathbf{I}_a) = 0, \tag{6.4b}$$

$$\mathscr{G}_{\text{rf}}(\boldsymbol{\phi}_s, \mathbf{I}_a) \leq 0, \tag{6.4c}$$

in which $Q_l(\boldsymbol{\phi}_s, \mathbf{I}_a)$, $\mathscr{F}_{\text{rf}}(\boldsymbol{\phi}_s, \mathbf{I}_a)$, and $\mathscr{G}_{\text{rf}}(\boldsymbol{\phi}_s, \mathbf{I}_a)$ are given in the appendix of this chapter. The objective (6.4a) is further subject to (6.2c) and (6.2e). Note that by comparison to (6.2), (6.4) has only $\big(n_n+n_p+1\big)K$ decision variables. Further note that when assuming $j_2 \ll j_n$, j_1 can be decoupled from j_2, and in $\mathbf{j}_2$ in (6.2) will no longer be a decision variable. This assumption is fair, as the battery should not age significantly within one cycle.

6.2.2. SQP APPROACH TO OPTIMAL AGING-AWARE CHARGING

As (6.4) is a nonlinear optimization problem, obtaining its solution requires a nonlinear optimization solver. In this chapter, we have solved (6.4) using SQP [14], which aims at solving a nonlinear optimization problem by sequentially solving linearly constrained quadratic programs (LCQP), which are formed, e.g., by approximating the objective function with a quadratic equation and linearizing the constraints. In particular, we will solve (6.4) by recursively solving the SQP subproblem

$$\{\hat{\boldsymbol{\phi}}_s, \hat{\mathbf{I}}_a\} = \underset{\boldsymbol{\phi}_s, \mathbf{I}_a}{\operatorname{argmin}} \tfrac{1}{2}\begin{bmatrix}\boldsymbol{\phi}_s \\ I\end{bmatrix}^\top H^i \begin{bmatrix}\boldsymbol{\phi}_s \\ I\end{bmatrix} + \left(F^i\right)^\top \begin{bmatrix}\boldsymbol{\phi}_s \\ I\end{bmatrix}, \tag{6.5a}$$

where

$$H^i = \nabla^2 Q_l(\boldsymbol{\phi}_s^i, \mathbf{I}_a^i), \tag{6.5b}$$

$$F^i = \nabla Q_l(\boldsymbol{\phi}_s^i, \mathbf{I}_a^i)^\top - \nabla^2 Q_l(\boldsymbol{\phi}_s^i, \mathbf{I}_a^i)\begin{bmatrix}\boldsymbol{\phi}_s^i \\ \mathbf{I}_a^i\end{bmatrix}, \tag{6.5c}$$

The objective (6.5a) is subject to the linearized state dynamics

$$\mathscr{F}_{\text{rf}}(\boldsymbol{\phi}_s^i, \mathbf{I}_a^i) + \nabla \mathscr{F}_{\text{rf}}(\boldsymbol{\phi}_s^i, \mathbf{I}_a^i)\begin{bmatrix}\boldsymbol{\phi}_s - \boldsymbol{\phi}_s^i \\ \mathbf{I}_a - \mathbf{I}_a^i\end{bmatrix} = 0, \tag{6.5d}$$

the linearized inequality constraints

$$\mathscr{G}_{\text{rf}}(\boldsymbol{\phi}_s^i, \mathbf{I}_a^i) + \nabla \mathscr{G}_{\text{rf}}(\boldsymbol{\phi}_s^i, \mathbf{I}_a^i)\begin{bmatrix}\boldsymbol{\phi}_s - \boldsymbol{\phi}_s^i \\ \mathbf{I}_a - \mathbf{I}_a^i\end{bmatrix} \leq 0, \tag{6.5e}$$

input bound constraints (6.2c) and the minimum-stored charge constraint (6.2e), for $i \in \mathbb{N}$, and for some suitably chosen $\{\boldsymbol{\phi}_s^0, \mathbf{I}_a^0\}$, such that a feasible solution exists for the next iteration of the SQP subproblem (6.5), on which we will elaborate upon in the next section. For the next iteration $i+1$, $\boldsymbol{\phi}_s^{i+1}$ and $\mathbf{I}_a^{i+1}$ can be given by $\hat{\boldsymbol{\phi}}_s$ and $\hat{\mathbf{I}}_a$, respectively. We have derived the SQP subproblem (6.5) by making a quadratic approximation of (6.4a), and linearizing the nonlinear constraints (6.4b) and (6.4c).

Note that the First-Order Necessary Conditions for optimality (FONC) [17] for (6.5) are identical to the FONC for (6.4) if the SQP problem has converged, i.e., $\boldsymbol{\phi}_s^{i+1} = \boldsymbol{\phi}_s^i$ and $\mathbf{I}_a^{i+1} = \mathbf{I}_a^i$. The SQP algorithm can be terminated when, e.g.,

$$|j^{i+1} - j^i| \leq \Delta_{\text{tol}}, \tag{6.6a}$$

in which Δ_{tol} is a certain specified tolerance, and

$$j^i = Q_l(\boldsymbol{\phi}_s^i, I^i) + \lambda \mathbf{1}^{1\times(n_n+n_p)K} |\mathscr{F}_{\text{rf}}(\boldsymbol{\phi}_s^i, I^i)| \tag{6.6b}$$

is the optimal cost at iteration i, which can be considered as a merit function for the SQP approach (6.5), and where the notation $\mathbf{1}^{n_r\times n_c}$ indicates a matrix of ones with n_r rows and n_c columns. In (6.6b) the weight $\lambda \geq 0$ is chosen such that infeasible solutions to the SQP subproblem (6.5) at iteration i return a higher cost than optimal feasible solutions. Note that in this SQP approach, we allow infeasible solutions for the original nonlinear optimal-control problem at iteration i, and as the algorithm converges, i.e., $|j^{i+1} - j^i| \to 0$, feasibility is obtained in the limit. Further note that we have not included the inequality constraints (6.5e) into the merit function (6.6b), as we assume that when the feasibility of (6.5d), which is included in the merit function (6.6b), holds within a certain tolerance, then the inequality constraints (6.5e) also hold within that same tolerance.

We remark that the state variables, and with that also the constraint (6.5d), may be eliminated in the SQP problem (6.5), by rewriting the linearized state equations (6.5d) in a prediction form, where the state variables are given by a set of prediction matrices and the inputs, i.e.

$$\boldsymbol{\phi}_s = \Pi(\boldsymbol{\phi}_s^i, \mathbf{I}_a^i) + \Gamma(\boldsymbol{\phi}_s^i, \mathbf{I}_a^i)\mathbf{I}_a, \tag{6.7a}$$

where

$$\Pi = -\left(\frac{\partial \mathscr{F}_{\text{rf}}(\boldsymbol{\phi}_s^i, \mathbf{I}_a^i)}{\partial \boldsymbol{\phi}_s^i}\right)^{-1} \left(\mathscr{F}_{\text{rf}}(\boldsymbol{\phi}_s^i, \mathbf{I}_a^i) - \nabla \mathscr{F}_{\text{rf}}(\boldsymbol{\phi}_s^i, \mathbf{I}_a^i) \begin{bmatrix} \boldsymbol{\phi}_s^i \\ \mathbf{I}_a^i \end{bmatrix}\right), \tag{6.7b}$$

$$\Gamma = -\left(\frac{\partial \mathscr{F}_{\text{rf}}(\boldsymbol{\phi}_s^i, \mathbf{I}_a^i)}{\partial \boldsymbol{\phi}_s^i}\right)^{-1} \frac{\partial \mathscr{F}_{\text{rf}}(\boldsymbol{\phi}_s^i, \mathbf{I}_a^i)}{\partial \mathbf{I}_a^i}. \tag{6.7c}$$

By substituting (6.7) into the objective function (6.5a) and the inequality constraints (6.5e), as is often done in model-predictive control, we can arrive at an SQP subproblem with only the input variables as decision variables, and the state variables can be updated with (6.7).

6.2.3. INITIALIZATION OF THE SQP ALGORITHM

As we can observe from (6.5), the SQP algorithm needs to be initialized with an initial guess $\boldsymbol{\phi}_s^0$ and $\mathbf{I}_a^0$ for the decision variables $\boldsymbol{\phi}_s$ and $\mathbf{I}_a$. Choosing a good initial guess is important, particularly when optimizing with the DFN model, for two reasons. The first reason is that with a good initial condition, the SQP algorithm will require fewer iterations i to converge, and will converge monotonically, i.e., the cost strictly decreases after each iteration. The second reason has to do with the fact that in the SQP approach we allow infeasible solutions at iteration i, and therefore we allow $\mathscr{F}_{\text{rf}}(\boldsymbol{\phi}_s^i, \mathbf{I}_a^i) \neq 0$. Therefore, it can occur that at iteration i, the linearized system is far from physically meaningful, and (6.5) becomes numerically sensitive due to the the logarithmic term in (4.13d), the various root terms in (4.15), and the exponential term in (4.16). Particularly, this can occur when the initial guess $\boldsymbol{\phi}_s^0, \mathbf{I}_a^0$ is far from the optimal solution $\boldsymbol{\phi}_s^*, \mathbf{I}_a^*$, such that the calculated Newton step in the SQP subproblem leads to a large change from $\boldsymbol{\phi}_s^i, \mathbf{I}_a^i$ to $\boldsymbol{\phi}_s^{i+1}, \mathbf{I}_a^{i+1}$, which will in turn lead to a large change from $\mathscr{F}_{\text{rf}}(\boldsymbol{\phi}_s^i, \mathbf{I}_a^i)$ to $\mathscr{F}_{\text{rf}}(\boldsymbol{\phi}_s^{i+1}, \mathbf{I}_a^{i+1})$, for which then the aforementioned numerical inaccuracies can occur. Note that as long as the initial guess is feasible, i.e., $\mathscr{F}_{\text{rf}}(\boldsymbol{\phi}_s^0, \mathbf{I}_a^0) = 0$, the numerical inaccuracies can be avoided by taking a sufficiently small step, i.e.,

$$\mathbf{I}_a^{i+1} = \lambda_s \hat{\mathbf{I}}_a + (1 - \lambda_s)\mathbf{I}_a^i, \tag{6.8}$$

where $\lambda_s \in [0, 1]$ can be chosen to warrant convergence. However, when $\lambda_s < 1$, convergence will also be slower, and therefore, λ_s should be 1 ideally. This can be achieved by an adequate intitial condition, to which we can assign two criteria, based on the observations above, i.e.,

- The initial guess should be feasible in the sense that $\mathscr{F}_{\text{rf}}(\boldsymbol{\phi}_s^0, \mathbf{I}_a^0) = 0$. In doing so, we can ensure that at least in the first iteration of the SQP algorithm, numerical inaccuracies do not occur.
- The initial guess should be somewhat close to satisfying the constraints. By choosing an initial guess that is close to satisfying the constraints, the solution to the first LCQP problem at iteration 1 does not need to substantially differ from the initial guess. For example, when the initial guess for $\mathbf{I}_a$ is chosen as zero, the initial guess will be far from satisfying the minimum stored-charge constraint (6.2e) (assuming, of course, a realistic choice for s_0 and s_f). The solution to the LCQP at the first iteration will ensure that this constraint is met, as it is a linear constraint, and the resulting solution will be far from the initial guess.

When determining an initial guess for $\boldsymbol{\phi}_s$ and $\mathbf{I}_a$, generally, first an initial guess for $\mathbf{I}_a$ is determined, from which $\boldsymbol{\phi}_s^0$ can be obtained by simulating the DFN model with $\mathbf{I}_a^0$. However, it can quite easily occur that the guessed current leads to the situation $c_s > c_s^{\max}$, $c_s < 0$ or $c_e \leq 0$, which is numerically an issue due to the logarithmic term in (4.13d) and the various root terms in (4.15). Thus, a methodological approach is required to reliably obtain an adequate initial guess. Note that based on the analysis done in Chapter 5, if the constraints

$$c_s(\delta_n, R_n, t) \leq c_{s,n}^{\max}, \quad c_s(L - \delta_p, R_p, t) \geq 0, \quad c_e(0, t) > 0, \tag{6.9}$$

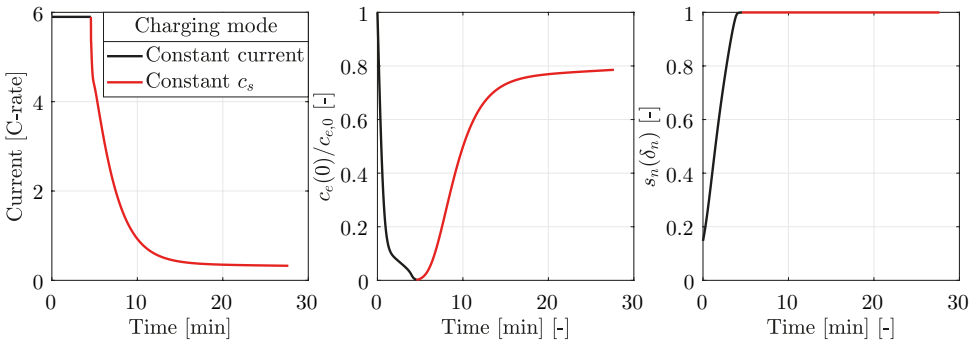

Figure 6.1: Constant-current-constant-c_s approach to obtain an initial guess of the decision variables for the optimization problem (6.5).

are satisfied, then the constraints $c_s(x,r,t) \leq c_s^{\max}$, $c_s(x,r,t) \geq 0$, and $c_e(x,t) > 0$ will also be satisfied. Then, we propose to base the initial guess to the original optimization problem (6.4) for a particular charging time on an approximate solution to the problem where the battery is charged in a minimum amount of time, i.e.,

$$\min_{c_s,c_e,\phi_s,\phi_e,j_1,j_2,I_a,t_f} t_f - t_0, \tag{6.10}$$

subject to (6.9) and the minimum-stored charge constraint (6.2e). An approximate solution to this problem can be reasoned as follows. In the first stages, the current is set to a maximum bound $I_{\max}$, which should be chosen as large as possible, while keeping $c_e > 0$, until either of the other limits $c_s > c_s^{\max}$ or $c_s < 0$ are met. However, we should remark that the choice for $I_{a,\max}$ is not crucial, as making it lower than necessary will only result in a larger charging time, which can still be sufficiently small for the purpose of finding an initial guess. Then, the battery is operated at whatever limit it has met first, until the next limit is met, after which the battery is kept at that limit. At any stage, if the minimum-stored charge constraint (6.2e) is met, the approximate solution $\mathbf{I}_a^*$ has been found, which charges the battery with a $t_f^* - t_0$ charging time. Note that keeping the battery at the limit defined by $c_e > 0$ should be avoided, because charging the battery at the limits defined by $c_s > c_s^{\max}$ or $c_s < 0$ is faster, since the amount of charged stored in the battery is directly related to these quantities, while that is not the case for c_e. Fig. 6.1 illustrates this with an example, where we can see that after charging with a large constant current, while avoiding $c_e \leq 0$, the limit $c_s = c_s^{\max} - \epsilon$ is reached, where ϵ is some small number, after which the battery is kept at this limit until it is fully charged. The applied current in the stages where it needs to be determined, can be found relatively easily by extending the model implementation given in Chapter 2 with an additional algebraic equation corresponding to the particular stage which the battery is in. For instance, if the battery is in a constant-c_s stage, we would need to add the algebraic equation $c_s(x_{n_n}, r_{n_{r,n}}, t_k) = c_s^{\max} - \epsilon$ to (2.14) and then solving the resulting set of algebraic equations in the same way as described in Chapter 2. Note that the battery is not kept at $c_s = c_s^{\max}$, as solving the resulting algebraic equations is numerically difficult, and instead the battery is kept slightly below this limit. The initial guess for the optimization

problem (6.2) for a particular charging time $(t_f - t_0) \geq (t_f^* - t_0)$, can then be found by scaling the approximate solution $\mathbf{I}_a^*$ as

$$I^0(t) = \frac{t_f^* - t_0}{t_f - t_0} I^*(t \frac{t_f^* - t_0}{t_f - t_0}), \tag{6.11}$$

and $\boldsymbol{\phi}_s^0$ is obtained by simulating the DFN model with I^0.

6.3. SIMULATION STUDY

In this section, we will validate the proposed optimal aging-aware charging method. In doing so, we will firstly compare the computational complexity of several solution methods based on the choices made in Section 6.2, as well as a solution method that uses an off-the-shelf solver. Then, we will study the impact of the coarseness of the spatial and temporal discretization of the optimal-control problem (6.2). This is followed by a study where several models for optimal aging-aware charging are compared in terms of the accuracy of the model output as well as the internal states. Here, we define a synthetic cell, that has concentration-dependent parameters as well as an error in the electromotive force (EMF), that represents a "true" battery, to which the other models (without concentration-dependent parameters and with the original EMF) are fit to, similar to the study done in Chapter 3. Specifically, we consider here the (simplified) DFN model, the SPM, and the surrogate modeling approach presented in Chapter 5. Finally, we will compare several aging-aware charging methods, including the multi-stage charging approach proposed in Chapter 4, the optimal-control approach using a surrogate model in Chapter 5, and the method proposed in this chapter. Additionally, we also include an optimal-control approach using the SPM in this comparison. The methods are validated against the optimal-control approach presented in this chapter using the synthetic cell model, which represents the best achievable trade-off between charging time and aging.

6.3.1. COMPARISON OF SOLUTION METHODS

In Section 6.2.2, we have made several choices in the formulation of the SQP subproblem. Firstly, we proposed to apply the method for the substitution of equations to arrive at (6.4). However, it is also possible to apply the SQP approach on the original discrete-time optimal-control problem (6.2). In this case, the various derivative matrices, i.e., the Jacobians and Hessian used in (6.5) would be highly sparse, of which solvers can possibly take advantage of. A second choice that has been made in Section 6.2.2 is that we have proposed to substitute the linearized state equations (6.5d) into the objective function and constraints of (6.5). In this way, the resulting SQP subproblem has only the input variables I as decision variables. However, the computation of the matrices in (6.7) involves either solving an inverse or solving a system of linear equations, which both may take a significant amount of computation time. To study impact of these choices on computation time, we have implemented the SQP problems resulting from the various possible combination of choices, which we will denote as follows:

- Variant 1A: (6.2) is solved using SQP without substituting the linearized dynamics into the objective function and constraints.

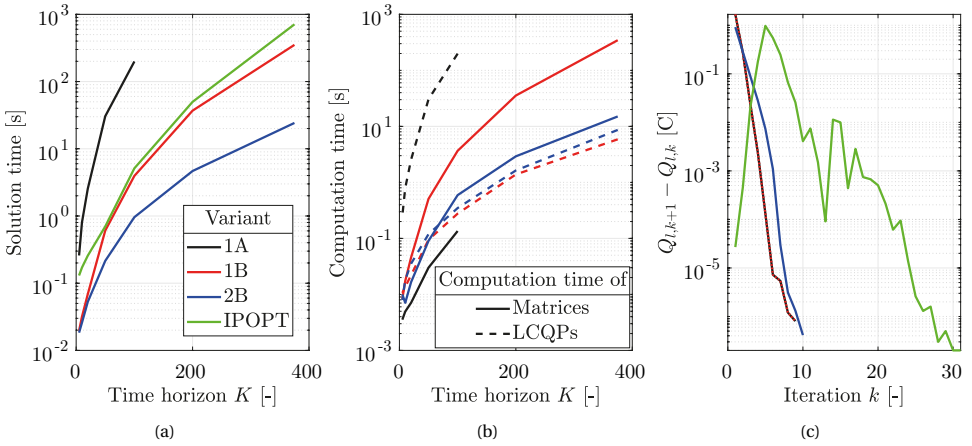

Figure 6.2: Results showing the comparison between the various considered solution methods, where in (a) the effect of the time horizon on the solution time of the optimization problem is shown, in (b) the computation times of the matrices in (6.5) and (6.7), and the computation time of the QP problem (6.5) is shown, and in (c) the convergence of the various solution methods is shown. Note here that the convergence of Variants 1A and 1B coincides exactly.

- Variant 1B: (6.2) is solved using SQP with the substitution of the linearized dynamics into the objective function and constraints.
- Variant 2A: (6.4) is solved using SQP without substituting the linearized dynamics into the objective function and constraints.
- Variant 2B: (6.4) is solved using SQP with the substitution of the linearized dynamics into the objective function and constraints. This is the proposed method.

We will furthermore solve (6.4) using IPOPT [13] to show the advantage of using the proposed SQP approach. Note that IPOPT optionally allows the Hessian function of the optimization problem to be specified by the user. However, determining the Hessian function is not trivial, and therefore this option has not been used, which means that the Hessian is approximated numerically by IPOPT. This may result in a slower convergence of the algorithm used in IPOPT. However, we have specified the Jacobian of the objective function and the nonlinear dynamics to IPOPT, as these are also used in the SQP approach. Further note that we have also solved (6.2) using IPOPT, however, this implementation was slower than when solving (6.4) with IPOPT, and therefore this implementation has been left out of the results shown below. Finally, we note that Variant 2A is also not shown in the results below, as the H^i matrix was nonconvex, even at a (locally) optimal solution (obtained using any of the other variants). However, when substituting the state dynamics into the objective function, as is done in Variant 2B, and as also described above, the objective function of the LCQP becomes convex.

In Fig. 6.2a, the solution times for the various considered variants is shown for a range of time horizons K. In these simulations, the grid parameters have been chosen as $n_n = n_s = n_p = n_{r,n} = n_{r,p} = 3$, and the battery is charged from 20% SoC to 99% in a given

charging time of 50 minutes. The time horizon is then varied by varying the step size δ_t. We observe that Variant 1A is the slowest in terms of computation. In Fig. 6.2b, we can see that the bottleneck in the solution time for this variant is given by the total time it takes to solve the LCQPs given by (6.5), which have vastly more decision variables than the LCQPs of Variants 1B and 2B. For example, with $K = 100$, the number of decision variables for the LCQPs of Variant 1A is 4900, while the number of decision variables for the LCQPs of Variants 1B and 2B is only 700. On the other hand, the computation time of the matrices in (6.5) and (6.7) actually takes the least amount of time compared to the other variants. This is largely because in Variant 1A the matrices in (6.7) do not need to be computed, which involves either computing an inverse or solving a linear system of equations, where both are computationally intensive operations. We can furthermore observe that the computation time of the LCQPs for Variants 1B and 2B is roughly the same, since they both have an equal amount of decision variables, while the large difference in solution time is caused by the computation time of the matrices. This is due to the fact that for Variant 1B, the matrices that are computed in (6.7) are of a significantly larger size than for Variant 2B. Thus, we observe that Variant 2B strikes the best balance in the computational effort required to compute the various matrices in (6.5) and (6.7), and the computational effort in solving the LCQPs of the SQP algorithm.

In Fig. 6.2a, we can also see the solution time of solving (6.4) with IPOPT. While IPOPT is much faster than Variant 1A and almost as fast as Variant 1B, it is roughly an order of magnitude slower than Variant 2B. In Fig. 6.2c, we can see that this is partly because IPOPT takes about 3 times as many iterations as the other variants to converge to the same solution. We can further see that all SQP variants converge at roughly the same speed, where Variants 1A and 1B converge in exactly the same manner, as these variants both solve the same SQP subproblem derived from (6.2), with the only difference being the method for solving the LCQPs, whereas Variant 2A solves the SQP subproblem derived from (6.4). However, the average computation time per iteration is also significantly larger for IPOPT, which could be because IPOPT has to numerically approximate a Hessian at every iteration. Therefore, if an analytic Hessian function would be supplied to IPOPT, a faster implementation could be obtained. However, besides the second derivates of the objective function, the Hessian function also requires the second derivatives of the constraints, which are not necessary for the proposed SQP approach, which can be seen as an advantage. Another advantage of the proposed SQP approach over IPOPT is that it is simpler in implementation, and therefore can more easily be implemented on an embedded system.

6.3.2. IMPACT OF DISCRETIZATION ON THE PARETO FRONT

As we have shown in Chapter 2, the spatial discretization of the DFN model has a large influence on the resulting computational complexity. Besides varying the spatial discretization of the DFN model, the choice for the coarseness of the temporal discretization of the optimization problem (6.4) is also of importance, as the number of decision variables for the optimization problem (6.4) decreases inversely with an increasing step size δ_t. To study the impact of spatial and temporal discretization of (6.4), we define a base choice of discretization that is fine, and compare different combinations of spatial and temporal discretization to this base choice. To define this base choice, we firstly de-

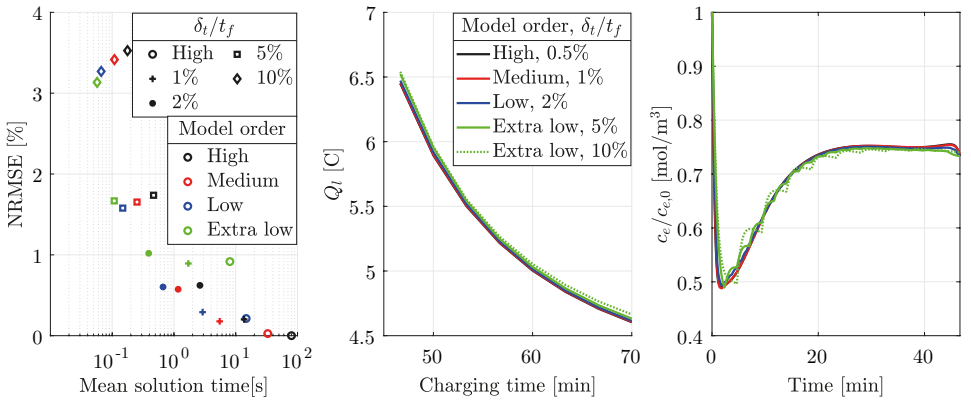

Figure 6.3: Results showing the trade-off that can be made in computational complexity and model accuracy by varying the spatial and temporal discretization for the purpose of optimal aging-aware charging, where in (a) the normalized root-mean-square error (NRMSE) and solution time of the optimization problem is shown, in (b) the obtained Pareto fronts using various combinations of spatial and temporal discretization are shown, and in (c) where the electrolyte concentration for these various combinations is shown.

fine various levels of model orders to consider, shown in Table 6.1, which have been obtained with the same methodology as presented in Chapter 2. In Table 6.1, the normalized root-mean-square error (NRMSE) given by (2.18) in relation to the output voltage of a base DFN model with grid parameters $n_n, n_s, n_p, n_{r,n}, n_{r,p} = 40$ is also shown. Then, the base choice of discretization that we compare other choices to is given by the combination of the high-order spatial discretization and a step size given by $\delta_t = 0.005\, t_f$, with $t_0 = 0$. For each combination of model order and step size, we solve (6.4) for a range of charging times, and then simulate the resulting solution with a DFN model with the high model order and a step size of 1 s.

In Fig. 6.3a, the NRMSE between the various considered combinations and the base choice of discretization, and the mean solution time of (6.4) for the range of charging times is shown. Specifically, the mean solution time of a particular combination of spatial and partial discretization is computed from the mean of the solution times of solving the optimization problem (6.4) for the range of charging times shown in Fig. 6.3b. We can firstly observe that even with a coarse spatial and temporal discretization, the resulting NRMSE can still be considered to be very low, as also illustrated in Fig. 6.3b. Note we can also observe that at large step sizes, it can occur that the combination of a large step

Table 6.1: Selected grid parameters of the varying degrees of model orders shown in Fig. 6.3.

Model order	Grid param.*	NRMSE [10^{-3}]
Extra low	[6, 2, 5, 3, 3]	9.6
Low	[8, 2, 6, 3, 3]	5.6
Medium	[11, 2, 8, 3, 3]	2.7
High	[16, 2, 12, 3, 3]	0.98

*The order of the grid parameters is $[n_n, n_s, n_p, n_{r,n}, n_{r,p}]$.

size and a high model order gives a larger NRMSE than the combination of a large step size and a low model order, which is counter-intuitive. This can be explained by the fact that, at large step sizes, the errors made due to the choice of step size dominate over the errors made due to the choice in model order. Since all solutions are simulated with the same model, it can then coincidentally occur that with the choice of a large step size, a higher model order shows a larger error than a lower model order.

While Fig. 6.3b shows that the obtained Pareto front with a large step size (dashed green line) shows a small error compared with the base Pareto front (black line), from Fig. 6.3c, we can see that the representation of the internal states is more significantly affected by the choice of the step size, which is especially relevant when the goal is to constrain the internal states to avoid certain regions (that are not considered in the aging model) in order to avoid excessive aging or to ensure a safe operation of the battery. Therefore, based on the results shown in Fig. 6.3, a good choice of discretization is an extra-low model order with a step size $\delta_t = 0.05 t_f$, achieving a mean solution time of 0.1 s, a NRMSE less than 2% (green square in Fig. 6.3a), and still an adequate description of the internal states. These results show that with the proposed SQP approach, and with a well-considered choice of spatial and temporal discretization of the optimization problem, the optimal aging-aware charging problem with the DFN model can be solved with a small computation time, which makes it suitable for a closed-loop implementation. Note that the solution times achieved here are with a control horizon that spans the entire charging time, which is in contrast to the MPC approaches taken in, e.g., [10, 11], where similar solution times were reported for a control horizon of only 5 time steps.

6.3.3. COMPARISON OF MODELS FOR OPTIMAL AGING-AWARE CHARGING

In the previous chapters, we have compared our proposed methods for aging-aware charging with the assumption that the DFN model represents a "real" battery. However, in doing so, we ignore any modeling errors that can also further affect the effectiveness of the proposed methods. Specifically, in the method proposed in Chapter 4, we select the design-adjustable variables of the multi-stage protocols using a DFN model, which is the same DFN model that is then used to validate the method. However, in reality, the methods should be validated with a real battery, although this would require extensive experimental work, which was not intended for the work done in Chapter 4. To reflect the effect of modeling errors on the proposed aging-aware charging methods, in this section, we represent the "true" battery with a DFN model, which we will refer to as the synthetic cell, that has concentration-dependent parameters, as well as an error in the electro-motive force (EMF), similar to the approach taken in Chapter 3. A DFN model without concentration-dependent parameters, which we will refer here to as the simplified DFN (SDFN) model, is then parameterized with the method described in Chapter 3. The aging-aware charging methods described in Chapters 4 and 5, as well as the method proposed in this chapter are then based on this estimated model, and all the methods are validated on the synthetic cell.

The parameters of the synthetic cell model are shown in Table 6.2, and are based on one of the parameter sets that have been obtained based on the experimental data presented in Chapter 7. The parameters $\hat{D}_{s,p}$ and $\hat{D}_e$ are considered to concentration-

dependent, and are given by

$$\hat{D}_{s,p}(s_p) = 2.6603 \times 10^{-4+21.5(s_p - s_{p,100\%})^2}, \tag{6.12a}$$

$$\hat{D}_e(c_e) = 0.17 \exp(\tfrac{-0.65 c_e}{c_{e,0}}), \tag{6.12b}$$

of which the type of functions have been chosen roughly based on the concentration-dependency of the parameters observed in Fig. 2.2 in Chapter 2 and the measured EMF of the battery used in Chapter 7 is also adapted to reflect an error in the EMF, as follows

$$U_{\text{EMF}}(s_c) = \bar{U}_{\text{EMF}} + 0.01 \sin(4\pi s_c), \tag{6.12c}$$

where $\bar{U}_{\text{EMF}}$ is the original EMF. The various values in (6.12) have chosen such that an RMSE of around 10 mV between the synthetic cell model output and the estimated model using the input currents shown in Fig. 6.4, which are the same current profiles that have been used in the experimental work of Chapter 7. This is a realistic error that has been observed in the analysis of the experimental data that will be presented in Chapter 7 as well. We should remark that in this chapter, aside from the parameters listed in Table 3.4, we also estimate $\frac{\partial \ln c_e}{\partial x}$ as a parameter, which was assumed to be zero in Chapter 3. We further remark that the range for $s_{n,100\%}$ has been chosen as $[0.7, 0.8]$ to reduce the effect of numerical sensitivities due to the root terms in the exchange current density i_0 in (2.5c). Such numerical sensitivities can occur when c_s is close to $c_s^{\max}$, where in the process of numerically solving the DFN model equations, c_s may exceed $c_s^{\max}$, leading to negative values in the root terms in i_0 in (2.5c). This is particularly a problem when simulating with a current profile that has been obtained using a different model, where in the model that is simulated with, c_s may reach $c_s^{\max}$ sooner than the model that has been used to determine the optimal current profile. By reducing the bounds in the range of $s_{n,100\%}$, this problem can be somewhat mitigated.

Aside from considering the methods proposed in Chapter 4, Chapter 5, and this chapter, we also compare these methods with an optimal-control approach with the

Table 6.2: Parameters of the synthetic cell model.

Parameter	Unit	Cell	Neg. electrode	Separator	Pos. electrode
Q	[C]	10802	-	-	-
$\hat{R}_{\text{cc}}$	[Ω]	0.000736	-	-	-
$s_{0\%}$	[−]	-	0.037	-	0.922
$s_{100\%}$	[−]	-	0.747	-	0.379
$\hat{D}_s$	[s^{-1}]	-	0.000343	-	*
$\hat{D}_e$	[Cs^{-1}]	-	*	*	*
$\hat{p}$	[−]	-	144	21785	638
t_+^0	[−]	-	0.306	0.306	0.306
$\hat{\sigma}$	[Ω^{-1}]	-	6.81×10^6	-	7.61×10^4
$\hat{\kappa}$	[Ω^{-1}]	-	3.62	3.62	3.62
$\hat{R}_f$	[Ω]	-	0.000443	-	0
α_a	[−]	-	0.506	0.506	0.506
$\hat{k}_0$	**	-	0.000361	-	0.000923
$\hat{\varepsilon}_e$	[C]	-	6927	586	2475

*Concentration-dependent parameters, given by 6.12

**[$\text{s}^{-1} \cdot (\text{m/mol})\hat{}(3(1-2\alpha_a))$]

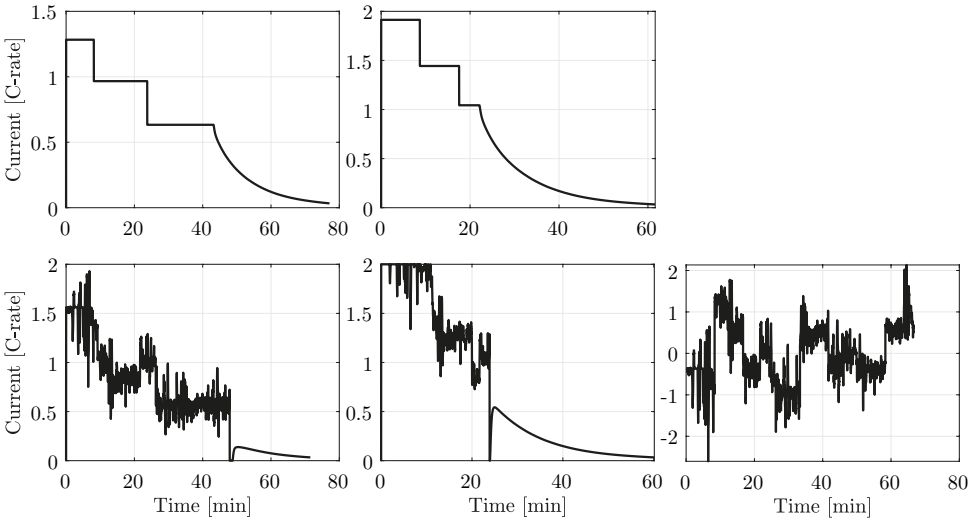

Figure 6.4: Current profiles used to generate data with the synthetic cell model for parameter estimation.

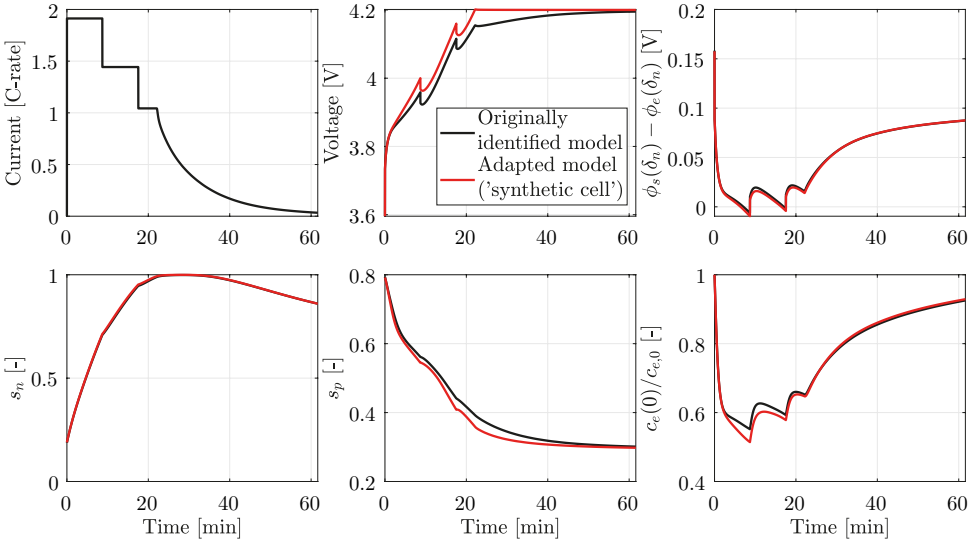

Figure 6.5: Difference between the output voltage and various internal states of the DFN model simulated with the original parameters obtained from the experimental data shown in Fig. 7.4 presented in Chapter 7, and the DFN model simulated with the synthetic cell model parameters.

SPM. Specifically, the SPM is used to solve the problem formulated in (6.1), since the SPM often used in literature for the purpose of aging-aware charging, see e.g. [5, 7]. The parameters of the SPM are estimated in the same way as for the SDFN, based on the same estimation data that has been generated with the synthetic cell.

In Fig. 6.5, the difference in the output voltage and several internal states is shown

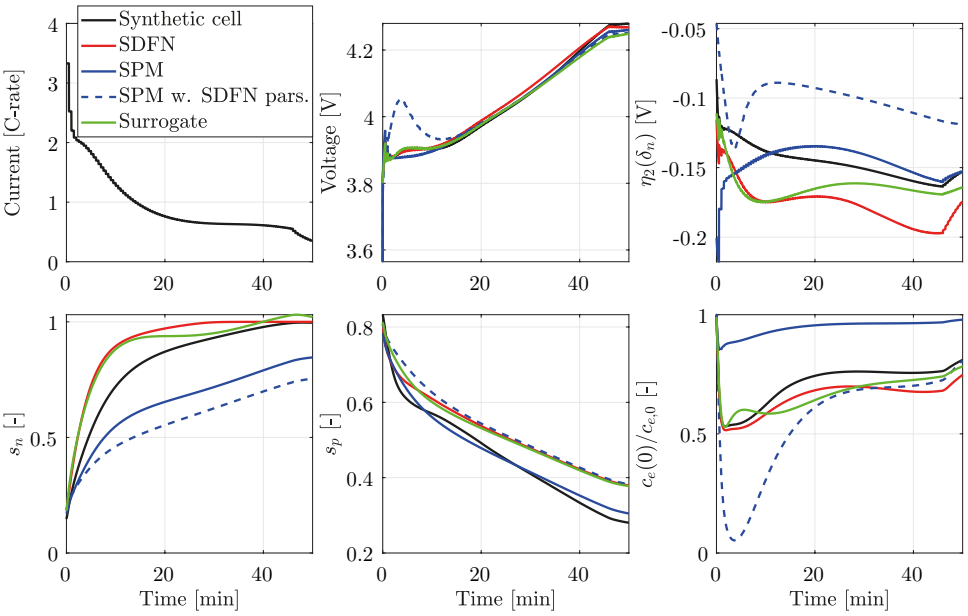

Figure 6.6: Comparison of the output voltage and several internal states resulting from the various considered models. The dashed-blue line has been obtained by simulating the SPM model with the same parameters that have been used to simulate the SDFN model. Further note that s_n is the stoichiometry at $x = \delta_n$, and s_p is the stoichiometry at $x = L - \delta_p$.

for the DFN model simulated with the original parameters obtained based on experimental data and the synthetic cell. It can be seen that the differences in the internal states can be considered to be small, while the difference in the output voltage can be considered large, which is around 28 mV for the data shown in Fig. 6.5. Furthermore, it seems that the difference in the output voltage is mostly caused by a difference in the positive-electrode solid-phase diffusion dynamics and a difference in the electrolyte diffusion dynamics. This can be explained by the fact that the concentration-dependent parameters introduced have a direct influence exactly on the two aforementioned dynamics. This again shows the difficulty in estimating the DFN model parameters based on only input/output data, as over-fitting of the parameters to the data can easily occur, since a small change in the internal model dynamics can lead to a large change in the output voltage, as can be observed from Fig. 6.5.

In Fig. 6.6, a validation simulation is shown of the various models that are considered in this study. As described above, the parameters of the models have all been estimated based on the same synthetic estimation data, of which the data shown in Fig. 6.6 is not a part of. The surrogate model parameters are based on the identified SDFN model using the methodology described in Chapter 5. Note that with the surrogate model it is crucial that the estimation data represents the data to which it will be applied to. Therefore, the surrogate model has been determined based on data obtained from solving the problem (6.2) with the identified SDFN model for two different charging times (specifically,

50 minutes and 83 minutes) when charging the battery from 20% to 99%. In Fig. 6.6, we observe that, with all models (excluding the dashed-blue line), an adequate fit to the output voltage is obtained of around 12 mV RMSE. However, the differences in the internal states are substantially larger. Notably, all the determined models seem to estimate the side-reaction over-potential η_2 conservatively, i.e., the estimated η_2 is at its extreme larger for the identified models compared to the η_2 from the synthetic cell. It is also notable that the SPM seems to perform rather well (in describing the output voltage) for what can be considered a high-energy (HE) cell, while with the HE cell parameters considered in Chapter 2, the output voltage of the SPM deviated significantly from the output voltage of the DFN model. On the other hand, we observe that most of the internal states are not adequately described by the SPM. The dashed-blue line in Fig. 6.6 shows the resulting output and internal states when simulating the SPM with the parameters obtained from estimation with the SDFN model. We observe then that both the output voltage and internal states do not correspond well to those of the SDFN model, which shows that the internal states described by the SPM in this case are not physically meaningful, even if its parameters would be physically meaningful. This supports the conclusion that the SPM does not adequately describe the internal dynamics of the battery, and therefore caution should be taken when using the SPM, particularly for HE cells.

We can furthermore observe from Fig. 6.6 that the estimated internal states of the SDFN model also deviate significantly from those of the synthetic cell, especially compared to the differences in internal states shown in 6.5. This supports the conclusion made in Chapter 3, that cell teardown should be used to determine tighter parameter ranges, in order to avoid over-fitting of the parameters to the estimation data. Finally, we can observe that the output voltage of the SDFN model and the surrogate model correspond relatively well, which additionally validates the surrogate modeling approach.

6.3.4. PARETO-OPTIMAL-FRONT COMPARISON

The Pareto front for the various approaches are shown in Fig. 6.7a. Here, the battery is charged from 20% to 99% with various charging times. Based on the conclusions stated in Section 6.3.2, the grid parameters of the SDFN model are selected as the extra-low model-order grid parameters, and the step size is selected as $\delta_t = 0.05 t_f$. The grid parameters of the synthetic cell model have been selected as the high model-order grid parameters, and the step size has been selected as $\delta_t = 0.005 t_f$. For the surrogate model, the step size is selected as $\delta_t = 0.01 t_f$, which we have found to strike a good balance between the solution time and the obtained Pareto front. The grid parameters of the SPM have been selected as the high model-order parameters, as for the SPM approach the difference between the solution time with the high model-order parameters and extra-low model-order parameters was marginal. Furthermore, for the SPM approach, the step size is selected as $\delta_t = 0.02 t_f$. The design-adjustable parameters of the CC-CV(1) and 3-CC-CV(5) protocols have been determined using the SDFN model with the methodology presented in Chapter 4. Note that the 3-CC-CV(5) protocol has 5 design-adjustable parameters, namely 3 CC-stage currents and 2 voltage thresholds, which specify when to switch to the next CC-stage. Therefore, with 5 parameters, it is not computationally feasible to find the best combination of parameters using brute-force optimization, as done in Chapter 4. Instead, we have found the parameters by switching the CC-stage currents

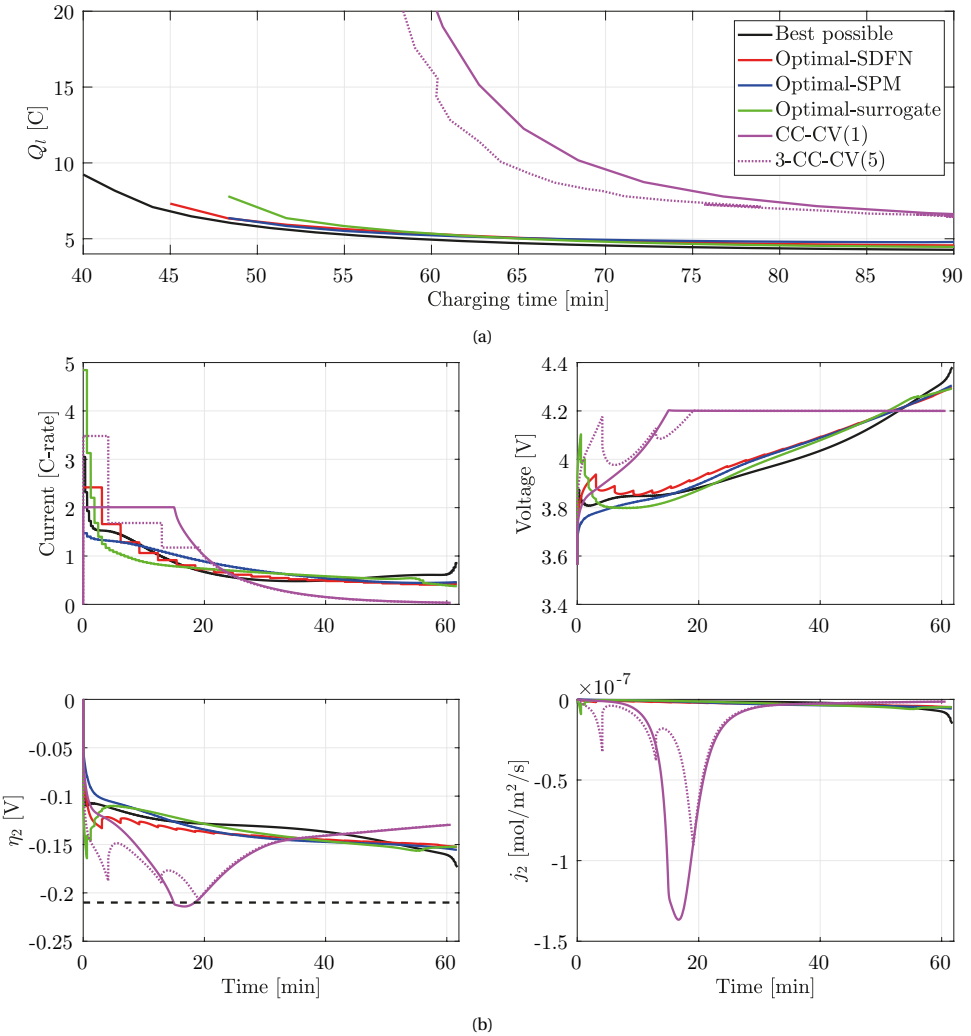

Figure 6.7: Comparison of the Pareto optimal fronts of the various considered aging-aware charging approaches, where in (a) the trade-off between charging time and Li-ion loss due side reactions Q_l is shown, and in (b) the current, voltage, side-reaction over-potential η_2 and side-reaction flux j_2 for the various aging-aware charging approaches is shown for a charging time of around 61 minutes. The dashed black line in (b) represents the threshold for when lithium plating occurs [16].

based on SoC thresholds, since we have found the obtained Pareto optimal front to be less sensitive to the selection of SoC thresholds than voltage thresholds, similar to what has been done in e.g., [3, 18]. The corresponding voltages at the threshold SoC are then selected as the threshold voltages, essentially leading to closed-loop controlled charging based on voltage levels. Finally, the multi-stage protocols are terminated when the CV-stage current becomes smaller than 1 A, which generally corresponds to the battery

being charged to around 99%.

The resulting current profiles from the various approach are all simulated with the synthetic cell model with $\delta_t = 1s$ and the high model-order parameters. Furthermore, we note that with the optimal approaches, the Pareto front could not be obtained for the same range as shown for the synthetic cell, because at low charging times, the solid-phase concentration c_s in the negative electrode would reach $c_s^{\max}$ sooner in the various models used in the optimal approaches than in the synthetic cell model with a particular current profile, as explained before. Note that this is a limitation of the DFN model. In reality, this would not be a limitation, of course, although over-lithiation of the negative electrode material can also have averse aging effects [19], although these aging effects are not considered in this study. Finally, we remark that in this simulation study, we apply the computed current profiles from the optimal approaches in open-loop to the synthetic cell. Unlike the multi-stage charging protocol, where the charging protocol switches the applied current based on voltage levels, robustness to modeling errors is not present in the optimal approach.

In Fig. 6.7a, we can first observe that, as could be expected, the optimal approaches have a substantially better Pareto front than the CC-CV and 3-CC-CV protocols. With a 60-minute charging time, for example, a roughly 2 times reduction in Li-ion loss due to side reactions is achieved with the optimal approaches compared to the 3-CC-CV(5) protocol. In Fig. 6.7b, we can see why a large difference between these approaches is observed. Due to the fact that the multi-stage protocols do not exceed 4.2 V, the charging protocols have a relatively long CV stage, in which the battery cannot be charged much, which also means that the battery has to be charged more in the CC-stage(s) with a relatively higher current compared to the optimal approaches. These large currents lead to a high side-reaction over-potential, which in turn leads to a large amount of Li-ion loss. Note that while the optimal approaches show a higher maximum voltage than the 3-CC-CV(5) protocol, the battery is not charged more with the optimal approaches than with the 3-CC-CV(5) protocol, which means that the EMF voltage at the end of charging is the same for all the various charging methods. This is in contrast to other studies, e.g., [20], where a higher CV voltage of their proposed fast-charging protocol leads to harmful effects. At the charging time of 61 minutes shown in Fig. 6.7b, the CC-CV(1) protocol even exceeds the lithium-plating threshold, which is $-0.21V$ in this case [16], indicated by the dashed black line. We can further observe that the 3-CC-CV(5) protocol does not exceed this threshold, and yet its current profile leads to a considerably larger aging compared to the optimal approaches. This again shows the importance of considering an actual aging model in aging-aware charging, since just imposing the lithium plating constraint $\eta_2 > -0.21$, as done in e.g., [4, 21–23], renders it impossible to make an effective trade-off between charging time and aging.

We can furthermore see in Fig. 6.7a that all the optimal approaches are close to the best possible Pareto front, obtained by solving the optimal aging-aware charging problem (6.1a) with the synthetic cell model. This shows that the accuracy of the model used is not crucial for obtaining a good trade-off between charging time and aging, as long as constraints on the internal states are not considered. This also means that, at least for the considered model parameters, modeling errors do not have a large effect on the minimization of Li-ion loss due to side reactions, which bodes well for a practical ap-

plication of these methods. We can observe in Fig. 6.7b that the charging currents of the optimal approaches also significantly differ from each other, and yet lead to similar amount of Li-ion loss. This suggests that the amount of Li-ions lost due to side reactions is not particularly sensitive to the exact choice of current profiles, which also explains why the Pareto front of the various optimal protocols are close to each other. The crucial aspect to avoid excessive aging seems to be to minimize the time spent in CV mode, by allowing a larger maximum voltage, and thereby allowing the battery to be charged relatively more in the final stages of charging.

While the optimal approaches show a good performance in 6.7a, their practical implementation should be considered. Firstly, we notice that the output voltage can become considerably large, up to around 4.3V. Although this does not have any averse aging effects according to the considered side-reaction model, in reality, it could be desirable to avoid excessively large voltages, as this could lead to unsafe phenomenons that have not been modeled. Secondly, in the considered approach, the current profiles are computed for a specific amount of charge transfer $s_f - s_0$. In a practical situation, the initial state of charge and the capacity of the cell may not be estimated accurately, which could lead to over-charging of the battery if care is not taken. Therefore, there should be some form of feedback in a practical implementation, in order to ensure that, at least, the battery is not overcharged. This could be achieved using a closed-loop optimal-control approach, as done in, e.g., [9–11] or a reference tracker approach, as done in, e.g., [24]. However, for these approaches, a state estimator is necessary, which additionally complicates the implementation. A relatively straight-forward alternative is to charge the battery with the computed optimal profile up to a maximum threshold voltage (if this is reached), after which the battery is relaxed until it reaches a threshold CV voltage, e.g., 4.2 V, followed by a CV stage until the threshold current of 1 A (corresponding to about 0.03 C-rate) is reached. In the next simulation study, we apply the latter approach to study its impact on the achievable Pareto front.

The results of this study are shown in Fig. 6.8. Here, the maximum allowable voltage is set to 4.28 V. Note here also that the Pareto front using the synthetic cell has been computed with a 4.28 V constraint on the output voltage, to reflect the best possible Pareto front with a 4.28 V voltage limit. Further note that the obtained Pareto front is only marginally worse than without the voltage limit, since in the simulations of the Pareto front of the synthetic cell in Fig. 6.7a this voltage limit was only exceeded slightly. We then consider two cases for the optimal SDFN approach. In the first case, the optimal aging-aware charging problem is solved with a 4.28 V constraint, shown as the solid red line in Fig. 6.8. However, due to modeling errors, the simulated voltage of the SDFN model is generally lower than the simulated voltage of the synthetic cell, which means that when constraining the SDFN model to 4.28 V, the voltage of the synthetic cell exceeds this limit when applying the corresponding current profile on the synthetic cell. We can observe this in Fig. 6.8b, where we see that the battery is charged with the optimal profile computed using the SDFN model, until the 4.28V limit is reached (red curve). After a brief relaxation period, the battery is kept in the CV mode for a considerable time, although still considerably less than with the 3-CC-CV(5) protocol. As we can observe in Fig. 6.8a, this has a large impact on the achieved Pareto front, although its pareto front is still better than those of the multi-stage protocols. In the second case, the

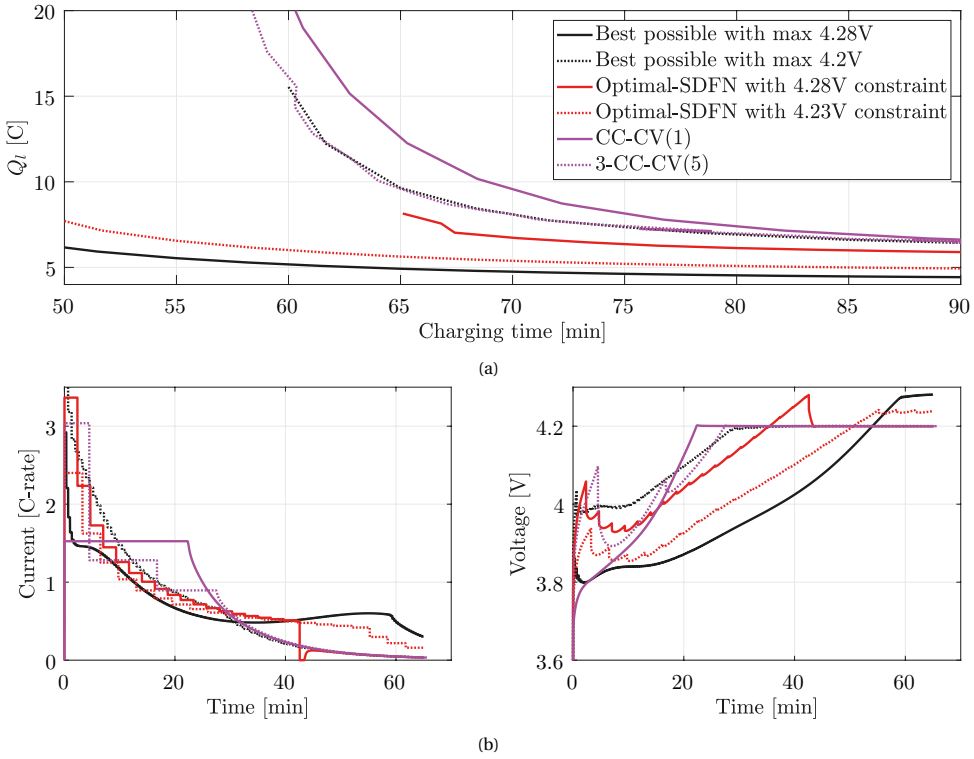

Figure 6.8: Results showing the impact of applying a voltage limit on the resulting Pareto front, where in (a) the trade-off between charging time and Li-ion loss due to side reactions Q_l is shown, and in (b) the current and voltage of the various considered cases for a charging time of around 65 minutes is shown.

optimal aging-aware charging problem is solved with a conservative 4.23 V constraint (dashed red curve), thereby avoiding the 4.28V with a significant margin. In doing so, a good Pareto front can still be achieved, without reaching an excessively large voltage. In Fig. 6.8a, we can furthermore see that the best possible Pareto front with a 4.2V voltage limit roughly coincides with the Pareto front of the 3-CC-CV(5) protocol, which shows that the design-adjustable parameters found for this protocol are close to optimal. It also shows again that in order to achieve a good trade-off between charging time and aging, the maximum voltage limit should be as large as possible.

6.4. CONCLUSIONS

In this chapter, we have presented an optimal aging-aware charging approach using the DFN model. Here, we have formulated the optimal aging-aware charging problem and applied the method of the substitution of equations presented in Chapter 2 to arrive at a reformulated optimal-control problem with a reduced computational complexity to the originally formulated optimal-control problem. Furthermore, to solve the optimal-control problem in a computationally efficient manner, we have employed a sequen-

tial quadratic programming (SQP) algorithm. To validate the proposed optimal aging-aware charging approach, we have compared our proposed approach to several rule-based protocols, such as those considered in Chapter 4, as well as optimal aging-aware approaches using the SPM and the surrogate modeling approach that we proposed in Chapter 5. To reflect the effect of modeling errors on the achieved trade-off between charging time and aging, we have defined a so-called synthetic cell, which is a DFN model with concentration-dependent parameters and an electro-motive force (EMF) that is different from the DFN model used for the proposed approach, similar to the study done in Chapter 3.

In the validation of the proposed optimal aging-aware charging approach, we have shown that with the employed SQP algorithm, the formulated optimal-control problem can solved roughly an order of magnitude faster than with an off-the-shelf solver. Furthermore, we have shown that with a well-considered choice of spatial and temporal discretization of the optimal-control problem, and with the employed SQP algorithm, the optimal-control problem can be solved in about 0.1 s for a full control horizon, which makes the proposed approach suitable for a closed-loop implementation, without compromising with a short control horizon, as is done in the MPC approaches taken in, e.g., [10, 11], where similar solution times were reported for a control horizon of only 5 time steps. Then, we have shown that despite large differences in internal states between the considered SDFN model for optimal aging-aware charging and the synthetic cell, a good trade-off in battery aging and charging time has been achieved using the proposed optimal aging-aware charging approach. This shows that the accuracy of the model used is not crucial for obtaining a good trade-off between charging time and aging, as long as constraints on the internal states are not considered, which may be important for safety considerations, in which case a well-parameterized DFN model is crucial.

6.A. APPENDIX: REFORMULATION OF THE DISCRETE-TIME OPTIMAL-CONTROL PROBLEM

Starting from the discrete-time optimal-control problem (6.2), we will derive the reformulated problem (6.4) through substitution of the model equations. Note that throughout this derivation, we assume that $j_2 \ll j_n$, and therefore $j_1 \approxeq j_n$, and we will apply Simplification [S1] introduced in Chapter 2, which will simplify the derivation. Under this assumption, the model equations are then given by

$$0 = \hat{A}_{c_s}\mathbf{c}_{s,k} + \hat{B}_{c_s}\mathbf{j}_{1,k} + \mathbf{c}_{s,k-1}, \tag{6.13a}$$

$$0 = \hat{A}_{c_s}\mathbf{c}_{e,k} + \hat{B}_{c_s}\mathbf{j}_{n,k} + \mathbf{c}_{e,k-1}, \tag{6.13b}$$

$$0 = A_{\phi_s}\boldsymbol{\phi}_{s,k} + B_{\phi_s}\mathbf{j}_{n,k} + C_{\phi_s}I_{a,k}, \tag{6.13c}$$

$$0 = A_{\phi_e}\boldsymbol{\phi}_{e,k} + B_{\phi_e}\mathbf{j}_{n,k} + D_{\phi_e}\log(\mathbf{c}_{e,k}), \tag{6.13d}$$

$$\mathbf{j}_{n,k} = \operatorname{diag}\left(\frac{\mathbf{i}_{0,1,k}}{RT}\right)\boldsymbol{\eta}_{1,k}, \tag{6.13e}$$

$$\mathbf{j}_{2,k} = -\frac{\mathbf{i}_{0,2}}{F}\exp\left(-\frac{2\alpha_{c,2}F}{RT}\boldsymbol{\eta}_{2,k}\right), \tag{6.13f}$$

in which the diag(v) denotes a diagonal matrix with the elements of vector v on the main diagonal, and where

$$\boldsymbol{\eta}_{1,k} = \boldsymbol{\phi}_{s,k} - \bar{\boldsymbol{\phi}}_{e,k} - \mathbf{U}(\bar{\mathbf{c}}_{s,k}) - FR_f \mathbf{j}_{n,k}, \tag{6.13g}$$

$$\boldsymbol{\eta}_{2,k} = \boldsymbol{\phi}_{s,k} - \bar{\boldsymbol{\phi}}_{e,k} - U_2 - FR_f \mathbf{j}_{n,k}. \tag{6.13h}$$

Over the entire time horizon, $\mathbf{c}_s$, $\mathbf{c}_e$, $\boldsymbol{\phi}_e$, and $\mathbf{j}_n$ can be given by

$$\mathbf{c}_s = \Omega_{c_s} \mathbf{j}_n + \Pi_{c_s}, \tag{6.14a}$$

$$\mathbf{c}_e = \Omega_{c_e} \mathbf{j}_n + \Pi_{c_e}, \tag{6.14b}$$

$$\boldsymbol{\phi}_e = \Omega_{\phi_e} \mathbf{j}_n + \Pi_{\phi_e} \log(\mathbf{c}_e), \tag{6.14c}$$

$$\mathbf{j}_n = \Omega_{\phi_s} \boldsymbol{\phi}_s + \Pi_{\phi_s} I_a, \tag{6.14d}$$

where

$$\Omega_{c_s} = -\left(\begin{bmatrix} \mathbf{0}^{n_{cm}(K-1) \times n_{cm}(K-1)} & \mathbf{0}^{n_{cm}(K-1) \times n_{cm}(K-1)} \\ \mathbf{I}^{n_{cm}(K-1)} & \mathbf{0}^{n_{cm}(K-1) \times n_{cm}(K-1)} \end{bmatrix} + \mathbf{I}^K \otimes \hat{A}_{c_m} \right)^{-1} \left(\mathbf{I}^K \otimes \hat{B}_{c_m} \right),$$

$$\Pi_{c_s} = -\left(\begin{bmatrix} \mathbf{0}^{n_{cm}(K-1) \times n_{cm}(K-1)} & \mathbf{0}^{n_{cm}(K-1) \times n_{cm}(K-1)} \\ \mathbf{I}^{n_{cm}(K-1)} & \mathbf{0}^{n_{cm}(K-1) \times n_{cm}(K-1)} \end{bmatrix} + \mathbf{I}^K \otimes \hat{A}_{c_m} \right)^{-1} \begin{bmatrix} \mathbf{c}_{m,0} \\ \mathbf{0}^{n_{cm}(K-1) \times 1} \end{bmatrix},$$

$$\Omega_{\phi_e} = -\mathbf{I}^K \otimes \left(A_{\phi_e}^{-1} B_{\phi_e} \right), \quad \Pi_{\phi_e} = -\mathbf{I}^K \otimes \left(A_{\phi_e}^{-1} D_{\phi_e} \right),$$

$$\Omega_{\phi_s} = -\mathbf{I}^K \otimes \left(B_{\phi_s}^{-1} A_{\phi_s} \right), \quad \Pi_{\phi_e} = -\mathbf{I}^K \otimes \left(B_{\phi_s}^{-1} C_{\phi_s} \right),$$

for $m \in \{s, e\}$, and where the notation $\mathbf{0}$ represents a matrix of zeros, $\mathbf{I}$ is the identity matrix, $\otimes$ is the Kronecker product, $n_{c_s} = n_{r,n} n_n + n_{r,p} n_p$, and $n_{c_e} = n_n + n_s + n_p$. Note that we can further substitute $\mathbf{j}_n$ into the other equations in (6.14), to arrive at

$$\mathbf{c}_s = \Gamma_{c_s} \mathbf{I}_a + \Phi_{c_s} \boldsymbol{\phi}_s + \Pi_{c_s}, \tag{6.15a}$$

$$\mathbf{c}_e = \Gamma_{c_e} \mathbf{I}_a + \Phi_{c_e} \boldsymbol{\phi}_s + \Pi_{c_e}, \tag{6.15b}$$

$$\boldsymbol{\phi}_e = \Gamma_{\phi_e} \mathbf{I}_a + \Phi_{\phi_e} \boldsymbol{\phi}_s + \Pi_{\phi_e} \log(\mathbf{c}_e), \tag{6.15c}$$

in which

$$\Gamma_{c,m} = \Omega_{c,m} \Pi_{\phi_s}, \quad \Phi_{c,m} = \Omega_{c,m} \Omega_{\phi_s}, \quad \Gamma_{\phi_e} = \Omega_{\phi_e} \Pi_{\phi_s}, \quad \Phi_{\phi_e} = \Omega_{\phi_e} \Omega_{\phi_s},$$

for $m \in \{s, e\}$. Then, by substituting (6.14d) and the equations in (6.15) into (6.13e), we can arrive at a set of equations that depends only on the variables $\boldsymbol{\phi}_s$ and I_a, which we will denote as

$$\mathscr{F}_{\text{rf}}(\boldsymbol{\phi}_s, \mathbf{I}_a) = 0. \tag{6.16}$$

The equations in (6.15) can subsequently be substituted in $\mathbf{j}_2$ in (6.13), which can then be written as

$$\mathbf{j}_2 = \Omega_{j_2} \exp\left(\Gamma_{j_2} \mathbf{I}_a + \Phi_{j_2} \boldsymbol{\phi}_s + \Pi_{j_2} \log(\mathbf{c}_e) \right), \tag{6.17}$$

in which

$$\Omega_{j_2} = \frac{i_{0,2}}{F}\exp\left(\frac{2\alpha_{c,2}FU_2}{RT}\right), \quad \Gamma_{j_2} = -\frac{2\alpha_{c,2}F}{RT}\left(\Gamma_{\phi_e}+\Pi_{\phi_s}\right),$$
$$\Phi_{j_2} = -\frac{2\alpha_{c,2}F}{RT}\left(FR_f\Omega_{\phi_s}+\Phi_{\phi_e}-\mathbf{I}^{n_nK}\right), \quad \Pi_{j_2} = -\frac{2\alpha_{c,2}F}{RT}\Pi_{\phi_e},$$

and Q_l can be expressed as

$$Q_l = \Theta_{j_2}\mathbf{j_2}, \tag{6.18}$$

where $\Theta_{j_2} = a_{s,n}AF\delta_t\frac{\delta_n}{n_n}\mathbf{1}^{1\times n_nK}$, in which $\mathbf{1}$ denotes a matrix of ones. Finally, the original optimal-control problem (6.2) can be reformulated as

$$\min_{\boldsymbol{\phi}_s,\mathbf{I}_a} Q_l = \min_{\boldsymbol{\phi}_s,\mathbf{I}_a}\Theta_{j_2}\Omega_{j_2}\exp\left(\Gamma_{j_2}\mathbf{I}_a+\Phi_{j_2}\boldsymbol{\phi}_s+\Pi_{j_2}\log(\mathbf{c}_e)\right), \tag{6.19a}$$

subject to

$$\mathscr{F}_{\mathrm{rf}}(\boldsymbol{\phi}_s,\mathbf{I}_a) = 0, \tag{6.19b}$$
$$\mathscr{G}_{\mathrm{rf}}(\boldsymbol{\phi}_s,\mathbf{I}_a) \le 0, \tag{6.19c}$$
$$\frac{\delta_t}{Q_b}\mathbf{1}^{1\times K}\mathbf{I}_a \ge s_f - s_0, \tag{6.19d}$$

where $\mathscr{G}_{\mathrm{rf}}(\boldsymbol{\phi}_s,\mathbf{I}_a)$ is obtained by substituting (6.14d) and the equations in (6.15) into the original $\mathscr{G}(\cdot)$.

REFERENCES

[1] H. J. Bergveld, W. S. Kruijt, and P. H. L. Notten, *Battery Management Systems: Design by Modeling* (Kluwer Academic publishers, 2002).

[2] D. Anseán, M. González, J. Viera, V. García, C. Blanco, and M. Valledor, *Fast charging technique for high power lithium iron phosphate batteries: A cycle life analysis,* Journal of Power Sources **239**, 9 (2013).

[3] P. M. Attia, A. Grover, N. Jin, K. A. Severson, T. M. Markov, Y.-H. Liao, M. H. Chen, B. Cheong, N. Perkins, Z. Yang, P. K. Herring, M. Aykol, S. J. Harris, R. D. Braatz, S. Ermon, and W. C. Chueh, *Closed-loop optimization of fast-charging protocols for batteries with machine learning,* Nature (2020).

[4] R. Klein, N. A. Chaturvedi, J. Christensen, J. Ahmed, R. Findeisen, and A. Kojic, *Optimal charging strategies in lithium-ion battery,* in *IEEE American Control Conference* (2011) pp. 382–387.

[5] H. E. Perez, X. Hu, and S. J. Moura, *Optimal charging of batteries via a single particle model with electrolyte and thermal dynamics,* in *IEEE American Control Conference* (2016) pp. 4000–4005.

[6] J. Liu, G. Li, and H. K. Fathy, *A Computationally Efficient Approach for Optimizing Lithium-Ion Battery Charging,* Journal of Dynamic Systems, Measurement, and Control **138**, 021009 (2015).

[7] C. Zou, X. Hu, Z. Wei, T. Wik, and B. Egardt, *Electrochemical Estimation and Control for Lithium-Ion Battery Health-Aware Fast Charging,* IEEE Transactions on Industrial Electronics **65**, 6635 (2018).

[8] B. Suthar, P. W. C. Northrop, R. D. Braatz, and V. R. Subramanian, *Optimal Charging Profiles with Minimal Intercalation-Induced Stresses for Lithium-Ion Batteries Using Reformulated Pseudo 2-Dimensional Models,* Journal of the Electrochemical Society **161**, F3144 (2014).

[9] C. Zou, C. Manzie, and D. Nešić, *Model Predictive Control for Lithium-Ion Battery Optimal Charging,* IEEE/ASME Transactions on Mechatronics **23**, 947 (2018).

[10] Y. Yin, Y. Bi, Y. Hu, and S.-Y. Choe, *Optimal Fast Charging Method for a Large-Format Lithium-Ion Battery Based on Nonlinear Model Predictive Control and Reduced Order Electrochemical Model,* Journal of the Electrochemical Society **167**, 160559 (2021).

[11] S. Lucia, M. Torchio, D. M. Raimondo, R. Klein, R. D. Braatz, and R. Findeisen, *Towards adaptive health-aware charging of Li-ion batteries: A real-time predictive control approach using first-principles models,* in *IEEE American Control Conference* (2017) pp. 4717–4722.

[12] S. Santhanagopalan, Q. Guo, P. Ramadass, and R. E. White, *Review of models for predicting the cycling performance of lithium ion batteries,* Journal of Power Sources **156**, 620 (2006).

[13] A. Wächter and L. T. Biegler, *On the implementation of an interior-point filter line-search algorithm for large-scale nonlinear programming,* Mathematical programming **106**, 25 (2006).

[14] P. T. Boggs and J. W. Tolle, *Sequential Quadratic Programming *,* Acta Numerica **4**, 1 (1995).

[15] Z. Khalik, G. Padilla, T. Romijn, and M. Donkers, *Vehicle Energy Management with Ecodriving: A Sequential Quadratic Programming Approach with Dual Decomposition,* in *American Control Conference* (2018) pp. 4002–4007.

[16] N. Chaturvedi, R. Klein, J. Christensen, J. Ahmed, and A. Kojic, *Algorithms for Advanced Battery-Management Systems,* IEEE Control Systems Magazine **30**, 49 (2010).

[17] S. Boyd, S. P. Boyd, and L. Vandenberghe, *Convex Optimization* (Cambridge University Press, 2004).

[18] T. T. Vo, X. Chen, W. Shen, and A. Kapoor, *New charging strategy for lithium-ion batteries based on the integration of Taguchi method and state of charge estimation,* Journal of Power Sources **273**, 413 (2015).

[19] K. Takahashi and V. Srinivasan, *Examination of Graphite Particle Cracking as a Failure Mode in Lithium-Ion Batteries: A Model-Experimental Study,* Journal of the Electrochemical Society **162**, A635 (2015).

[20] P. Notten, J. Op het Veld, and J. van Beek, *Boostcharging Li-ion batteries: A challenging new charging concept,* Journal of Power Sources **145**, 89 (2005).

[21] Z. Chu, X. Feng, L. Lu, J. Li, X. Han, and M. Ouyang, *Non-destructive fast charging algorithm of lithium-ion batteries based on the control-oriented electrochemical model,* Applied Energy **204**, 1240 (2017).

[22] H. Perez, N. Shahmohammadhamedani, and S. Moura, *Enhanced Performance of Li-Ion Batteries via Modified Reference Governors and Electrochemical Models,* IEEE/ASME Transactions on Mechatronics **20**, 1511 (2015).

[23] R. Romagnoli, L. D. Couto, A. Goldar, M. Kinnaert, and E. Garone, *A feedback charge strategy for Li-ion battery cells based on Reference Governor,* Journal of Process Control (2019).

[24] H. Fang, Y. Wang, and J. Chen, *Health-Aware and User-Involved Battery Charging Management for Electric Vehicles: Linear Quadratic Strategies,* IEEE Transactions on Control Systems Technology **25**, 911 (2017).

PART III

EXPERIMENTAL VALIDATION AND CONCLUSIONS

7

EXPERIMENTAL VALIDATION OF OPTIMAL AGING-AWARE CHARGING METHODS

In this chapter, we experimentally validate several aging-aware charging methods using an electrochemistry-based battery model. Specifically, we consider the conventional constant-current-constant-voltage (CC-CV) protocol, a multi-stage charging protocol, and an open-loop optimal-control-based approach. In order to visualize the achieved trade-off between aging and charging time of the various considered protocols, two different charging speeds are evaluated for each of the charging protocols. We show that both the multi-stage charging protocol as well as the optimal-control-based protocol achieve a substantially improved trade-off between charging time and aging compared to the conventionally used CC-CV protocol. We further show that the multi-stage charging protocol achieves a better trade-off between charging time and aging compared to the optimal-control-based protocol. This may be due to a lack of feedback in the open-loop optimal-control-based approach, which shows the importance of feedback in aging-aware charging, in order to adequately compensate for modeling errors. These results also show the importance of considering relatively simple multi-stage protocols in the validation of more complex aging-aware charging approaches, as relatively simple multi-stage protocols can already be a significant improvement over the conventional CC-CV protocol.

7.1. INTRODUCTION

In Part II of this thesis, we have investigated various aging-aware charging methods using an electrochemistry-based battery model. The electrochemistry-based model considered in this part of the thesis was a Doyle-Fuller-Newman (DFN) model [1], extended with a capacity-loss side-reaction model introduced in [2]. The aging-aware charging methods considered range from relatively simple rule-based charging protocols to complex optimal-control-based charging protocols. Leveraged by the implementation of the DFN model proposed in Chapter 2, a computationally efficient optimal-control-based approach was obtained in Chapter 6. This optimal-control-based approach allowed for a significantly improved trade-off between charging time and aging compared to the rule-based protocols.

It should be noted that the validation of the methods considered in Part II of this thesis has only been done in simulation using the DFN model with capacity-loss side reactions. However, this model only considers one, albeit major, aging mechanism, namely solid-electrolyte-interface (SEI) build-up due to side reactions [2]. In reality, many other aging mechanisms may occur while charging a battery, such as the loss of active electrode material, through stress or fractures [3]. However, as the considered SEI build-up aging mechanism is one of the major contributors to aging [3], the results obtained in simulation could still correspond to an experimental validation of the charging methods.

Ample attention has been paid to the experimental validation of rule-based charging methods [4–8]. The rule-based protocols considered in these papers are mostly multi-stage constant-current-constant-voltage (CC-CV) protocols, where the battery is charged in a sequence of CC and CV stages, and can be considered an extension of the conventional CC-CV protocol. On the other hand, there has been little literature devoted to the experimental validation of optimal-control-based methods, where to the author's knowledge, the only examples are found in [9, 10]. However, in these papers, the (complex) proposed optimal-control-based method is only validated against the conventional CC-CV protocol. Meanwhile, it has been shown that multi-stage CC-CV charging protocols, which are only marginally more complex than the CC-CV protocol, can be a considerable improvement over the CC-CV protocol, e.g., in [6]. Of course, for a complex optimal-control-based approach to be worthwhile, it should not only perform better than the conventional CC-CV protocol, but it should also perform better than considerably less complex and well-known alternatives, such as multi-stage CC-CV protocols.

In this Chapter, an experimental validation of several aging-aware charging methods is done. Specifically, we consider a multi-stage CC-CV charging protocol, as investigated in Chapter 4 and 6, and further consider the open-loop optimal-control-based approach using the DFN model with capacity-loss side reactions of Chapter 6. We will experimentally validate these charging methods against the conventionally used CC-CV protocol. In experimentally validating the methods, each charging method is applied with two different charging speeds, in order to visualize the trade-off between charging time and aging that can be achieved with the considered charging methods.

The remainder of this chapter is structured as follows. In Section 7.2, details on the experimental set-up are given. In Section 7.3, we will show how the design-adjustable variables (DAVs) of the various considered charging protocols are computed. Here, the

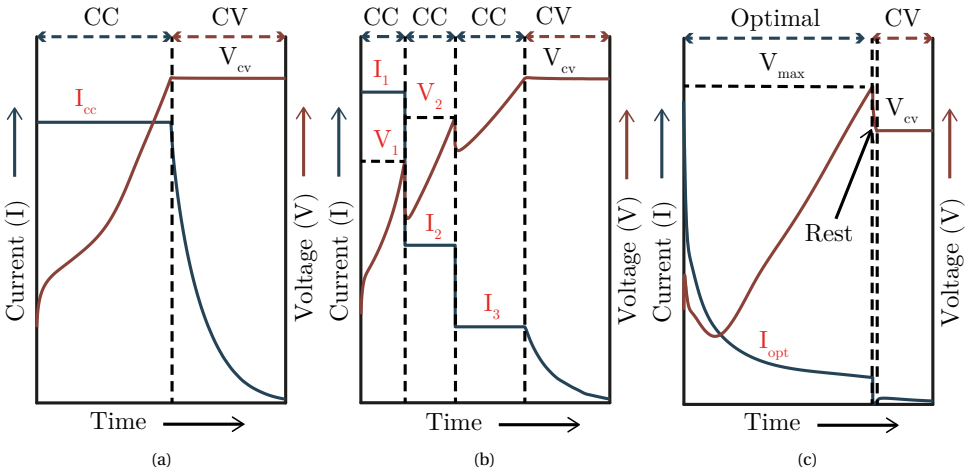

Figure 7.1: Schematic representation of the considered charging methods, where in (a) the CC-CV(1) protocol is shown, in (b) the 3-CC-CV(5) protocol is shown, and in (c) the optimal-control-based charging protocol is shown. The red-marked variables indicate the design-adjustable variables of the respective protocols.

model used to compute the DAVs is experimentally validated, and the simulated Pareto-optimal fronts of the charging protocols are shown. In Section 7.4, the experimental aging results are given, where the trade-off between charging time and aging achieved by the considered charging protocols is compared. Finally, conclusions are drawn in Section 7.5.

7.2. EXPERIMENTAL SET-UP

The experimental validation of aging-aware charging methods has been done using a climate-controlled chamber at a testing facility in Forschungszentrum Jülich. Batteries can be charged or discharged with a particular pre-defined current profile. Additionally, there is functionality for keeping the batteries at a pre-defined voltage. In this work, we tested 10 high-energy pouch cells with a nominal capacity of 25 Ah with varying charging strategies in the climate-controlled chamber. Due to the proprietary nature of the considered cells, the chemistry of the cells is unknown. The considered charging methods for experimental validation are shown in Fig. 7.1. Note that the nominal capacity of 25 Ah is used in the definition of the C-rate unit. As a baseline strategy, we consider the conventionally used CC-CV protocol, which we will denote here as the CC-CV(1) protocol, since we only consider the CC-stage current to be a DAV. We furthermore also consider a multi-stage CC-CV protocol, which is similar to the one considered in Chapter 6, i.e., the 3-CC-CV(5) protocol. We refer the reader to Chapter 6 for how this protocol is defined. Finally, we consider an optimal-control-based charging protocol, where an optimal current profile is computed by solving (6.2) using the methods presented in Chapter 6, which is then applied in open-loop to the battery. In order to prevent over-charge of the battery, while at the same time ensuring that all the protocols are charged approximately to the same state of charge, the battery is allowed to be charged using the optimal profile until a cer-

tain threshold voltage $V_{\max}$, after which the battery is relaxed until it reaches a threshold CV voltage V_{cv}, followed by a CV stage until a minimum threshold current is reached. For all the protocols, the minimum threshold current is 1 A, V_{cv} is 4.2 V, and $V_{\max}$ is selected as 4.3 V. Furthermore, for all experiments, the climate-controlled chamber is set to a 25 °C temperature. To reflect a realistic scenario, the DAVs of the rule-based protocols are determined once and are kept fixed throughout the entire battery aging test. On the other hand, to consider a best-case scenario of the optimal-control-based charging protocols, given the hardware and safety limitations, the optimal profile that is applied to the battery is re-computed every 200 cycles. In doing so, the optimal-charging-based protocols also have some degree of adaptability to aging.

One of the goals of the experimental validation is to obtain the experimental Pareto front for the various considered protocols. To do so, each considered charging protocol is evaluated at two different charging times. Furthermore, to check the variability in aging between cells with identical charging protocols, each considered protocol with a certain charging time should be tested at least twice. However, with 10 available battery cells, a choice must be made between the amount of different charging times tested for each protocol, and the number of protocols that are repeated for the variability check. The assignment of the battery cells made in this work is shown in Table 7.1. Here, all the protocols with a certain charging time, except for the CC-CV protocols, are repeated twice. Furthermore, for each protocol, two different charging speeds are considered, one with a relatively low charging time and another one with a relatively high charging time. Note that finding the DAVs for the protocols that give a certain desired charging time is not trivial. However, as the goal is to eventually compare the Pareto optimal fronts of the charging protocols, it is not necessary for the charging time between the various protocols to match exactly. In the next section of this chapter, we elaborate on how the DAVs are computed.

In Fig. 7.2, a schematic overview of the experiments for testing the charging protocols is shown, where we can see that the experiments are repeated with four main stages:

1. EMF measurements: here, the relation between the electro-motive force (EMF) and state of charge (SoC) is determined using an extrapolation method, where the battery is charged from a certain initial voltage with a constant current at several C-rates, and the charging is terminated at 4.2 V. The result of these measurements are used to determine the EMF based on the voltage extrapolation towards zero

Table 7.1: Assignment of the battery cells

Battery	Protocol	Charging speed	Measured capacity [Ah]
1	CC-CV(1)	Fast	31.7
2	CC-CV(1)	Slow	31.7
3	3-CC-CV(5)	Fast	31.8
4	3-CC-CV(5)	Fast	31.5
5	3-CC-CV(5)	Slow	31.7
6	3-CC-CV(5)	Slow	31.6
7	Optimal	Fast	31.2
8	Optimal	Fast	31.5
9	Optimal	Slow	31.5
10	Optimal	Slow	31.7

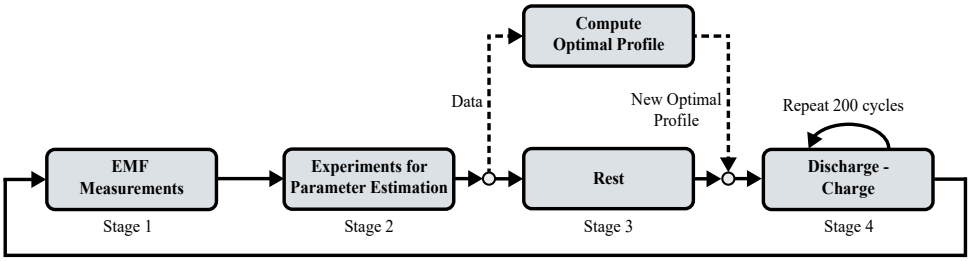

Figure 7.2: Schematic overview of the experiments for testing the charging protocols. The dashed lines indicate the processes that are only necessary for the optimal-control-based charging protocols.

current. For more detail on this method of determining the EMF, the reader is referred to [11]. The experiments done for determining the EMF can also be used to get an estimate of the battery capacity, which can later be used for the battery aging analysis.

2. Experiments for parameter estimation: here, data is gathered to estimate the parameters of the DFN model, which will be used to compute a new optimal current. The results of this stage are only used for the optimal-control-based charging protocols, although this stage is done for all charging protocols, to be able to make a fair comparison between the various protocols. The currents shown in Fig. 7.3 are applied to the battery, with an initial SoC values of approximately 20% for the top four current profiles. The last three current profiles are identical, although the initial SoC values are different, which are 40%, 60%, and 80%. The intention of the bottom three experiments are to minimize the influence of EMF modeling errors on the estimated parameters, which was observed in Chapter 3. In these experiments, the battery is charged and discharged around a certain state of charge, which means that there is also less variation in the EMF, and thereby reducing the influence of EMF modeling errors on the estimated parameters. However, in doing so, in these experiments, the diffusivity behavior is less pronounced, which leads to the diffusivity-related parameters to be less identifiable. Therefore, the top four current profiles in Fig. 7.3 are also applied, where the battery is mostly charged, such that diffusivity behavior is more pronounced. Note that in the first iteration of this stage only the bottom three experiments in Fig. 7.3 were done, as the top four experiments were added from the second iteration onward based on the observations made from estimating the parameters using the experiments done at the first iteration.

3. Compute optimal profile and rest: in this stage, the new optimal profile I_{opt} is computed based on the experimental data from the previous stage. Specifically, the DFN model parameters are first estimated based on the experimental data, after which the identified model is used to compute a new optimal profile using the methods described in Chapter 6. In the first iteration of this stage, the DAVs of the rule-based protocols, i.e., the CC-CV(1) protocol and the 3-CC-CV(5) protocol are also computed. We refer to Section 7.3 for details on how the DAVs of the con-

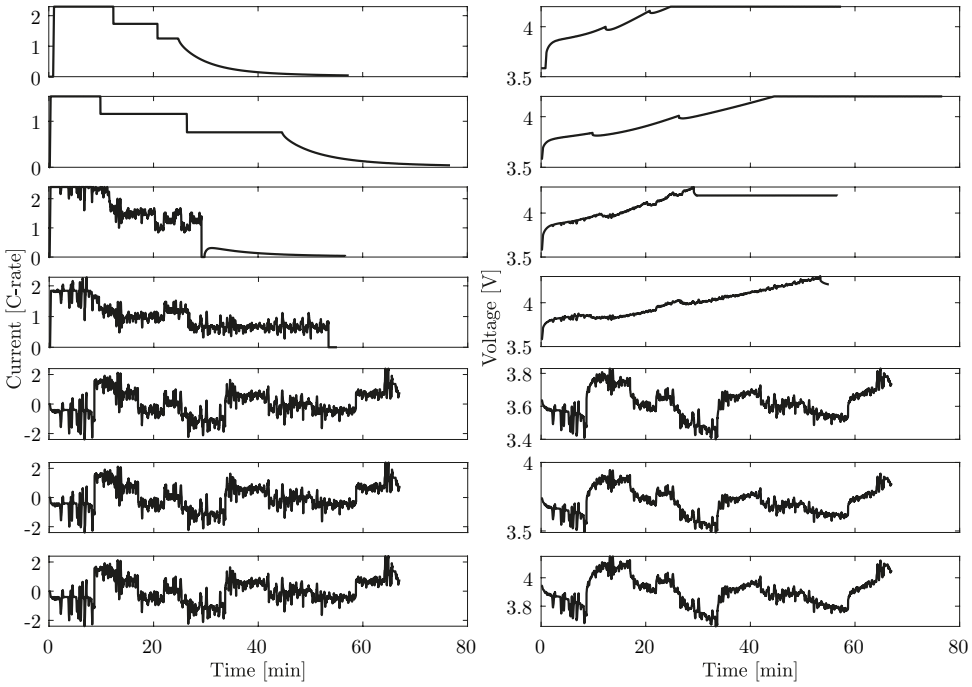

Figure 7.3: Experimental data used for parameter estimation.

sidered protocols are calculated. In the mean-time, the battery remains at rest at around 20% SoC to minimize the aging loss occurring in this stage. Note again that while the optimal profile is only computed for the optimal-control-based charging protocols, the batteries charged with the other protocols also remain at rest until the new optimal profiles are computed, to ensure that a fair comparison can be made between the various charging protocols.

4. Discharge-charge: each cycle in this stage itself will follow 4 sub-stages, which are repeated for 200 cycles.

   (a) Discharge the battery with 30 A until 3.4V, discharging the battery to around 25% SoC, in which the SoC range corresponds to a typical usage of (commercial) electric vehicles.

   (b) Rest for 1 hour.

   (c) Charge the battery with the respective charging protocol.

   (d) Rest for 15 minutes.

   Besides the EMF measurement data gathered in the first stage, the data gathered in this stage can also be used to get a measure of the battery capacity, e.g., the amount of discharged capacity at every cycle.

7.3. COMPUTATION OF THE DESIGN-ADJUSTABLE VARIABLES OF THE CHARGING PROTOCOLS

To obtain the Pareto optimal front of a particular charging protocol, the DAVs should be carefully chosen. The choice of the DAVs determines the trade-off between charging time and aging. Ideally, this trade-off lies on the Pareto optimal front, which would amount to the least possible aging at a particular desired charging time that is feasible with the considered protocol. As the CC-CV(1) protocol only has 1 DAV, any choice of the DAV leads to a point on the Pareto optimal front, since each value of the DAV corresponds to a single and unique charging time. Therefore, the only consideration that should be made in determining the DAV of the CC-CV(1) protocol, is that it is chosen such that a desired charging time is obtained. The 3-CC-CV(5) protocol, on the other hand, has 5 DAVs, which means that not every particular choice of DAVs leads to a point on the Pareto optimal front, since several DAV combinations may lead to the same charging time, while only one combination will yield the lowest amount of aging. To optimally determine the DAVs of the 3-CC-CV(5) protocol, many combinations of the DAVs would have to be tested experimentally, to select the ones that are Pareto optimal. However, this would take a large amount of experimentation and, therefore, we instead follow the method of determining the DAVs proposed in Chapter 4. In this approach, a DFN model with capacity-loss side reactions is utilized in order to determine the combinations of the DAVs that lie on the Pareto curve through a form of brute-force optimization. We should remark that due to modeling errors, these obtained combinations of the DAVs that lie on the modeled Pareto curve, do not necessarily lead to a point on the actual (experimental) Pareto front. However, in Chapter 6, we have shown that even considering modeling errors, the proposed approach of determining the DAVs for the 3-CC-CV(5) protocol still leads to a good trade-off between charging time and aging. To determine the optimal profile for the optimal-control-based protocol, we again use the DFN model with capacity-loss side-reactions presented in Chapter 3. Following the approach of Chapter 6, the optimal profile can be computed using this model. In the remainder of this section, we will first show the validation of the identified battery model, after which the results on the obtained Pareto front of the various protocols in simulation are given.

7.3.1. PARAMETER ESTIMATION VALIDATION

The DFN model used for determing the DAVs of the 3-CC-CV(5) protocol, as well as the optimal profile applied at the first 200 cycles of the optimal-control-based protocol, has been parameterized using the experimental data obtained in the second stage of the aging experiments shown in Fig. 7.2. As mentioned above, only the bottom three experiments shown in Fig. 7.3 were performed at the first iteration of the second stage of the aging experiments. However, in validating the parameters determined based on the data obtained from these experiments with a CC-CV experiment, the modeled voltage deviated significantly from the experimental voltage, as can be seen in Fig. 7.4a. This indicates that the experiments designed for parameter estimation were not informative enough to reliably estimate the parameters of the DFN model. Since no other experimental data was available, the parameters were estimated using the bottom three experiments shown in Fig. 7.3, as well as the CC-CV experiment, which did not leave any data

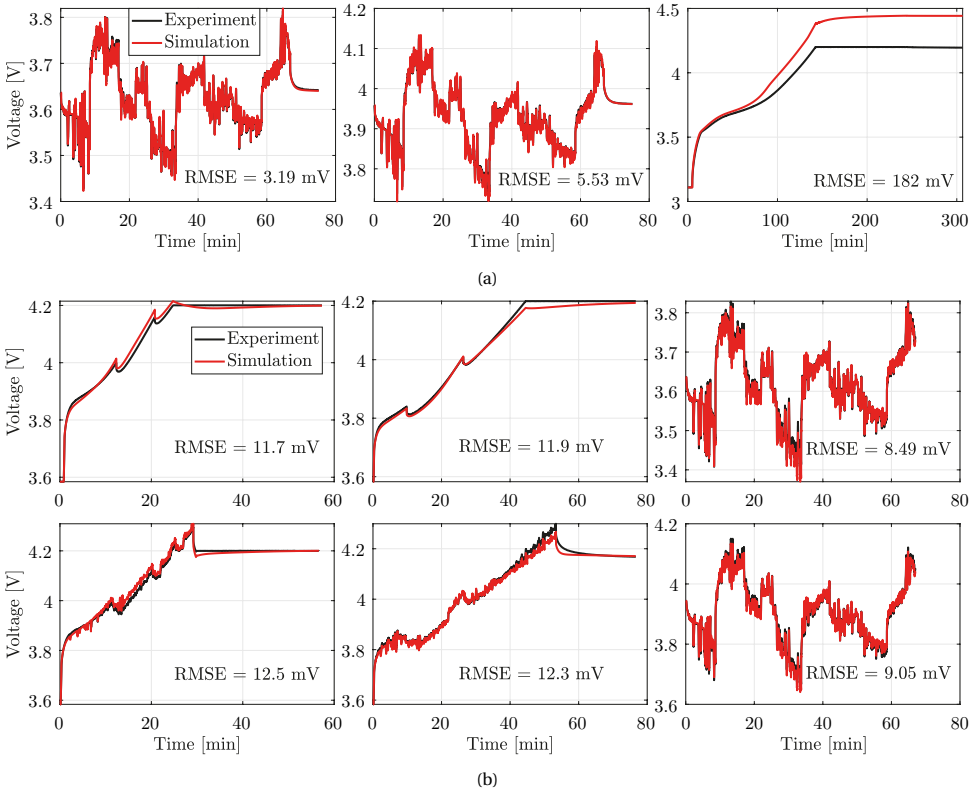

Figure 7.4: Obtained fit after parameter estimation, where in (a) the model fit is shown when only the bottom three current profiles of Fig. 7.3 are used for parameter estimation, and in (b) the model fit is shown for the second iteration of the aging experiments, where all the current profiles of Fig. 7.3 were used. Note that in (a) and (b) only 2 out of the three bottom experiments of Fig. 7.3 are shown, since the fit of the remaining experiment was similar in both cases of (a) and (b).

for validation. This improved the fit with the CC-CV experiment to 11 mV, since this data now was also accounted for in the estimation of the parameters. Based on these observations, for the second iteration of the aging experiments, the top four experiments in Fig. 7.3 were added to get more informative data for parameter estimation. An example of the fit obtained using this data is shown in Fig. 7.4b. Here, we can observe that the root-mean-square error (RMSE) between the simulated voltage and experimental voltage is around 8-13 mV. These errors are significantly larger than those observed in the results of Chapter 3, where RMSEs between 3-5 mV were observed. This difference is attributed to two factors. A first factor is that the currents applied to the battery are substantially larger, relatively, than those in Chapter 3, since the data in Chapter 3 did not involve charging the battery. A larger current induces more unmodelled (non-linear) battery behavior, which in turn will lead to larger observed errors. A second factor is that in this chapter, experimental data is used where the current is mostly applied in one direction, i.e., either mostly charging or discharging, as is done in the first four experi-

ments that are shown in Fig. 7.3. Combined with a relatively large charging current, this induces large concentration gradients in the cell, which further induces unmodelled battery behavior. Therefore, while the data used in this chapter to estimate the parameters can be considered to be more informative, it may also affect the estimated parameters to a larger degree due to modeling errors. Thus, it may be that the model used to simulate Fig. 7.4a better reflects the internal states of the battery, while the model used to simulate Fig. 7.4b better reflects the voltage output. This shows that there is a trade-off that needs to be considered between the informativity of the estimation data and the induced unmodelled battery behavior.

7.3.2. SIMULATED PARETO FRONT OF THE CHARGING PROTOCOLS

With the model obtained using the experimental data from the first iteration of the aging experiments, the simulated Pareto fronts can be obtained using the methods of Chapters 4 and 6. Note that since the parameters of the side-reaction model are not estimated with the parameter determination approach of Chapter 3, we have assumed them as the values given in Chapter 4. However, the choice of the $\alpha_{c,2}$ parameter, in particular, affects the computed optimal current profile. Therefore, ideally, these parameters of the side-reaction model should be determined and validated based on aging experiments, although to the author's knowledge, the estimation of these side-reaction model parameters has not been investigated yet in literature. The Pareto fronts of the various considered protocols are shown in Fig. 7.5a. We observe that, consistent with the results shown in the previous chapters, the multi-stage protocol is an improvement over the CC-CV protocol, while the optimal approach provides for a further improvement in the trade-off between charging time and aging. We further observe that the differences between the Pareto fronts is largest at lower charging times. Therefore, the points on the Pareto curve that will be experimentally evaluated are at a (simulated) charging time time of 50 minutes to capture one extreme, and a charging time of 65 minutes, to capture the other extreme. The current profiles and the corresponding simulated voltages are shown in Fig. 7.5b. These current profiles are applied to the corresponding batteries, as summarized earlier in Table 7.1.

The experimentally realized current profiles are shown in Fig. 7.6. Here, we observe that the actual batteries reach the threshold voltage of 4.3 V earlier than the model predicts, which leads to a rest and subsequent CV stage in the realized profiles. Since the battery is charged more slowly in CV, the total charging time of the realized profiles is longer than the designed profile. As we have seen in Chapter 6, the necessity of the rest and CV stage in the realized profile leads to a significantly worse trade-off between charging time and aging than an optimal profile. However, this trade-off may still be better than what a rule-based protocol can achieve as was also shown in Chapter 6. Note that the designed current profiles at the first iteration differ significantly from those at the second iteration of the aging experiments. This is explained by the fact that the models used to design the current profiles were significantly different, due to the large difference in estimation data that was used in the first and second iterations, as explained in Section 7.3.1. This is also reflected in the difference in modeling errors that can be observed in Fig. 7.6, where the modeling errors at the second iteration in Fig. 7.6b are clearly smaller than at the first iteration in Fig. 7.6a, since the estimation data at the sec-

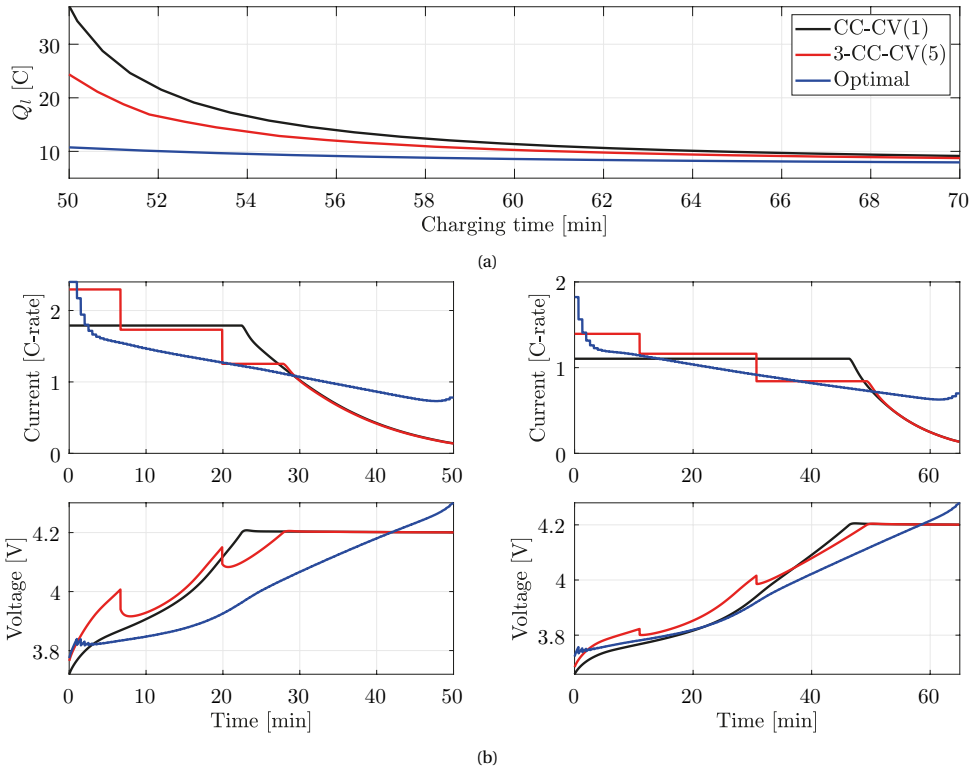

Figure 7.5: Comparison of the simulated Pareto optimal fronts of the various considered aging-aware charging approaches, where in (a) the trade-off between charging time and Li-ion loss due side reactions Q_l is shown, and in (b) the current and voltage for the various aging-aware charging approaches are shown at two different charging times.

ond iteration better reflected the implemented charging current profiles.

7.4. EXPERIMENTAL AGING RESULTS

In this section, the results of the aging experiments are given. Due to time limitations, the batteries were cycled for only 400 iterations. As we will show below, this was not enough to age the batteries to what is typically considered to be end-of-life, i.e., 80% state of health (SoH), defined as

$$\text{SoH} = \frac{Q_{\text{aged}}}{Q_{\text{fresh}}}, \tag{7.1}$$

where Q_{aged} and Q_{fresh} are a measure of the aged and fresh battery capacity, respectively. Therefore, it should be kept in mind that some of these results shown below may change when the batteries reach their end-of-life. In the first part of this section, we will show the course of aging of the experimentally tested batteries. This is followed by a part where we will show the experimental trade-off between charging time and aging that is achieved

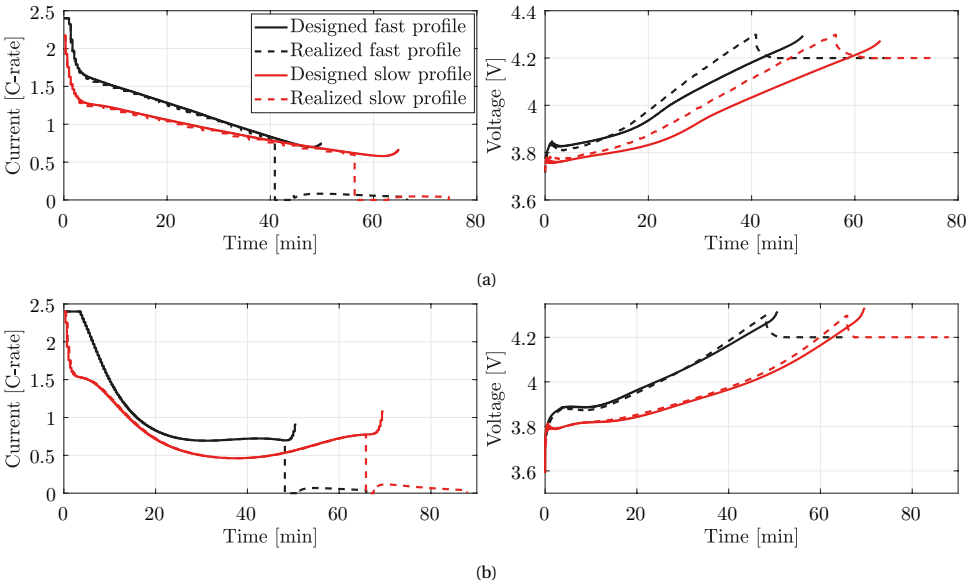

Figure 7.6: Comparison of the designed optimal current profile versus the realized experimental current profile, where in (a) the results are shown for the first iteration of the aging experiments, and in (b) the results are shown for the second iteration of the aging experiments.

with the various considered charging protocols.

7

7.4.1. EXPERIMENTAL AGING

In Fig. 7.7a, the course of aging for the batteries is shown, where in the definition of the SoH in (7.1), the amount of discharged capacity at every cycle is taken for Q_{aged}. In this definition of the SoH, besides the effect of capacity fade, the effect of power fade is also included, since a higher battery impedance also results in a lower discharged capacity. Note that Q_{fresh} is taken as the highest measured discharged capacity throughout the cycling experiments. One of the most notable observations that can be made in Fig. 7.7a, is that after 200 cycles, all the batteries seem to regain a significant amount of capacity of around 3-5 % SoH. Furthermore, Cells 1 and 3 even have a larger discharged capacity at cycle 400 than at cycle 200, which is also unexpected. The reason for this jump is not yet known, although it could be a diffusion phenomenon with a large time constant. After 200 cycles, the second iteration of the aging experiments starts, where in stages 1 through 3 (see Fig. 7.2), the battery is at rest at various instances, which may have allowed the battery to recover from this speculated diffusion phenomenon, leading to a rise in the discharged capacity at the subsequent cycling experiments. However, this rise in capacity may also be due to the various experiments performed in the first 3 stages of the aging experiments, where the battery is subjected to several full charge and discharge cycles, which may reactivate certain parts inside the battery. These experiments may therefore also have led to a recovery of capacity in some way. This observed phenomenon could have practical implications, where it may be that the considered battery

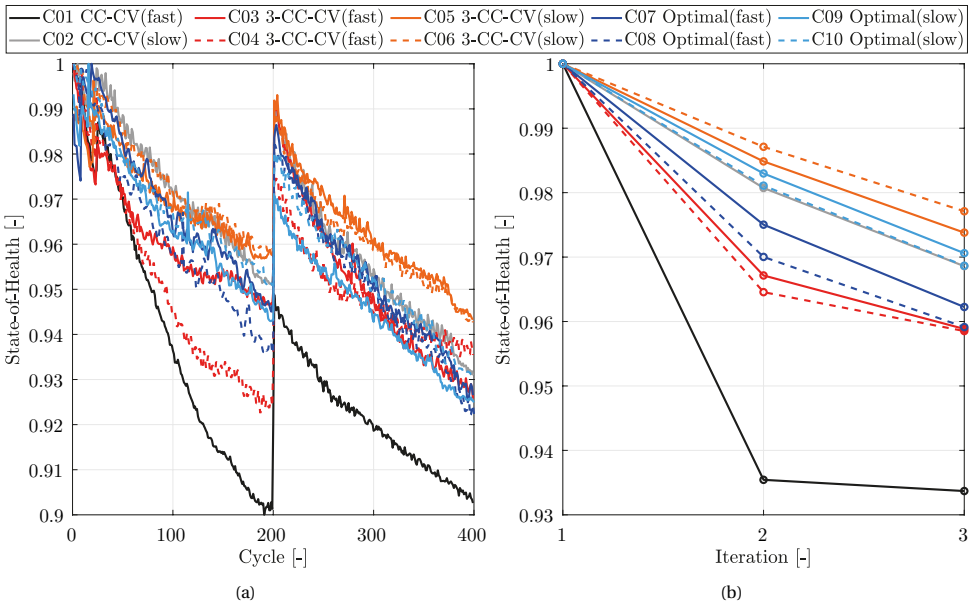

Figure 7.7: Results on the aging of the cells, where in (a), the state of health derived from the discharged capacity at every cycle according to (7.1) is shown, and in (b) the state of health derived from a full charge of the battery at every iteration of the aging experiments is shown.

needs to be serviced once in a while in order to recover capacity.

In Fig. 7.7a, we can further observe that there seems to be a considerable difference between some batteries that have been tested in an identical way. Most notably, this is observed with Cells 3 and 4, which particularly until 200 cycles show a large difference in discharged capacity, although this difference decreases suddenly after 200 cycles. Furthermore, it is clear that the battery with the CC-CV protocol with a fast charging speed (solid black line) ages considerably more than the batteries with the other protocols, while the protocols with a slower charging speed also age less generally, as could be expected. In Fig. 7.7b, the measured capacity in stage 1 of the batteries at each iteration of the aging experiments is shown. As opposed to the definition of SoH used in Fig. 7.7a, in this case, the SoH only includes the effect of capacity fade. Although the general trends in aging observed in Fig. 7.7b are similar to Fig. 7.7a, there are also some notable differences. The differences in SoH observed in Fig. 7.7a do not seem to correspond to those observed in Fig. 7.7b. For instance, in Fig. 7.7a, Cell 9 generally shows a higher degree of aging compared to Cell 10, while in Fig. 7.7b, it is the other way round, i.e., Cell 10 shows a higher degree of aging than Cell 9. This suggests Cell 10 has lost more capacity, but has a lower increased resistance than Cell 9, leading to a smaller loss in discharged capacity as can be observed in Fig. 7.7a. The results in Fig. 7.7 show that in comparing charging protocols, the definition of SoH should be carefully considered, as different definitions of SoH can lead to different conclusions. Furthermore, even when cells of the same chemistry are tested in an identical manner, they may still show a significant difference in aging. This uncertainty in the observed aging of the cells should be taken

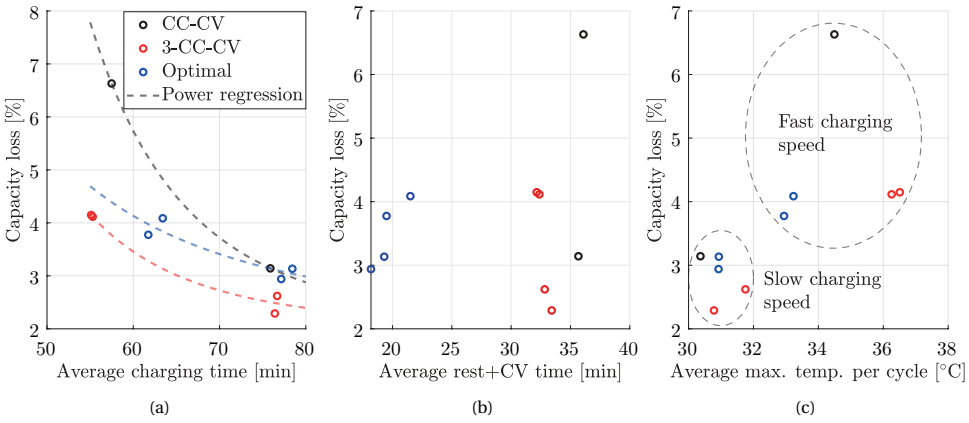

Figure 7.8: Results showing the correlation between the measured capacity loss and (a) average charging time, (b) average time spent in rest and CV mode during charging, (c) average measured maximum temperature per cycle.

into account when comparing various protocols.

7.4.2. IMPACT OF THE CHARGING PROTOCOLS ON THE TRADE-OFF BETWEEN CHARGING TIME AND AGING

Since all the cells are charged with different charging times, an adequate comparison between different charging protocols cannot be made by only observing the course of aging of the cells. Instead, the trade-off between aging and charging time should be considered, as is shown in Fig. 7.8a for the charging protocols considered in this work. To facilitate the comparison between the charging protocols, a power regression is made for each of the protocols, where the regression model is given by

$$Q_l = p_1 c_t^{-p_2} + 2, \tag{7.2}$$

where Q_l is the capacity loss, c_t is the charging time, and $p_1 > 0$ and $p_2 > 0$ are fitting parameters. Note that this regression model is not necessarily accurate, and only serves as an approximation of the achievable trade-off between charging time and aging. In Fig. 7.8a, we can firstly observe that the CC-CV protocol allows for a significantly worse trade-off compared to the other protocols, particularly at a low charging time. With a charging time of around 55 minutes, the 3-CC-CV protocol ages the battery almost twice as less as the CC-CV protocol. This validates the approach of Chapter 4, which shows that a DFN model with capacity-loss side reactions can be used to choose the design-adjustable variables of rule-based protocols effectively. Comparing the trade-off curves of these two protocols with those shown in the simulated Pareto optimal fronts in Fig. 7.5a, we observe that the trends roughly match, where the difference between the protocols is largest at low charging times and smaller at high charging times. However, in Fig. 7.8a, we also observe that the optimal-control-based protocol, while still being better than the CC-CV protocol, seems to have a worse trade-off curve than the 3-CC-CV protocol, which is unexpected. It could not have been expected to lead to as large of an

improvement as in Fig. 7.5a, due to the implementation of the optimal-control-based protocol, where in Chapter 6 we have shown that this implementation sacrifices the optimality of the protocol for robustness. The 3-CC-CV protocol, on the other hand, has an inherent feedback mechanism, where the current is regulated based on several measured voltage limits. This shows an advantage of the 3-CC-CV protocol compared to the considered optimal-control-based protocol, where due to a higher degree of feedback in the protocol, it is affected to a lesser degree by modeling errors. Thus, to alleviate the lack of feedback in the optimal-control-based protocol, a closed-loop optimal-control approach, as done in, e.g., [9, 12, 13], should be considered. However, such an approach would also be more complex in implementation compared to the open-loop approach taken in this work. The results in Fig. 7.8a show that when validating a particular (complex) charging protocol, the multi-stage CC-CV protocols should be considered in the comparison, rather than only making a comparison with the conventional CC-CV protocol, as done in, e.g., [9, 10]. The multi-stage CC-CV protocols are only slightly more complex in implementation than the CC-CV protocol, while still allowing for a substantially better trade-off in charging time and aging.

In Fig. 7.8b, the average time spent in rest and CV mode during charging for the various protocols is shown on the horizontal axis. Here, we observe that the optimal-control-based protocol spends significantly less time in rest and CV mode compared to the other protocols. Based on this observation, it could also have been expected that the optimal-control-based protocol would allow for a better trade-off in charging time and aging compared to the other protocols, as in Chapter 4 and Chapter 6, we observed that the rule-based charging protocols with a better Pareto front also had a comparatively shorter CV stage. In Fig. 7.8b, we observe that this is still true when comparing the 3-CC-CV protocol with the CC-CV protocol, although the relation does not hold for the optimal-control-based protocol. This may point to aging phenomena, other than side reactions, that are induced to a larger degree by the optimal-control-based protocol compared to the 3-CC-CV protocol.

In Fig. 7.8c, the average maximum temperature per cycle is shown for the various protocols. Here, it seems that there is a correlation between the temperature of the cells and the resulting capacity loss. However, this correlation can be mostly explained by the fact that at faster charging speeds, the battery is charged with higher currents, leading to higher temperatures. When comparing batteries with a similar charging time, it is clear that there is no clear correlation between temperature and capacity loss. For example, when comparing the batteries with a fast charging speed, the 3-CC-CV protocol reaches higher temperatures than the CC-CV protocol with a smaller capacity loss. These results also rule out the possibility that the optimal-control-based protocol performs worse than the 3-CC-CV protocol due to reaching higher temperatures, since the temperatures reached using the optimal-control-based protocol are lower than with the 3-CC-CV protocol. Thus, although it is generally known that battery temperature has a significant effect on aging, the fluctuations in temperature observed during charging and discharging in these experiments has not had an observable effect on aging. This shows that, at least for the considered batteries, using temperature as an aging indicator does not allow for making an effective trade-off between charging time and aging, as done in, e.g., [14–16].

7.5. CONCLUSIONS

In this chapter, we have experimentally validated several aging-aware charging methods. Specifically, we have considered the conventional CC-CV protocol, a multi-stage charging protocol, such as those investigated in Chapter 4 and Chapter 6, and the open-loop optimal-control-based approach of Chapter 6. For the experimental validation, a total of 10 high-energy commercial battery cells have been used. For each charging protocol, we have evaluated two different charging speeds, in order to visualize the trade-off that can be achieved with the charging protocols. Furthermore, we have done a consistency check on the aging of the cells, where we have duplicated several cycling tests in order to check the deviation in aging that may occur between different cells of the same chemistry. In validating the considered aging-aware charging methods, we have found that even when cells of the same chemistry are tested in an identical manner, they may still show a significant difference in aging. This shows that this uncertainty in the observed aging of the cells should be taken into account when comparing the various protocols. Furthermore, we have shown that both the multi-stage protocol and the optimal-control-based protocol achieve a substantially improved trade-off between charging time and aging compared to the CC-CV protocol. However, contrary to what the simulations have shown in Chapter 6, where the same cells were used to fit the models to, we have observed that the multi-stage protocol actually achieves a better trade-off between charging time and aging compared to the optimal-control-based protocol. This result may be explained by a lack of feedback of the considered open-loop optimal-control-based approach. Therefore, a closed-loop implementation of the considered optimal-control-based approach may still allow for a better trade-off between aging and charging time than a multi-stage charging protocol. These results also show the importance of considering relatively simple multi-stage protocols in the validation of more complex aging-aware charging approaches, as multi-stage protocols can already be a significant improvement over the conventional CC-CV protocol, as also observed in this chapter.

REFERENCES

[1] M. Doyle, T. F. Fuller, and J. Newman, *Modeling of galvanostatic charge and discharge of the lithium/polymer/insertion cell,* Journal of the Electrochemical society **140**, 1526 (1993).

[2] P. Ramadass, B. Haran, P. M. Gomadam, R. White, and B. N. Popov, *Development of First Principles Capacity Fade Model for Li-Ion Cells,* Journal of the Electrochemical Society **151**, A196 (2004).

[3] A. A. Franco, M. L. Doublet, and W. G. Bessler, *Physical Multiscale Modeling and Numerical Simulation of Electrochemical Devices for Energy Conversion and Storage*, Green Energy and Technology (Springer London, 2016).

[4] M. Abdel-Monem, K. Trad, N. Omar, O. Hegazy, P. Van den Bossche, and J. Van Mierlo, *Influence analysis of static and dynamic fast-charging current profiles on ageing performance of commercial lithium-ion batteries,* Energy **120**, 179 (2017).

[5] D. Anseán, M. González, J. Viera, V. García, C. Blanco, and M. Valledor, *Fast charging technique for high power lithium iron phosphate batteries: A cycle life analysis,* Journal of Power Sources **239**, 9 (2013).

[6] Y.-H. Liu, C.-H. Hsieh, and Y.-F. Luo, *Search for an Optimal Five-Step Charging Pattern for Li-Ion Batteries Using Consecutive Orthogonal Arrays,* IEEE Transactions on Energy Conversion **26**, 654 (2011).

[7] P. Notten, J. Op het Veld, and J. van Beek, *Boostcharging Li-ion batteries: A challenging new charging concept,* Journal of Power Sources **145**, 89 (2005).

[8] P. M. Attia, A. Grover, N. Jin, K. A. Severson, T. M. Markov, Y.-H. Liao, M. H. Chen, B. Cheong, N. Perkins, Z. Yang, P. K. Herring, M. Aykol, S. J. Harris, R. D. Braatz, S. Ermon, and W. C. Chueh, *Closed-loop optimization of fast-charging protocols for batteries with machine learning,* Nature (2020).

[9] Y. Yin, Y. Bi, Y. Hu, and S.-Y. Choe, *Optimal Fast Charging Method for a Large-Format Lithium-Ion Battery Based on Nonlinear Model Predictive Control and Reduced Order Electrochemical Model,* Journal of the Electrochemical Society **167**, 160559 (2021).

[10] M. Pathak, D. Sonawane, S. Santhanagopalan, R. D. Braatz, and V. R. Subramanian, *(Invited) Analyzing and Minimizing Capacity Fade through Optimal Model-based Control - Theory and Experimental Validation,* ECS Transactions **75**, 51 (2017).

[11] V. Pop, H. J. Bergveld, D. Danilov, P. P. Regtien, and P. H. Notten, *Battery management systems: Accurate state-of-charge indication for battery-powered applications*, Vol. 9 (Springer Science & Business Media, 2008).

[12] S. Lucia, M. Torchio, D. M. Raimondo, R. Klein, R. D. Braatz, and R. Findeisen, *Towards adaptive health-aware charging of Li-ion batteries: A real-time predictive control approach using first-principles models,* in *IEEE American Control Conference* (2017) pp. 4717–4722.

[13] C. Zou, C. Manzie, and D. Nešić, *Model Predictive Control for Lithium-Ion Battery Optimal Charging,* IEEE/ASME Transactions on Mechatronics **23**, 947 (2018).

[14] J. Yan, G. Xu, H. Qian, and Y. Xu, *Battery fast charging strategy based on model predictive control,* in *IEEE 72nd Vehicular Technology Conference* (2010) pp. 1–8.

[15] E. Inoa and J. Wang, *PHEV Charging Strategies for Maximized Energy Saving,* IEEE Transactions on Vehicular Technology **60**, 2978 (2011).

[16] S. Pramanik and S. Anwar, *Electrochemical model based charge optimization for lithium-ion batteries,* Journal of Power Sources **313**, 164 (2016).

8

Conclusions and Recommendations

The increase in popularity of battery-electric vehicles (BEVs) has made aging-aware charging a crucial problem to be solved in order to further accelerate the adoption of BEVs, which facilitates a transition into a more sustainable society. While the charging time of a battery should be ideally as small as possible, charging a battery faster usually leads to an acceleration in aging. However, the severity in aging is influenced by the charging strategy. The goal in aging-aware charging is to find a charging solution that achieves a best-possible trade-off in charging time and battery aging. In this thesis, we have approached the aging-aware charging problem from an optimal-control perspective, where computationally efficient modeling and optimization are instrumental to arrive at an implementable optimal aging-aware charging solution. While physics-based models provide information on the internal states of the battery that can be crucial to limit battery aging, their complexity has made it a challenge to incorporate such models into an optimal-control approach. This resulted in the following main research question, formulated in Chapter 1.

Main Research Question

Do optimal-control-based charging algorithms that use electrochemical aging models lead to a better trade-off between aging and charging time compared to rule-based protocols, while having a manageable computational complexity?

In order to answer this main research question, in Chapter 1, we have posed several research sub-questions. In this chapter, we will state the conclusions of this thesis through answering each of the research sub-questions in Section 8.1. This is followed by the recommendations for future research that are provided in Section 8.2. Finally, the possible implications of the contributions of this thesis are given in Section 8.3.

8.1. CONCLUSIONS

In this section, the conclusions and contributions of this thesis are given through answering each of the research sub-questions presented in Chapter 1. In doing so, we will present the sub-questions again, that relate to each of the three parts of this thesis, and state the conclusions that address the respective sub-question.

8.1.1. BATTERY MODELING AND PARAMETERIZATION

Research Sub-Question 1

What is the impact of model simplifications on the trade-off between computational complexity and model accuracy of electrochemistry-based battery models?

This sub-question has been addressed in Chapter 2, where we have studied the impact of several types of model simplifications on the trade-off between model accuracy and computation time for the Doyle-Fuller-Newman (DFN) model. As a base model for comparison, we considered a, what we referred to as, a complete DFN (CDFN) model. Furthermore, we have proposed a computationally efficient implementation of the CDFN model that has led to a significant reduction in computation time. We have shown that while several parameters are typically considered to be concentration-dependent, their influence on the model dynamics were marginal for both studied parameter sets. By ignoring these concentration-dependencies, we have shown that the computation time of the DFN model can be significantly decreased, with a small sacrifice in model accuracy. Finally, we have shown that with the proposed implementation, and by selectively making the proposed simplifications, as well as selectively choosing the discretization grid parameters, a model can be obtained that has a small impact on model accuracy, while the computation time can be drastically decreased, to achieve a simulation time of over 5000 times faster than real-time. This has been an important enabler into using the DFN model in optimal aging-aware charging, as has been done in Chapter 7.

Research Sub-Question 2

How can the parameters of electrochemistry-based battery models be determined to obtain an accurate model with physically meaningful parameters?

In Chapter 3, we have addressed this sub-question, where we have compared two DFN model parameterization approaches, one where cell teardown experiments are used to determine the parameters, and another where the parameters are based only on current/voltage data. In doing so, we have proposed a model parameterization approach of the DFN model that can estimate the parameters based on current/voltage data and an assumed range of the model parameters. In this approach, the DFN model is reparameterized through normalization and grouping, followed by a sensitivity analysis and a parameter estimation procedure. Through this comparison, we have shown that using the proposed approach, a model can be obtained that better describes the output voltage than a model of which its parameters have been obtained through cell teardown. Fur-

thermore, we have validated the physical meaningfulness of the estimated parameters using the proposed approach by analyzing the parameter estimation routine for a synthetic cell. Through this analysis, we have demonstrated that modeling errors can lead to a large bias and variability in the estimated parameters, which can lead to parameters that are not physically meaningful. Finally, we have shown that this bias and variability can be reduced by determining tighter parameter ranges, which can be done through cell teardown. The results of this analysis motivate the need for an approach that combines parameter estimation using current/voltage data and parameter estimation through cell teardown, in order to obtain parameters that are both physically meaningful and still possibly lead to a model that can accurately describe the output voltage.

8.1.2. AGING-AWARE CHARGING

Research Sub-Question 3

Can aging indicators, such as the negative-electrode over-potential, be used to effectively make a trade-off between charging time and battery aging?

This sub-question has been answered in Chapter 4, where we have utilized a DFN model including capacity-loss side reactions to compare several rule-based charging protocols by obtaining the Pareto front that describes the optimal trade-off between charging time and aging for the considered protocols. Through this comparison, we have shown that by obtaining the Pareto front that describes the optimal trade-off between charging time and aging for a single cycle, the results can be extended to the lifetime of the battery, which facilitates the comparison between different charging strategies. Furthermore, we have shown that the negative-electrode over-potential is not always a good indicator for aging, and that aging will occur even when the battery operates in over-potential regions that are not considered to lead to aging. Therefore, by only considering the negative-electrode over-potential as an aging-indicator, an effective trade-off between charging time and battery aging cannot be made.

Research Sub-Question 4

What modeling approach, with a lower computational complexity than the DFN model, is suitable to approximate aging-related DFN model states accurately, such that it can be used in optimal aging-aware charging?

This sub-question has been addressed in Chapter 5, where we have presented an optimal-control-based method for aging-aware charging using a surrogate model. In the proposed surrogate modeling approach, the aging-related DFN model states are approximated by a combination of a black-box finite-dimensional linear-time-invariant model and a static nonlinear model that is a function of state of charge. Through the validation of the surrogate model, we have shown that the DFN model states can be well approximated using the proposed surrogate modeling approach, while the computation time when simulating with the surrogate model is over 70 times smaller than when simulating with the considered DFN model. Furthermore, we have compared the Pareto

front achieved with the proposed optimal-control-based method with the Pareto fronts achieved with various multi-stage CC-CV charging protocols from Chapter 4. Here, we have shown that the proposed optimal-control-based method achieves a significantly improved Pareto front over the multi-stage CC-CV charging protocols.

Research Sub-Question 5

Can the computational complexity of the optimal aging-aware charging problem using the DFN model be reduced such that it is suitable for a closed-loop implementation?

To address this sub-question, in Chapter 6, we have presented an optimal aging-aware charging approach using the DFN model. Here, we have used the resulting model implementation from Chapter 2 to reformulate the optimal-control problem with a reduced computational complexity compared to the originally formulated optimal-control problem. Furthermore, to solve the optimal-control problem in a computationally efficient manner, we have employed a sequential-quadratic-programming (SQP) algorithm. To reflect the effect of modeling errors on the achieved trade-off between charging time and aging, we have defined a so-called synthetic cell, which is a DFN model with concentration-dependent parameters and an EMF that is different from the DFN model used for the proposed approach, similar to the study done in Chapter 3. In the validation of the proposed optimal aging-aware charging approach, we have shown that despite large differences in internal states between the considered simplified DFN model for optimal aging-aware charging and the synthetic cell, a good trade-off between battery aging and charging time has been achieved using the proposed optimal aging-aware charging approach. This shows that the accuracy of the model used is not crucial for obtaining a good trade-off between charging time and aging, as long as constraints on the internal states are not considered, in which case a well parameterized DFN model is crucial. Furthermore, we have shown that with the employed SQP algorithm, the formulated optimal-control problem can be solved roughly an order of magnitude faster than with an off-the-shelf solver. Finally, we have shown that with a well-considered choice of spatial and temporal discretization of the optimal-control problem, and with the employed SQP algorithm, the optimal-control problem can be solved in about 0.1 s for a full control horizon, which makes the proposed approach suitable for a closed-loop implementation, without compromising with a short control horizon.

8.1.3. EXPERIMENTAL VALIDATION

Research Sub-Question 6

Do optimal-control-based charging algorithms that use electrochemistry-based models lead to a better trade-off between aging and charging time than rule-based algorithms in practice?

This sub-question has been addressed in Chapter 7, where we have compared an open-loop optimal-control-based charging method to two rule-based charging protocols through experimental validation. The rule-based charging protocols considered

were the conventional CC-CV protocol and a multi-stage CC-CV protocol. In order to visualize the achieved trade-off between aging and charging time of the various considered protocols, two different charging speeds were evaluated for each of the charging protocols. We have shown that both the multi-stage protocol and the optimal-control-based protocol achieve a substantially improved trade-off between charging time and aging compared to the CC-CV protocol. However, contrary to what the simulations have shown in Chapter 6, where the same cells were used to fit the models to, we have observed that the multi-stage protocol actually achieves a better trade-off between charging time and aging compared to the optimal-control-based protocol. This result may be explained by a lack of feedback of the considered open-loop optimal-control-based approach. Therefore, a closed-loop implementation of the considered optimal-control-based approach may still allow for a better trade-off between aging and charging time than a multi-stage charging protocol. These results also show the importance of considering relatively simple multi-stage protocols in the validation of more complex aging-aware charging approaches, as relatively simple multi-stage protocols can already be a significant improvement over the conventional CC-CV protocol, as also observed in Chapter 7.

8.2. RECOMMENDATIONS FOR FUTURE RESEARCH

In this thesis, optimal aging-aware charging using electrochemistry-based models has been studied. However, there are still several important limitations to the work presented in this thesis, that should be addressed in future research. In this section, we will discuss several recommendations for future research, based on the findings of this thesis.

8.2.1. MODELING

ADVANCING BATTERY AGING MODELING

In this thesis, we have mainly considered the capacity-loss side-reaction model to describe aging of the battery. However, while side reactions are one of the major contributors to aging, they are still only a part of the puzzle that is battery aging. Therefore, there is a need for research into battery aging, for which we have several recommendations. Firstly, battery aging for Li-ion batteries is still not fully understood, particularly by researchers that are in the field of the control of batteries. Therefore, there is a need for developing aging models that can be coupled with the known and commonly used electrochemistry-based models, such as the DFN model. For instance, while fatigue and stress effects on electrode particles have been studied and modeled, the connection of these effects to battery aging, in terms of modeling, has not been investigated, even though these fatigue and stress effects are considered to be a major contributor to aging. A second approach that can be taken to advance battery aging modeling, is to investigate aging models that only consider the observed effects of aging, rather than modeling specific aging mechanisms. For example, if there are two different aging mechanisms that lead to aging under the same circumstances, then there is no point in individually modeling these aging mechanism for the purpose of aging-aware charging. Only focusing on the observed aging effects instead of on the mechanisms may lead to interesting insights

into battery aging, and could lead to accurate battery aging models that can then be used for aging-aware charging, among other applications.

VARIABLE STEP-SIZE SOLVERS

In Chapter 2, we have proposed a highly computationally efficient model implementation that has led to a significant reduction in computation time. This implementation could be further improved by considering a variable-time-step discretization approach, rather than using the fixed-step backward Euler method of discretization, as was done in the proposed implementation. In a variable-time-step approach, the step size is varied throughout the simulation, where the step size is reduced to increase the model accuracy when the model dynamics are changing rapidly, and the step size is increased when the model dynamics are changing slowly. This could significantly reduce the simulation time of the DFN model further compared to the implementation proposed in Chapter 2.

8.2.2. PARMETERIZATION

PARAMETERIZATION OF BATTERY AGING MODELS

In the use of the capacity-loss side-reaction model for experimental validation of the considered aging-aware charging methods, we have determined the parameters of the aging model through a rather pragmatic approach. In determining the parameters, we have first estimated the DFN model parameters based on current/voltage data on a short time scale, and the parameters of the capacity-loss side-reaction model were assumed from literature. If aging data would have been available, the DFN model parameters could have been fixed, after which the aging model parameters could have been determined using the cycling data and the observed aging of the battery. However, in doing so, the assumption is made that the aging of the battery is not affected by the DFN model parameters, which is an assumption that does not actually hold. In order to improve the physical meaningfulness of the DFN model parameters, and the accuracy of the aging model, this assumption should not be made. Therefore, a possible research direction would be to investigate the use of both the observed aging data as well as current/voltage data to determine the parameters of the DFN model and the capacity-loss side-reaction model simultaneously.

EXPERIMENTAL VALIDATION OF PARAMETERIZATION

In Chapter 3, the results motivated the need for an approach that combines both parameter estimation using current/voltage data and parameter estimation through cell teardown. However, performing a cell teardown and validating this approach experimentally was outside the scope of this work. Therefore, there is still a need to experimentally validate this recommended approach. The two aforementioned parameter estimation approaches can possibly be combined, by using the cell teardown experiments to determine the possible range that a parameter can have based on the estimated measurement error. Other ways of determining the parameter ranges based on cell teardown can also be investigated.

COMPARISON OF SEVERAL CURRENT/VOLTAGE-BASED PARAMETER ESTIMATION METHODS

As stated in the introduction of Chapter 3, there are generally two approaches taken to estimate the DFN model parameters based on current/voltage measurements. One approach is to estimate some (or all) of the parameters simultaneously based on measured current/voltage data, which is also the approach that we have considered in our proposed model parameterization approach in Chapter 3. However, another approach is to design experiments specifically in an attempt to isolate the effects of parameters in the output. However, the justification for this approach is often lacking. Therefore, a possible research direction is to make a direct comparison between these two aforementioned model parameterization approaches. This could provide insight into the possible advantages and disadvantages of the considered approaches. This comparison could be done along similar lines as done in Chapter 3, where the influence of modeling errors could be included using a synthetic cell.

8.2.3. AGING-AWARE CHARGING

CLOSED-LOOP IMPLEMENTATION

In Chapter 7 of this thesis, we have experimentally validated an open-loop approach to the optimal-control-based aging-aware charging methodology using the DFN model, using the methods presented Chapter 6. In the experimental validation, this proposed approach has a worse Pareto front compared to the considered multi-stage CC-CV protocol, as the open-loop approach could not adequately compensate for modeling errors. Therefore, a possible research direction would be to consider the proposed approach in a closed-loop implementation, such as the closed-loop optimal-control approach presented in Chapter 1. An experimental validation of such as approach will provide insight into whether the proposed approach can actually achieve a significantly improved trade-off between charging time and aging compared to rule-based protocols. Furthermore, such a study would provide insight into how to implement the proposed approach in a closed-loop application.

8.2.4. STATE ESTIMATION OF THE DFN MODEL FOR OPTIMAL AGING-AWARE CHARGING

Continuing from the previous recommendation, an important part of the optimal-control-based approach to aging-aware charging taken in this work, is the state estimator. In a closed-loop optimal-control implementation, as presented in Chapter 1, the state estimator estimates the model states based on the observed output. These estimated states define the initial condition of the optimization problem that is solved to find the optimal input current. However, estimating the DFN model states is not trivial, as the DFN model states are likely not observable, as indicated by the results in Chapter 3 and Chapter 6, where we have observed that an equal output model accuracy can be obtained through significantly different internal state dynamics. Therefore, an investigation on how to estimate the DFN model states from the observed output should be considered.

8.2.5. INCLUDING THERMAL BEHAVIOR

Throughout this thesis, we have mostly considered isothermal battery models, as well as isothermal conditions for aging-aware charging, although in the developed TOOFAB toolbox, we have shown that it is possible to extend the DFN model implementation with a thermal model. Of course, in reality, the battery cell temperature can significantly fluctuate while charging, which should be considered when designing an aging-aware charging strategy, since aging is well known to be temperature-dependent. Therefore, a possible research approach is to extend the work that has been done in this thesis with thermal models. This could involve an investigation into how battery aging is affected by temperature, and how this relation can be modeled, rather than just using temperature as an aging indicator, as is often done in literature.

8.2.6. OPTIMIZATION UNDER UNCERTAINTY

In the experimental validation of the open-loop optimal-control based aging-aware charging approach in Chapter 7, we have observed the importance of feedback to account for modeling errors. However, introducing feedback, in this case, requires a state estimator, which as we have mentioned in Section 8.2.4, is not trivial to obtain. An alternative approach to introducing feedback is to account for the uncertainty in modeling when defining the constraints of the optimization problem, which could lead to a solution that is robust to modeling errors. While such an uncertainty-based open-loop approach could lead to a worse trade-off in charging time and aging compared to a closed-loop approach, it may have a significant advantage in computational complexity.

8.3. IMPLICATIONS

The contributions of this thesis can be used as a basis for future research, and have led to an advancement in aging-aware charging. The contributions made in battery modeling and implementation can facilitate the research into the analysis and control of batteries, through the use of computationally efficient models. Furthermore, the method of comparing various model parameterization approaches can be used as a framework to validate any model parameterization approach. An important part in this framework, is the consideration of modeling errors, and their impact on the resulting estimated parameters and the estimated states of the battery.

The main contribution of this thesis is the approach of systematically making a trade-off between computational complexity and accuracy of various methods. Using this approach, we have been able to considerably reduce the complexity of the optimal-control-based approach to aging-aware charging using elecrochemistry-based models. This has made an important step into using the proposed aging-aware charging approach in a closed-loop application, such that an optimal trade-off can be made between charging time and battery aging. In making a comparison between various aging-aware charging methods, we have shown that optimal-control-based algorithms that use electrochemical aging models lead to a better trade-off between aging and charging, while having a limited computational complexity. The implementation of this optimal-control-based method can lead to a more aging-aware use of batteries in electric vehicles, which can lead to shorter charging times and longer lasting batteries. As a result, these advance-

ments in aging-aware charging can contribute to a more sustainable society by accelerating the adoption of electric vehicles.

ACKNOWLEDGEMENTS

Over the last four years, I have had tremendous support from people around me to achieve the results presented in this thesis.

I would first like to express my gratitude towards my supervisor and promoter Tijs Donkers for all your guidance during my academic tenure. The start of our collaborations started in 2015, when you supervised my Bachelor's end project. At this point, your high level of involvement, positiveness, and endless enthusiasm were already very apparent to me, which did not make me think twice about pursuing my internship and graduation project during my Master's with you as well. Your qualities as a supervisor were a big contributor to then embark on my journey to do a PhD with you, although it did also help that the solicitation procedure consisted of an informal lunch. Throughout knowing you for almost 7 years now, I owe much of what I have learned to you. However, throughout all these years, you have not only been a great supervisor, but also a mentor who has helped me to grow on a personal level. Certainly your positive attitude has rubbed off on me as well. I have also thoroughly enjoyed our drinks together at the various conferences, and of course our over-the-Internet drink (together with Henk Jan) after our first journal paper together was published. For all this, I am very grateful, so thank you, Tijs.

I am indebted to my promoter Henk Jan Bergveld for his continued guidance. Your great experience and knowledge in batteries have had a major influence on the results presented in this thesis. Your more 'visual' take on modeling concepts has also often helped me to understand these concepts in a way that equations alone could sometimes not achieve. Your illustrative drawings were often followed with the saying that "a picture says more than a thousand words", although Tijs would always quickly refute this by saying that "an equation says more than a thousand pictures". These moments are also a testament to the level of humor that we have had in our meetings together with Tijs, for which I am also very grateful for. Your meticulous attention to detail is also inspiring, where I have often been perplexed at how you were able to find the smallest mistakes and inconsistencies when reviewing our draft papers and, of course, this thesis. Finally, I would like to thank you for your level of personal involvement, where I have been invited into your 'man-cave' and have seen a live performance of you playing in your band.

I would also like to thank the members of my promotion commission: Prof. Peter Notten, Prof. Fokko Mulder, Prof. Michel Kinnaert, Prof. Scott Moura, and Prof. Davide Raimondo. The feedback that you have provided has lifted the quality of this thesis to another level.

Thank you to my colleagues within the AUTODRIVE and EVERLASTING projects: Anouk Hol, Rahul Shah, Camiel Beckers, Aswin Linden, Thomas Gerrits, Dmitri Danilov, Luc Raijmakers, and Johannes Sturm. Special thanks to Anouk Hol for inviting me to present at VDL regularly as well as including me in the VDL family by inviting me to various social events. I would also like to thank Johannes Sturm in particular for our various

discussions together and his contributions in Chapter 3 of this thesis. Without his contributions, the results presented in that chapter would not have been possible. Finally I would like to thank Luc Raijmakers for our discussions and the collaboration that has led to the results presented in Chapter 7.

I am grateful for having worked with my colleagues at the Control Systems group, particularly Paul, Henrik, and Feye for all the discussions and coffee moments. With Feye and Henrik, having the application of batteries in common between us, allowed us to have fruitful discussions and exchange ideas. Thank you Henrik as well for letting me use your data that you had measured as a result of your thesis. It has greatly contributed to the results of Chapter 3. Thank you Paul for all the beers during my Master's when you were supervising me during my graduation project. It was a true pleasure working with you during my Master's, and I am glad that we could share an office afterwards, not only as colleagues, but also as friends.

Thank you as well to Daming, Giuseppe, Amritam, Mannes, Tom, Carlos, Ioannis, Karthik, Gustavo, Harm, Ruben, David, Shenglin, Clarisse, and many more for all the company and drinks at the various conferences, lunches, and group events. Special thanks goes to Will as well, who has taught me a lot about teaching and managing students during the Energy Management in Hybrid Vehicles course. Furthermore, I would like to thank Dmitri for our various discussions that we have had on battery modeling. Finally, I would like to thank Diana and Hiltje for not only taking care of the organizational tasks in our group, but also doing their best to keep interaction alive within the group when we could not see each other physically in Corona times.

I am very appreciative of all the support given by my friends and family during the course of my promotion. First, I would like to thank my friends Alan and Achmed, who have almost been like siblings to me. Our various gatherings and holidays together have been essential in providing some much-needed distraction. In particular, I would like to thank Alan for always trying to convince me to go on a vacation if he was going somewhere as well. Although it did not always work, I am glad that it did in the most cases, as it has brought me some great memories. I would also like to thank Prashant, with whom I have also had very good memories with.

Thank you to my siblings, Zokar, Ziar, Alan, and Ara. As siblings, we have always had a great bond, and I am very grateful for being able to regularly spend time with you all. I am also grateful for being able to find emotional support in you, and the ability to discuss any doubts or decisions going on in my life. I am also thankful for my siblings-in-law, Zhakar and Aram, with whom I have spent great time with. Thank you Zhakar for your delicious food and hospitality whenever I come over. With Aram, I have especially enjoyed our evenings together talking and drinking wine. Furthermore, although Madeleine is officially not my sister-in-law, I already view you as family, and I am also grateful for the time that we have spent together, particularly when playing board games. My thanks also goes to my girlfriend's mother, Margaret, for her kindness and the constant supply of delicious homemade syrup. Finally, I am also thankful towards my nieces and nephews, Honi, Las, Aryas, Rozi, and Arin, who have all provided me with a source of happiness and joy.

I also owe a huge debt of gratitude to my girlfriend, Klaudia. Your continuous display of love and support has been instrumental for me to stay in a healthy state of mind.

Thank you as well for your patience when there were periods where I could not spend much time with you. You are an amazing person, and I am glad to have had you by my side.

Finally, I want to thank my parents, to whom I dedicate this thesis to. Daya Baba damawe zor supastan bkam lo hamw aw yarmati w palpshtiai la mntan krdia la hamw qonaxakai xwnen hata amwro. Wa aw briaratan hatntan Bo Hollanda barz danrxenm Ka darfati awai ba mn xwendnakam ba sarkawtwi tawaw bakm awmro. Ango hamw kat xoshawisti xotan bo MN dwpat krditawa tananat law katanai Ka baxotan BA Kati saxt da tepariwn. Tananat law katanai Ka MN bryarekm bawa Ka dzh BA bahakani ewa bwa pshtan te nakrdwm w hamshia palshtm bwn la xoshi w naxoshai da. Loia hamisha supasgwzari ewam.

CURRICULUM VITÆ

Zuan Khalik was born on 27-03-1993 in Salah Eddin, Iraq (Kurdistan). After finishing his pre-university eduction in 2012 at IJsselcollege in Capelle aan den IJssel, he studied Electrical Engineering (track: Automotive) at the Eindhoven University of Technology. In 2017 he graduated within the Control Systems group at the Eindhoven University of Technology on ecodriving and energy management for hybrid-electric vehicles. He then continued in the Control Systems group as a PhD candidate, carrying out research that involves modeling and optimal control for ageing-aware charging of batteries, of which the results are presented in this dissertation. The research has been conducted as a part of the projects 'Electric Vehicle Enhanced Range, Lifetime And Safety Through INGenious battery management' (EVERLASTING) and 'Advancing fail-aware, fail-safe, and fail-operational electronic components, systems, and architectures for fully automated driving to make future mobility safer, affordable, and end-user acceptable' (Autodrive) within the Horizon 2020 program of the European Union.